
FACULTY
OF MATHEMATICS
AND PHYSICS
Charles University

# DOCTORAL THESIS

Martin Šubr

## Optical Responses of Biomolecules on Regular Metal Plasmonic Nanostructures

Institute of Physics of Charles University

Supervisor of the doctoral thesis: prof. RNDr. Marek Procházka, Dr.

Study programme: Physics
Study branch: Biophysics, Chemical and Macromolecular Physics

Prague 2018

I declare that I carried out this doctoral thesis independently, and only with the cited sources, literature and other professional sources.

I understand that my work relates to the rights and obligations under the Act No. 121/2000 Coll., the Copyright Act, as amended, in particular the fact that the Charles University has the right to conclude a license agreement on the use of this work as a school work pursuant to Section 60 paragraph 1 of the Copyright Act.

In…....…..... date..... Martin Šubr

I would like to thank my supervisor, prof. Procházka, for his guidance, constant help and valuable advice during writing this thesis. My thank also goes to other members of the Division of Biomolecular Physics, namely prof. Štěpánek, doc. Praus, dr. Kočišová and dr. Peksa for help with experimental measurements and fruitful theoretical discussion. Last but not least, I would like to express my gratitude to our external collaborators, namely from the Department of Macromolecular Physics (group of doc. Kylián) where the plasmonic nanostructures were fabricated, and the group of dr. Veis (Institute of Physics of Charles University) for assistance with ellipsometry measurements.

Financial support from the Czech Science Foundation (projects No. P205/13/20110S, P205/12/G118 and 18-10897S) and Charles University (projects SVV 260092, SVV 260214, GAUK No. 572216 and UNCE/SCI/010) is gratefully acknowledged.

**Title**: Optical Responses of Biomolecules on Regular Metal Plasmonic Nanostructures

**Author**: Martin Šubr

**Department**: Institute of Physics of Charles University

**Supervisor of the doctoral thesis**: prof. RNDr. Marek Procházka, Dr., Institute of Physics of Charles University

**Abstract**: Adsorption of molecules on metal plasmonic nanostructures leads to significant enhancement of many optical processes, such as Raman scattering (surface-enhanced Raman scattering – SERS) or fluorescence (surface-enhanced fluorescence – SEF). Two groups of substrates were tested within this thesis: (i) Silver nanorods prepared by oblique angle vapor deposition, and (ii) silver and gold nanoislands growing on magnetron-sputtered polytetrafluoroethylene film. Step-by-step optimization process was performed on the nanoislands in order to obtain optimum SERS sensitivity and reproducibility. Detailed SERS intensity profiles were obtained using gradient nanostructures with the localized surface plasmon resonance (LSPR) condition varying across the sample and three different excitation wavelengths. It was also found that spectral position and height of the LSPR band can be controlled simultaneously using mixed gold/silver nanoislands. Detailed investigation of polarization- and angular- dependences of anisotropic silver nanorods was performed in the 90°-scattering geometry in which two out of three angles determining the nanorod spatial orientation were varied simultaneously. A theoretical model for elucidation of the anisotropic SERS properties based on ellipsometric characteristics of the substrate is presented. Silver nanoislands were used for SEF study of riboflavin on PTFE spacer of various thicknesses. Very good correspondence between SEF enhancement and fluorophore lifetime shortening was found.

**Keywords**: Surface-enhanced Raman scattering, biomolecules, surface-enhanced fluorescence, nanoislands, nanorods

**Název**: Optické odezvy biomolekul na pravidelných kovových plasmonických nanostrukturách

**Autor**: Martin Šubr

**Ústav**: Fyzikální ústav UK

**Vedoucí disertační práce**: prof. RNDr. Marek Procházka, Dr., Fyzikální ústav UK

**Abstrakt**: Adsorpce molekul na kovové plasmonické nanostruktury vede k výraznému zesílení řady optických procesů, jako je Ramanův rozptyl (povrchem zesílený Ramanův rozptyl – SERS) nebo fluorescence (povrchem zesílená fluorescence – SEF). V rámci práce byly testovány dva druhy substrátů: (i) Stříbrné nanotyčky připravované naprašováním pod šikmým úhlem, a (ii) stříbrné a zlaté nanoostrůvky rostoucí na teflonovém filmu připravované magnetronovým naprašováním. Postupnou optimalizací procesu přípravy byla získána optimální SERS citlivost i reprodukovatelnost. Podrobné SERS-intenzitní profily byly získány při použití tří excitačních vlnových délek a gradientních struktur, kde se poloha plazmonové rezonance (LSPR) mění spojitě v rámci konkrétního substrátu. Bylo zjištěno, že spektrální poloha a výška LSPR pásu mohou být nezávisle modifikovány při použití smíšených zlato/stříbrných ostrůvků. Dále byla provedena detailní analýza polarizačních a úhlových závislostí stříbrných nanotyček v pravoúhlé geometrii rozptylu, která umožňuje nezávisle měnit dva ze tří úhlů, které určují prostorovou orientaci nanotyček. Pro teoretickou analýzu získaných výsledků byl použit model využívající elipsometrické parametry vzorku. Stříbrné ostrůvky byly dále použity ke studiu povrchem zesílené fluorescence riboflavinu s použitím teflonového spaceru různých tlouštěk. Byla získána velice dobrá shoda mezi SEF zesílením a zkracováním dob života.

**Klíčová slova**: Povrchem zesílený Ramanův rozptyl, biomolekuly, povrchem zesílená fluorescence, nanoostrůvky, nanotyčky

# Contents

# Preface

Optical spectroscopy is represented by a widely used set of techniques for investigation of various biological molecules and their interactions. Among its biggest advantages, high specificity, ease of sample handling, reduced time consumption and low cost stand out as the most prominent. For these reasons, optical spectroscopy has proven useful in a wide range of biophysical, biochemical or medical applications. However, the need for reduced detection limits is still opposed by rather low cross section of the underlying physical processes and/or background emission from the sample (such as in the case of Raman spectroscopy) or low quantum yields and photobleaching (such as in the case of fluorescence). These limitations may be partly overcome by enhancing the optical signal from molecules placed in the vicinity of roughened metal nanostructures. The most established is Raman scattering (surface-enhanced Raman scattering – SERS), followed by fluorescence (surface-enhanced fluorescence – SEF) and absorption (surface-enhanced infrared absorption – SEIRA). High sensitivity of the surface-enhancing spectroscopic techniques along with the molecular specificity makes these methods extremely attractive for molecular detection in such fields like analytical chemistry, food safety monitoring, security systems, medical diagnostics and many others.

This thesis is organized as follows: The first part is devoted to theoretical introduction of the underlying physical processes, especially to basic description of interaction of light with matter such as absorption, emission (fluorescence) and light scattering. Particular focus is placed on modification of these processes in the vicinity of plasmonic nanostructures, followed by a brief summary of the most important plasmonic nanostructures commonly used, especially those studied within this thesis. Second part of this thesis gives basic description of the experimental methods used. Section 4 summarizes all main results which have been published in 5 peer-reviewed journals, 1 article is currently being considered for publication in *Vacuum* and 1 article is under preparation (10$^{th}$ December, 2018). All the original works mentioned above are attached at the end of this thesis.

# 1. Theoretical part

## 1.1. Interaction of light with matter – classical description

Interaction of light with matter can take many distinct forms. When light is incident upon a medium of different index of refraction, part of the energy of the incident light is reflected, whereas the other component propagates through the medium and deviates from a straight continuation of the incident light ray. Both the reflected and the transmitted light can undergo a change in polarization as determined by the Fresnel equations. All these macroscopic phenomena are derivable from Maxwell's equations and were known already in the 19th century [1]. The ratio of the speed of light in vacuum ($c$) to the speed of light in another medium ($v$) defines the refractive index $n$ of the medium: $n = \frac{c}{v}$. As we will show, the refractive index inherently depends on frequency ($\omega = 2\pi f$) of light as it allows for different responses of materials to different frequencies of the incoming radiation. This dependence, causing different plane waves to travel at different speeds in a given material, is termed dispersion. The refractive index is related to the relative permittivity $\varepsilon_r$ by a well-known formula $n^2(\omega) = \varepsilon_r(\omega)$, which is valid for non-magnetic materials (relative permeability $\mu_r \sim 1$). With no absorption involved, both the relative permittivity and the refractive index are real numbers. In general, however, both the refractive index and the relative permittivity become complex within a certain range of frequencies, which is when absorption occurs. Indeed, by inserting the equation of the plane wave propagating in the $z$-direction

$$\vec{E} = \vec{E}_0 e^{i(kz-\omega t)} \tag{1.1}$$

into the wave equation [1]

$$\Delta\vec{E} - \mu\varepsilon\frac{\partial^2\vec{E}}{\partial t^2} - \mu\sigma\frac{\partial\vec{E}}{\partial t} = 0 \tag{1.2}$$

we obtain

$$\tilde{k}^2 = (k_R + ik_I)^2 = \mu\varepsilon\omega^2 + i\mu\sigma\omega = \frac{\omega^2}{c^2}\left(\varepsilon_r + i\frac{\sigma}{\varepsilon_0\omega}\right), \tag{1.3}$$

where $\tilde{k}$ denotes the wavevector with the real part $k_R$ and the imaginary part $k_I$, $\varepsilon = \varepsilon_0\varepsilon_r$ is the permittivity of the given medium ($\varepsilon_0$ being the permittivity of the vacuum and $\varepsilon_r$ the relative permittivity), $\mu$ permeability of the medium, $i = \sqrt{-1}$

and $\sigma$ the electric conductivity. Complex quantities are marked with a tilde. Then, the plane wave takes the form

$$\vec{E} = \vec{E}_0 e^{i(k_R z - \omega t)} e^{-k_I z}, \tag{1.4}$$

from which it is obvious that the non-zero imaginary part of the wavevector, arising from non-zero conductivity, is responsible for exponential decay of a light wave propagating in an absorptive medium. In terms of light intensity, we have

$$I = |E|^2 = |E_0|^2 e^{-2k_I z} = I_0 e^{-2k_I z}, \tag{1.5}$$

which is known as the Lambert's law [2, 3]. Clearly, absorption coefficient for a given material is related to the imaginary part of the wavevector. Similarly, in an absorptive medium, the refractive index and relative permittivity of the medium become complex, obeying the relationships

$$\tilde{n}^2 = (n_R + i n_I)^2 = \frac{c^2}{\omega^2}\tilde{k}^2 = \frac{c^2}{\omega^2}(k_R + i k_I)^2, \tag{1.6}$$

$$\tilde{n}^2 = \tilde{\varepsilon}_r. \tag{1.7}$$

This relationship allows to compute the explicit formulae for $\tilde{n}$, $\tilde{k}$ and $\tilde{\varepsilon}_r$ (which are linked by eqs. 1.3, 1.6 and 1.7) as functions of $\sigma$ and $\omega$.

Functional relationship between the frequency and the phase velocity (dispersion) or light attenuation (absorption) is a result of specific molecular constitution of matter which is phenomenologically manifested in eq. 1.3 by a non-zero conductivity. Although interaction of light with atoms or molecules can not be fully described unless quantum theory comes into play, even by using rather simplified classical models one can obtain a basic insight into the interaction of light with matter and help to explain a large number of optical phenomena. Since correlation between macroscopic parameters and atomic or molecular structure is of great importance to different spectroscopic techniques, in the following paragraphs, we will investigate the microscopic nature of the index of refraction. In the next section, particular focus will be placed on derivation of the dielectric function of metals. This approach will turn out to be the key to understanding of the electromagnetic mechanism of enhancement in various plasmonic methods, such as SERS or SEF.

In general, molecules respond to an external time-dependent electromagnetic field by producing an oscillating induced dipole (in addition to the one they may already possess). Applying an electromagnetic field to a group of atoms or molecules causes the electron distribution to be distorted, which in turn cause the electromagnetic wave's phase velocity to be slowed in the material. This approach actually provides an insight into the refractive index of materials from a microscopic standpoint [1]. In the approximation of a linear response, the induced dipole moment is propotional to the external electric field

$$\vec{p} = \vec{\alpha}\vec{E}, \tag{1.8}$$

where $\vec{\alpha}$ denotes polarizability represented by a tenzor in a three-dimensional space (the directions of $\vec{p}$ and $\vec{E}$ do not necessarily have to be parallel) with generally complex frequency-dependent constituents (as there may be a particular phase shift between the time-dependent electromagnetic field and the oscillating induced dipole). Therefore, the polarizability tenzor is considered to represent the bridge between the macroscopic Maxwell's theory and the structure of the material.

According to a simplified Lorentz model, electrons in dielectrics can be viewed as harmonic oscillators with the force binding the electron to the nearest nucleus propotional to its displacement from equilibrium. Thus, the differential equation for an electron bound to the nucleus with such an elastic force driven by an external electric field takes the form

$$m\ddot{x} + m\gamma\dot{x} + kx = -eE_x, \tag{1.9}$$

where $m$ denotes the electron mass, $e$ the electron charge, $\gamma$ the damping factor and $k$ is a positive constant. With no loss of generality, we suppose that the movement is restricted to the $x$-direction. As the electron displacement $x$ follows the oscillation of the external electric field, assumed in the form $E_x = E_{0x}e^{-i\omega t}$, we find the particular solution of the eq.1.9 in the form

$$\tilde{x} = \tilde{x}_0 e^{-i\omega t}. \tag{1.10}$$

We again use a complex notation as there can exist a phase shift between the field $E$ and the displacement $\tilde{x}$. A double-deriving of eq. 1.10 and putting in eq. 1.9 yields

$$\tilde{x}_0 = -\frac{eE_{0x}}{m}\frac{1}{\omega_0^2 - \omega^2 - i\gamma\omega}. \tag{1.11}$$

In eq. 1.11, the natural frequency of the electron: $\omega_0 = \sqrt{\frac{k}{m}}$, has been introduced. Amplitudes of the electric dipole moment $d$ and of the polarization of the material $P$ are equal to

$$d = -ex_0, \qquad P = Nd = \frac{Ne^2 E_{0x}}{m} \frac{1}{\omega_0^2 - \omega^2 - i\gamma\omega}, \qquad (1.12)$$

where $N$ denotes the total number of dipoles in a unit volume. Comparison to a well-known relation between polarization and electric field amplitude suggests the formula for the frequency-dependent relative permittivity (dielectric constant) of the material $\varepsilon(\omega)$ in the form

$$\varepsilon(\omega) \equiv \tilde{\varepsilon}_r = 1 + \frac{Ne^2}{\varepsilon_0 m} \frac{1}{\omega_0^2 - \omega^2 - i\gamma\omega}. \qquad (1.13)$$

The above expression shows that the relative permittivity (dielectric function) depends on frequency of the electromagnetic field. When $\omega$ is sufficiently distant from $\omega_0$, the damping term in eq. 1.13 can usually be neglected. Thus, $\varepsilon(\omega)$ becomes real and no absorption occurs. By contrast, if $\omega$ approaches $\omega_0$, the damping term in eq. 1.13 becomes dominant and it is when absorption takes place. For $\omega = \omega_0$, the system is said to be in resonance as it experiences the maximum energy transfer from the electromagnetic wave to the molecules [1, 2] [1]. In spectroscopic experiments, a specific molecular signature consisting of a set of spectral lines is usually observed, which can be interpreted as the fact that a molecule possesses different natural frequencies $\omega_{0i}$ $(i = 1, 2, 3, \ldots)$ and absorption occurs when frequency of the incident light matches any of these proper frequencies. Let us notice that the corresponding expression in quantum mechanics, responsible for the strength of coupling between the electromagnetic field and matter, is the square of the transition matrix element, which will be briefly discussed later on.

[1] Under the previous approximation, the shape of the spectral line is dictated by the Lorentz curve with the damping constant $\gamma$ being associated with the half-width of the resonance curve (the bigger the damping constant the broader the resonance curve and vice versa).

## 1.2. Interaction of light with matter – quantum description

Although the classical Lorentz model is very illustrative, it can not describe the interaction of light with matter in full scope. According to basic principles of quantum mechanics, atoms and molecules can occupy only discrete energy levels, given as solutions (eigenvectors) of the Schrödinger's equation, and all we can predict are transition probabilities between different quantum states, induced by radiation of a particular frequency. In the case of molecules, an often used approximation (Born-Oppenheimer) for solving the Schrödinger equation enables separation of nuclear and electronic motions [4]. Therefore, each molecule possesses a set of discrete electronic levels, each of which holds different vibrational levels. Energy differences between electronic levels are roughly ~ 10× – 100× bigger than energy differences between neighbouring vibrational levels, and thus correspond to ~ 10× – 100× energetically more demanding transitions. Generally, energy differences between vibrational levels correspond to energies of infrared (IR) photons, whereas energy differences between electronic levels mostly match energy of UV/Vis photons. In the state of thermodynamic equilibrium, populations of respective energy levels obey the Boltzmann distribution, which says

$$\frac{N_i}{N_j} = \frac{g_i}{g_j} \cdot e^{-\frac{E_i - E_j}{k_B T}}, \tag{1.14}$$

where $k_B$ is the Boltzmann constant, $T$ the thermodynamic temperature, $N_i$ and $N_j$ respective populations with energies $E_i$ and $E_j$ and degeneracy factors $g_i$ and $g_j$. Therefore, at room temperatures, for most vibrational levels, there will be less than ~ 1/100 – 1/1000 molecules occupying higher energy states, and this ratio is yet many orders of magnitude lower for the electronic states.

Among all possible interactions of light with molecules, transitions between different quantum states become most probable when frequency of the incident light (a photon) closely matches the energy differences between proper molecular levels. Basically, when light of the frequency corresponding to energy difference between different energy levels of the molecule is incident on a sample, absorption usually occurs, during which the molecules gain energy needed for a transfer to a higher energy state and the electromagnetic field loses the same portion of energy. Absorption may taky place between different vibrational levels within a given

(usually ground) electronic state of the molecule (IR absorption) or between different electronic states (UV/Vis absorption). Moreover, the electronic absorption is very often accompanied by a change in the vibrational structure (vibronic transitions).

The probability of transition between two quantum states of an atom/molecule is in a first approximation governed by the Fermi's golden rule. This rule says that in order for the transition to be allowed, the matrix element

$$\langle 2|\widehat{W}|1\rangle \tag{1.15}$$

must be different from zero. In eq. 1.15, $|1\rangle$ represents the wavefunction of the initial state, $\langle 2|$ the wavefunction of the final state and $\widehat{W}$ is a perturbation operator, which usually corresponds to the presence of the electromagnetic wave [5]. Thus, matching the frequency of the incident radiation with the energy difference between corresponding quantum levels is a necessary but not sufficient condition for energy exchange between light and matter to take place. Closer analysis shows that further conditions must be satisfied, known as the selection rules [2, 4, 6]. Symmetry of both the final and the initial quantum states imposes some restrictions on quantum numbers of the states between which the transition may take place, some of which will be in brief discussed in the following lines.

A molecule comprised of $N$ atoms possesses $3N$ degrees of freedom altogether, i.e. 3 independent variables for each atom are needed for unambiguous description of the molecule. However, 3 out of these $3N$ variables are associated with translational motion of the molecule as a whole and further 3 variables with rotational motion. In vibrational spectroscopy, we are mostly concerned about internal movements of the molecule, and therefore 6 degrees of freedom are abundant [2]. The resting $3N-6$ (internal) degrees of freedom represent internal deformations (vibrations) of the molecule. In the approximation of small oscillations around equilibrium positions, one can consider molecular vibrations as a set of $3N-6$ independent linear harmonic oscillators (normal vibrational modes), each of which is characterized by its reduced mass, force constant and frequency. Every mode is represented by a periodically oscillating position of each atom of the

[2] For a linear molecule, any rotation can be thought of as a superposition of two rotations along two independent axes, considering that the rotation around the interparticle axis has no physical meaning. That is why linear molecules do not have $3N-6$ internal degrees of freedom, but $3N-5$. We will not distinguish between linear and nonlinear molecules within this thesis for simplicity.

molecule and can be ascribed a certain quantum number. Thus, vibrational state of the molecule is determined by a set of $3N-6$ quantum numbers (representing particular vibrational modes). As a consequence, the vibrational wavefunction may be decoupled into a product of $3N-6$ wavefunctions of linear harmonic oscillators, however, each of them in a different coordinate (so-called normal coordinate).

The general term 1.15 is further simplified using so-called long wave approximation, which relies on the fact that molecules are usually much smaller than the optical wavelength. This approximation allows to rewrite the perturbation operator in the form of the electric dipole moment of the molecule ($\vec{d}$) and the probability of the transition then derives from the transition dipole moment matrix element

$$\langle 2|\hat{d}|1\rangle \tag{1.16}$$

(in quantum mechanics, the molecular dipole moment becomes an operator). The electric dipole moment can be expanded in a Taylor series with respect to normal vibrational coordinates ($q_i$) with the first non-zero term determining the selection rules:

$$\vec{d} = \vec{d}|_{q_{i0}} + \sum_{i=1}^{3N-6} \frac{\partial \vec{d}}{\partial q_i}|_{q_{i0}}(q_i - q_{i0}) + \cdots \tag{1.17}$$

Obviously, the lowest contributing term in the expansion 1.17 is directly proportional to a linear function of normal coordinates. Since

$$\langle m|n\rangle \sim \delta_{m,n}, \qquad \langle m|q|n\rangle \sim \delta_{m,n\pm1} \tag{1.18}$$

for $|m\rangle$, $|n\rangle$ being the wavefunctions of a linear harmonic oscillator, one may deduce that the only possible vibrational transitions (in the lowest degree of approximation) take place between a given vibrational mode whose quantum number changes by 1 and the quantum numbers of the other modes remain unchanged (fundamental transitions). Moreover, the intensity of a given vibrational line is proportional to the change in the dipole moment during the given vibrational motion. Since the dipole moment is a vector quantity, the transition probability is expected to scale with the projection of light polarization in the direction of the transition dipole moment of the molecule. In the case of randomly oriented molecules, this effect is averaged out

(a closer look on the polarization effects in spectroscopy is provided in our review article [5], Attachment A5).

Apart from purely vibrational transitions within one electronic state of a molecule, transitions between different electronic states may also be invoked. As already mentioned, these transitions are very often accompanied by changes in vibrational quantum numbers, giving rise to vibronic structure of the purely electronic absorption/emission band. Due to the fact that the position of the electronic energy minimum with respect to a given normal coordinate may change upon excitation of the molecule to a higher electronic state, eqs. 1.18 may no longer have to be valid. Assuming that $|m\rangle$ and $|n\rangle$ are vibrational wavefunctions in different electronic states, their overlap is no longer necessarily zero, which gives rise to a wider variety of allowed transitions, such as combinations (2 or more different vibrational modes change their quantum number) and overtones (a vibrational mode changes its quantum number by > 1).

After absorption, the molecule is found in a temporal state of thermodynamic disequilibrium, which is soon after followed by removal of the energy excess, which restores the Boltzmann distribution. In principle, there are several ways how a molecule in an excited state can lose its energy and return back to the ground state: basically, radiative and non-radiative decay pathways can be distinguished. In the case of absorption to a higher electronic state (and higher vibrational state at the same time), molecules in condensed phases usually release a part of their excitation energy in the form of heat and cross to a ground vibrational state (still being in an elevated electronic state). This process is termed the internal conversion. The ensuing relaxation process is a result of several competing processes: The energy excess may again dissipate in the form of heat or in the form of radiation red-shifted with respect to the excitation frequency. The latter process is called luminescence, which can be defined as the spontaneous emission of radiation from an excited electronic state to a ground state [3]. Luminescence can be further classified into fluorescence, where the transition takes place between two electronic energy levels of the same spin multiplicity (usually between two singlet states), and phosphorescence, where the

[3] Apart from absorption and emission of light, third process of interaction of light with matter can be distinguished, which is termed stimulated emission. In the stimulated emission, light of resonance frequency induces the transition from a higher excited state to a lower state. The process of stimulated emission is important for the function of lasers.

spin multiplicity is changed during the crossing (the crossing usually takes place between a singlet and a triplet state).

Typically, absorption occurs in about $\sim 10^{-15}$ s, the internal conversion within $10^{-12}$ s or less and typical fluorescence lifetimes are near $10^{-8}$ s [7]. In the case of phosphorescence, transition to the ground state of the opposite spin orientation is forbidden and thus corresponding lifetimes are much longer ($10^{-3} – 10^{0}$ s) [7].

Supposing that both radiative and non-radiative mechanisms contribute to the fluorescence decay [4], the total decay rate will be the sum of partial decay rates attributable to respective mechanisms:

$$k_{tot} = k_{nr} + \Gamma, \tag{1.19}$$

where $k_{nr}$ denotes the non-radiative decay rate, $\Gamma$ the radiative decay rate and $k_{tot}$ the total decay rate. The partial lifetimes are coupled to the corresponding decay rates via the equations

$$\frac{1}{\tau_F} = k_{tot}, \qquad \frac{1}{\tau_r} = \Gamma, \qquad \frac{1}{\tau_{nr}} = k_{nr}. \tag{1.20}$$

In eq. 1.20, $\tau_r$ represents the radiative lifetime, $\tau_{nr}$ the non-radiative lifetime and $\tau_F$ the total lifetime (when both radiative and non-radiative decay pathways are present). Combination of eqs. 1.19 and 1.20 yields

$$\frac{1}{\tau_F} = \frac{1}{\tau_r} + \frac{1}{\tau_{nr}}. \tag{1.21}$$

After exciting the sample with a laser pulse much shorter than the respective lifetimes, the population of the elevated state would drop as

$$N(t) = N_0 e^{-k_{tot}t} = N_0 e^{-\frac{t}{\tau_F}}, \tag{1.22}$$

where $N_0$ corresponds to the number of molecules in the elevated electronic state at the time $t = 0$. Since

$$\langle t \rangle = \frac{\int_0^\infty tN(t)dt}{\int_0^\infty N(t)dt} = \tau_F, \tag{1.23}$$

$\tau_F$ may also be interpreted as the average time the molecule stays in a higher excited state. In a heterogeneous environment, fluorophores may be found to exhibit more

[4] Similar considerations also hold for the case of phosphorescence.

complex intensity decay, exhibiting a distribution of lifetimes obeying multiexponential behaviour [7].

The proportion of the radiative decay in the total fluorescence decay (or equivalently the ratio of the number of photons emitted to the number of those absorbed) defines the luminescence quantum yield:

$$\mathrm{Q}_0 = \frac{\Gamma}{\Gamma + k_{nr}}, \tag{1.24}$$

which is always less than unity. Both the lifetime and quantum yield of a fluorophore strongly depend on the surrounding environment, pH, temperature, solvent polarity, presence of a specific ligand etc. [7]

The last types of interaction of light with matter that will be studied in this section are light-scattering processes. As already mentioned, the most probable optical transitions occur when the energy quanta match the energy differences between two given energy levels of a molecule (resonance processes). Processes that do not satisfy this requirement are forbidden in the first-order perturbation theory and thus intrinsically very weak. Light scattering can be explained from a classical standpoint by the fact that electromagnetic waves induce oscillating electric dipoles in the molecules (generally electric and magnetic multipole moments among which the electric dipole moment is usually by far the most significant one), which become a source of secondary (scattered) radiation [6, 8, 9]. Generally, light scattering processes can be classified as elastic (Rayleigh), which do not involve net exchange of energy between the radiation and the molecule (i.e. the frequency of the scattered radiation is the same as that of the incident radiation) and inelastic (Raman), accompanied by a change in the internal energy of the sample. All the optical processes described above are schematically depicted in Fig. 1.

A common insight into the existence of the light-scattering processes is provided by eq. 1.8. After expanding molecular polarizability in the Taylor series with respect to normal vibrational coordinates, we obtain

$$\vec{p} = \left( \overleftrightarrow{\alpha}|_{q_{i0}} + \sum_{i=1}^{3N-6} \frac{\partial \overleftrightarrow{\alpha}}{\partial q_i}|_{q_{i0}} (q_i - q_{i0}) + \cdots \right) \vec{E}. \tag{1.25}$$

Since the term $q_i - q_{i0}$ oscillates at the frequency of molecular vibrations ($\omega_i$), one may expect that after illuminating the sample with monochromatic light (say of

frequency $\omega_0$), in the spectrum of the scattered radiation will not only be present the constituent with the frequency $\omega_0$, but even frequencies

$$\omega = \omega_0 \pm \omega_i, \qquad i = 1, 2, \ldots 3N - 6, \tag{1.26}$$

i.e. frequencies that are shifted from the incident frequency by specific values.

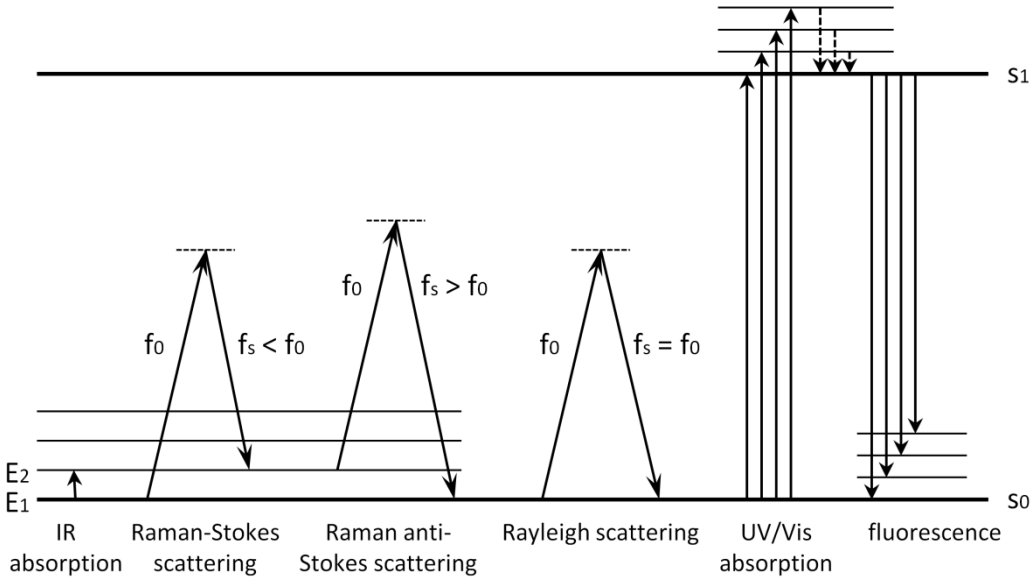


Figure 1. A simplified diagram of molecular energy levels. Purely electronic states are marked in bold, corresponding vibrational levels are depicted as solid lines, virtual states are marked as dashed lines. $s_0$ denotes the ground electronic state (assumed to be a singlet) and $s_1$ denotes the first excited electronic singlet state. For simplicity, only 2 out of $3N - 6$ sets of vibrational levels are shown in the ground state and 1 is shown in the excited electronic state. Electronic (UV/Vis) absorption usually takes place between the ground state and different vibrational levels of the excited singlet state. Fluorescence usually takes place between the lowest vibrational level of the excited singlet state and different vibrational levels of the ground state. IR absorption transitions occur between two vibrational levels within the same vibrational mode with a change in the quantum number by 1. The scattering processes are classified into elastic (with no net energy exchange between light and matter, such as the Rayleigh scattering) and inelastic (Raman-Stokes, where photons lose energy after the interaction with the molecule, and Raman anti-Stokes, where photons gain energy after the interaction).

According to Fig. 1, Raman scattering can be thought of as a process in which the following sequence occurs: An annihilation of a photon of energy $hf_0$, at the same time creation of a new photon with slightly different energy $hf_s$, and the transition of the molecule from an initial quantum state $|1\rangle$ (possessing an energy $E_1$) to a final quantum state $|2\rangle$ (possessing an energy $E_2 = E_1 + hf_0 - hf_s$) [8].

However, the energy $hf_0 + E_1$ does not have to correspond to any stationary state of the molecule. That is why Raman scattering is sometimes interpreted in terms of so-called virtual states as a transition from an initial stationary state $|1\rangle$ to a so-called virtual state, which is immediately followed by an emission of a secondary photon, which brings the molecule to a final quantum state $|2\rangle$.

If $E_2 > E_1$ (the final vibrational state is more energetic than the initial state), the energy of the emitted (secondary) photon is decreased at the expense of the increase in the internal energy of the molecule. This transition is called Stokes scattering. By contrast, if the roles of the quantum states $|1\rangle$ and $|2\rangle$ are swapped, the energy of the emitted photon is increased at the expense of the decrease in the internal energy of the sample. This transition is called anti-Stokes scattering. According to the law of conservation of energy, we have

$$hf_0 = hf_s + E_2 - E_1 \tag{1.27}$$

for Stokes scattering, and analogously

$$hf_0 = hf_s - (E_2 - E_1) \tag{1.28}$$

for anti-Stokes scattering. In both cases, $f_0$ denotes the frequency of the incoming radiation, $f_s$ the frequency of the scattered radiation and $h$ the Planck's constant.

In Raman spectroscopy, shifts of vibrational frequencies from the incident beam frequency are measured (usually in the units of wavenumbers), that is why Raman spectroscopy is considered a technique of vibrational spectroscopy complementary to IR absorption spectroscopy. As follows from eq. 1.25, intensity of a given Raman line is proportional to the derivative of the polarizability of the molecule with respect to the corresponding normal coordination. Thus, in order for a given line to be observed in Raman spectrum of a particular molecule, the polarizability of the molecule must necessarily change during the vibrational motion. The most polarizable molecules are that with "ring-like" structures possessing a large number of delocalized electrons in $\pi$ orbitals, such as aromatic compounds and fluorescence dyes. According to a well-established notion that light scattering happens whenever an inhomogeneity (in the scale of $\lambda$) occurs, molecular vibrations may be viewed as the inhomogeneities giving rise to Raman scattering.

From the quantum-mechanical point of view, the probability of transition between two quantum states by means of the Raman scattering is derived using second-order time dependent perturbation theory. A molecular quantity describing the disposition to $|1\rangle \rightarrow |2\rangle$ transition by means of the Raman scattering is a second-rank tensor [8]

$$\alpha_{pq}^{12} = \sum_{s \neq 1,2} \left[ \frac{\langle 2|\hat{d}_p|s\rangle\langle s|\hat{d}_q|1\rangle}{E_1 - E_s + hf_0} + \frac{\langle 2|\hat{d}_q|s\rangle\langle s|\hat{d}_p|1\rangle}{E_2 - E_s - hf_0} \right], \tag{1.29}$$

where $E_1$ and $E_2$ denote the energies of the initial ($|1\rangle$) and final ($|2\rangle$) quantum states of the molecule, $\hat{\vec{d}}$ is the electric dipole moment operator and the s-indices refer to all remaining quantum states of the molecule. The intensity of a given Raman spectral line is

$$I \sim P \cdot (e_p^{sc} \alpha_{pq}^{12} e_q^i)^2 \cdot \theta(T) \cdot f_{sc}^4, \tag{1.30}$$

where $P$ is the laser power, $f_{sc}$ frequency of the scattered radiation, $\vec{e}^{sc}$ the unit vector of the scattered field and $\vec{e}^{i}$ the unit vector of the incident field [5], and $\theta(T)$ is a temperature-dependent factor, which can be in the state of thermodynamic equilibrium worked out from the Boltzmann distribution (eq. 1.14). Thus, the intensities of Stokes lines are usually much higher than the intensities of anti-Stokes lines, because the probability of a molecule occupying the ground state is much higher than the probability of occupying a higher excited state. Directions $\vec{e}^{i}$ and $\vec{e}^{sc}$ are determined by the illumination-observation geometry, including the scattering angle and polarization of the incident beam (and possibly also polarization of the collected beam). This aspect is in more detail discussed in our review article [5] (Attachment A5).

In normal Raman spectroscopy, the frequency of the excitation line is chosen so that its energy is far below the first excited electronic state. This case is called non-resonance Raman scattering. When frequency of the excitation radiation approaches the electronic transition energy, the term resonance Raman scattering is used. In this case, Raman scattering is enhanced $\sim 10^3\times$ – $10^6\times$ [9]. Apart from the enhancement effect, characteristic properties of resonance Raman scattering differ in some important aspects from those of normal Raman scattering. For example, in the

[5] The same $f^4$-dependence applies also in the case of elastic scattering, which can be explained in terms of classical physics within the dipole radiation approximation.

case of non-resonance Raman spectroscopy, the lowest contributing terms allow for the existence of fundamental vibrations (as well as in the case of IR spectroscopy), whereas in the case of resonance Raman scattering the situation is much more complex [8].

When a molecule possesses some degree of symmetry, further restrictions for observable vibrational transitions come into play. For each normal mode, only certain dipole moment/polarizability components may change during the vibration and it is convenient to make use of the group theory formalism to predict which Raman/IR lines will be active in a given spectrum. According to the group theory, classification of normal vibrations is performed on the basis of their symmetry properties. In the following paragraph, some simple considerations pertaining to the group formalism will be made.

According to the number of symmetry elements characterizing a given isolated molecule, molecules can be classified into one out of 32 molecular point groups [10]. Having assigned a molecule to a point group, the methods of group theory allow one to decompose the vibrational signature of the molecule into so-called irreducible representations. The number of normal modes belonging to each irreducible representation (out of the $3N-6$ normal modes in total) is calculated using a well-established algorithm, making use of character tables of molecular point groups [6, 10]. For the purpose of spectroscopy, it is important to note that each irreducible representation may transform as a particular linear or quadratic function of coordinates. Since the constituents of the electric dipole moment have the same transformation properties as $x, y$ and $z$ and elements of the Raman tensor as $x^2$, $y^2$, $z^2$, $xy$, $xz$ and $yz$, it is relatively easy to predict which vibrations will be active in Raman/IR spectra: In order for a given vibrational mode to be allowed in IR absorption spectra, its irreducible representation must span at least one of $x$,$y$ and $z$ species (in the case of randomly-oriented molecules). For the transition to be allowed in Raman spectra, its irreducible representation must span at least one of $x^2$, $y^2$, $z^2$, $xy$, $xz$ and $yz$ species (again in the case of randomly-oriented molecules) [5].

Efficiencies of the principal optical processes briefly summarized above may be very different. For example, while the quantum yield for some fluorescence dyes may be more than 90% (more than 90% of the photons falling on the sample are detected as fluorescence photons), only less than 1 out of $10^6$ photons usually

interacts with matter via the mechanism of Raman scattering. As will be shown in section 1.3, this difference may be smashed by the presence of a metal nanostructure.

## 1.3. Modification of optical processes in the vicinity of plasmonic nanostructures

In the introduction of this section, we will give answer to the question what makes the optical properties of metals so special that placing molecules in the vicinity of nanometer-scale metal structures leads to significant increase in the cross section of various optical processes, such as SERS or SEF. We will follow considerations made in section 1.1 regarding the classical expression for the refractive index of dielectrics and expand these considerations also for metals. We will see that the interface between a metal nanostructure and a dielectric where the real part of the relative permittivity changes sign across the interface enables concentration of the electromagnetic field, giving rise to great amplification of the local laser field. With the light of a suitable frequency, the cloud of free electrons in the metal may be driven to perform collective oscillations called surface plasmons. Coupling between the laser light and electron oscillations is accompanied by sharply enhanced amplitude of the electromagnetic field in the closest proximity of the roughened metal surface. This phenomenon, termed localized surface plasmon resonance (LSPR), is of great experimental importance since it enables to significantly improve the cross section of various optical processes, some of which will be described further.

In the classical description of dielectrics, we assumed that electrons are bound to the positive ion cores with an elastic force analogous to that of a harmonic oscillator. Metals, however, can be in a first approximation viewed as materials where the electrons are completely free [6]. After putting $\omega_0 = 0$ in eq. 1.13, an explicit expression for the dielectric function of metals as a function of $\omega$ takes the form

[6] This idea was first introduced by P. Drude in 1900 and the modification of the Lorentz model for metals is therefore called the Drude model.

$$\varepsilon(\omega) = n^2(\omega) = 1 - \frac{Ne^2}{\varepsilon_0 m}\frac{1}{\omega^2 + i\gamma\omega}. \qquad (1.31)$$

As a further approximation, neglecting the imaginary part ($\omega \gg \gamma$) yields the simplified expression for the dielectric constant of metals in the form

$$\varepsilon(\omega) = 1 - \frac{Ne^2}{\varepsilon_0 m}\frac{1}{\omega^2} = 1 - \frac{\omega_p^2}{\omega^2}, \qquad (1.32)$$

where $\omega_p = \frac{Ne^2}{\varepsilon_0 m}$ denotes so-called plasma frequency of given metal. If $\omega > \omega_p$, then $\varepsilon(\omega)$ is between 0 and 1 and thus the refractive index of the metal is real. By contrast, if $\omega < \omega_p$, then $\varepsilon(\omega)$ is negative and the refractive index becomes purely imaginary, which is responsible for strong reflectance of metals at sufficiently long wavelengths. The latter case is important in the field of plasmonics as only materials with the negative real part of the dielectric constant in a given spectral interval can support plasmon resonances.

### 1.3.1. Surface-enhanced Raman scattering

From the historical point of view, SERS [7] was the first surface-enhanced spectroscopic technique, discovered already in 1974 [11]. Since the very early days of SERS, it has been agreed that two different effects contribute to the observed enhanced Raman signal [12, 13]. The simplest idea on the origins of both these mechanisms involves the proportionality between the induced electric dipole moment and the laser field $E$, given by eq. 1.8

$$\vec{p} = \vec{\vec{\alpha}}\vec{E}. \qquad (1.8)$$

This equation supports the basic understanding of the SERS enhancing mechanism, because in principle, both $\vec{\vec{\alpha}}$ and $\vec{E}$ can be amplified when molecules are placed in the vicinity of metal nanostructures.

By far the most dominant contribution to the total enhancement not only in SERS, but in any surface-enhanced optical phenomenon, is attributable to the electromagnetic effect. Basically, electromagnetic mechanism originates from the interaction of light with free conduction electrons (electron gas) of metal, which

[7] Supposing the frequency of the excitation beam approaches the slope of the absorption band of the studied analyte, the term surface-enhanced resonance Raman scattering is used (SERRS).

results in significant increase in the electromagnetic field experienced by molecules adsorbed in the vicinity of nanostructured metal surface. When a small metal nanoparticle is irradiated by a plane monochromatic wave, the time-varying electromagnetic field causes the conduction electrons to oscillate coherently, leading to a charge separation. These collective excitations, representing a coupled state between the electromagnetic field (a photon) and electron oscillations with respect to positive ionic cores in the crystal lattice, are termed surface plasmons.

As already mentioned, the ability to support the surface plasmons at the metal-dielectric interface is made possible due to different signs of real parts of the relative permittivities of both the metal and the ambient dielectric (metals possessing a negative real part and a small imaginary part of the relative permittivity). Under the conditions of surface plasmon excitation, local electromagnetic field can be greatly amplified and a molecule placed in the vicinity of the metal object may be subjected to much stronger electromagnetic field relative to the field without the metal object present. However, in order for the enhancement effect to occur, several other conditions must be safisfied: (i) the metal surface must possess some form of nanometer-scale roughness, and (ii) the excitation wavelength must be tuned to match the resonance condition of the system. The location of the plasmonic frequency in the electromagnetic spectrum is determined by the relative permittivities of both the metal and the surrounding medium, shape and size of the metal particle, interparticle interactions, and in the case of non-spherical particles also on polarization of the incident light.

In the case of surface plasmons localized around sufficiently small nanoparticles (in comparison to the excitation wavelength), the oscillating charge density may be viewed as an oscillating electric dipole and the term dipolar plasmon resonance is often used. However, when the dimensions of the particle become comparable to the excitation wavelength, other terms of the multipole expansion have to be taken into account. This gives rise to higher-order plasmon resonances (usually quadrupolar) that do not couple to light very effectively [3, 13, 14].

In order to illustrate the enhancement effect provided by metal nanostructures, let us consider a small metal object embedded in a non-absorbing dielectric medium (with the relative permittivity of $\varepsilon_r > 1$) being illuminated by an electromagnetic wave with the wavelength $\lambda$ (Fig. 2). If we want to know what

happens to the electromagnetic field around the sphere, it is necessary to solve the Maxwell's equations with appropriate boundary conditions. In general, this may be rather a lengthy and tedious procedure, most of which has to be carried out only by resorting to numerical computations [3, 15, 16]. However, there exist some special geometries in which the solution may be expressed explicitly under a certain approximation. An often used approximation widely used in literature is so-called electrostatic (Rayleigh) approximation, which requires the dimensions of the metal object to be $< \sim 20\times$ lower than the wavelength (in most cases, this corresponds to $\sim$ 20-30 nm sized structures). In this case, the field distribution can be computed using the Poisson's equation instead of solving the Maxwell's equations. Further, we will limit our attention (for the case of simplicity) on a sphere-shaped object of a radius $a \ll \lambda$, which is a situation depicted in Fig. 2. Solution of the Poisson's equation outside the sphere can be (under the electrostatic approximation) thought of as a superposition of the external (homogeneous) field and the field of an induced dipole located at the centre of the sphere – that is why this approximation is also referred to as the dipole approximation (dipolar plasmon resonance). The boundary conditions (demanding that normal components of $\vec{D}$ and tangential components of $\vec{E}$ be equal inside and outside the sphere) imply that the explicit solution outside the sphere in standard spherical coordinates $r, \vartheta, \varphi$ is

$$\phi_{out}(r, \vartheta, \varphi) = -E_0 r \cos\vartheta + E_0 \frac{a^3}{r^2} \frac{\varepsilon(\omega) - \varepsilon_r}{\varepsilon(\omega) + 2\varepsilon_r} \cos\vartheta, \qquad (1.33)$$

and the local field strength at the distance $r$ from the centre of the sphere may be written as (denoting the factor $\frac{\varepsilon(\omega)-\varepsilon_r}{\varepsilon(\omega)+2\varepsilon_r}$ as $g(\omega)$ for simplicity)

$$\vec{E} = -\nabla\phi = E_0 \left(1 + 2g(\omega)\frac{a^3}{r^3}\right) \cos\vartheta\, \vec{e}_r - E_0 \left(1 - g(\omega)\frac{a^3}{r^3}\right) \sin\vartheta\, \vec{e}_\vartheta. \qquad (1.34)$$

From previous expression, one may readily understand the importance of the dielectric constant's of the metal being negative: The enhancement is greatest when the denominator of $g(\omega)$ approaches zero. In that case, the enhancement factor strongly depends on the imaginary part of the dielectric function $\varepsilon(\omega)$. Providing that the excitation wavelength matches the resonance condition, the enhancement factor falls off rapidly with the increasing imaginary part of the dielectric function. Thus, molecules adsorbed in close vicinity of metal nanostructures experience

significantly higher electromagnetic field and their signal may be amplified by many orders of magnitude.

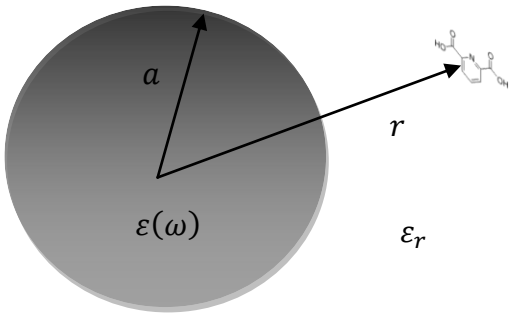


Figure 2. A molecule in presence of a spherical metal particle with a radius $a$.

When the dimensions of the metal structures rise, the previous formula may no longer be sufficient for describing the field distribution and more complicated analysis (relying mostly on numerical solution of the Maxwell's equations) has to be carried out. For nanoparticle sizes comparable to λ, the electrostatic approximation does not hold anymore and the coupling between the incident light and the oscillating electron density gives rise to higher-order (multipolar) plasmon resonances which appear at shorter wavelengths [3, 15]. In principle, the field outside the metal nanoparticle can be expanded in an infinite series (with the first term being the dipolar one), each of which can exhibit a resonance. For example, resonance frequencies of a sphere may be obtained from the relation $\varepsilon(\omega) = -\frac{N+1}{N}\varepsilon_r$ [3, 13, 17], where $N$ is an integer ($N = 1$ corresponding to an oscillating dipole and higher terms corresponding to higher-order multipolar resonances), which results in higher-order multipolar resonances shifted to the blue [18]. By contrast, for larger $\varepsilon_r$, the resonance wavelength is typically shifted to the red [3, 15]. Another consequence of the size effects is that LSPR peak progressively broadens, accompanied by reduced local field enhancements due to retardation effects [3, 15, 16, 19]. Therefore, there exists a certain optimum size of the nanoparticles providing the highest enhancement, usually in the range $\sim 5 - 200$ nm [14, 20-23]. However, it is still the imaginary part of $\varepsilon(\omega)$ which is crucial for the enhancement provided since in determines how damped the plasmon resonance is.

Taking into account that both the primary and the secondary radiation may be enhanced (as the Raman shift between the frequencies of the primary and the

secondary radiation, corresponding to energies of vibrational levels of a measured molecule, is usually so small that the scattered radiation still lies within the region of surface plasmon resonance), the total enhancement is a product of both aforementioned contributions. Therefore, the enhancement effect is expected to scale as $g^4$ ("$E^4$ approximation") and is expected to drop with the twelfth power of the distance from the surface, although the molecule does not necessarily have to be in direct contact with the metal surface. Under this approximation, we may define the SERS enhancement factor as

$$\mathrm{EF} = g(\omega_0)^2 \cdot g(\omega_{sc})^2 \cdot \frac{a^{12}}{r^{12}}, \tag{1.35}$$

where $\omega_0$ denotes frequency of the incident radiation, $\omega_{sc}$ frequency of the scattered radiation and $g(\omega) = \frac{\varepsilon(\omega)-\varepsilon_r}{\varepsilon(\omega)+2\varepsilon_r}$. More generally, a SERS enhancement factor expresses strength of the electromagnetic field relative to what it would be without the presence of the metal nanostructure. However, precise experimental determination of the SERS enhancement factor suffers from difficulties in estimating the number of molecules that contribute to the SERS signal as well as discrepancies resulting from a wide variability in the EF definition quoted in literature [24]. Some of these aspects will be briefly discussed later on.

In SERS spectroscopy, silver and gold are the most widely employed metals as the resonance condition is fulfilled in the visible spectral range. Silver is the best enhancing metal due to its specific dielectric function, allowing the greatest enhancements of all metals. On the other hand, gold may be sometimes preferred thanks to its chemical stability, lower susceptibility to oxidation and biocompatibility. We have to note that while the optical properties of silver follow the Drude model well, gold possesses a greater imaginary part of the dielectric function than it would possess taking only the Drude model into account. That is because the Drude model neglects the contribution of bound electrons [25]. Interband transitions must be taken into consideration in this case, which makes the total enhancement of gold surfaces somewhat smaller in comparison to silver. Several other metals, namely Cu, Al, Pd etc., are also applicable, although they are usually several orders less enhancing than Ag and Au. Moreover, for most of these metals, the resonance frequency is shifted towards ultraviolet region.

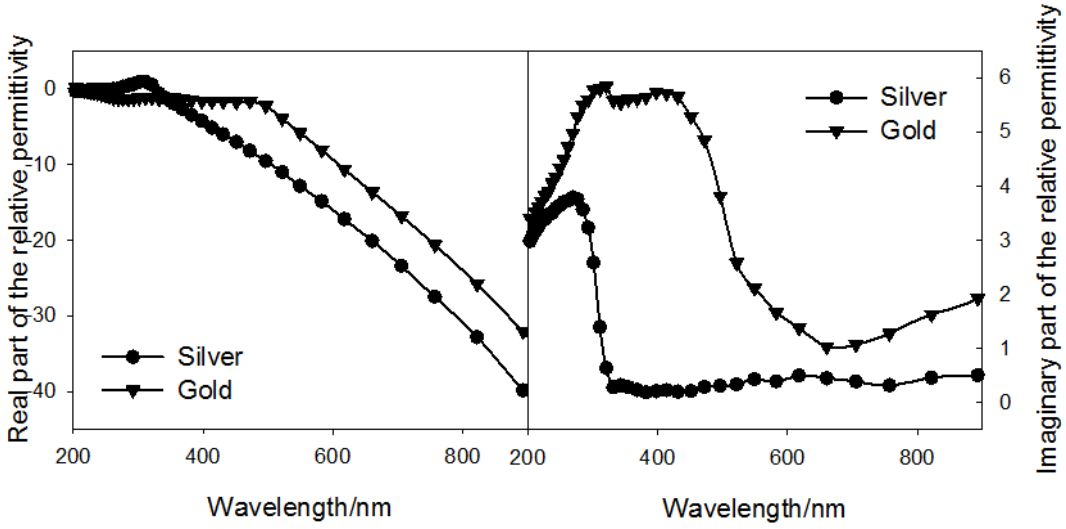


Figure 3. Wavelength-dependent real and imaginary part of the relative permittivity of silver and gold in the UV/Vis range [26]. Experimental values were adapted from [27].

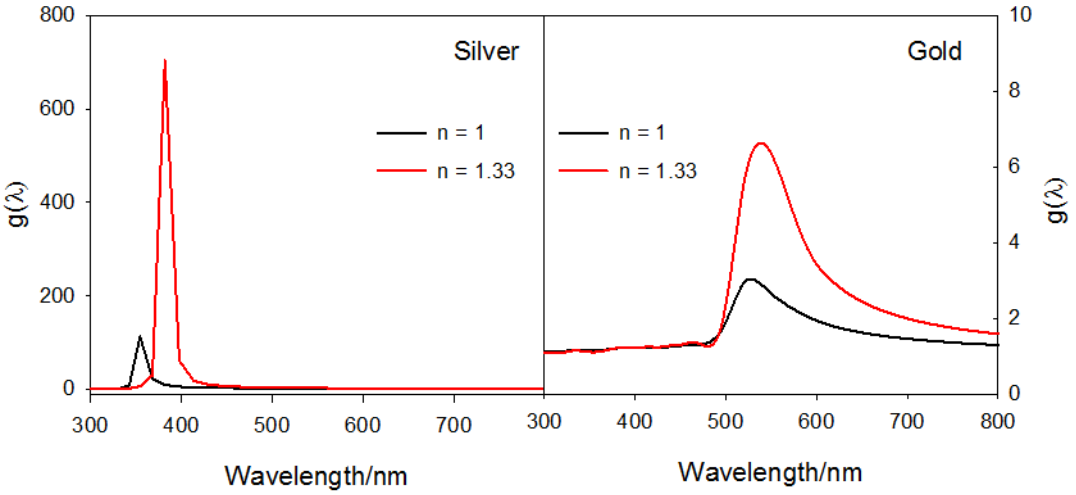


Figure 4. Wavelength-dependent $g$-factor for silver and gold [26]. Calculation was performed for a metal sphere in the electrostatic approximation based on the values contained in Fig. 3. Resonance condition is defined by the equation $\varepsilon(\omega) + 2\varepsilon_r = 0$. Due to the specific relative permittivities of silver/gold, the enhancement for gold is shifted more to the red. Broadening of the resonance curve and significantly lower $g$-factor for gold is caused by bigger value of the imaginary part of the relative permittivity. Effect of the refractive index of the surrounding environment is also demonstrated. Size effects are not captured in these calculations.

Both the experimental results as well as theoretical calculations show that the electromagnetic field can be confined in nanometer-sized metal clefts. Analytical

treatment of a two sphere system, performed already in the 1980s [28, 29], suggests that molecules residing in a nanogap between the nanoparticles are subjected to $\sim 10^5\times$ stronger electromagnetic field in comparison to the field enhanced by one single nanoparticle. Due to mutual interaction, electromagnetic field in such cavities is much larger than the sum of the fields caused by two non-interacting spheres, which has been explained by strong electromagnetic coupling between the nanoparticles, giving rise to coupled plasmon resonances [3, 13, 30-32]. However, this happens only if the incident polarization is along the interparticle axis. For light polarized across the interparticle axis, the enhancement is almost negligibly different from its value at a single, isolated particle [14]. Closer analysis shows that with nanoparticle radii of 45 nm (average size of the silver nanoparticles used) and the separation distance of $d = 5.5$ nm (diameter of a hemoglobin molecule, [30]), the enhancement effect adds another $\sim 2 - 3$ orders of magnitude in comparison to isolated nanoparticles and further $\sim 2 - 3$ orders of magnitude after decreasing the nanoparticle gap down to $\sim 1$ nm, making the total enhancement factor of $\sim 10^{11}$. Although the first reports of single-molecular SERS in 1997 [33, 34] quoted enhancement factors higher than $\sim 10^{14}$, this number has been critically revisited [24, 31, 35]. Nowadays, SERS enhancement factors of $\sim 10^{11}$ are considered to be theoretical limits (for silver) on account of the electromagnetic contribution, sufficient even for observation of single-molecular SERS [5].

The extremely spatially-localized sites providing extreme enhancement were dubbed hot-spots in literature. However, geometry of hot-spots is not restricted only to two mutually interacting spheres. Geneally, for systems of aggregated particles with nanoscale crevices or junctions where interparticle separation can be made very small, extremely localized regions of ultrahigh enhancement were predicted [31] as well as experimentally demonstrated [36, 37]. It means that the enhancement in the gap region where majority of the electromagnetic energy is packed completely overwhelms the surface average and produces the dominant contribution to single-molecular sensitivity in SERS. Besides, theory also predicts very strong enhancement of the electromagnetic field at sharp metal tips and large curvature regions due to so-called lightning-rod effect. On the other hand, the hot-spot molecule coincidence is statistically a very rare event. It is expected than only a very small fraction of molecules, difficult to estimate precisely, actually reside in the hot-

spots and the rest of the molecules in other weakly enhancing sites [35], which makes the typical enhancement factor averaged over a sufficiently large area/volume in most cases around $10^4 – 10^7$. The occurrence of hot-spots often complies with the Poisson distribution [38].

If the shape of the nanostructures is different, different boundary conditions have to be taken into account in numerical analysis of the enhancement factor, however, the importance of the dielectric constant's of the metal being negative holds true. Supposing a SERS-active substrate consisted of rather uniform, isolated nanoparticles, the resonance curve is expected to reflect its size and shape. However, most SERS-active substrates usually consist of assemblies of interacting particles, i.e. collection of nanoparticles with different shapes, sizes and mutual spacings, which cause the resonance curve to be inhomogeneously broadened and which also modifies the condition for surface plasmon excitation. In the average SERS regime where the role of hot-spots is rather negligible, the "near-field" (Raman-enhancing) properties were found to correspond well with the "far-field" properties such as extinction [39]. In other words, the wavelength corresponding to the maximum of the extinction peak of the nanostructures is close to the wavelength providing maximum SERS response [40]. For non-transparent structures, measurements of reflectivity may supply the need for knowing extinction spectra to characterize the plasmonic properties [20, 41]. However, for hot-spot dominated systems such as colloids, the relationship is less straightforward with the maximum enhancement usually red-shifted with respect to the LSPR maximum [42, 43]. In the case of more complicated (typically anisotropic) SERS-active platforms, no correlation between these two phenomena was found [44, 45].

In addition to the electromagnetic effect, for some analytes, there exists a chemical (molecular) contribution to the total enhancement, which results from absorption (chemisorption) of the molecule to the surface. The chemical mechanism requires the molecule to be in direct contact with the metal (sometimes referred to as the first-layer effect), although nanometer-scale roughness is not a precondition for the chemically-induced enhancement. In this instance, polarizability tensor of the molecule may be amplified as a result of the formation of a metal-ligand coordination complex, which produces changes in intensities of particular vibrational modes. Current understanding of the chemical mechanism posits that the act of

forming a chemical bond between the metal and the analyte opens up new molecular resonances, such as charge transfer transitions [19, 35, 46-48]. Upon excitation with laser light of a suitable wavelength, charge transfer may occur between the highest occupied molecular orbital (HOMO) and the Fermi level of the metal and/or between the Fermi level and the lowest unoccupied molecular orbital (LUMO), accompanied by increase in vibrational intensities of the analyte. Amplification of the Raman scattering intensity is thus analogous to resonance Raman scattering. The provided enhancement can be up to $\sim 10^3$ [49], although, according to some estimations, the enhancement factor arising from the chemical contribution hardly ever exceeds a factor of 10 [13, 35]. As a consequence of interaction of the molecule with the metal surface, positions of some Raman bands of the molecule may be slightly shifted in frequency and changed in line width compared with spectra obtained by means of normal Raman scattering. This may therefore make the attempts to interpret obtained data and to identify a specific molecular pattern more difficult and less straightforward in comparison to classical Raman spectroscopy.

### 1.3.2. Surface-enhanced fluorescence

Similarly to the case of Raman scattering, two photons are involved in the case of fluorescence: The excitation one and the fluorescence one. Thus, from a naive point of view, the enhancement process should be very similar to that in SERS. However, closer analysis shows that the situation is more complicated in this case.

Indeed, vast survey of literature data reveals that the SEF enhancement factor (defined in a manner analogous to the SERS enhancement factor, i.e. fluorescence intensity in presence of a metal structure divided by fluorescence intensity of a fluorophore in a "free" space) is "only" in the order of $10^0 – 10^3$ and hardly ever exceeds the factor of 50 [50-52]. The principal difference between SERS and SEF lies in the fact that SERS is an instanteneous process, while fluorescence is a two-step phenomenon consisting of two distinct processes: Absorption of an excitation photon and consecutive emission of a secondary fluorescence photon. For this reason, fluorescence enhancement is rather interpreted as a combination of the following mechanisms: (i) enhancement of the local electromagnetic excitation field, leading to an increased absorption of the fluorophore, and (ii) increase in the

radiative decay rate [3, 50, 53, 54]. In other words, the latter mechanism increases the quantum yield of the fluorophore, which can not be larger than 1. Moreover, close contact of a fluorophore with a metal surface (iii) increases fluorescence quenching by providing new decay channels between the excited fluorophore and the metal. All these three processes depend, in a non-trivial way, on the fluorophore distance from the metal surface, and affect both the fluorophore lifetime as well as the quantum yield. Since these phenomena have contradictory effects on the fluorescence intensity, the total distance-dependent SEF intensity profile results from competition between amplification of the local field, falling off rapidly with the growing distance between the metal nanoparticle and the fluorophore, and enhanced radiationless energy transfer at very short distances. It is the quenching effect at the metal-dielectric interface that takes the leading role at very short distances (up to $\sim 2 - 3$ nm) [3, 50, 53, 55] and another reason which prevents the SEF enhancement factor from matching those values attained in the case of SERS. The quenching effect fades out with approximately $\sim d^3$ dependence [56] and may be considered negligible for distances $> \sim 4 - 5$ nm. As discussed in section 1.3.1, the distance dependence for the electromagnetic effect of a fluorophore in the proximity of a small metal sphere is given by $d^{12}$ (i.e. $d^6$ for enhancement of the primary radiation). Thus, there exists an optimum distance between the fluorophore and the metal surface for which the enhancement effect is most significant (usually in the range between 3 nm and 20 nm) and a spacer must be used to keep the interspace between the metal and the fluorophore. Different spacings were tested in literature to keep this optimum distance, such as silicon oxides [21, 52, 57, 58], polymers [59, 60], proteins [61, 62] or DNA strands [63-65].

Let us discuss previous considerations more quantitatively. Assuming that the presence of a nearby metal surface increases the radiative decay rate from $\Gamma$ to $\Gamma + \Gamma_m$ and the non-radiative decay rate from $k_{nr}$ to $k_{nr} + k_m$ ($\Gamma_m,\ k_m > 0$), the fluorophore lifetime becomes

$$\tau_{F,m} = \frac{1}{\Gamma + \Gamma_m + k_{nr} + k_m}, \tag{1.36}$$

and the fluorophore quantum yield becomes

$$\mathrm{Q} = \frac{\Gamma + \Gamma_m}{\Gamma + \Gamma_m + k_{nr} + k_m}. \tag{1.37}$$

While Γ and $k_{nr}$ are intrinsic fluorophore characteristics, the values of $\Gamma_m$ and $k_m$ depend on the metal-fluorophore interactions. Comparison between eq. 1.20, 1.24, 1.36 and 1.37 yields

$$\frac{\tau_{F,m}}{\tau_F} = \frac{\Gamma + k_{nr}}{\Gamma + \Gamma_m + k_{nr} + k_m} < 1, \tag{1.38}$$

$$\frac{Q}{Q_0} = \frac{\Gamma + \Gamma_m}{\Gamma + \Gamma_m + k_{nr} + k_m} \frac{\Gamma + k_{nr}}{\Gamma}. \tag{1.39}$$

Eq. 1.38 says that presence of a metal nanostructure is accompanied by lifetime shortening. In this instance, contrary to fluorescence intensity, the effect of both radiative and non-radiative decay channels on the lifetime is mutually reinforcing. Supposing that the two enhancing processes, i.e. amplification of the local electromagnetic field and increase in the quantum yield, can be decoupled, the total fluorescence enhancement is [50]

$$EF = EF(d) \cdot \frac{Q}{Q_0} = EF(d) \cdot \frac{\Gamma + \Gamma_m}{\Gamma + \Gamma_m + k_{nr} + k_m} \frac{\Gamma + k_{nr}}{\Gamma}, \tag{1.40}$$

where $EF(d)$ denotes the distance-dependent local field enhancement factor, responsible for the increase in absorption intensity.

The ratio $\frac{Q}{Q_0}$ is usually bigger than 1, which means that fluorescence is enhanced. However, because of the limited range of the electromagnetic effect, the enhancement drops off rapidly when further increasing $d$. On the other hand, the rate of nonradiative decay ($k_m$) is greatly enhanced when the fluorophore and the metal surface are closely contacted, which results in fluorescence suppression. This is considered to be one of major advantages of SERS over classical Raman scattering.

Finally, let us remark that in order to theoretically elucidate the difference in enhancements provided by SERS/SEF, more elaborate analytical models were published recently, pointing out the role of quenching [55, 66]. However, because a typical fluorescence cross section is much bigger in comparison to Raman scattering cross section, it makes sensitivities of the both surface-enhanced techniques approximately equal. Another work, aiming to resolve certain discrepancy between theoretically-predicted and experimentally-measured enhancement factors, described the SERS amplification within higher-order perturbation theory [67]. In this approach, fully quantum nature of the plasmonic excitation was taken into

account, treating the surface plasmons as quasiparticles. It is important to note that some aspects of this approach remain rather controversial and have not been yet resolved. Therefore, fully quantum, unified approach to both SERS and SEF still remains a challenge.

## 1.4. Plasmonic nanostructures for spectroscopic methods

Proper plasmonic substrate is a prerequisite for successful surface-enhanced measurement and thus plays a key role in any of these applications. Most of the following considerations pertain to SERS measurements, but are easily extendable to the case of SEF as well. In the SERS community, there exists a general consensus on the qualities that a proper plasmonic substrate should possess. This consensus was first established by Natan in 2006, who suggested that the following criteria should be fulfilled [68]:

The substrate should provide sufficient enhancement effect (sufficient sensitivity). However, proper determination of the enhancement factor may be difficult to achieve, either due to big variability of the EF definitions in literature and/or the need to properly characterize the non-SERS properties of the analyte. An often used method of calculation, referred to as the substrate enhancement factor, requires knowing the amount of molecules contributing to the Raman/SERS signal [24]. This, in turn, depends on the surface coverage and it is important to keep in mind that not all molecules are at the same distance from the surface. Especially in higher concentrations, molecules may exhibit a certain distance distribution with a particular proportion in the first layer and the rest in the remaining layers, which may underestimate the EF. On the other hand, so-called analytical enhancement factor normalizes respective intensities to analytical concentrations without the aim of determining the actual number of adsorbed molecules. This option is thus less acurate. A well-established method of evaluating the enhancing capability of a given substrate is determining the limit of detection, which usually requires a series of concentration-dependent experiments and finding the concentration (possibly by extrapolation) for which the intensity of the strongest peak drops below 3 standard deviations of the blank sample [69]. In all cases, however, the obtained quantity

depends not only on the plasmonic substrate, but also on the mutual chemical affinity between the analyte and the substrate, and may thus be very different when using different analytes.

For measurements in the average SERS regime, the substrate should be uniform enough. According to Natan, the maximum acceptable variation in the SERS signal should be less than 20% over a 10 $mm^2$ area. However, the critical value of 20% should not only be exceeded when measuring on a given sample, but even across different substrate batches, prepared by the same procedure. In the case of solid substrates, reproducibility can be easily quantified by performing spectral mapping and subsequent statistical evaluation. On the other hand, reproducibility can be very poor in hot-spot dominated systems where achieving big sensitivity is of paramount importance. Since the enhancement ability of the substrate is very often inversely proportional to the reproducibility, this finding has been dubbed the SERS uncertainty principle. It is worth noting that both the SERS sensitivity as well as reproducibility depend, among other things, also on the experimental arrangement and the way of adsorbate deposition [70]. In the case of solid substrates, deposition of a droplet of the analyte and letting it dry often results in rather inhomogeneous drying patterns with adsorbate molecules accumulated at the edges of the former drop, similarly to the coffee ring effect [71], which may underestimate the reproducibility, but may contribute to better sensitivity. Measurements using objectives with a lower numerical aperture affect a larger scattering area/volume, which causes the presence of occassional highly-/weakly-enhancing sites to average out and contribute to better reproducibility. On the other hand, lower effectiveness of collection of the scattered radiation in this case results in decrease in the SERS sensitivity (another consequence of the uncertainty principle).

Another means of spectra retrival, which we applied in the case of SEF, is the strategy of dripping a droplet of a stock solution on the plasmonic substrate and focusing the laser spot on the interface between the droplet and the supporting layer. In this case, signal accumulation is performed before the droplet is fully evaporated. This approach works well because after evaporation, the SEF signal is extremely irreproducible (and weak), while using the above mentioned strategy, reproducibility is no worse than in the case of SERS. It also enables more direct comparison of fluorescence lifetimes to that measured in a solution in the non-enhancing case.

However, the main drawback is little information about the number of molecules affected in this case as both the adsorbed molecules (contributing with the enhanced signal) as well as the molecules in the bulk medium (contributing with the non-enhanced signal) contribute to the total obtained SEF signal.

Plasmonic substrates should provide sufficient stability and survive free of contaminants even after a long shelf life (~ months). This is mainly the problem with silver which suffers from oxidation and for which the surface contamination irrespective of the fabrication method is often observed. It comes either from the preparation procedure or from the ambient atmosphere during storage and involves organic (carbonaceous) species that are adsorbed on the surface. The contaminants manifest themselves, even in very small concentrations, by their anomalous SERS bands/fluorescence background and overlap the signal of the molecule to be studied [38]. Such problems have been reported both in the case of colloids [26, 72, 73] as well as solid substrates [74-77]. Thus, special care must be exercised when analysing any spectral pattern in an effort to reliably distinguish the bands coming from the studied analyte from those of the contaminants or, better still, to develop a method for preventing the contamination. Methods aiming to overcome this problem published in literature involves for example electrochemical [74] or ozone cleaning [78], ion etching [75, 76] or keeping the substrates in a vacuum chamber overnight immediately after the deposition [38].

Last but not least, it is necessary to maintain a compromise between the ease of the fabrication procedure and low cost.

In the following sections we will take a closer look at some of the most common SERS-active substrates.

### 1.4.1. Metal colloids

Metal colloid is a heterogenous system consisting of solid metal particles in the 1 – 100 nm size range dispersed in a liquid medium. In literature, numerous ways of colloid fabrication have been described, mostly making use of chemical reduction of different chemical salts containing an atom of silver or gold (mostly $AgNO_3$ od $HAuCl_4$) by means of different reducing agents: sodium borohydride [79], sodium citrate [80] or hydroxylamine hydrochloride [81]. The properties of colloid depend

mainly on the conditions of the fabrication process, including initial concentrations of the reagents, temperature, pH and many others that are rather difficult to control. A big advantage of colloids is their cheapness and simple preparation procedure, capable of being carried out in a chemical laboratory in almost no time. Another advantage is the easiness of characterization of the colloid plasmonic properties by extinction measurements. However, the main disadvantage of colloids lies in the fact that even a small perturbation in the preparation protocol can imply drastical differences in the final physical properties of the colloid and significantly different ability to serve as a plasmon-enhancing substrate. That is why metal colloids are not suitable for quantitative analysis, although the provided enhancement may be often higher in comparison to most solid metal nanostructures.

### 1.4.2. Metal nanorod arrays

The nanofabrication technique based on oblique angle vapor deposition (OAD) to produce regular nanorod arrays for SERS applications was first introduced by Chaney and co-workers [82], although similar technology had been known already in the 1990s [83, 84]. For preparation of the columnar structures, magnetron sputtering of a silver target is usually used (although gold is also possible [85, 86]). In the early stages of the deposition process, the deposited material usually forms islands on the substrate. Under the conditions of limited surface diffusion, the growing nuclei shadow the area opposite to the incoming flux, and therefore the film grows through the formation of columnar structures separated from each other by voids and inclined towards the source of the flux (Fig. 5) [38]. Supposing the deposition is carried out at an angle $\alpha$ with respect to the substrate normal, the preferable angle of the nanocolumns (with respect to the substrate normal) $\beta$ will be [87]

$$\beta = \alpha - \arcsin\left(\frac{1-\cos\alpha}{2}\right), \tag{1.41}$$

i.e. $\beta < \alpha$. The substrate is usually a glass slide or a Si wafer. Morphology of the nanostructured layer is sensitive to a wide range of experimental parameters such as the deposition angle, temperature, pressure in the deposition chamber, deposition time or spinning of the substrate around its normal during the deposition process [84, 88, 89]. This set of parameters defines the thickness, porosity (the bigger angle of

incidence, the bigger is usually the nanocolumn separation) and typical dimensions of the nanocolumns, ranging from several tens to several hundreds of nanometers. These structures may be easily characterized by scanning electron microscopy (SEM). Typical structure images are shown in Fig. 6

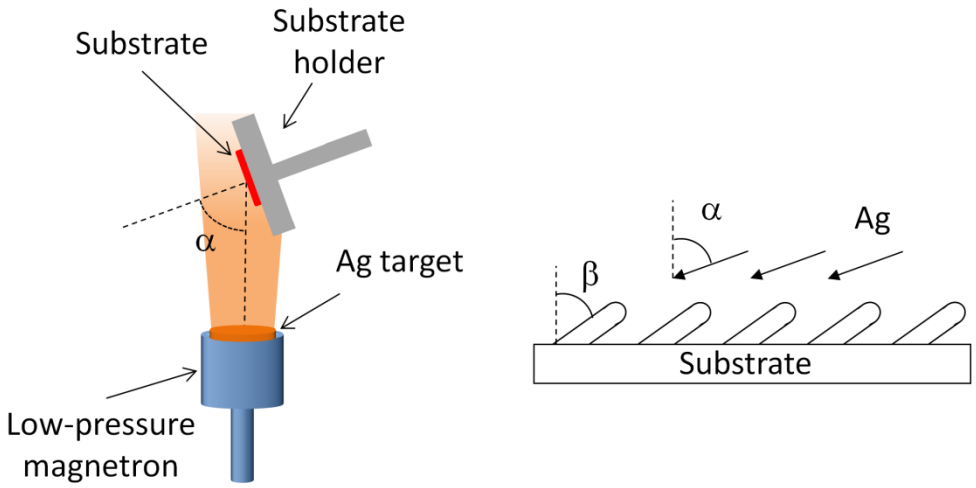


Figure 5. Schematic illustration of the deposition procedure with a typical deposition angle (left), schematic representation of the growing nanorods (right) [26].

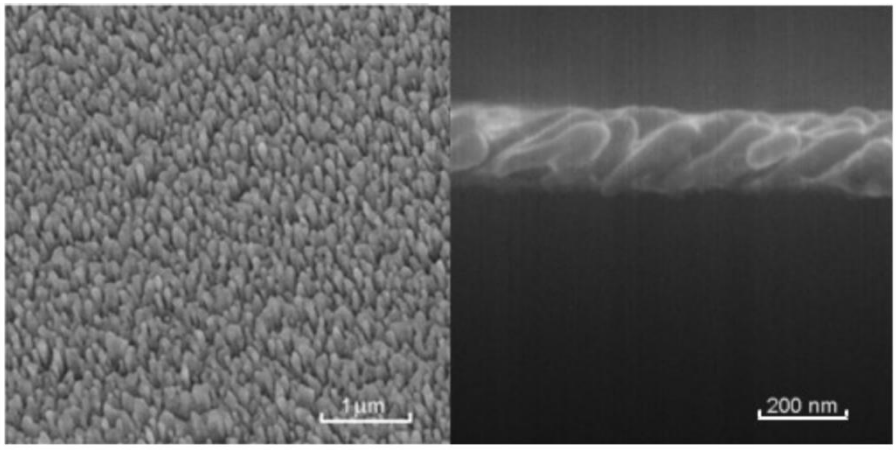


Figure 6. SEM images of a typical nanorod array (top and side view). 15 kV accelerating voltage, deposition angle was $\alpha = 85°$.

The main advantage of the OAD is its simplicity. It is a one-step, vacuum-based process and since no chemical substances are required, is also environmentally friendly. It was proved that OAD offers uniform, reproducible, large area SERS-

active substrates with high SERS enhancement [85, 90-92]. Due to their anisotropic nature, Ag nanorod arrays have also been used to study polarization- and angular-resolved SERS response [41, 44, 93] (Attachments A3, A5).

### 1.4.3. Metal nanoislands

Metal nanoislands belong to one of the first substrates ever used in the field of SERS spectroscopy [13, 94]. These structures are usually prepared by vapor deposition of metal (usually Ag or Au) on supporting substrates. When rather short deposition time is used, the individual metal nuclei are randomly distributed on the substrate and start to merge into islands with typical dimensions ~ 50 – 200 nm after longer deposition times [95]. Longer deposition times increase the probability of nanoparticle condensation, reduce the interparticle spacings and finally result in creation of an interconnected network (Fig. 7), accompanied by a gradual shift of the LSPR peak to the red [39].

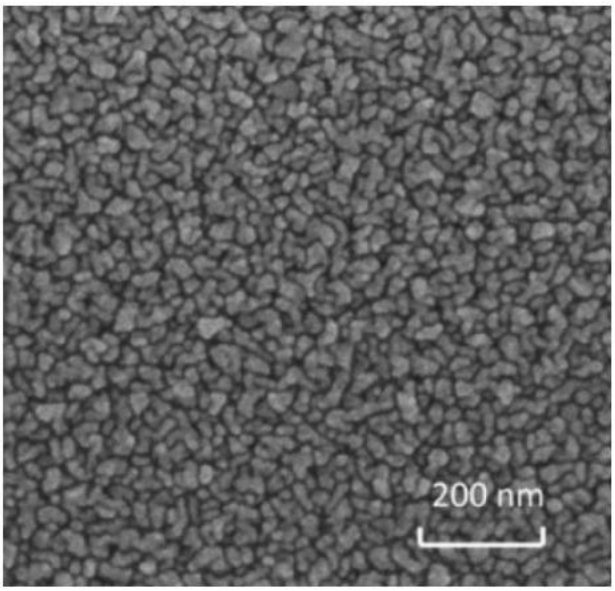


Figure 7. SEM image of typical silver nanoislands.

Details of the underlying physical processes such as surface diffusion, adsorption or desorption strongly depend on the fabrication conditions such as temperature, pressure or adhesive properties of the supporting material. The main advantage of nanoislands is the simplicity of the fabrication process and the

possibility of tuning the LSPR wavelength by varying the film's thickness and confluence. Although the SERS enhancement factor of metal nanoislands is generally considered to be rather modest ($10^4$ – $10^6$), nanoislands still represent a very good compromise between sensitivity and reproducibility [96].

### 1.4.4. Other regular SERS-active platforms

Since mid 1990s, significant effort has been devoted to more precise nanostructure fabrication to keep the nanoparticle sizes, shapes and aggregation process under more careful control. A detailed account of these methods can be found in [97, 98]. In this paragraph, several other methods being used in our department will be briefly described. A frequent example of some highly-ordered metal nanostructures is provided by polystyrene nanoparticles serving as a mask for subsequent metal deposition. This principle is used in a range of methods commonly referred to as the nanosphere lithography (NSL) [99]. At first, polystyrene beads are dispersed in a water-ethanol solution and then deposited onto Si wafer support. After drying, these structures form hexagonal close-packed patterns. Metal films over nanospheres (FONs) can be created by subsequent vapor deposition of a nanometer metal layer over the nanospheres [100]. In another variant of NSL, removing of a polystyrene mask results in rather triangular arrays [101]. Even more elaborated approach is used in the similar method, referred to as hole-mask colloidal lithography (HCL) [102]. In HCL, a sacrificial layer of polymer is spin-coated onto a flat surface prior to the deposition of polystyrene beads. After the process of metal evaporation, the polystyrene beads are tape-stripped away, followed by reactive-ion etching through the polymer to create small nanoholes upon which a new layer of metal is evaporated. The process is terminated by a final disposal of the superfluous polymer by lifting-off in acetone. By controlling the size/shape of the nanostructures or the evaporation angle, one may achieve the desired resultant pattern and the distribution of nanoparticles on the surface, thereby adjusting the plasmon resonance condition of a given system. Most common are disc-, ring- or crescent-shaped structures with overall sizes ranging between several tens and several hundreds of nanometers [70].

# 2. Aims of the thesis

As the title of this thesis suggests, the main aim of this work involves testing of regular metal plasmonic nanostructures for the surface-enhanced optical processes – primarily Raman scattering and fluorescence with the support of transmission measurements and ellipsometry characteristics as well as time-resolved measurements in the case of fluorescence. Principal tasks of this work involved clarification of the dependence on a wide range of parameters, such as the substrate deposition time, deposition rate, angle of deposition and other experimental details, determining the spectral position of the localized surface plasmon resonance (LSPR) maximum, analyte used and the excitation wavelength. These experimental details were adapted for the study of particular analyte with the aim of extending the range of possible molecules studied by the surface-enhanced optical techniques. Attention has also been devoted to prevention of contamination of the substrates from ambient environment and maintaining their time stability. Another goal of this thesis (in part experimental and in part theoretical) includes elucidation of polarization and angular optical characteristics of the morphologically-anisotropic plasmonic substrates. To sum up, goals of this thesis should contribute to better theoretical understanding of the plasmonic enhancement mechanism and provide a starting point for optimization of plasmonic-based sensors for analytical applications.

# 3. Experimental methods and chemicals

## 3.1. Raman measurements

Raman and SERS spectra were acquired using home-built Raman spectroscopic system operating in the 90°-scattering geometry. This system is primarily adapted for Raman measurements from cuvettes (liquid samples), but solid substrates are also possible to measure. The excitation source was frequency-doubled Nd:$YVO_2$ laser providing the excitation wavelength 532 nm. Spectra were collected using an 1800 grooves/mm grating and a liquid-nitrogen-cooled CCD detector (Princeton Instruments). A holographic notch-plus filter (Kaiser) was placed in front of the 60-μm entrance slit of the monochromator to remove the Rayleigh line from the scattered light. For polarization-resolved measurements, light polarization falling on the sample was altered by a half-wave plate (Thorlabs) and an analyser was placed between the sample and the monochromator to allow only the light polarized in one plane fall on the detector. To overcome different grating responses for different light polarizations a scrambler was inserted between the analyser and the monochromator. Correct function of the scrambler and other optical components were checked using $CCl_4$ bands (measured in a cuvette) with well-known polarization-dependent behaviour [8]. All spectra were recorded at room temperature.

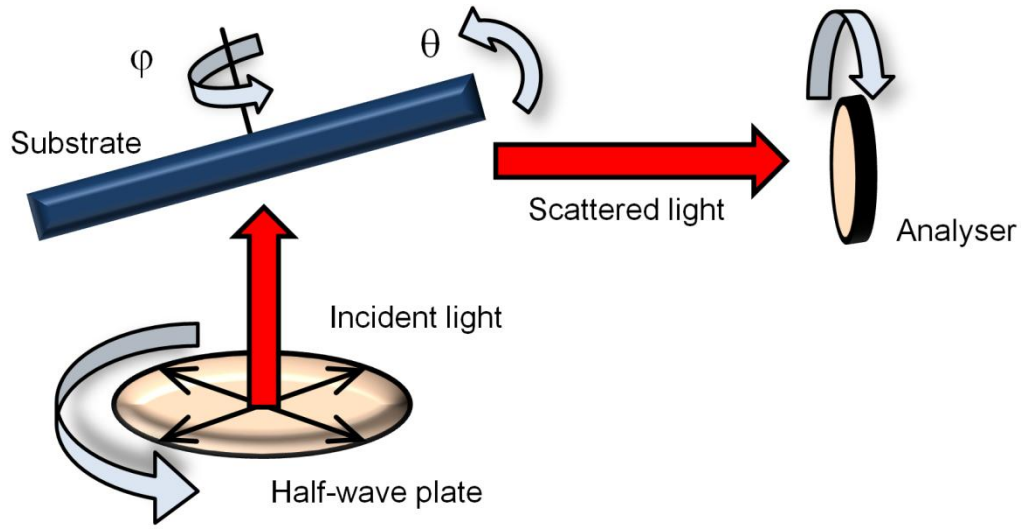


Figure 8. Scheme of the experimental geometry for Raman scattering measurements.

In the case of angular-resolved experiments of solid substrates, a revolvable substrate holder was used as sketched in Fig. 8. Spectra were retrieved with varying tilting angle of the substrate $\theta$ and the azimuthal angle $\varphi$.

Another system used for Raman measurements (and preliminary fluorescence measurements) was an integrated confocal Raman microscopic system LabRam HR800 (Horiba JobinYvon), equipped with a diffraction grating with 600 grooves/mm and a nitrogen cooled CCD detector. Different laser wavelengths (488 nm, 515 nm, 633 nm and 785 nm), different objectives (mostly 10×, 50× and 100×) and different laser powers (ranging from ~ 0.02 to 0.5 mW as adjusted using grey filters) were tested within this thesis. Scattered radiation was collected in a back-scattering geometry and filtered by an edge filter for Rayleigh rejection before focusing it onto the 100 μm entrance slit of the spectrometer. For the purpose of reproducibility evaluation, spectral mapping was performed. Signal homogenity in each of these maps was evaluated by means of factor analysis (FA) procedure using a singular value decomposition (SVD) algorithm [103, 104]. Reproducibility of the Raman signal was usually determined as the relative standard deviation (RSD) of the $V_{i1}$ coefficients.

## 3.2. Fluorescence measurements

For fluorophore lifetime determination the frequency-domain method was used. In this approach, the sample was excited with light with a harmonically-modulated intensity at a set of frequencies close to the inverse of the expected fluorophore lifetime. In this case, the fluorescence response follows the same frequency, delayed by a particular phase shift ( $\varphi$ ) and exhibiting intensity demodulation [7]. Supposing that the intensity of the excitation source is modulated as $I = I_0 \cos \omega t$ , the detected fluorescence intensity is expected to obey the differential equation

$$\frac{\mathrm{d}i}{\mathrm{d}t} = -\frac{i}{\tau_F} + I_0 \cos \omega t. \qquad (3.1)$$

Inserting the expected behaviour of the fluorescence intensity $i$ as $i = i_0 \cos(\omega t - \varphi)$ in eq. 3.1, it can be shown that the equation is fulfilled if and only if

$$\tan \varphi = \omega \tau_F, \tag{3.2}$$

$$\frac{i_0}{I_0} = \frac{\tau_F}{\sqrt{(\omega\tau_F)^2 + 1}}. \tag{3.3}$$

Thus, using one single excitation frequency $\omega$, it is possible to experimentally determine $\varphi$ and $i_0$, which provides information on the lifetime of the analyte. However, it is convient to carry out the measurements at a set of different frequencies. In this case, fluorescence lifetimes can be evaluated by fitting the corresponding curves given by eqs. 3.2 and 3.3 using either single exponential or multiexponential model (Fig. 9).

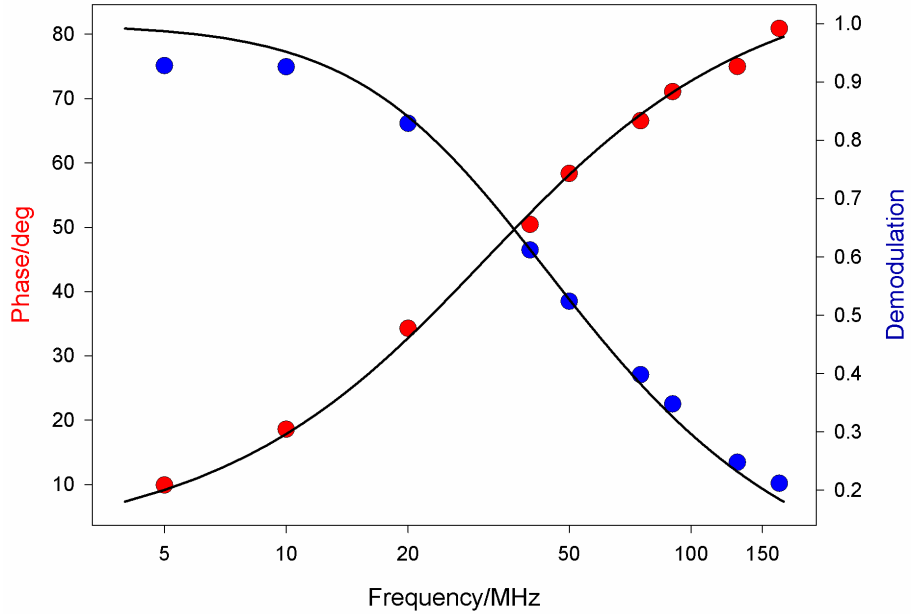


Figure 9. Illustration of the frequency-domain approach for the determination of riboflavin lifetime ($c = 10^{-5}$ M). 9 frequencies were used. Fitting of the corresponding curves via eqs. 3.2 and 3.3 revealed the riboflavin lifetime to be $\tau_F = 5.0$ ns.

Fluorescence lifetime measurements were carried out in cooperation with Laboratoire Jean Perrin, Université Pierre et Marie Curie, Paris using confocal microspectrofluorimeter with a phase-modulation principle. The fluorescence lifetime was determined for all emission wavelengths by acquiring several evenly phase shifted spectral images of the modulated excitation laser beam in relation to fixed detector gain modulation phase shift. Fluorophore lifetimes were resolved by spectra recording with setting of individual modulation frequencies covering evenly

10 – 180 MHz interval and subsequent global fitting of the data. Laser diode module (Omicron LDM 442.50.A350, Germany) with sinusoidal intensity modulation (50 mW peak output, attenuated to one to tens of μW at the sample level) was used for the excitation at 445 nm wavelength. Confocal epifluorescence upright microscope (Zeiss UMSP–80, Germany) was used with a 10× objective (NA = 0.1) to collect the SEF signal which was focused on the entrance slit of the Jobin–Yvon HR640 spectrograph equipped with a 100 line/mm grating. The detection part consists of a gain modulated image intensifier driven by amplified output of the slave synthesizer (IFR Aeroflex 2025 signal generator, USA) working at precise synchronism with the master one. The image intensifier is optically coupled with a CCD detector. For data evaluation, software developed at the Institute of Physics was used [105].

## 3.3. Ellipsometry measurements

Spectral ellipsometry measures changes in light polarization after reflecting from a material structure. In order to describe reflection from the surface, it is convenient to resolve the electric field into two orthogonal components: parallel (p) and perpendicular (s) with respect to the plane of incidence. Both the amplitude and the phase of both field components undergo a change upon reflection as determined by the Fresnel reflection coefficients $\tilde{r}_s$, $\tilde{r}_p$:

$$\tilde{r}_s = \frac{\cos\vartheta - \sqrt{\tilde{n}^2 - \sin^2\vartheta}}{\cos\vartheta + \sqrt{\tilde{n}^2 - \sin^2\vartheta}}, \qquad \tilde{r}_p = \frac{\tilde{n}^2\cos\vartheta - \sqrt{\tilde{n}^2 - \sin^2\vartheta}}{\tilde{n}^2\cos\vartheta + \sqrt{\tilde{n}^2 - \sin^2\vartheta}}, \tag{3.4}$$

where $\tilde{n}$ is the (complex) refractive index of the structure (for a given wavelength) and $\vartheta$ is the angle of incidence. A commonly measured ellipsometric quantity, describing changes in polarization upon reflection, is the complex reflectance ratio, defined as

$$\tilde{\rho} = \frac{\tilde{r}_s}{\tilde{r}_p}, \tag{3.5}$$

which is a complex quantity since it is defined as the ratio of two complex numbers. Eq. 3.5 allows computing $\tilde{\rho}$ depending on the refractive index $\tilde{n}$ and the angle of

incidence $\vartheta$ of which Fresnel reflection coefficients are functions. The inverse transformation is

$$\tilde{n}^2 = \sin^2\vartheta\left[1 + \tan^2\vartheta\left(\frac{1-\tilde{\rho}}{1+\tilde{\rho}}\right)^2\right], \tag{3.6}$$

allowing to compute the pseudo-refractive index of the structure, knowing the complex reflectance ratio $\tilde{\rho}$. Both $\tilde{\rho}$ and $\tilde{n}$ depend inherently on light frequency.

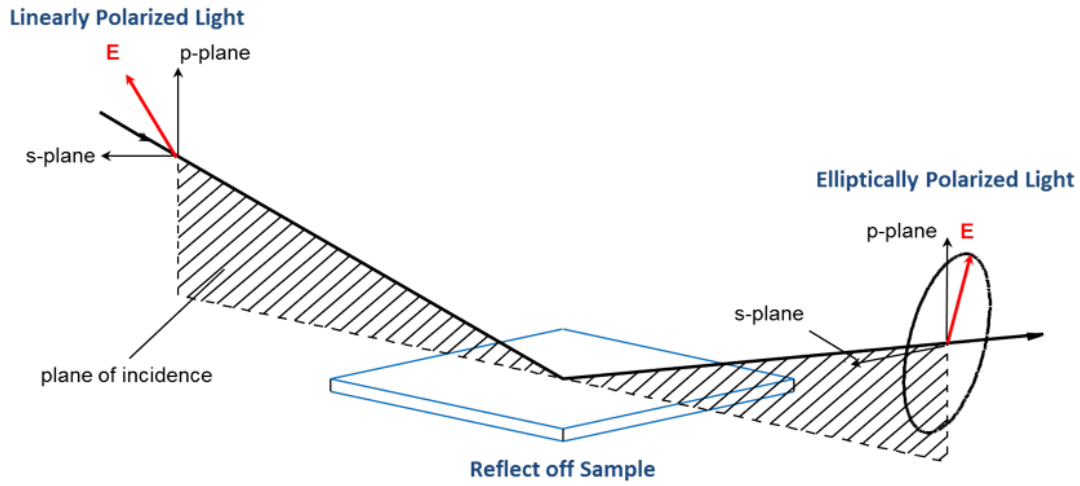


Figure 10. Scheme of ellipsometry measurements. Arbitrarily polarized beam falls on the interface and reflects off the sample. After reflection, both field components undergo a change in intensity and phase, which results in a (generally) elliptical polarization. Ellipsometry measures the complex reflectance ratio for given angles of incidence across a particular spectral range. Adapted from [106].

For smooth, homogeneous and isotropic samples, the pseudo-refractive index is independent of the incident angle, which means it is sufficient to measure $\tilde{\rho}$ only for one angle $\vartheta$ for unique description of the reflective properties of the material. Then, the pseudo-refractive index becomes identical with the refractive index of the material. However, the above mentioned criteria are hardly ever met, often due to surface-roughness, native oxide layers (the case of a Si wafer) or presence of other films and overlays. Therefore, the pseudo-refractive index of silicon may be different from its refractive index. Moreover, in the case of nanostructured materials, the assumption that the pseudo-refractive index is independent of the incident angle does not hold anymore, which is due to the presence of subwavelength structures.

In a more general case such as anisotropic, but still non-depolarizing materials, it is convenient to make use of the Jones formalism and express the components of the reflected light in the matrix form

$$\begin{pmatrix} E_r^p \\ E_r^s \end{pmatrix} = \begin{pmatrix} \tilde{r}_{pp} & \tilde{r}_{sp} \\ \tilde{r}_{ps} & \tilde{r}_{ss} \end{pmatrix} \begin{pmatrix} E_i^p \\ E_i^s \end{pmatrix}, \tag{3.7}$$

where the subscript $i$ stands for the incident and $r$ for the reflected radiation. Generalized ellipsometry measures the ratios of the Jones matrix elements, i.e.

$$\frac{\tilde{r}_{pp}}{\tilde{r}_{ss}}, \qquad \frac{\tilde{r}_{ps}}{\tilde{r}_{pp}}, \qquad \frac{\tilde{r}_{sp}}{\tilde{r}_{ss}}, \tag{3.8}$$

the two latter of them being identically zero in the case of smooth, homogeneous and isotropic samples.

Finally, samples which exhibit depolarization are not compatible with standard or generalized ellipsometry measurements and thus should be treated by the Mueller-matrix formalism. This formalism employs Stokes vectors and 4×4 matrices to account for depolarization, i.e. loss of coherence of the phase and amplitude of the electric field [107, 108]. The conversion of the polarized light into partially polarized or unpolarized happens due to surface roughness, film thickness inhomogeneity or presence of plasmonic resonances. Occuring depolarization may be surmised from the comparison between Mueller-matrix and Jones-matrix elements or between reflection intensities and corresponding intensities calculated using Jones-matrix elements [41].

Anisotropic SERS structures were characterized using a commercially available spectroscopic ellipsometer Woollam RC2. This ellipsometer employs dual rotating compensator enabling standard ellipsometry, generalized ellipsometry, Mueller-matrix ellipsometry and reflectivity measurements in the energy spectral range from 0.7 to 6 eV. The reflectivity spectra were calibrated with respect to the oxidized silicon wafer. Woollam ellipsometric software CompleteEase was used to analyse the experimental data [106].

## 3.4. Other experimental techniques used

Apart from the principal experimental techniques described i sections 3.1 – 3.3, some other complementary techniques were used: Absorption measurements of biomolecules were measured in a 2 mm cuvette using the UV/VIS absorption spectrometer Specord 250 (Analytik Jena) in the UV/Vis spectral range (190 – 900 nm) at the Division of Biomolecular Physics. Basic characterization of freshly prepared samples was carried out by the colleagues at the Department of Macromolecular Physics: The extinction spectra of the prepared plasmonic structures were obtained using a UV-Vis spectrophotometer Hitachi U-3300. Their surface morphology was investigated by scanning electron microscopy (SEM, TESCAN Mira 3, 15 kV accelerating voltage) and topography of the samples was analysed by AFM in a semicontact mode with standard silicon cantilevers (Multi75DLC, Budget Sensors). Thicknesses of deposited layers were measured by spectroscopic ellipsometry (Woollam M-2000DI). The elemental composition of the produced nanostructures was determined from the survey X-ray photoelectron spectra (XPS) acquired by an XPS spectrometer that consists of Al Kα X-ray source (Specs, XR-50) and a hemispherical electron analyser (Specs, Phoibos 100). Wettability of produced samples was evaluated by a goniometer of custom construction that consisted of substrate holder, manually operated syringe and a camera connected to a PC. Image analysis of deposited droplets was done to determine the contact angle and contact radius.

## 3.5. Chemicals

All chemicals used within this thesis were purchased from Sigma-Aldrich:

Methylene blue (MB) is a well-established SERS probe molecule and a very efficient Raman scatterer. This molecule was mostly used for preliminary SERS testing of selected plasmonic nanostructures and also for the study of polarization and angular characteristics of anisotropic SERS-active substrates.

Riboflavin (vitamin B2) serves as a cofactor of many key enzymes. Riboflavin absorbs light in the region between ~ 400 – 500 nm and thus is suitable

for the study of SERS, SERRS and SEF in the spectral region determined by the LSPR of our structures.

Cysteine is an important structural and functional component of many proteins and enzymes and one out of two amino acids containing an atom of sulphur, which makes this molecule promising to attach to metal surfaces.

Dipicolinic acid (DPA) is a biomarker for bacterial spores such as Bacillus anthracis [109].

Porphyrins are important biomolecules and their derivatives are applied in photodynamic therapy of cancer, antiviral treatments, molecular biology, specific sensing of DNA sequences, selective cleavage of nucleic acids, transport of oligonucleotides into the cell etc [110]. 5,10,15,20-tetrakis(1-methyl-4-pyridyl)-porphyrin ($H_2$TMPyP) was used for the SERS testing.

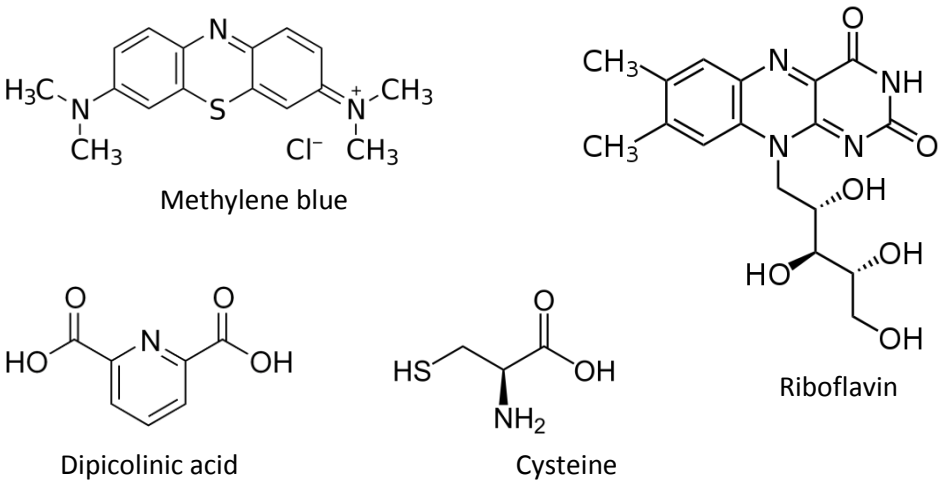


Figure 11. Chemical structure of several (bio)molecules used within this thesis.

# 4. Results and discussion

This section summarizes the main scientific results, most of which has already been published in peer-reviewed articles in international journals. All these works are attached at the end of this thesis. Attachment A1, focused on testing of Ag nanorod arrays for SERS, contains data obtained partly during the diploma thesis [26]. Attachment A2 deals with Ag nanoislands stabilized by a magnetron-sputtered PTFE, their preparation, characterization and SERS testing. Both the silver nanorods as well as silver nanoisland, fabricated at the Department of Macromolecular Physics, represent two principal substrates investigated during this thesis. Anisotropic nature of the Ag nanorods was in detail investigated in our work using polarization- and angular- resolved SERS spectroscopy and ellipsometry. These experimental findings form the base of our article presented in Attachment A3. Later, fabrication of silver nanoislands was upgraded, giving rise to gradient surfaces with the optical properties varying across the sample length. Analysis of their SERS performance is contained in an article presented in Attachment A4. Experience from polarization- and angular- resolved measurements worked as an inspiration for us to write a review article focusing on polarization- and angular- resolved optical response of molecules on anisotropic plasmonic nanostructures (Attachment A5). Attachment A6 focuses on fabrication of mixed gold/silver nanoislands in order to further increase the SERS signal in comparison to single silver coatings. The article on silver nanoislands for surface-enhanced fluorescence is currently ($10^{th}$ December, 2018) under preparation.

## 4.1. Measurements on silver nanorods

### 4.1.1. Optical characterization and SERS testing

Basic principles of nanorod fabrication were described already in section 1.4.2. Nanorods used within this thesis were fabricated by colleagues at the Department of Macromolecular Physics, MFF UK. Depositions were performed in a cylindrical stainless steel vacuum chamber (40 l) pumped by scroll and turbomolecular pumps to base pressure lower than $10^{-3}$ Pa. Films were deposited onto Si wafer support introduced into the deposition chamber by a load-lock system.

Ar (purity 99.99%) was used as a working gas. The pressure during deposition was 0.18 Pa, magnetron current was 300 mA and the distance between magnetron and the substrate was 10 cm. The fabrication setup enables the choice of the deposition angle $\alpha$ between ~ 70° and 85° (Fig. 5). For most SERS measurements, the deposition angle was set to 85° and the deposition time to 15 minutes. Under these conditions the mean diameter of individual Ag nanorods was 60 nm, the mean distance between their centers was 150 nm and the height of the nanorod array was around 200 nm. This situation is depicted in Fig. 6 where top and side views of the silver nanorods, acquired by scanning electron microscopy, are presented.

For the sake of characterization of the surface plasmon properties of the silver nanorods, silver deposition was performed on glass and extinction spectra of structures fabricated in this way were obtained. Extinction spectra of the silver nanorods are displayed in Fig. 12. From here it follows that the structures exhibit plasmon resonance over a very broad range of wavelengths.

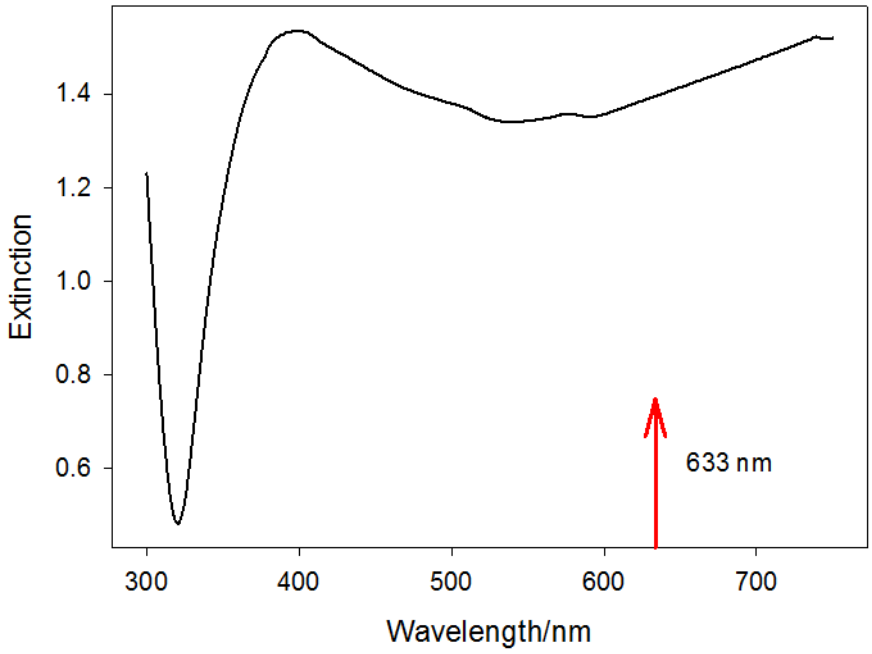


Figure 12. Extinction spectra of Ag nanorod arrays with the main excitation wavelength used for SERS testing.

Preliminary SERS testing of silver nanorods has already been carried out in the diploma thesis [26] where spectra of methylene blue, certain amino acids,

proteins and porphyrins were obtained. It was also found that keeping the substrates in a vacuum chamber immediately after the deposition significantly reduced the occurence of spurious bands resulting from the preparation procedure.

Two strategies of substrate deposition were chosen for the SERS testing: (i) a droplet of a stock solution of a particular analyte was deposited on the sample and left to dry, and (ii) the nanorod substrates were cut into ~ 0.5 cm × 0.5 cm pieces and immersed in the stock solution of a particular analyte for some time. The latter approach was used for the testing of uniformity and spectral reproducibility of the nanorod arrays (using MB as the model molecule) since it results in a more regular distribution of molecules on the metal surface. Different batches of silver nanorod arrays were tested by mapping random places at the samples covering 10 × 10 spectral points with an increment of 5 μm. Different excitation wavelengths were tested (515, 633 and 785 nm), but the biggest SERS signal was provided by the 633 nm wavelength. In the case of methylene blue, the best quality of the SERS signal at 633-nm wavelength may not only be due to the biggest scattering cross section of silver nanorods around this wavelength, but also due to the fact that this excitation wavelength closely matches the shoulder of the MB absorption band (resonance effect, Fig. 13). Thus, the wavelength of 633 nm was used for most of other remaining SERS experiments with silver nanorods. The substrates were found to provide stable SERS enhancement even when stored for 1 year after the preparation.

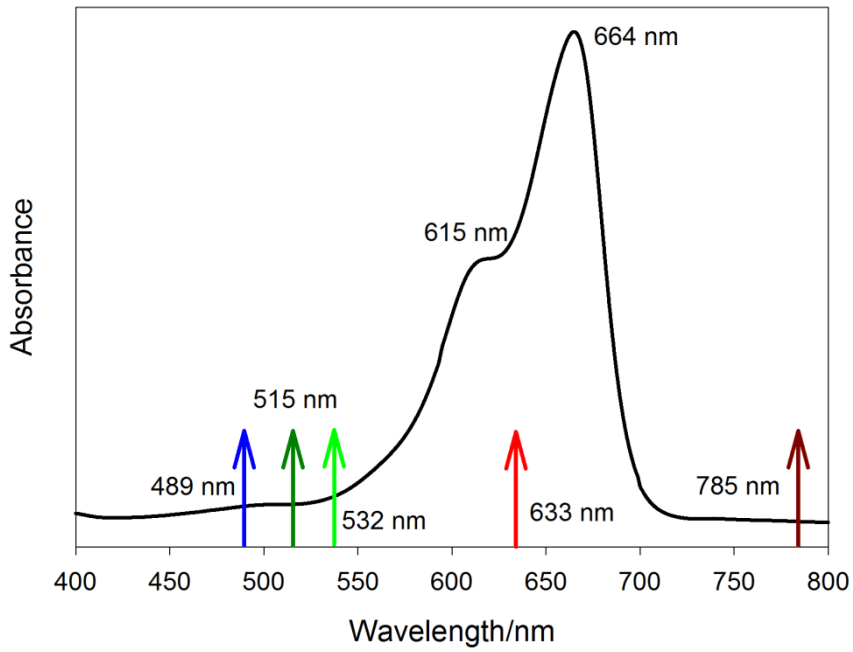


Figure 13. Absorption spectrum of MB. All excitation wavelengths tested are marked in the picture.

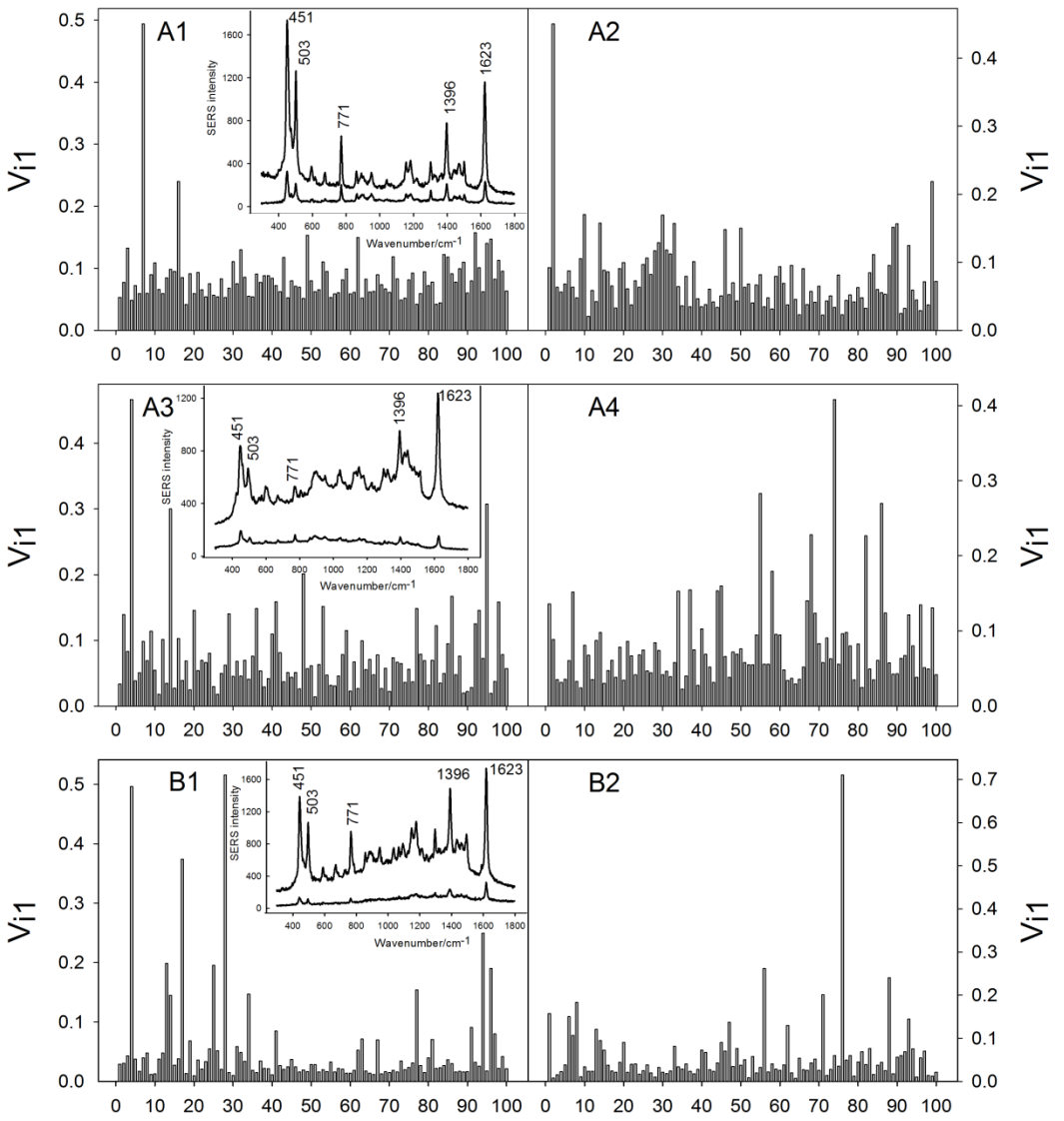


Figure 14. Reproducibility of MB spectral maps on two different batches of silver nanorod arrays (A and B) determined using FA. Increments between neighbouring mapping points were 5 μm. Spectral maps on the batch A were taken two days after their fabrication (A1, A2) and after 1-year storage (A3, A4). Examples of MB spectra with an average enhancement and spectra obtained from hot-spot sites are depicted as insets of graphs A1, A3 and B1.

Fig. 14 reveals that both substrate batches as well as 2-day and 1-year aged substrates provide reproducible SERS enhancement (signal variation up to 20%) apart from occasional hot-spots where the intensity is higher. Higher SERS intensity obviously comes from the excitation of hot-spots, which are sparsely distributed over the surface and which negatively influence the SERS reproducibility. In order to describe this effect more quantitatively, we determined the relative frequency of

number of hot-spots in a given mapping area (10 × 10 spectral points) using 20 separate spectral maps of MB on a given substrate as well as across different substrate batches. Assuming for simplicity that hot-spot is a point where the SERS intensity was at least 3 times the average intensity of a given spectral map, the relative frequency of hot-spot was found to exhibit the expected Poisson distribution. The mean number of hot-spots was found to be $\sim 4$ with the mean deviation of $\sim \sqrt{4} = 2$. Therefore, we conclude that the number of hot-spots represents $\sim 2\%$ – 6% of the SERS active sites of the mapping substrate area (Fig. 15).

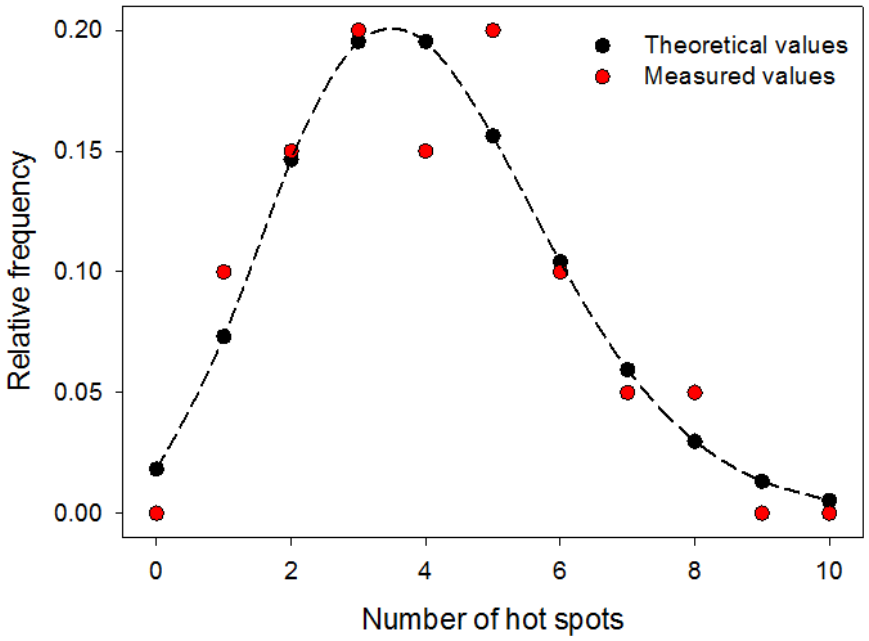


Figure 15. Comparison of the relative frequency of number of hot-spots in a given map of 10 x 10 spectral points (out of 20 maps in total) with the values predicted by the Poisson distribution with a fixed mean value of 4.

### 4.1.2. Polarization and angular dependences of Ag nanorods

Due to the anisotropic nature of the nanorod arrays, this substrate was used for the study of anisotropic optical response. For this purpose, silver nanorods fabricated at the deposition angle $\alpha = 70°$ were used. That was because this deposition angle was found to provide the best-reproducible results during preliminary measurements. The polarization- and angular-resolved SERS experiments were carried out in the 90°-scattering geometry in which two out of three Euler angles determining the nanorod spatial orientation and four polarization

combinations can be varied simultaneously. This experimental advantage enabled us to carry out the most in-depth investigation of polarization- and angular-resolved characteristics of the silver nanorods to date, as far as we know. The testing molecule was methylene blue. Before SERS measurements, the substrates were cut into ~ 1 cm × 1 cm pieces, immersed in $1\times10^{-6}$ M MB solution for 1 hour, then removed and dried with an air stream. Since this excitation wavelength approaches the slope of the electronic absorption band of MB, obtained SERS spectra should be considered as pre-resonance ones (Fig. 13).

For better description of experiments in this section, let us adopt the laboratory-fixed coordinate system with axes lined up as sketched in Fig. 16. Let us label the direction along the wavevector of the incident beam ("vertical") the $z$ direction, analogously the $y$ direction along the wavevector of the scattered beam and the $x$ direction perpendicular to $y$ and $z$ (perpendicular to the plane of sheet). In this notation, $yz$ determines the scattering plane. SERS spectra of methylene blue were retrieved with varying tilting angle of the substrate $\theta$ (corresponding to rotation about the $x$ axis) and the azimuthal angle $\varphi$ (corresponding to rotation about the $z$ axis). Four angles $\varphi$ were used in our measurements (0°, 90°, 180° and 270°) with the angle $\theta$ bound between 20° and 70° (increment 4°, with the exclusion of the interval between ~ 40° – 50° in order to avoid direct reflection from the surface falling on the detector). To better describe changes in SERS intensities with both angles, we further introduce the primed (sample-fixed) Cartesian coordinate system $x'$, $y'$, $z'$ where $x = x'$ and $z'$ lies at any instant along the substrate normal. Since there are two basic possibilities of setting the polarization of the incident beam as well as the scattered beam, a total of 4 different polarization combinations arise, which we will abbreviate as:

$$I(e_x^{exc}, e_x^{det}) = I_{vv}, \qquad I\left(e_y^{exc}, e_x^{det}\right) = I_{hv}, \tag{4.1a}$$

$$I(e_x^{exc}, e_z^{det}) = I_{vh}, \qquad I\left(e_y^{exc}, e_z^{det}\right) = I_{hh}, \tag{4.1b}$$

with the first subscript standing for the excitation light and the second subscript standing for the scattered (detected) light; $v$ stands for vertical (with respect to the scattering plane) and $h$ for horizontal polarization. One of the four above-mentioned polarization arrangements together with angles $\theta$ and $\varphi$ unambiguously define the experimental configuration for SERS response measurements.

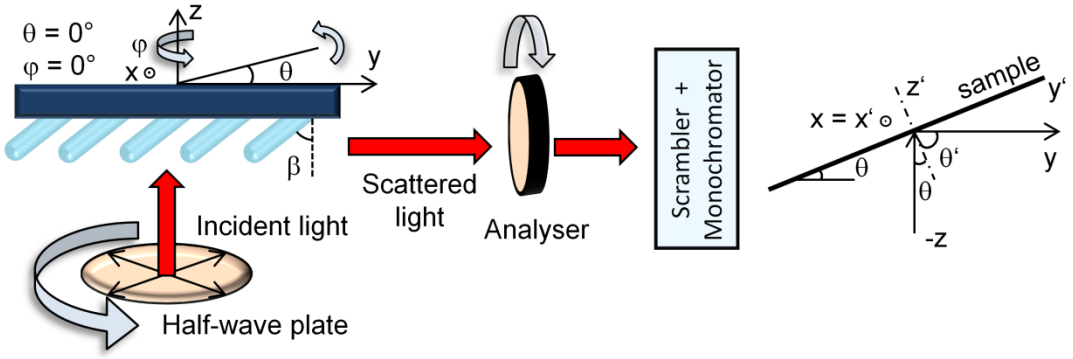


Figure 16. Scheme of the experimental geometry for polarization- and angular-resolved SERS experiments.

The samples were glued to a supporting glass slide and fixed to a substrate holder capable of rotation about the $x$ axis (see Fig. 16). The exact $y$ position of the holder was set so that the incident beam would intersect the $x$ axis to achieve optimal focus. Moreover, its $z$ position was slightly readjusted after each change in the angle $\theta$ if needed to retain the laser spot at any instant exactly in the objective axis and to obtain the highest SERS signal. To keep the sample heating and photodecomposition at a bare minimum, the laser power was set to 100 mW (focused to a spot of ~ 10 mm$^2$ at an angle $\theta = 45°$). A very simple consideration may help to estimate the role of hot-spots in the uncertainty of the SERS measurements in this case: Supposing, for simplicity, 4 hot-spots over the area of 50 × 50 μm$^2$, it makes ~ 16000 hot-spot sites over 10 mm$^2$ with the standard deviation of $16000^{1/2}$ ~ 126 and the relative standard deviation of the SERS intensity < 1%. In other words, the actual number of hot-spots is expected to average out on the mm scale. Uncertainty in our measurements was therefore caused mainly by slight sample photodecomposition in the course of our measurements. In order to partly overcome this problem, measurement in each of the 4 polarization arrangements was repeated twice (4 spectra $I_{vv}$, $I_{hv}$, $I_{vh}$, $I_{hh}$ were measured in a given order and immediately after in the exactly opposite order) and the geometric mean of two corresponding spectra was used for further analysis to account for slight signal diminishment with time. All spectra were recorded using 30s acquisition time (1s exposition × 30 accumulations).

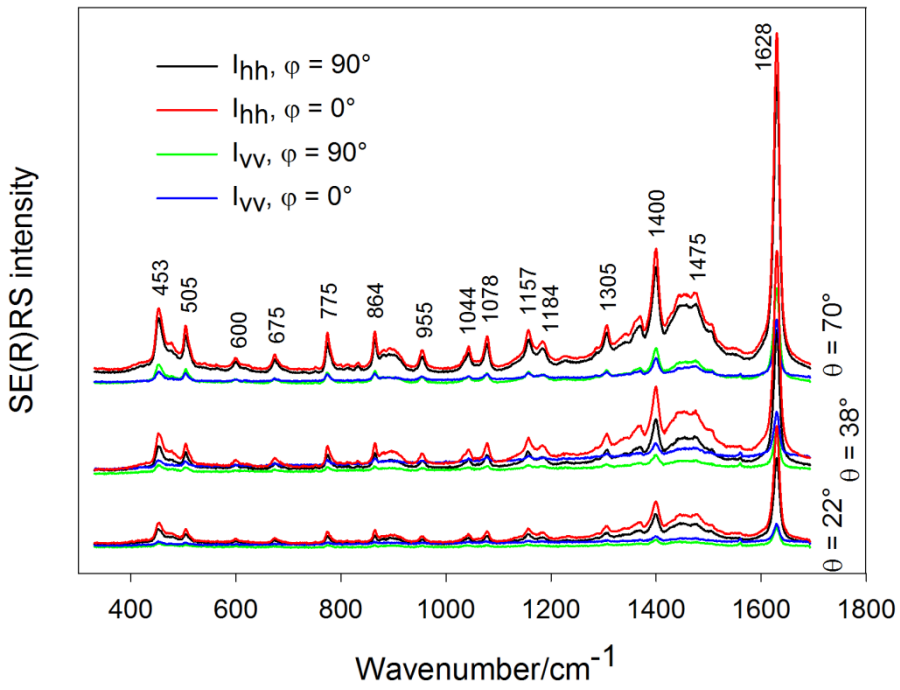


Figure 17. Examples of MB SERS spectra obtained under different configurations. Spectra for different angles $\theta$ are offset for clarity.

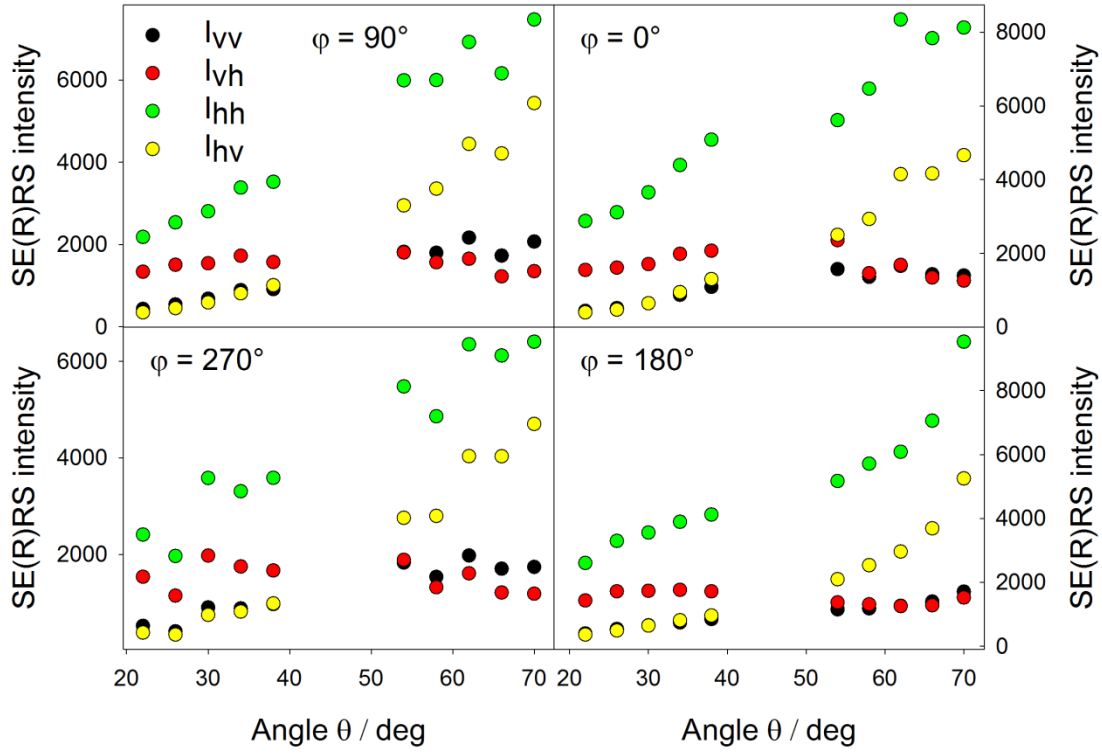


Figure 18. Variation in MB SERS intensities with angles $\theta$, $\varphi$ and polarization arrangement for the 1628-cm$^{-1}$ band.

Examples of MB SERS spectra obtained under different configurations are given in Fig. 17. A more detailed account of varying SERS intensities with varying angles $\theta$, $\varphi$ and polarization arrangement is given in Fig. 18. These intensities, assumed as height of the 1628-cm$^{-1}$ peak above spectral background, vary up to ~ 1 order of magnitude when measured under different configurations.

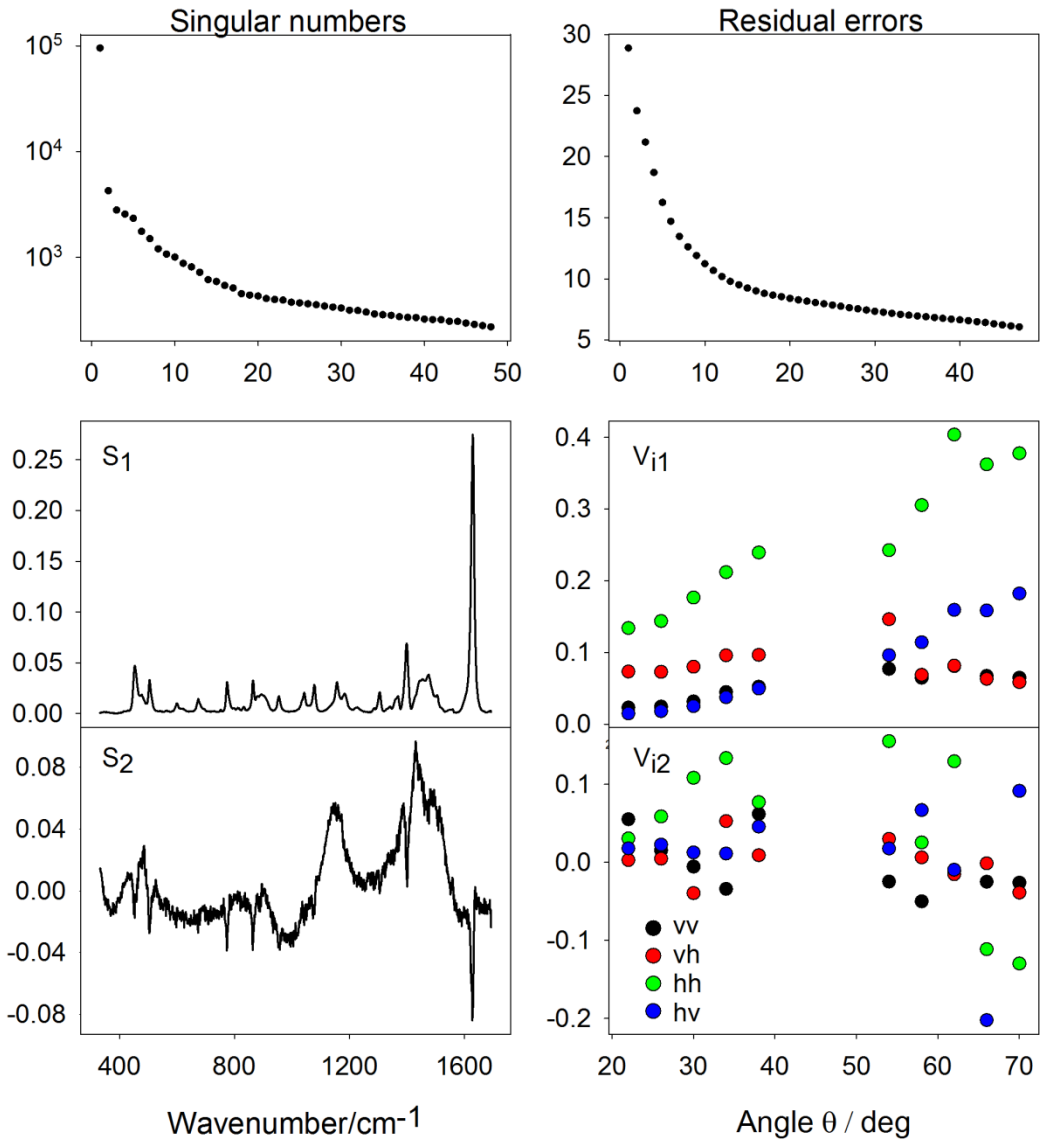


Figure 19. FA results of baseline-corrected MB SERS spectra measured at an angle $\varphi$ = 0°. The subspectrum $S_1$ represents the basic spectral profile and the profile of the $V_{i1}$ coefficients very well fits the intensity profile of the 1628-cm$^{-1}$ MB band given in Fig. 18. Different polarization arrangements are distinguished by different colours. Shape of the subspectrum $S_2$ and profile of the $V_{i2}$ coefficients were not reproducible in our measurements and were both extremely sensitive to slight changes in background subtraction.

In order to obtain even deeper understanding of varying SERS intensities with different experimental configurations and to possibly identify subtle spectral changes such as varying relative intensities across different bands, FA was employed (Fig. 19). FA results suggest that only the first subspectrum is sufficient so that the original spectral information is retained within the noise level. Therefore, all observable MB bands in Fig. 19 exhibit the same polarization and angular-dependent behaviour. This is in agreement with the fact that most observable bands in the spectrum are of the same symmetry [111].

Obtained polarization and angular characteristics may be attributed to many different factors, such as: (i) different surface plasmon coupling efficiency between the incident/scattered laser field and silver nanorods with changing polarization/wavevector direction ("plasmonic anisotropy"), (ii) effectiveness of collection of the scattered radiation and different laser spot size with a given angle $\theta$ (scaling approximately as $\sim \cos\theta$) [112], and especially (iii) interference between the incident/scattered and reflected radiation as dictated by the surface selection rules [5, 13, 113]. Briefly, an adsorbed molecule may be thought to be illuminated by two beams, a direct beam and the beam reflected from the surface, which superimpose coherently. By analogy, the total scattered radiation results from interference between a directly scattered beam and the one experiencing a reflection from the surface. Having adopted the system of coordinates $x'$, $y'$, $z'$ as shown in Fig. 16, the surface selection rules for the 90°-scattering geometry read

$$I_{vv} \sim |\alpha'_{xx}(1+r_s)(1+r'_s)|^2, \tag{4.2a}$$

$$I_{hv} \sim \left|\alpha'_{xy}(1+r'_s)\left(1-r_p\right)\cos\theta + \alpha'_{xz}(1+r'_s)\left(1+r_p\right)\sin\theta\right|^2, \tag{4.2b}$$

$$I_{vh} \sim \left|\alpha'_{yx}(1+r_s)\left(r'_p-1\right)\cos\theta' + \alpha'_{zx}(1+r_s)(1+r'_p)\sin\theta'\right|^2, \tag{4.2c}$$

$$I_{hh} \sim \left|\alpha'_{yy}\left(1-r_p\right)\left(r'_p-1\right)\cos\theta\cos\theta' + \alpha'_{yz}\left(1+r_p\right)\left(r'_p-1\right)\sin\theta\cos\theta'\right.$$

$$\left.+\alpha'_{zy}\left(1-r_p\right)\left(1+r'_p\right)\sin\theta'\cos\theta + \alpha'_{zz}\left(1+r_p\right)\left(1+r'_p\right)\sin\theta\sin\theta'\right|^2, \tag{4.2d}$$

where $\theta$ is the incident angle, identical to the inclination angle sketched in Fig. 16, $\theta' = 90° - \theta$ in our geometry, $r_s$ and $r_p$ are the Fresnel reflection coefficients [8] related to the frequency of the incident radiation, their primed counterparts refer to

[8] For the sake of better clarity, Fresnel reflection coefficients are not marked by a tilde (~) within this section, although they are generally complex.

the frequency of the scattered radiation and $\alpha'_{ij}$ refers to orientation-averaged components of the Raman tensor of the adsorbed molecule in the primed frame of reference (for more details see [5]).

In order to better understand intensity changes with varying angle $\theta$, Raman spectrum of a Si wafer was measured as a reference (Fig. 20). Fig. 20 demonstrates the difference between experimentally measured Raman intensities of a Si wafer and corresponding theoretical values predicted by the surface selection rules, both with the changing inclination angle $\theta$ measured in the $vv$ arrangement. For this purpose, optical pseudo-refractive index of a Si wafer $\tilde{n} = n + ik$ was obtained using spectral ellipsometry as $n = 4.11$, $k = 0.35$ (for $\lambda = 532$ nm) and $n' = 4.05$, $k' = 0.33$ for $\lambda' = 547$ nm (corresponding to the wavelength of the scattered radiation of the 520-cm$^{-1}$ silicon mode). The $vv$ arrangement was chosen due to the fact that corresponding intensities depend only on one term of the Raman tensor [5].

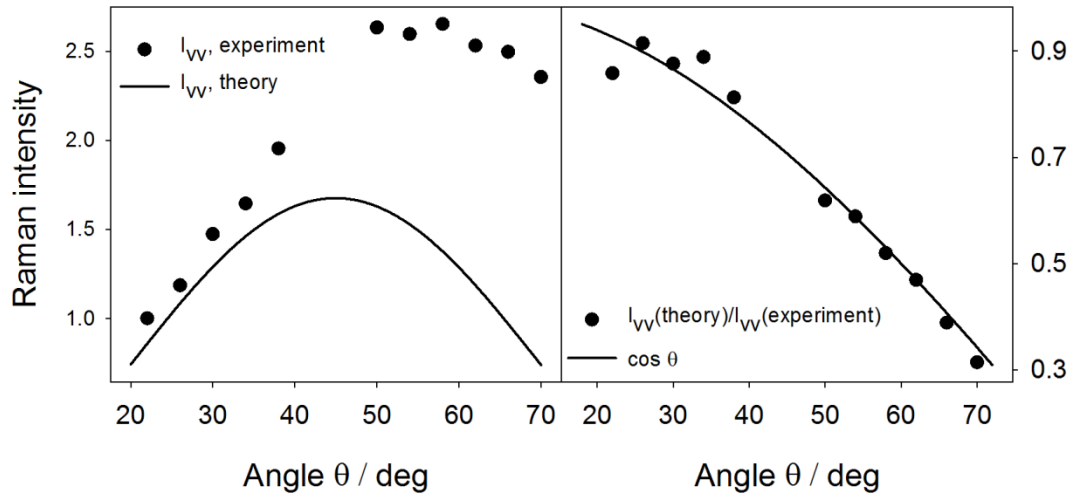


Figure 20. Left: Comparison between Raman intensities of a Si wafer (black points) and (normalized) theoretical line predicted by the surface selection rules with the varying inclination angle $\theta$ as measured in the $vv$ arrangement. Right: The ratios of theoretical/experimental values from the left graph and their fit by a $\cos\theta$ function.

Comparison between experimental and theoretical values implies that their ratio can be well fitted by an expected $\cos\theta$ function [112] and suggests that very similar effect (variation in the laser spot size with the angle $\theta$, point (iii)) will play a dominant role also in the case of nanorod arrays. Therefore, in order to diminish the effect of the geometrical layout, to highlight the difference between different angles

$\varphi$ and since we are interested rather in the relative ratios of MB Raman tensor elements instead of their magnitudes, the depolarization ratios were further analysed instead of intensities (Fig. 21). For the sake of this section, let us define the depolarization ratios as

$$\rho_1 = \frac{I_{hv}}{I_{vv}}, \qquad \rho_2 = \frac{I_{vh}}{I_{vv}}, \qquad \rho_3 = \frac{I_{hh}}{I_{vv}}, \tag{4.3}$$

all of them normalized to $I_{vv}$ since this polarization arrangement provides information only on one element of the Raman tensor of the analyte.

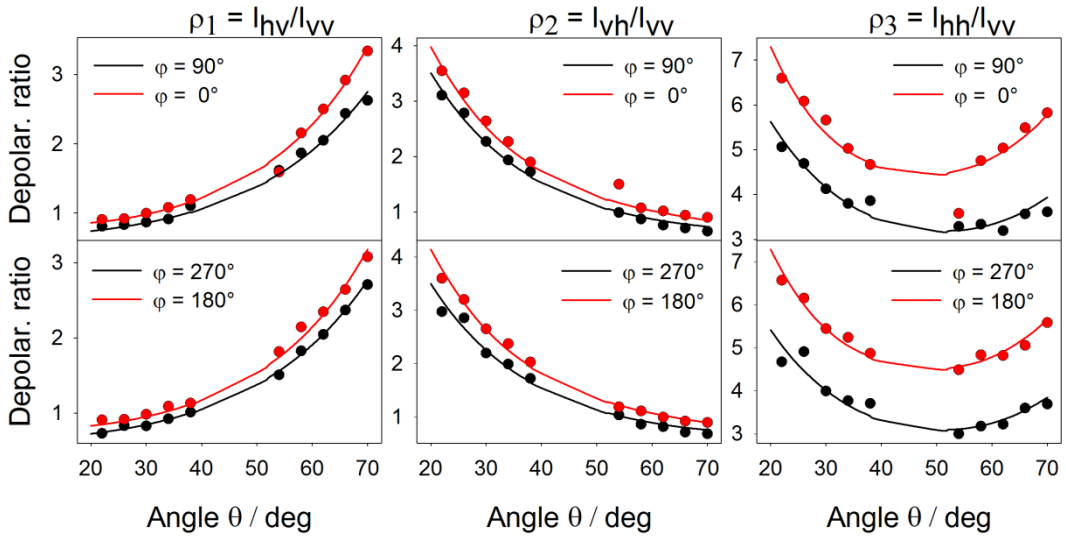


Figure 21. Depolarization ratios of the 1628-cm$^{-1}$ MB band for different angular arrangements (colour points) and their fit by the surface selection rules with pseudo-refractive indices obtained from ellipsometry measurements (lines; see further text).

From Fig. 21, it is obvious that the depolarization ratios exhibit strong dependence on rotating the sample by 90°, although they are fairly insensitive to flipping the sample by 180°. This was expected for $\varphi = 90°$ and 270° since in both cases the angle between the axes of the nanorods and incident/scattered wavevector is the same. More surprisingly, even the ratios for $\varphi = 0°$ and 180° are similar (but still distinct from $\varphi = 90°$ and 270°), indicating that different surface plasmon coupling efficiency of light polarized rather parallel/rather perpendicular to the nanorods has very little effect on the observable characteristics. In other words, although our nanostructures are morphologically anisotropic, the plasmonic properties around the wavelength used (532 nm) are rather isotropic and therefore it

can not be the main reason for the anisotropic behaviour we observed in the SERS experiments.

In order to theoretically describe the SERS response, ellipsometry measurements were performed on the nanostructures with the aim of retrieving their optical constants which enter the surface selection rules (eq. 4.2). Ellipsometry measurements of the nanostructures were carried out after MB adsorption with varying angles $\theta$ and $\varphi$ in the same range as in the case of SERS measurements (Figs. 22 and 23).

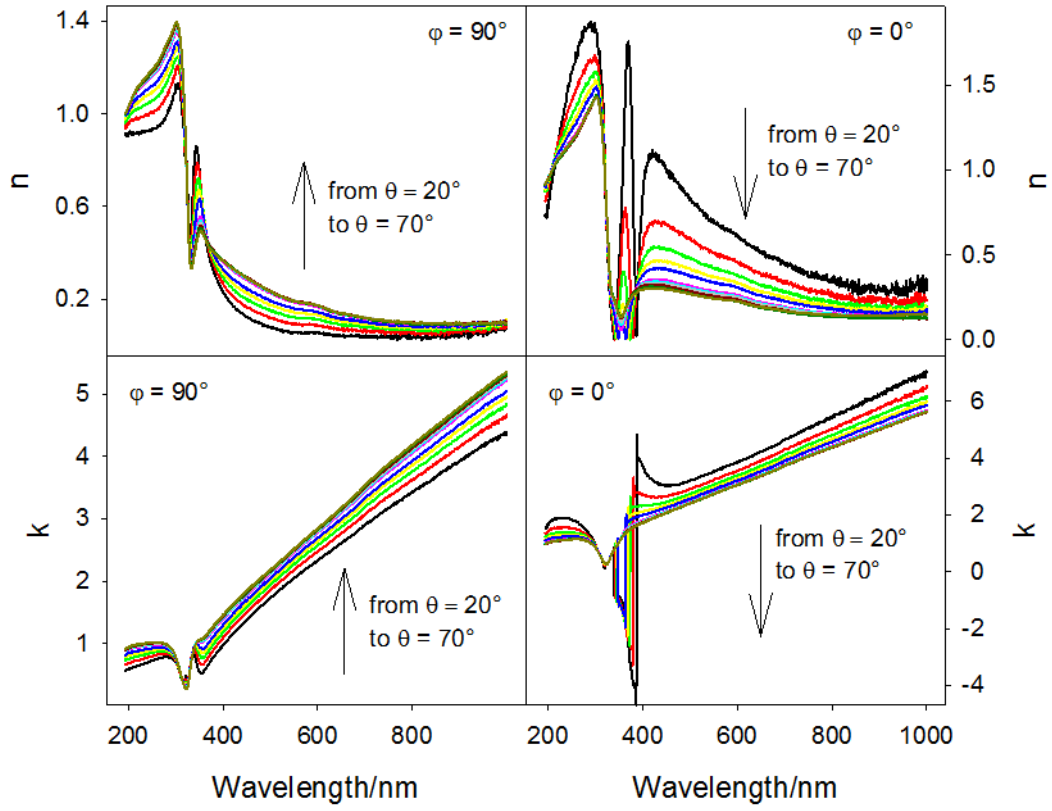


Figure 22. Wavelength dependence of the real and imaginary part of the pseudo-refractive index of silver nanorod arrays for different angles of incidence $\theta$. Left: $\varphi = 90°$ (virtually identical to $\varphi = 270°$). Right: $\varphi = 0°$ (virtually identical to $\varphi = 180°$). Variation with the angle of incidence $\theta$ around $\lambda = 500$ nm is indicated by arrows.

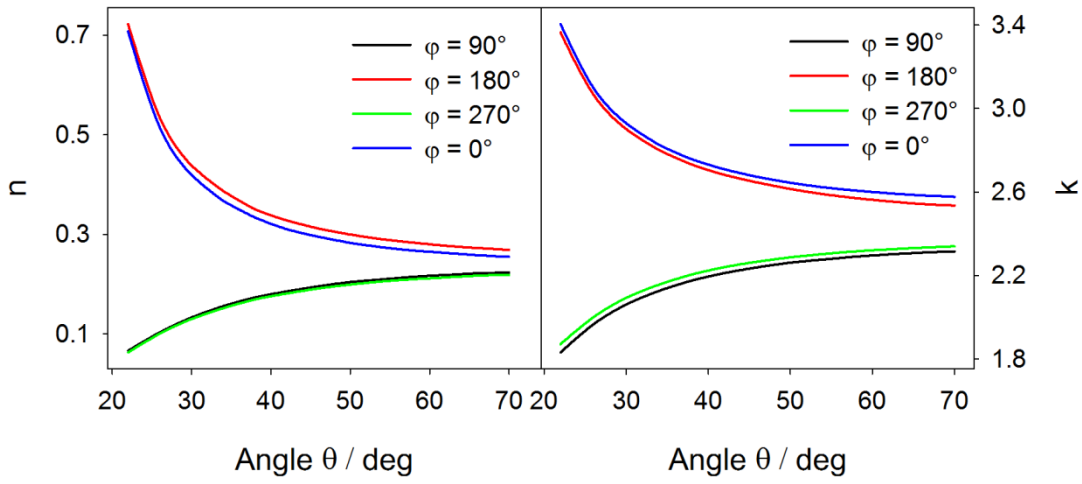


Figure 23. Real and imaginary part of pseudo-refractive index $\tilde{n} = n + ik$ of the nanostructures and their variation with angles $\theta$ and $\varphi$ as measured by standard ellipsometry. The values pertain to substrates after MB adsorption, $\lambda = 532$ nm.

From ellipsometry measurements several basic conclusions were drawn: As expected, the optical (pseudo)parameters of the nanostructured layers are strongly different from the optical constants of the constituent materials. Unlike optical constants of homogeneous materials, optical constants of silver nanorods depend (due to the presence of subwavelength structures) on the incident angle $\theta$ and are strongly influenced by rotating the sample by 90° about the $z'$ axis (Figs. 22 and 23). On the other hand, the optical constants are virtually insensitive to rotating the sample by 180°, which is in full compliance with the SERS results.

Apart from standard ellipsometry measurements, more elaborate approaches were performed on the nanostructures to take their anisotropic nature in account. Generalized ellipsometry measurements of the silver nanorod arrays showed that the ratios $\frac{r_{ps}}{r_{pp}}$, $\frac{r_{sp}}{r_{ss}}$ are < 0.01 (not shown here) and thus the non-diagonal terms of the Jones matrix were neglected in our calculations. We expect that this is due to rather densely packed nanocolumns and low porosity of the structures. Measurements in the reflection mode further revealed that our structures may be treated (around the wavelength of 532 nm) as non-depolarizing and thus analysed by the standard Jones formalism. To sum up, all these results justify using standard ellipsometry for theoretical description of the optical properties of the nanostructured surfaces as well

as application of the surface selection rules in the form given by eqs. 4.2 for theoretical analysis of the SERS response.

Another purpose of ellipsometry measurements was that it can reveal more detailed information on the plasmonic properties of the nanorod arrays. Calculated extinction spectra of our structures for given angles $\varphi$ are depicted in Fig. 24. The extinctance presented there $(E)$ was computed as $E = 1 - R$, where the reflectivity $R$ was obtained based on the values contained in Fig. 22. Extinctance features a sharp transverse plasmon peak around 357 nm and a broad band above ~ 400 nm, attributed to the longitudinal plasmon mode [44, 114]. The latter is less intense than expected, probably due to very high reflectivity of the sample above ~ 400 nm, which may be partly attributed to the supporting Si wafer.

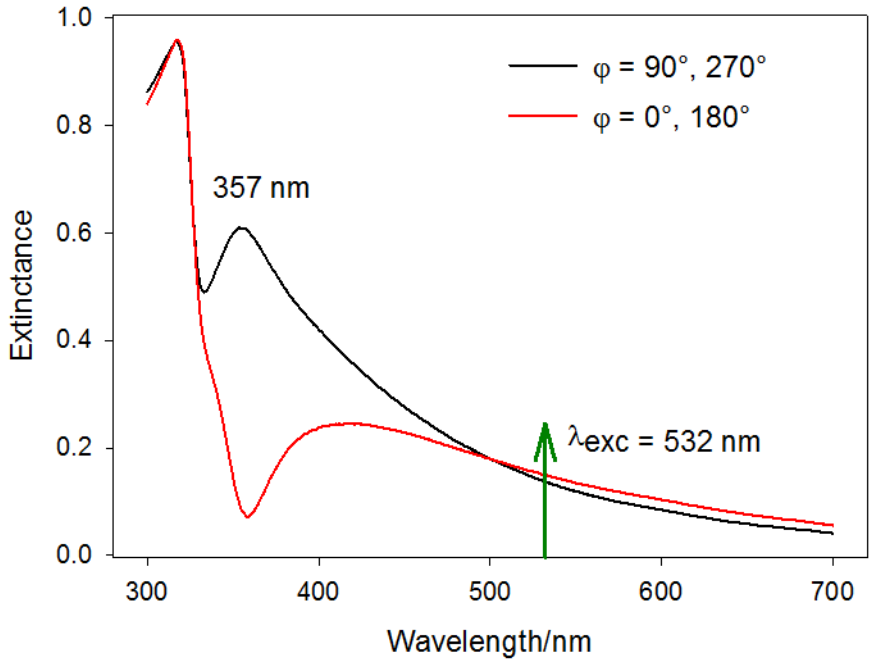


Figure 24. Extinctance of the silver nanorod arrays for angles $\varphi = 90°$ (virtually identical to $\varphi = 270°$) and $\varphi = 0°$ (virtually identical to $\varphi = 180°$). Extinctance $(E)$ was calculated as $E = 1 - R$, where the reflectivity $R$ was obtained based on the values $\tilde{n} = n + ik$ from Fig. 22. The excitation wavelength is marked with a green arrow, the angle $\theta$ was 45°.

We suppose that the distinction between these two profiles may be attributed to different periodicity of our structures in the $x'/y'$ direction. The prepared nanorods are almost perfectly aligned in the direction perpendicular to the nanorod axes (the

deviation of the nanorod axes from the $x'$ axis is negligible from 90°) while the tilting angle of the nanorods $\beta$ exhibits a certain distribution around the value of $\sim 50°$. Since the $\varphi = 90°/270°$ configuration is sensitive predominantly to the former case, the corresponding plasmonic resonance is expected to be rather sharp. On the other hand, in the $\varphi = 0°/180°$ arrangement, the angle made between the polarization vector and axes of respective nanorods exhibits a certain distribution which is reflected in the inhomogeneously broadened longitudinal plasmon peak above ~ 400 nm. Fig. 24 indeed suggests that the coupling efficiency for $\lambda = 532$ nm is almost identical for all four angles $\varphi$ and therefore the difference in the SERS responses when rotating the sample about the $z'$ axis is mostly dictated by interference between the incident/scattered and reflected radiation. "Higher plasmonic anisotropy" is more likely to arise at shorter wavelengths as can be seen in Fig. 24 where the two curves differ more obviously, although more extensive research is required to confirm this.

To again summarize the basic idea of our approach, the experimentally-measured SERS intensities were used to calculate the depolarization ratios. These depolarization ratios are related to specific values of the Raman tensor element of the analyte via optical (pseudo)parameters of the sample. Thus, knowing the optical (pseudo)parameters of the sample, it is possible to use the surface selection rules 4.2 to fit the measured SERS depolarization ratios (colour points in Fig. 21). These fits provide information on the relative ratios of Raman tensor elements of the probe molecule and are represented by solid lines in Fig. 21. The obtained results are summarized in table 1.

Table 1 clearly demonstrates basically comparable values of $\alpha'_{xx}$, $\alpha'_{yy}$, $\alpha'_{xy}$ and $\alpha'_{yx}$ and considerably lower values of $\alpha'_{zz}$, $\alpha'_{xz}$, $\alpha'_{zx}$, $\alpha'_{yz}$ and $\alpha'_{zy}$. MB belongs to the C2 point group symmetry with the vibrational representation $\Gamma^{3N-6} = 54\,\mathrm{A} \oplus 54\,\mathrm{B}$ [111]. The strongest MB band at 1628 $cm^{-1}$ belongs to the A species which transform as $x'^2$, $y'^2$, $z'^2$ and $x'y'$ ($z'$ being the axis of symmetry of the molecule) [111]. Moreover, almost all the other observable bands in the SERS spectrum exhibit very similar intensity profile and thus very similar relative magnitudes of Raman tensor elements as already discussed using FA. This conclusion is also justified by the fact that the pseudo-refractive indices change very little within the Raman shift wavelengths. Thus, for the MB orientation on the surface with the symmetry axis along the $z'$ direction (the plane of the fused phenyl rings perpendicular to the

substrate), the $\alpha'_{xx}$, $\alpha'_{yy}$, $\alpha'_{xy}$ and $\alpha'_{yx}$ Raman tensor elements are expected to be enhanced most while the $\alpha'_{xz}$, $\alpha'_{zx}$, $\alpha'_{yz}$ and $\alpha'_{zy}$ elements should tend to zero. Therefore, we conclude that the orientation of the MB molecule on the surface is predominantly edge-on. This is in aggreement with literature since at higher concentrations the MB is supposed to take rather edge-on adsorptive stance on the surface with the face-on orientation preferable at lower concentrations [5, 111, 115]. The concentration used in our experiments ($10^{-6}$ M) is expected to be slightly above the complete surface coverage [111, 116].

| | $\varphi = 90°$ | $\varphi = 0°$ | $\varphi = 270°$ | $\varphi = 180°$ |
|---|---|---|---|---|
| $\alpha'_{xx}$ | 1 | 1 | 1 | 1 |
| $\alpha'_{yy}$ | 0.91 | 0.97 | 0.90 | 0.92 |
| $\alpha'_{zz}$ | 0.01 | 0.05 | 0.01 | 0.06 |
| $\alpha'_{xy}$ | 0.81 | 0.84 | 0.80 | 0.85 |
| $\alpha'_{yx}$ | 0.80 | 0.89 | 0.81 | 0.91 |
| $\alpha'_{xz}$ | 0.06 | 0.10 | 0.08 | 0.04 |
| $\alpha'_{zx}$ | 0.18 | 0.12 | 0.17 | 0.12 |
| $\alpha'_{yz}$ | 0.01 | 0.09 | 0.01 | 0.01 |
| $\alpha'_{zy}$ | 0.24 | 0.16 | 0.23 | 0.16 |

Table 1. Relative magnitudes of Raman tensor elements (normalized to $\alpha'_{xx}$) of the 1628-cm$^{-1}$ MB band for different angles $\varphi$. These fits were obtained by fitting the SERS depolarization ratios against the surface selection rules. Values revealed by the fit of $\rho_1$ are highlighted in red, by $\rho_2$ highlighted in yellow and by $\rho_3$ highlighted in grey.

The similarity between the MB Raman tensor elements for four angles $\varphi$ is rather peculiar since it indicates that the molecules do not follow the curved orientation of the nanostructured surface. It suggests that the molecules actually do not cover the lateral surface of the nanowires and probably aggregate in the vicinity of the nanorod tips. This may be caused by rather densely-packed nanocolumns, low porosity of the nanostructures and surface tension of the solution [117], but obviously more in-depth experiments are required to confirm this. We propose that this could be further validated by testing different solvents, different analytes and their concentration-dependence or by preparing different nanocolumn height, porosity or constituent materials.

## 4.2. Measurements on metal island films

### 4.2.1. Optimization of silver nanoislands for SERS

Another plasmonic substrate used within this thesis were silver nanoislands growing on a magnetron-sputtered polytetrafluoroethylene (PTFE) film. Fig. 25 shows the scheme of the multilayered design of these SERS-active structures. Their topmost layer is formed by silver nanoislands that are responsible for the SERS effect. Silver nanoislands are supported by a dielectric film made of magnetron-sputtered PTFE, which works as a dielectric separation layer and stabilizes the nanoislands in aqueous environment. This film may be deposited directly on the supporting glass slide, but often a smooth layer of metal was introduced between the glass and the PTFE film. We showed that the presence of the base metal layer serves as a mirror for the incident laser beam, reflecting part of the incoming radiation back to the surface, which increases sensitivity of our measurements by another ~ 1 order of magnitude [95].

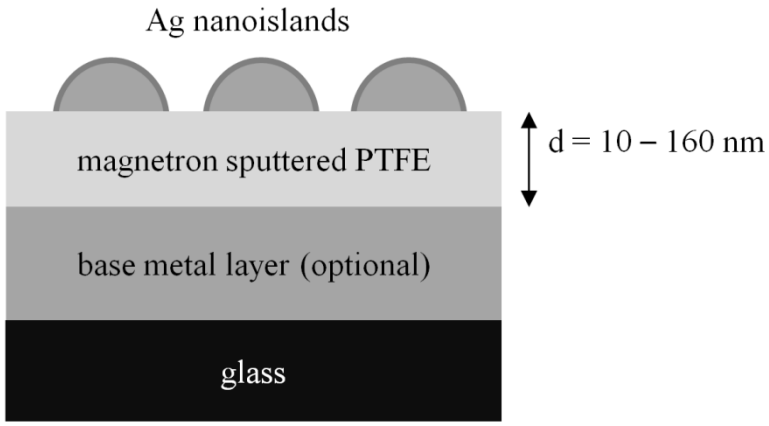


Figure 25. Schematic representation of the prepared nanostructures.

Our optimization strategy of the fabrication procedure was carried out in the following way: The first parameter varied was the deposition time of the silver nanoislands, while the thickness of the PTFE film was kept constant (40 nm) and no back-reflector layer was utilized. Then, a smooth layer of metal was introduced between the supporting glass slide and the PTFE film, while the thickness of the

PTFE film (40 nm) and the deposition time of the silver nanoislands (100 s) [9] remained unchanged. The final step of the optimization process involved variation in the thickness of the dielectric PTFE layer between 10 and 160 nm in efforts to further maximize the SERS signal. In all stages of the optimization process, MB was used as the SE(R)RS probe molecule.

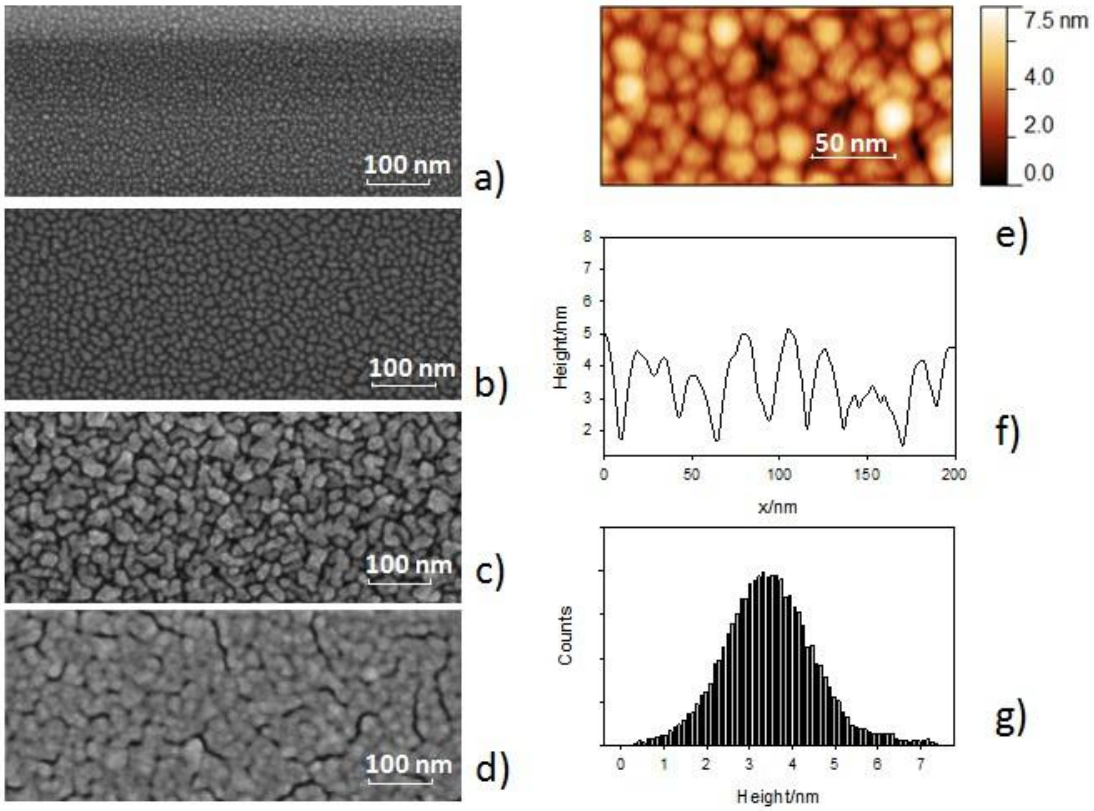


Figure 26. SEM images of sputtered Ag onto PTFE film. Deposition time was a) 20 s, b) 50 s, c) 100 s and d) 200 s; e) 100 nm x 200 nm section of AFM image of Ag deposited onto PTFE film for 100 s, f) corresponding height profile and g) height histogram.

Variation of the deposition time resulted in different morphologies of the nanostructures ranging from small individual silver nanoparticles of dozens of nm at short deposition times to an interconnected silver network observed at longer deposition times (Fig. 26, a – d). Different morphologies of silver coatings consequently resulted in different extinction spectra, and thus different LSPR

[9] The total amount of silver grown on the supporting PTFE layer depends not only on the deposition time, but also on the deposition speed (lower deposition speed requires higher deposition time and vice versa). As the deposition speed was not kept strictly constant for all measurements throughout all experiments described in this thesis, corresponding optimum deposition times may differ from the value of 100 s (see sections 4.2.2. – 4.2.4.).

condition (Fig. 27). For further SERS testing, the deposition time was set to 100 s, corresponding to the surface composed of individual silver nanoislands in close proximity to each other. In this case, the average height of Ag nanoislands was ~ 6 nm, the root-mean-square roughness ~ 1.1 nm (Fig. 26, e – g) and the extinction maximum wavelength (673 nm) slightly red-shifted with respect to the incident laser wavelength (633 nm). The rightmost part of obtained SERS spectral region (~ 1700 $cm^{-1}$) corresponds to the wavelength of approximately 710 nm, which means that both the incident and the scattered radiation may be optimally enhanced. The position and the shape of the extinction band were found to be unchanged within 6 weeks storage after the deposition (Fig. 27 right).

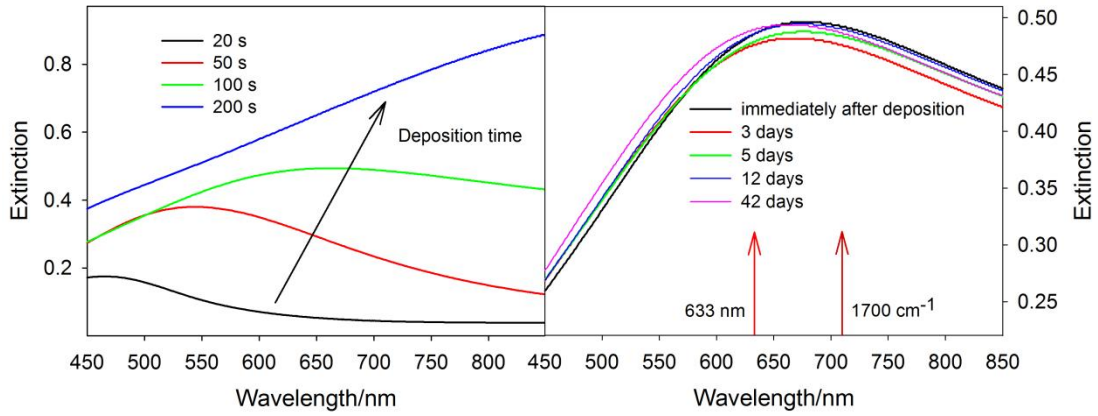


Figure 27. Left: Extinction spectra of Ag sputtered onto PTFE film under different deposition times. Right: Extinction spectra evolution with storage time (100s deposition). The excitation wavelength (633 nm) and the rightmost part of measured SERS spectral region (corresponding to 1700 $cm^{-1}$) are marked by arrows.

In the second step of the optimization process, a smooth layer of metal back-reflector was introduced in the structures as sketched in Fig. 25, expected to provide stronger SERS signals on account of the optical interference effect [118]. Different metal back-reflectors (Ag, Au, Al and Cu) were tested as can be seen in Fig. 28. Our results clearly show the role of the bottom layer of metal, acting like a mirror for the incident laser beam. The maximum signal increase was found for Ag, which is consistent with the fact that Ag is the most reflective metal in the 600 – 700 nm region [3].

Finally, thickness of the dielectric PTFE layer was adjusted. Changes in the thickness of the PTFE films were accompanied by changes in the SERS signal as can be seen in Fig. 28. Fig. 28 demonstrates that the SERS signal rises very sharply as the thickness $d$ of the PTFE layer increases up to $d \sim 80$ nm and reaches a plateau for $d > 80$ nm (corresponding MB intensities for $d = 80$ nm and $d = 160$ nm tend to be the same within the experimental error).

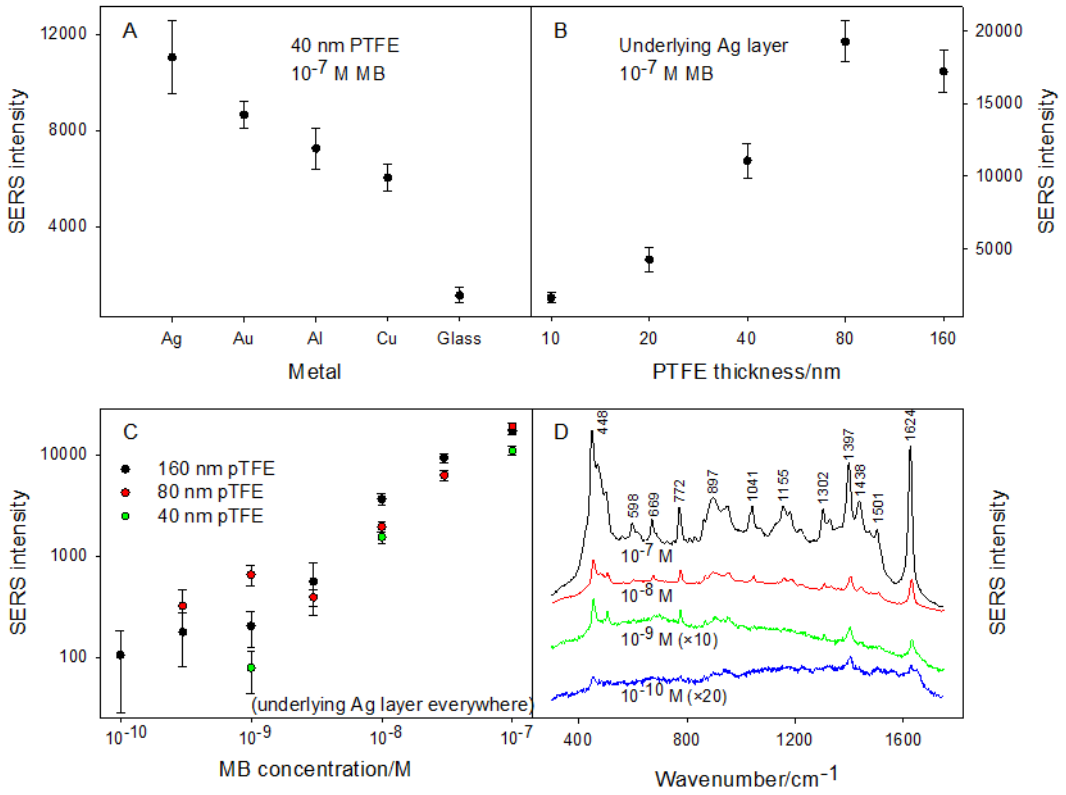


Figure 28. (A) Dependence of the SERS signal on the type of the underlying metal layer (including glass), (B) dependence of MB SERS signal on the thickness of the PTFE film with the underlying Ag layer, (C) concentration dependence of MB SERS spectra on different structures with the underlying Ag layer (intensity determined as the height of the MB peak at 1624 $cm^{-1}$ above spectral background), (D) MB spectra on the optimized structures – concentration dependence (80 nm PTFE, underlying Ag layer). Note logarithmic axes in graphs (B) and (C). Spectra in graph (D) are offset for clarity.

Concentration dependence of MB SERS spectra on the optimized structures (100s nanoisland deposition, underlying silver back-reflector) is displayed in Fig. 28. In all cases, substrates were cut into $x^2 \sim 3$ mm × 3 mm pieces, immersed in a MB stock solution of a particular concentration for 30 minutes, then removed from the solution and dried with an air stream. For MB concentrations lower than $10^{-10}$ M the

signal is overlapped by strong PTFE background and that is why we conclude that the $10^{-10}$ M concentration is the detection limit of MB. Indeed, spectral background intensity for $c_{SERS} = 10^{-10}$ M is ~ 900, corresponding to the noise level of $\sigma \sim 900^{1/2} = 30$, whereas the MB intensity is ~ 100 above spectral background. This is in agreement with the commonly established definition of the limit of detection (LOD), according to which the condition for limit of detection is given by $c_{\mathrm{LOD}} = 3\sigma$ [69].

Another quantity evaluating the SERS performance of our optimized structures is the SERS enhancement factor. We determined the substrate enhancement factor, which requires estimation of the number of molecules contributing to the SERS signal. The exact number of MB molecules present in the measured spot is difficult to determine precisely, however, we tried to estimate the surface coverage of the silver substrate by estimating the drop in the initial stock solution concentration ($10^{-7}$ M) after soaking the silver substrate. After the 30 min soaking, the final concentration of the stock solution is expected to be $(1-\delta)\times10^{-7}$ M for a certain $\delta \in (0,1)$. Because this concentration range is too low for absorption measurements, we let another substrate soaked in the stock solution and investigated the drop in the SERS intensity with respect to the $10^{-7}$ M soaking concentration intensity. This experiment was repeated twice and in both cases the SERS intensity decreased to ~ 80% of the original value. Therefore, we estimate $\delta$ to be ~ 0.2 (assuming constant sensitivity at a certain small vicinity of the $10^{-7}$ M MB concentration as the first approximation).

The substrate enhancement factor was calculated considering the intensity ratio of the strongest MB band at SERS spectra ($I_{SERS}$) and at non-SERS (resonance Raman) spectrum ($I_{RRS}$) acquired from a $1.5\times10^{-2}$ M MB solution dropped onto a glass slide and left to dry, measured at the same experimental conditions and normalized to number of respective molecular scatterers:

$$\mathrm{EF} = \frac{I_{SERS}/N_{SERS}}{I_{RRS}/N_{RRS}}, \tag{4.4}$$

where $N_{SERS}$ is the number of molecules participating in SERS measurements and $N_{RRS}$ in the non-SERS case.

The MB drop on the glass surface had a diameter of $a \sim 2.6$ mm and the pipetted volume was $V_{RRS} = 2$ µl, which implies that the surface coverage in the case

of non-SERS measurements was ~ $3\times10^{17}$ molecules/cm$^2$. Substituting these values in eq. 4.4 yields

$$\mathrm{EF} = \frac{I_{SERS}/N_{SERS}}{I_{RRS}/N_{RRS}} = \frac{4}{\pi\delta}\frac{x^2}{a^2}\frac{c_{RRS}V_{RRS}}{c_{SERS}V_{SERS}}\frac{I_{SERS}}{I_{RRS}}. \qquad (4.5)$$

Since the MB molecules are evenly distributed on the Ag surface, the biggest uncertainty of the previous formula lies in the determination of $I_{RRS}$ and in the factor $\delta$ representing the efficiency of binding the molecules in the solution to the silver substrate. The distribution of MB molecules on glass is rather nonuniform due to creation of molecular aggregates. That is why $I_{RRS}$ was determined on the basis of averaging of ~ 1000 spectra (and verified by multiple separate calculations carried out on different areas of the drop), producing the value of $I_{RRS}$ ~ 24 (as compared to $I_{SERS}$ ~ 90, Fig. 29). Even if the value of $\delta$ were unknown, $1/\delta$ must be > 1 with the most likely value of ~ 5. Putting the numerical values in eq. 4.5 (taking the aforementioned uncertainties into account) leads to the biggest EF (for $10^{-10}$ M concentration) between $2\times10^6$ and $10^7$. Thus, EF of our substrates is about 2 orders of magnitude higher than EF commonly reported in literature for Ag nanoislands growing directly on glass [96].

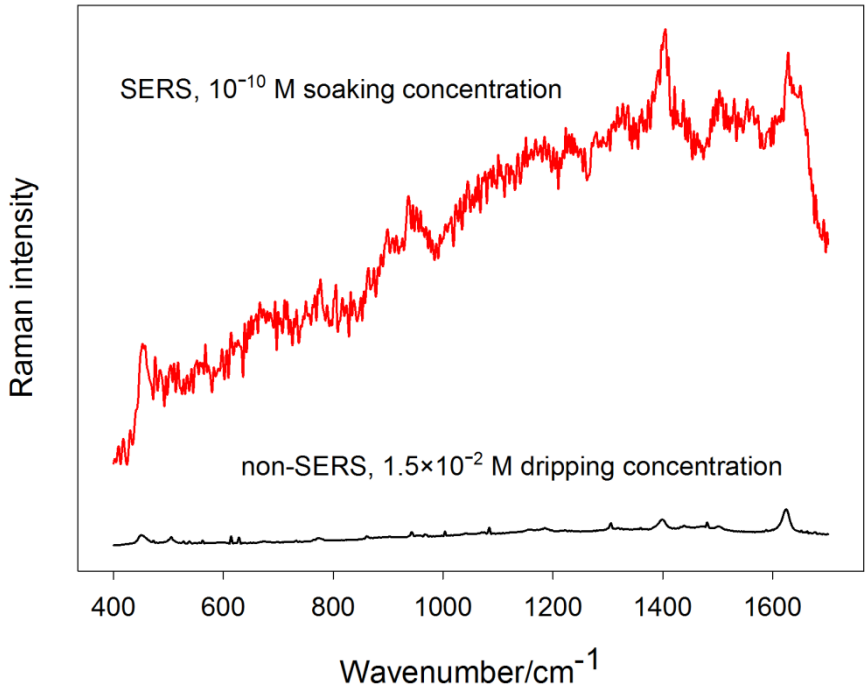


Figure 29. Comparison of SERS and non-SERS MB spectra. Non-SERS spectrum is averaged from 1000 spectra taken across the drop. Spectra are offset for clarity, but the relative proportion between corresponding band intensities (above spectral background) is maintained.

Similarly to the case of silver nanorods, reproducibility of silver nanoislands was evaluated on the basis of spectral mapping (several maps for each measured MB concentration including maps obtained both across a single substrate as well as on different substrate batches), usually comprising 10 × 10 spectral points with an increment of 5 μm. Freshly prepared substrates as well as samples ~ 5 months old (being stored in normal laboratory condition) were included in the reproducibility determination. Examples of spectral maps for various MB concentrations measured under the same experimental conditions are given in Fig. 30.

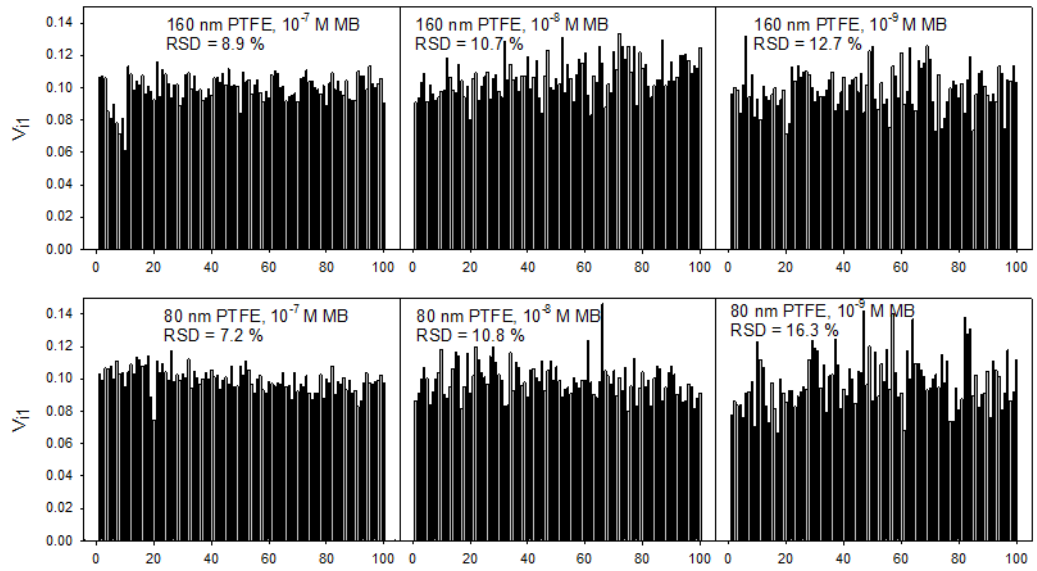


Figure 30. Reproducibility of six representative spectral maps for various MB concentrations measured under the same experimental conditions in terms of coefficients $V_{i1}$ as evaluated using FA.

For all the measured maps on optimized structures down to $10^{-9}$ M MB concentration, the RSD calculated over the whole spectral range did not consistently exceed 20% (Fig. 30), which demonstrates excellent spectral reproducibility. Spectral reproducibility of silver nanoislands is thus better than reproducibility of silver nanorods with almost no presence of hot-spots, making silver nanoislands an ideal candidate for biomolecular quantitative (sensing) applications.

Let us briefly turn back to the surface coverage, discussed previously. Although the equilibrium constant between the number of adsorbed molecules and the number of molecules in the solution may be slightly different for different concentrations, our calculations suggest the surface coverage of ~ $10^{11}$

molecules/cm$^2$ for the lowest measured ($10^{-10}$ M) MB concentration and thus ~ $10^3$ MB molecules in selected measured spots that we are able to detect. On one hand, our nanostructures do not provide the single-molecular sensitivity, which is in turn overcome by very good reproducibility of our substrates.

The potential of our substrates for quantitative SERS analysis of biomolecules was further tested using $H_2$TMPyP, DPA and amino acid cysteine. SERS spectra of these analytes are depicted in Figs. 31 – 33.

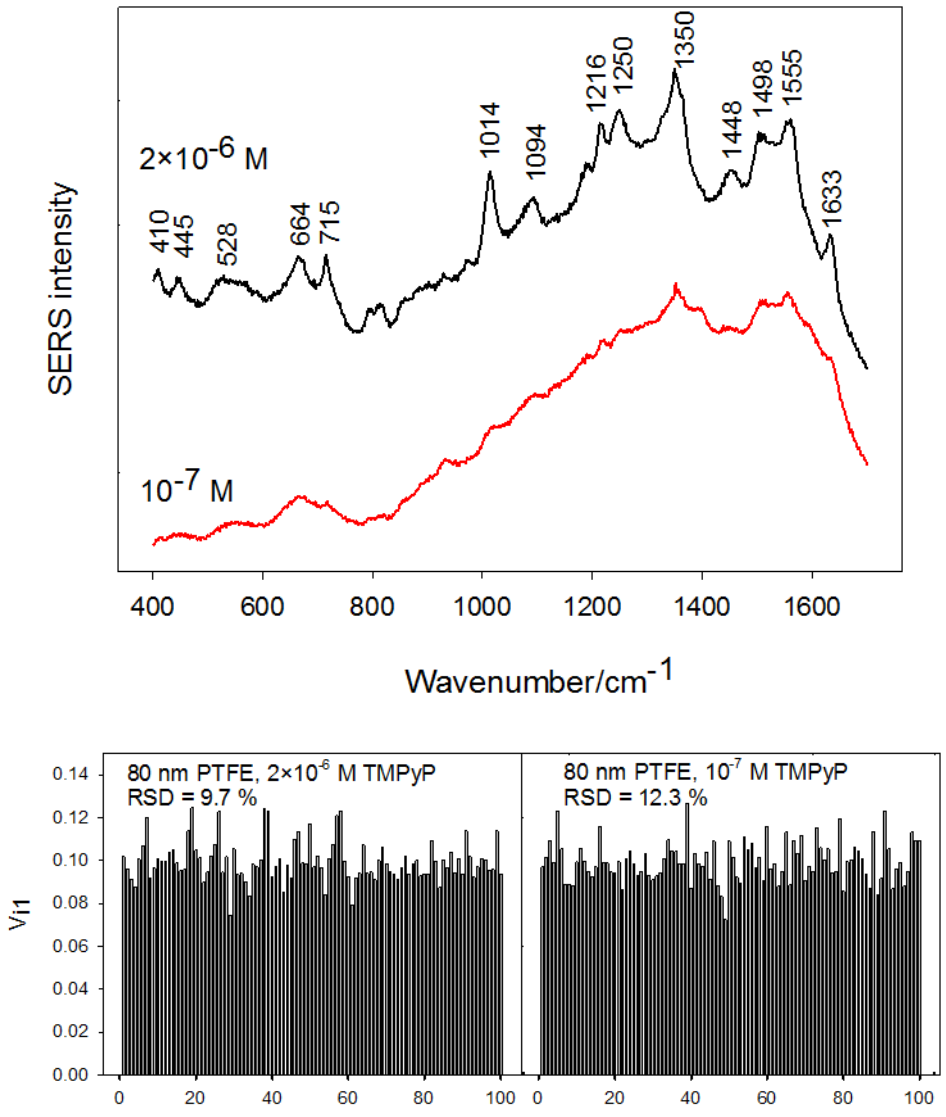


Figure 31. SE(R)RS spectra of $H_2$TMPyP on the SERS nanoislands and two representative spectral maps for two different concentrations. Ag substrate was dipped in adsorbate aqueous solution for 30 min.

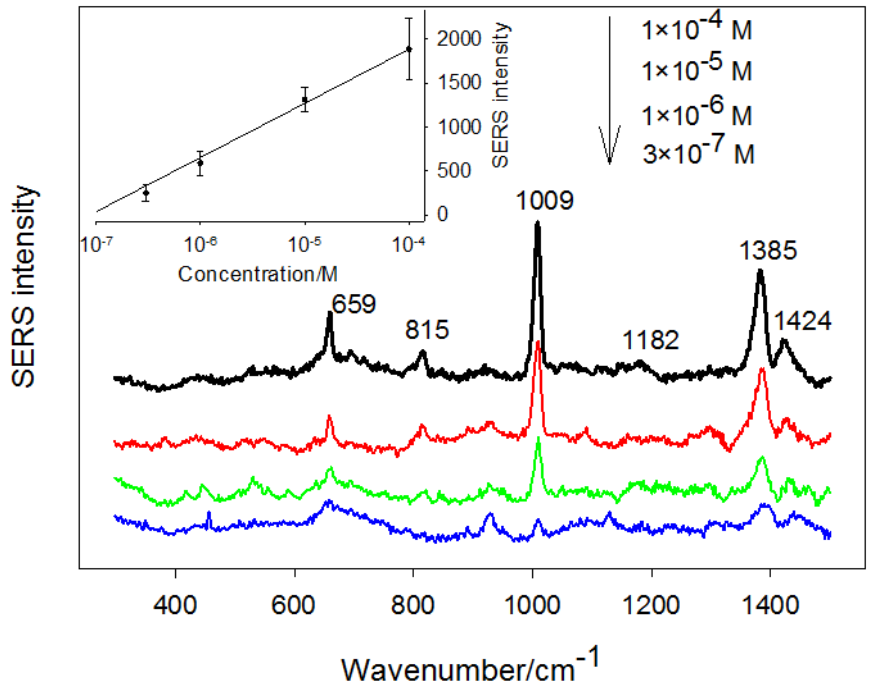


Figure 32. SERS spectra of DPA on the silver nanoislands. Ag substrate was dipped in adsorbate aqueous solution for 30 min, spectra are baseline-subtracted. Inset: Dependence of SERS intensity (assumed as the height of the strongest peak in the DPA spectrum around 1009 $cm^{-1}$) on DPA concentration. This dependence can be well fitted by a line (in a semi-logarithmic scale), which could allow easy quantitative determination of DPA concentration in an unknown sample.

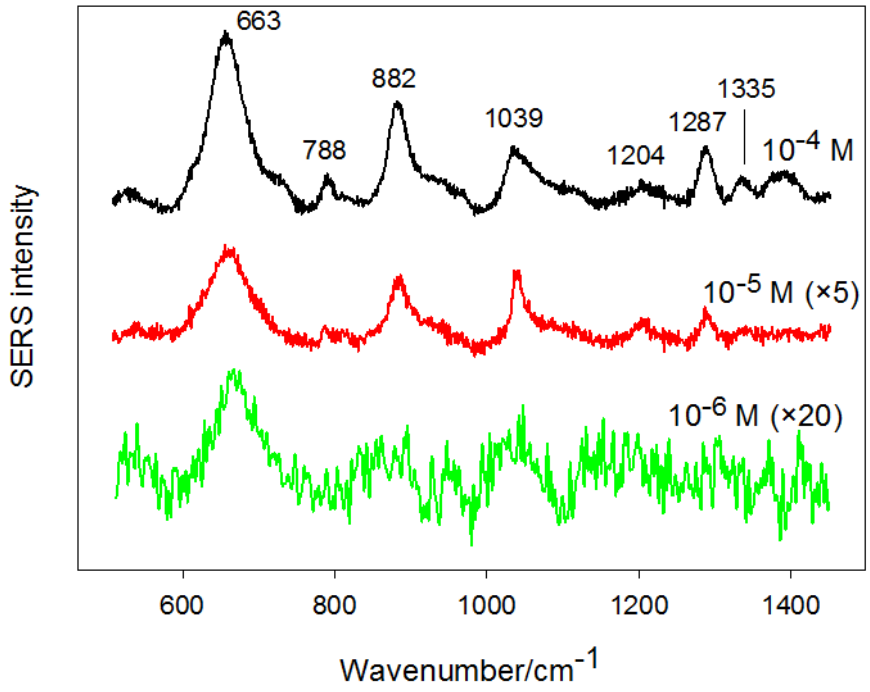


Figure 33. SERS spectra of cysteine on the silver nanoislands. SERS signal was obtained by dropping a 2 µl drop of a cysteine stock solution on the optimized nanostructures. Presented spectra are averaged from 1000 spectra taken across a mapping array and offset for clarity.

### 4.2.2. Gradient silver nanoislands

Later, gradient silver nanoislands, i.e. structures with the LSPR properties changing continuously along the sample length, were fabricated at the Department of Macromolecular Physics. In this case, a moveable mask was introduced in between the substrate and the magnetron during the process of deposition of the nanoislands in order to enable fabrication of surface gradients of the silver coatings. Since different spots on the sample differ in the deposition time of the silver nanoislands, different spots on the sample are expected to be characterized by different LSPR condition and different morphology across the sample length, similar to that in Fig. 26. Moreover, by implementing different mask speeds, one can tailor the course of the LSPR gradient and width of the resonance curves. Lower speed of the mask caused bigger differences in the amount of incoming atoms and thus also bigger differences in inter-particle distances on particular positions on the sample [119]. Therefore, LSPR curves corresponding to lower mask speed are much more inhomogeneously broadened. Examples of extinction spectra of the prepared structures (characterized by the same methods as in the case of "normal" (non-gradient) silver nanoislands) and dependence of the spectral position of the LSPR peak on exposure time and position on the sample, respectively, is shown in Figs. 34 and 35.

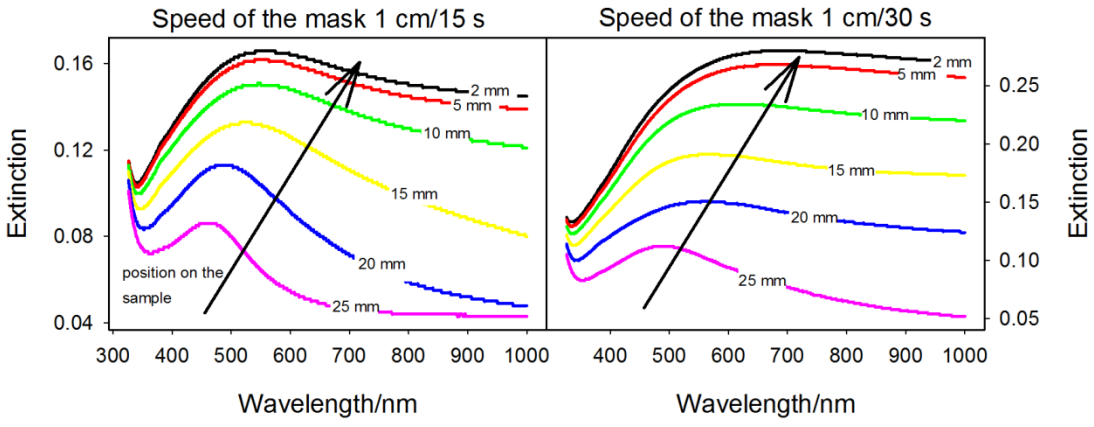


Figure 34. Extinction spectra of the prepared structures. Dependence on the speed of the mask and position on the sample is shown.

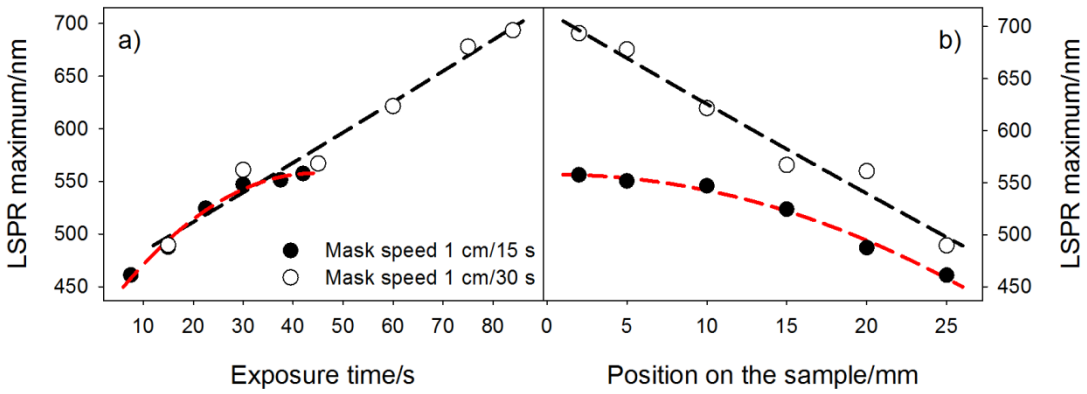


Figure 35. Dependence of spectral position of the LSPR maximum on a) exposure time, and b) position on the sample for two different mask speeds.

Detailed SERS intensity profiles were measured using riboflavin ($c = 3 \times 10^{-5}$ M in water) as the model biomolecule. 3 – 4 drops (2 μl) of the riboflavin solution were deposited evenly across the sample length ($\sim 3$ cm), each of the droplets possessing a different LSPR condition. The limited spatial resolution, imposed by an uncertainty in the determination of the LSPR maximum in respective positions on the sample, is comparable to the droplet diameter ($\sim 2$ mm) in our case. In order to enable rough intensity comparison across different wavelengths, Si wafer was employed as an external intensity standard. This approach accounts for fluctuating laser power as well as the $f^4$-dependence imposed by using different excitation wavelengths [3]. It is obvious that using the excitation wavelength 488 nm, the SERS may be considered as resonance (SE(R)RS), as pre-resonance in the case of the excitation wavelength 515 nm and as out-of-resonance in the case of the 633-nm excitation wavelength (Fig. 36).

Spectral positions of respective riboflavin vibrational modes are virtually identical for all three excitation wavelengths and correspond well with riboflavin SERS spectra reported in literature [120, 121]. The SERS spectrum is dominated by bands centered around 1342 and 1624 $cm^{-1}$, attributed to the vibrational motion of the isoalloxazine ring, which interacts with the Ag surface. These two bands have also obviously biggest contribution from the molecular resonance as their relative proportion with respect to other observable bands is most significant in the case of 488-nm excitation wavelength (to a lesser extent, this effect may be attributable to the $f^4$-dependence of different vibrational modes).

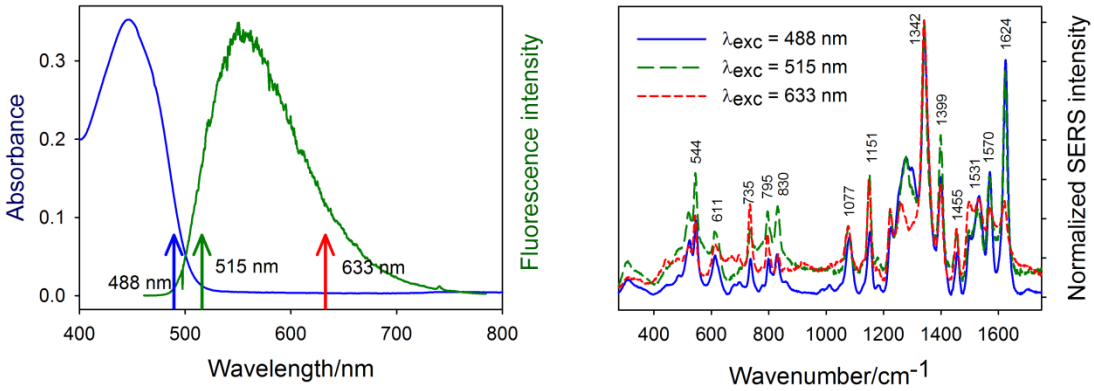


Figure 36. Left: Absorption spectrum (blue) and fluorescence spectrum (green) of riboflavin with the excitation wavelengths marked. Right: Examples of riboflavin SERS spectra taken with different excitation wavelengths normalized with respect to the most intense Raman band.

Most importantly, the effect of the wavelength used is expected to be reflected in the SERS intensity profile when measured along the sample length (in different positions possessing different LSPR conditions). This situation is depicted in Fig. 37.

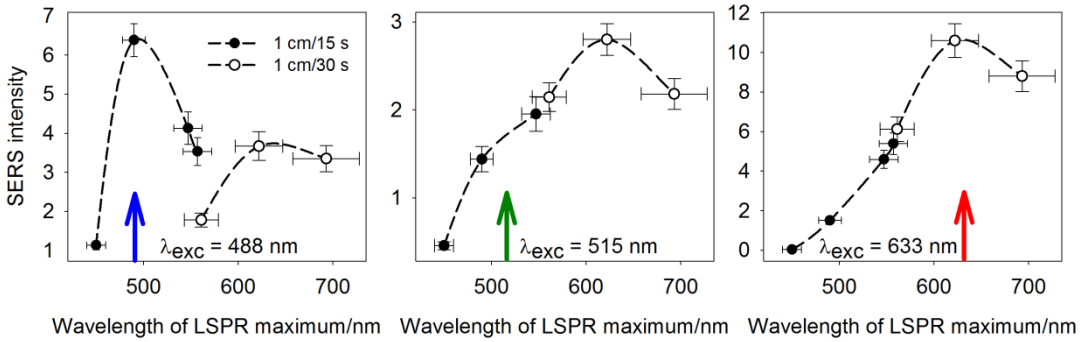


Figure 37. SERS intensity profile with different wavelengths of LSPR maxima across the sample. 2 different mask speeds and 3 different excitation wavelengths were tested. SERS intensities were normalized using a Si wafer as an external intensity standard. The horizontal error bars represent uncertainty in determination of the LSPR maxima (drop size). The vertical error bars were determined from spectral mapping.

The SERS intensity profile with respect to the LSPR maximum position in Fig. 37 results from an interplay between two basic effects: (i) the electromagnetic scattering cross section of the nanostructure (depending on the exposure time of

a particular position on the sample to the Ag flux and consequently different extinction profile and LSPR condition), and (ii) the spectral position of molecular resonance with respect to the excitation wavelength. For the excitation wavelengths 515 nm and 633 nm, the electromagnetic enhancement mechanism is the most dominant. In these instances, the SERS intensity is dictated mainly by (i) the degree of spectral overlap between the LSPR band and the excitation wavelength, and (ii) the scattering cross section on the nanostructures. The scattering cross section of the nanostructures rises when the LSPR position shifts to the red and starts to decrease when a certain size limit is reached [20, 22, 122, 123]. The maximum enhancement in this case was found around the position of LSPR maximum of ~ 630 nm, irrespective of the excitation wavelength used. This can be possibly explained by the fact that using the mask speed 1 cm/30 s, extinction maxima are rather broad and all wavelengths (partly including also the 488-nm wavelength) fall into the LSPR band. It suggests that not only spectral position of LSPR maximum, but also the shape and width of the LSPR peak is decisive for the optimum SERS enhancement. The shape of the SERS intensity profile well correlates with the dependence of the extinction maximum on the LSPR position except for a small shoulder around 500 nm in the case of the 515-nm excitation wavelength, which is obviously due to the fact that this excitation wavelength approaches the slope of the riboflavin absorption band (pre-resonance SERS). Above ~ 650 nm, the SERS nanostructures turn into a smooth film, which results in decrease in the SERS signal. In total, under the conditions of optimum excitation (position of LSPR maximum around 630 nm), the SERS intensity in the case of 633-nm excitation wavelength is about 4× higher in comparison to the 515-nm and 488-nm wavelengths.

For the resonance SERS (excitation wavelength 488 nm), a sharp maximum was found close to the excitation wavelength. This is most likely because of the decisive role of the molecular resonance, which decays rapidly when shifting the LSPR condition of a particular position on the sample off resonance [39].

An aspect, which has not been yet resolved by our measurements, is whether or not the enhancement effect (intensity profile, Fig. 37) is different for different riboflavin modes depending on the excitation wavelength. Our measurements revealed that the trend followed by the graphs in Fig. 37 is (within the experimental error) identical for all riboflavin modes and no significant difference was observed

for larger or smaller Raman shifts (not shown here). However, since SERS benefits from enhancement of both the incident as well as the scattered radiation, different enhancement of different riboflavin modes is predicted, which has also been experimentally demonstrated previously [40, 124]. However, in the case of the 633-nm excitation, the Raman-shift for the 1624-$cm^{-1}$ mode is no bigger than ~ 72 nm, which is obviously too little with respect to the width of the LSPR curves (FWHM ~ 100 – 300 nm) and their shallow maxima to be observable. A strategy which could more likely elucidate this effect would require dipping the gradient substrate in a stock solution (instead of measuring from droplets) and taking large amount of spectra continuously across the substrate (alternatively, this could be performed by examining the ratio of Stokes to anti-Stokes modes [124, 125]). FA could reveal small differences in the enhancement factors of different vibrantional bands. Unfortunately, due to high required consumption of silver substrate in this case, this type of experiment could not have been performed.

### 4.2.3. Gold nanoislands and mixed gold/silver nanoislands

As already mentioned, the theoretical enhancement provided by gold is smaller in comparison to silver, mainly due to bigger imaginary part of the dielectric function. Another consequence is that for the fixed deposition time, LSPR peak for gold appears at higher wavelengths in comparison to silver. This is demonstrated in Fig. 38 where the evolution of extinction spectra of silver and gold nanoislands grown on magnetron-sputtered PTFE film is shown.

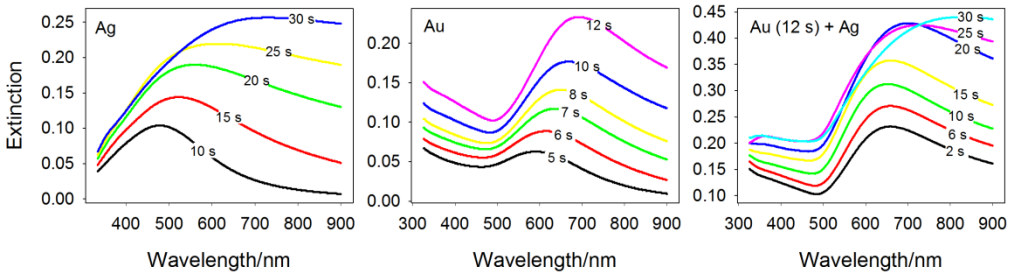


Figure 38. Evolution of extinction spectra of Ag (left), Au (middle) and mixed Au + Ag (right) nanostructures with deposition time.

However, the main drawback of this approach is that the spectral position, height and width of the LSPR band are coupled and can not be independently controlled. This limitation may be overcome using bi-metallic coatings. In this approach, the substrates are first seeded with gold nanostructures that are in the second step overcoated with silver. Fig. 38 (right) shows extinction spectra of these structures with 12 s pre-deposition time of gold and varying deposition time of silver overcoat. As can be seen, spectral position of the LSPR peak does not virtually change (except for the longest Ag deposition time) which enables to examine the dependence of the SERS intensity on height of the LSPR peak. This dependence is depicted in Fig. 39.

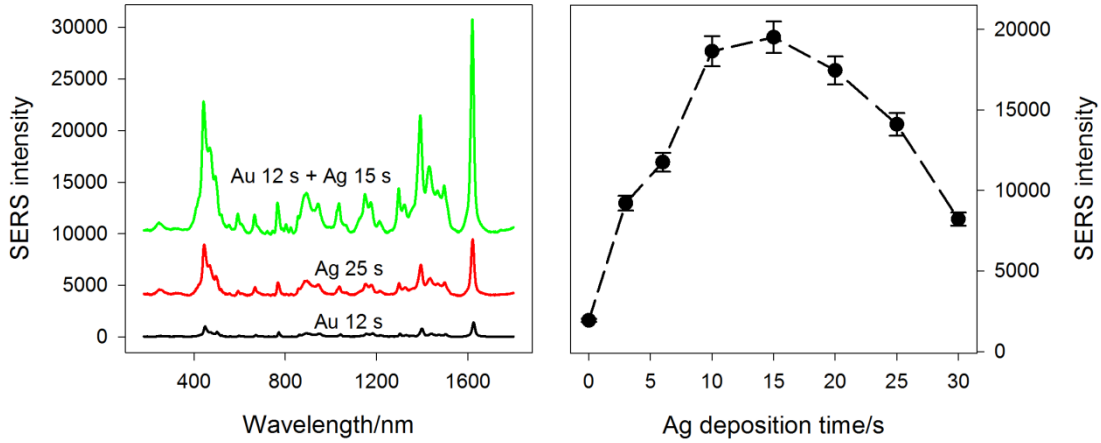


Figure 39. Left: Comparison of MB SERS spectra for optimized Au, Ag and Au/Ag nanostructured coatings. Right: Dependence of MB SERS intensity (peak around 1632 $cm^{-1}$) on the deposition time of Ag for mixed Au/Ag nanostructured coatings with fixed pre-deposition time of Au (12 s).

It is obvious that optimization of single-metal (silver) nanostructured using Au/Ag bi-metallic structures, it is possible to tune in a certain range both the position and the height of the LSPR peak simultaneously, which is not attainable for single metal Ag and Au coatings prepared by the same technique. This can be explained by the assumption that the Ag nanostructures do not grow laterally, but mainly in the direction perpendicular to the surface (silver preferentially grows on gold nanoislands and does not fill the voids in between them). This finding was also supported by very similar morphology for Ag and Au/Ag nanostructures (revealed by SEM) and by the XPS data [126]. Using MB as the testing molecule, mixed Au/Ag

nanostructures provide ~ 4× higher SERS signal in comparison to single Ag coatings and ~ 20× higher SERS signal in comparison to single Au coatings.

Opposite strategy, i.e. seeding the substrates with silver nanostructures and overcoating them with gold, did not in our experiments produce stronger SERS signal in comparison to single Ag or mixed Au/Ag nanostructures (not shown here). This can be explained by the fact that the layer predominantly responsible for the enhancement effect is the upper layer (due to the distance effect) and the enhancement provided by gold is generally weaker in comparison to the enhancement provided by silver. We assume that this approach could be beneficial to molecules which specifically bind to gold (and not to silver) as very small gold overcoat over silver nanoislands could promote the surface adsorption while retaining the enhancement capability of silver. However, the molecules used in our case (MB, riboflavin, porphyrins) tend to bind strongly to both silver and gold, therefore utilization of the gold overcoat resulted in total in decrease of the SERS signal.

### 4.2.4. Silver nanoislands for surface-enhanced fluorescence

Silver nanoislands overcoated with magnetron-sputtered PTFE were used for the study of surface-enhanced fluorescence of riboflavin in water and DMSO, respectively. In this case, deposition time of Ag nanoislands was set at 22 s, corresponding to a broad extinction peak centered around 500 nm, overlapping both the absorption and the emission band of the fluorophore. After deposition of the PTFE cover layer, spectral position of the plasmon resonance did not virtually move, only the intensity of the peak slightly increased (Fig. 40). Different thicknesses of the PTFE overlay were used, ranging between 5 nm and 25 nm as measured by spectroscopic ellipsometry. We systematically monitored the SEF intensity and lifetime dependence of riboflavin with respect to the thickness of the PTFE spacer.

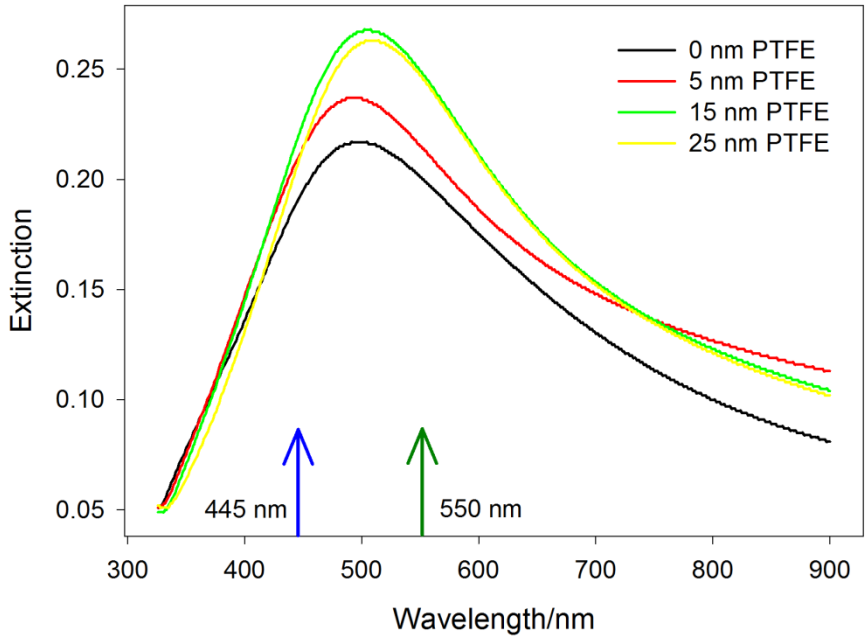


Figure 40. Extinction spectra of silver nanoislands overcoated with PTFE layer of various thicknesses used for the SEF of riboflavin Excitation wavelength (445 nm) is incidated by a blue arrow, approximate position of emission maximum wavelength of riboflavin in a water solution is indicated by a green arrow.

Different strategies were tested in order to optimize the conditions for retrieving riboflavin fluorescence spectra. Deposition of a droplet of the riboflavin stock solution on the sample and letting it dry produced inhomogeneous drying patterns and extremely irreproducible SEF signal when scanning the area. Due to hydrophobicity of the PTFE spacer, most of the molecules aggregated at the edges of the former drop, similarly to the coffee ring effect [71, 127]. Since the target molecules do not attach to the substrate simultaneously when incubating the sample in the riboflavin stock solution, we tried depositing the droplet of the riboflavin stock solution on the sample and collecting the SEF signal after focusing the laser beam on the interface between the droplet and the topmost layer of the sample (Fig. 41). A major advantage of this approach is also absorption of thermal energy of the laser beam in the droplet reservoir, significantly reducing the photodegradation rate of the analyte in comparison to measurements on the dried surface. It also enables direct comparison between lifetimes measured in this way and riboflavin lifetime measured in a solution. In this instance, reproducibility of the SEF spectra, determined by

spectral mapping on 7×7 points over ~ 100×100 μm droplet area, was around 11% (Fig. 42).

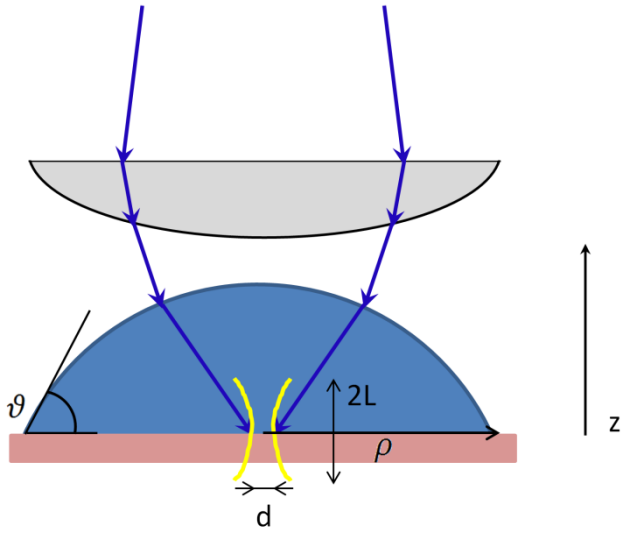


Figure 41. Scheme of the SEF measurements. Profile of the field distribution when focus is placed exactly on the interface is shown. Quantities determining geometry of the experiment are described in the text.

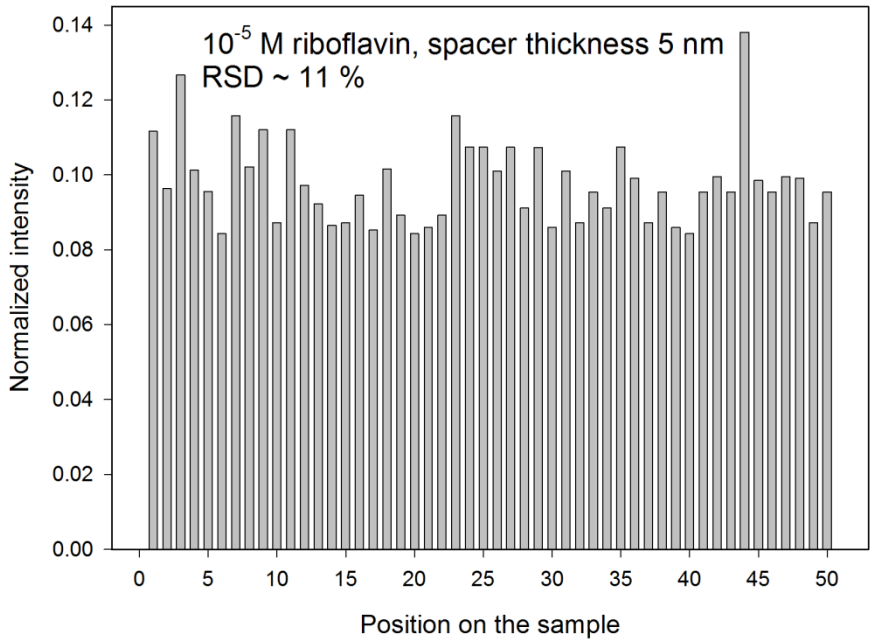


Figure 42. Typical reproducibility of SEF measurements, determined by spectral mapping of the droplet on 7×7 points over ~ 100×100 μm surface area.

A simple geometry of the droplet (Fig. 41) reveals that

$$V = \frac{\pi v}{6}(3\rho^2 + v^2) = \frac{\pi\rho^3(1-\cos\vartheta)^2(2+\cos\vartheta)}{3\sin^3\vartheta}, \qquad (4.6)$$

where $V$ is the droplet volume, $v$ the droplet height, $\rho$ the contact base radius of the droplet and $\vartheta$ the contact angle. 5µl droplets were used in the case of DMSO and 10µl droplets in the case of water (bigger droplets were used in the case of water in order to slow down the rate of droplet evaporation, which negatively influences obtained data). Thus, dimensions of the droplet can be computed numerically depending on the droplet volume $V$ and the contact angle $\vartheta$.

Intensity profile of SEF spectra of riboflavin and corresponding lifetimes (averaged from 4 – 5 independent measurements) are depicted in Figs. 43 (DMSO) and 44 (water). Intensities were assumed as height of the riboflavin emission band centered between ~ 550 – 600 nm above spectral background. In both cases, dependence of fluorescence intensity on the thickness of the PTFE overlay follows the characteristic pattern and exhibits the maximum around the thickness of ~ 5 nm. Fluorescence quenching is observed when no overlay is used, while for the thickness of the spacer ≥ 10 nm the distance effect caused the intensity to fall off rapidly.

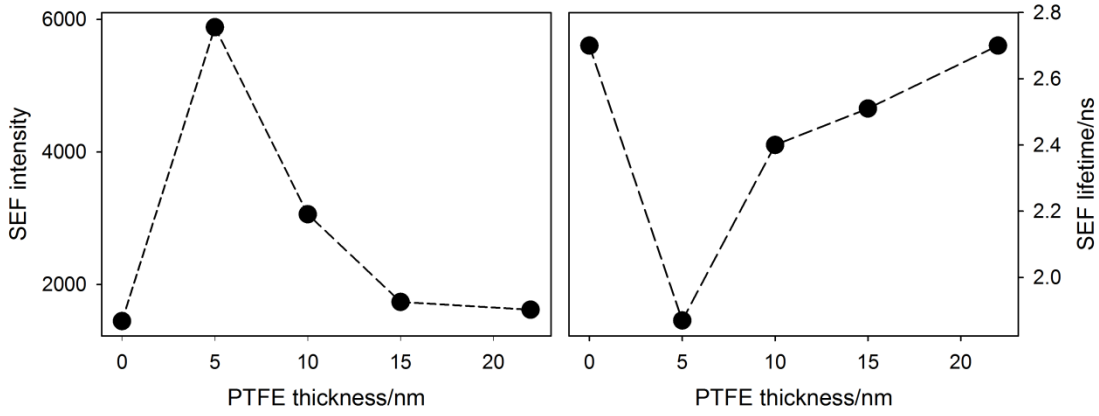


Figure 43. Emission intensity spectra of riboflavin in DMSO dropped on Ag nanoislands covered by a PTFE spacer of various thicknesses (left). Right: Riboflavin lifetimes. Concentration of the riboflavin stock solution was $10^{-5}$ M. Riboflavin lifetime in a $10^{-5}$ M DMSO solution was measured as $\tau_{F,D} = (2.9 \pm 0.1)$ ns.

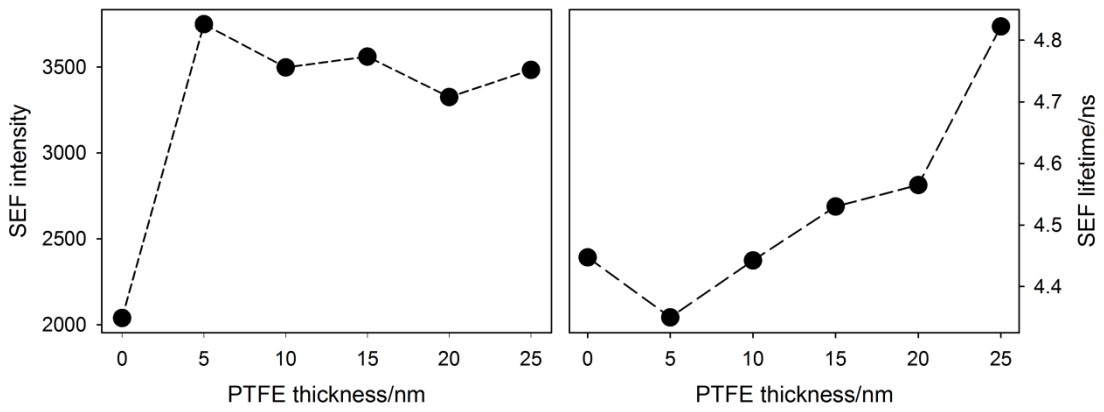


Figure 44. Emission intensity spectra of riboflavin in water dropped on Ag nanoislands covered by a PTFE spacer of various thicknesses (left). Right: Riboflavin lifetimes. Concentration of the riboflavin stock solution was $10^{-5}$ M. Riboflavin lifetime in a $10^{-5}$ M water solution was measured as $\tau_{F,w} = (5.0 \pm 0.1)$ ns.

The riboflavin lifetime in a $10^{-5}$ M water solution was measured as $\tau_{F,w} = (5.0 \pm 0.1)$ ns, which corresponds well with the values in literature [128, 129]. The value of $\tau_r$ reported therein is $\tau_{r,w} = (18 \pm 1)$ ns, which produces the values $\Gamma_w \sim 5.6 \cdot 10^7\ \mathrm{s}^{-1}$, $k_{nr,w} \sim 14 \cdot 10^7\ \mathrm{s}^{-1}$ and $\mathrm{Q}_{0,w} \sim 0.28$ using eqs. 1.19 – 1.24. For $10^{-5}$ M DMSO solution, the corresponding values are $\tau_{F,D} = (2.9 \pm 0.1)$ ns, $\tau_{r,D} = 13.5$ ns, $\Gamma_D \sim 7.4 \cdot 10^7\ \mathrm{s}^{-1}$, $k_{nr,D} \sim 2.7 \cdot 10^8\ \mathrm{s}^{-1}$ and $\mathrm{Q}_{0,D} \sim 0.21$.

Since the quenching effect fades out with approximately $d^3$ dependence [56], $k_m$ may be considered negligible for distances > ~ 4 – 5 nm. Under this approximation, all variables occurring in eqs. 1.36 – 1.40 can be unambiguously computed (table 2). In this instance, the ratio $\frac{\mathrm{Q}}{\mathrm{Q}_0}$ is bigger than 1, which means that fluorescence is enhanced. However, because of the limited range of the electromagnetic effect, the enhancement drops off rapidly with further increasing $d$. On the other hand, the rate of nonradiative decay is greatly enhanced when the fluorophore and the metal surface are closely contacted, which results in fluorescence suppression.

| | Water | | | |
|---|---|---|---|---|
| PTFE thickness/nm | $\tau_{F,m}$ /ns | $\tau_{F,m}/\tau_F$ | $\Gamma_m$ [$10^7$ $s^{-1}$] | $Q/Q_0$ |
| 0 | 4.45 | 0.89 | × | × |
| 5 | 4.35 | 0.87 | 2.99 | 1.34 |
| 10 | 4.44 | 0.89 | 2.51 | 1.29 |
| 15 | 4.53 | 0.91 | 2.08 | 1.24 |
| 20 | 4.57 | 0.91 | 1.91 | 1.23 |
| 25 | 4.82 | 0.96 | 0.74 | 1.09 |

| | DMSO | | | |
|---|---|---|---|---|
| PTFE thickness/nm | $\tau_{F,m}$ /ns | $\tau_{F,m}/\tau_F$ | $\Gamma_m$ [$10^7$ $s^{-1}$] | $Q/Q_0$ |
| 0 | 2.70 | 0.93 | × | × |
| 5 | 1.87 | 0.64 | 18.99 | 2.30 |
| 10 | 2.40 | 0.83 | 4.17 | 1.39 |
| 15 | 2.51 | 0.87 | 3.11 | 1.30 |
| 22 | 2.70 | 0.93 | 1.48 | 1.15 |

Table 2. Lifetime characteristics of riboflavin in respective environments and their implication on quantum yield enhancement ($Q/Q_0$). Lifetimes were experimentally measured, all other characteristics were computed using eqs. 1.36 – 1.40 under the approximation $k_m = 0$.

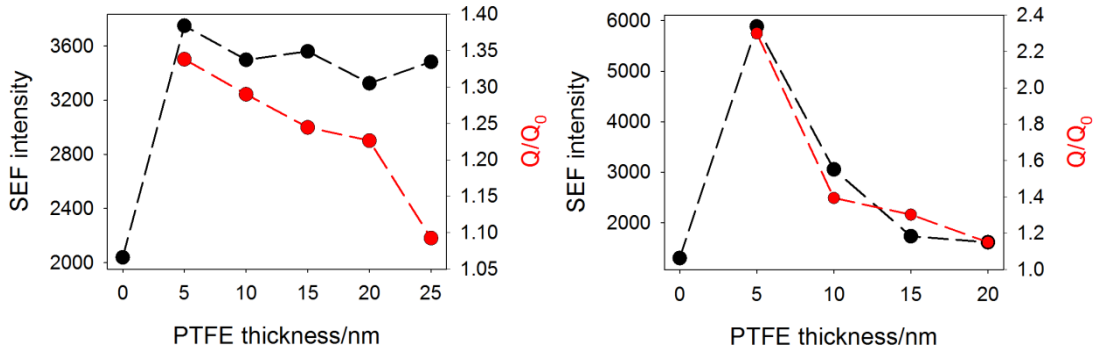


Figure 45. Fluorescence enhancement correlated with quantum yield enhancement as computed using fluorophore lifetime characteristics for both water (left) and DMSO (right).

From Figs. 43 and 44, it is obvious that fluorescence enhancement corresponds well with fluorophore lifetime shortening. Using eqs. 1.36 – 1.40, it is also obvious that in the case of DMSO, the quantum yield enhancement computed using the information regarding lifetime shortening almost perfectly fits the enhanced fluorescence intensity (Fig. 45 right). However, several important issues must be yet addressed before more precise conclusions are made:

It is clear that the enhanced fluorophore characteristics (lifetime and intensity) are much more pronounced in the case of DMSO than in water, although the riboflavin quantum yields in water and DMSO, respectively, differ by less than 20%. We hypothesize that this difference is caused by different efficiency in binding the riboflavin molecules from the "free" solution on the metal interface and also different contact angles of DMSO/water droplet on the interface ($\vartheta \sim 71°$ for DMSO and $\vartheta \sim 105°$ for water, virtually irrespective of the spacer thickness). Even in the case of DMSO, the enhancement is not very high, considering typical SEF enhancement factor in literature up to $\sim 10^3$ [54] [10]. This may be partly due to the fact that total fluorescence intensity obtained during the experiment may be thought of to be comprised of two main contributions: (i) a certain proportion of molecules adsorbed on the interface (either enhanced or quenched), and (ii) molecules in the bulk medium. Using our experimental setup, the theoretical diffraction-limited laser spot size on the sample is

$$d \sim \frac{1.22\lambda}{\mathrm{NA}} \sim 5.5\ \mu\mathrm{m}, \tag{4.7}$$

and the theoretical focal depth is [130, 131]

$$L \sim \frac{4\lambda}{\mathrm{NA}^2} \sim 180\ \mu\mathrm{m}, \tag{4.8}$$

which implies that out-of-focus contributions to the total collected signal can not be neglected. Following efforts have been made with the aim to identify the relative proportion of the two contributions to the total signal:

In order to estimate the surface coverage, we performed a set of experiments consisting of dripping a series of droplets on the substrates used for SEF measurements, consequently removing the liquid phase (part of the molecules not attached to the interface) with a pipette and determining the drop in absorbance with respect to absorbance of the stock solution. In the case of DMSO, absorbance of the free droplet was found to be ~ 50% of absorbance of the stock solution (after several

[10] The question how to actually define the SEF enhancement factor in our case is not trivial (see further text). It is not very intuitive to use the definition as the ratio of the fluorescence signal as measured from the drop on the enhancing substrate and from the drop on a Si wafer as the contact angle measured on Si is completely different (31° for water and 19° for DMSO) from the values obtained on the enhancing substrates. Therefore, the total number of molecules affected when measuring on Si and the enhancing substrate is typically completely different.

repetitive measurements), which suggests that roughly half of the molecules present in the DMSO droplet attach to the surface and half of the molecules remain "free" in the solution. Although this method is not very accurate considering the concentration used ($10^{-5}$ M) and the cuvettes used (optical path = 2 mm), it provides the first wild guess of the number of adsorbed molecules. Using the experimental parameters described above, eq. 4.6 suggests that the surface coverage is $\sigma \sim 2 \times 10^{18}$ $\mathrm{m}^{-2}$, the inverse of which roughly corresponds to an area occupied by one riboflavin molecule. In the case of water, the drop in absorbance was not measurable, which suggests that the binding efficiency of riboflavin molecules to the surface in the case of water is smaller than in the case of DMSO. This is in compliance with the SEF results.

Figs. 46 and 47 show FA results of depth profile measurements, i.e. a series of measurements when position of the laser focus is placed in different $z$ positions (Fig. 41) in DMSO and water, respectively, using substrates with 5 nm PTFE overlay. In both cases, the first subspectrum $S_1$ represents the basic spectral profile with the $V_{i1}$ coefficients representing its statistical weigth, i.e. the average spectral intensity, as a function of $z$. As expected, in the case of DMSO, highest fluorescence intensity is observed when focus is placed exactly on the interface, which clearly corresponds with the enhancement effect. As the centre of the focal volume retracts from the interface, the total fluorescence intensity is decreasing monotonously and exhibits a red-shift, which is obvious from the second subspectrum. It suggests that the spectral fluorescence profile of the molecules bound to the surface is different (blue-shifted) from molecules in the bulk medium. Counterintuitively, in the case of water, the intensity starts to increase when the centre of the focal volume retracts from the interface, confirming that the enhancement effect of riboflavin in water is actually rather small. Subspectra $S_j(\lambda), j \geq 3$ in the case of DMSO, and $S_j(\lambda), j \geq 2$ in the case of water, represent only pure noise.

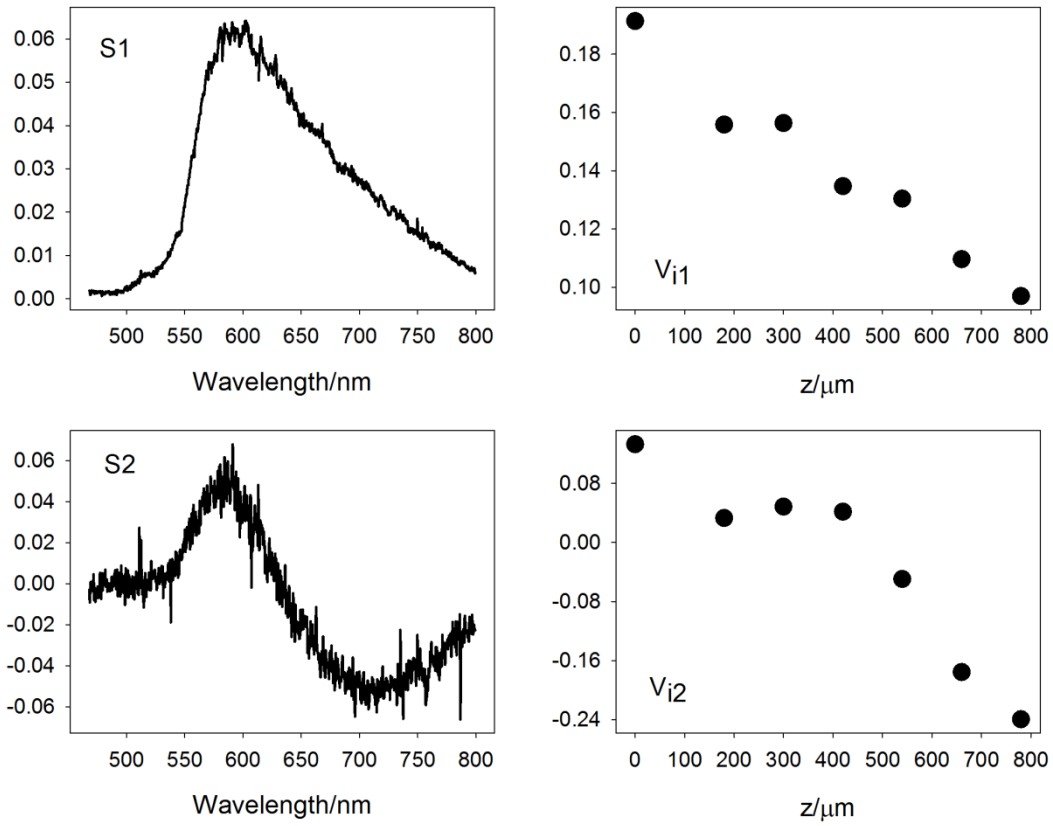


Figure 46. Factor analysis of the depth profile measurements for riboflavin in DMSO. As the centre of the focal volume retracts from the interface, the total fluorescence intensity is decreasing and exhibits a red-shift. Subspectra $S_j(\lambda), j \geq 3$ represent only pure noise. The ratio of singular values $W_1/W_2$ is 18.

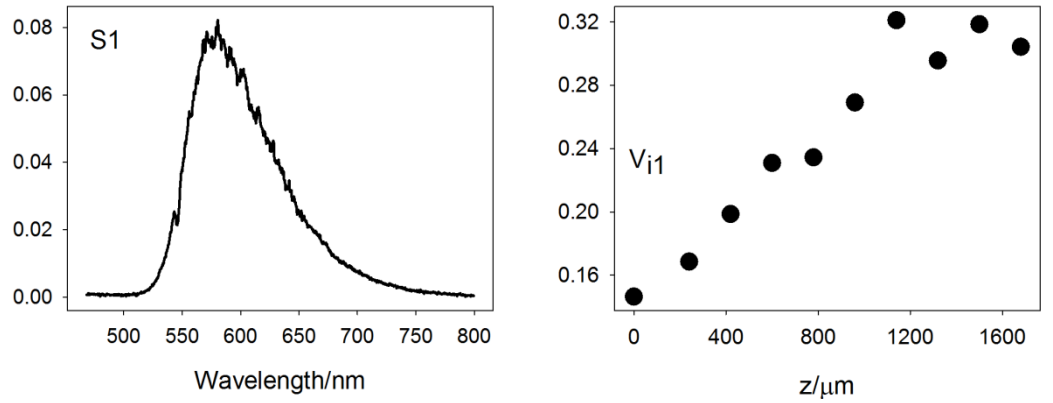


Figure 47. Factor analysis of the depth profile measurements for riboflavin in water. As the centre of the focal volume retracts from the interface, the total fluorescence intensity is increasing. Subspectra $S_j(\lambda), j \geq 2$ represent only pure noise. The ratio of singular values $W_1/W_2$ is 101.

To sum up, when retracting the centre of the focal volume from the interface, the contribution of molecules attached to the interface to the total signal is decreasing, while contribution of the "free" molecules can be increased due to bigger overlap between the laser field distribution and the droplet. Contribution of the thin layer ($z = 0$) is expected to scale as dictated by the Lorentz function [130, 131]

$$\mathcal{L}(z) = \frac{1}{1 + \left(\frac{z}{L}\right)^2}, \tag{4.9}$$

while contribution of the molecules in the bulk medium is given by convolution of eq. 4.9 with a function describing the molecular distribution in the droplet [130]. Assuming uniform distribution of molecules in the bulk medium, the formula for contribution from the "free" molecules when focusing the laser spot at a certain distance above the interface $h$ can be approximated as

$$I_{bulk}(h) \sim \int_0^v \frac{dz}{1 + \left(\frac{z-h}{L}\right)^2} = L\left[\mathrm{arctg}\left(\frac{h}{L}\right) + \mathrm{arctg}\left(\frac{v-h}{L}\right)\right]. \tag{4.10}$$

For evaluation of the contribution of the adsorbed molecules and molecules in the bulk medium to the total fluorescence signal, fluorescence intensity profile in DMSO ($V_{i1}$ coefficients, Fig. 46) was fitted by the sum of contributions 4.9 and 4.10. Outputs of the fit were the relative weights of both contributions and the parameter $L$. During the fitting procedure, $L$ was found to be $L \sim 352$ μm, which is a worse value in comparison to the theoretically predicted one (eq. 4.8), which can be possibly explained by optical imperfections of the experimental system. More importantly, results of the fit suggest that when the focus is placed exactly on the interface, the contribution of the bulk medium is $\sim 28\%$ and contribution of the adsorbed molecules is $\sim 72\%$ (Fig. 48).

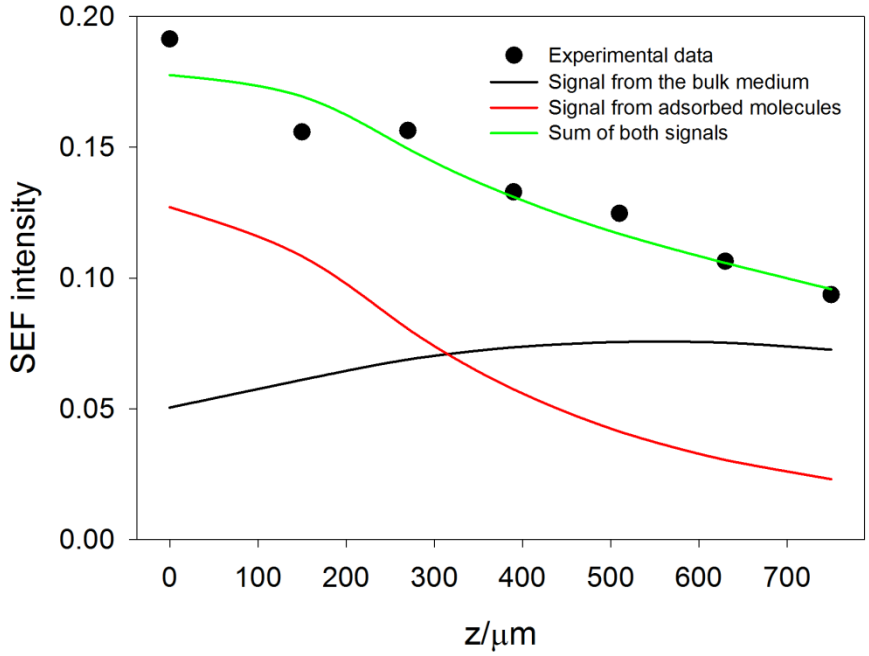


Figure 48. Depth profile of SEF measurements in DMSO (black points) and its fit (green line) by the sum of contribution of the bulk medium (black line) and contribution from the adsorbed molecules (red line). Ratio of both signals for $z = 0$ suggests that the contribution of the adsorbed molecules is $\sim$ 72%.

Certain information regarding the number of adsorbed molecules could also be aided by droplet-size-dependent measurements. Fig. 49 shows SEF intensity profile with different droplet volumes as measured in DMSO (5 nm spacer thickness). Considering the range of droplet volumes used, contact angles for all droplets may be considered identical (in our experiments, contact angles started to decrease with increasing droplet size due to gravity for volumes $\sim$ 5 – 10 μl). The intensity profile was found to be an increasing function of the droplet volume. Our theoretical analysis suggest that this is due to the fact that with increasing droplet volume, higher proportion of the signal comes from the bulk medium. Our model suggests that for sufficiently small droplets, almost all molecules are adsorbed on the interface as the total number of molecules in the droplet is not sufficient to create a monomolecular layer, assuming the surface coverage $\sigma$ (the ratio $N/S$, where $N$ is the number of molecules in the droplet, and $S$ is the droplet area, scales as $\sim V^{1/3}$). When a certain size of the droplet is reached, the number of molecules in the droplet is bigger than required for creation of the monomolecular coverage and contribution

from the molecules in the bulk medium starts to take the leading role. This model is depicted in Fig. 49 [11].

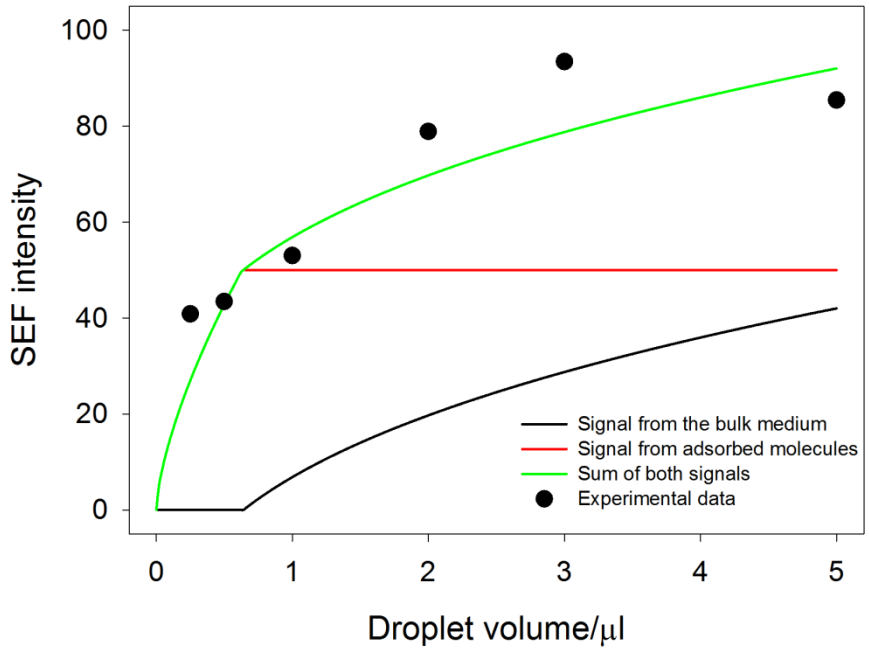


Figure 49. Intensity profile of SEF measurements as measured with different droplet volumes in DMSO (5 nm spacer thickness, black points) and its fit (green line) by the sum of contribution of the bulk medium (black line) and contribution from adsorbed molecules (red line). Ratio of both signals for $V = 5$ μl suggests that the contribution of the adsorbed molecules is $\sim 54\%$.

Although the contribution of the adsorbed molecules deduced from the droplet-size-dependent measurements (54%) does not perfectly correspond to the value obtained from measurements of the depth profile (72%), both these results suggest that due to the contribution from the molecules in the bulk medium, the enhancement factor can be somewhat underestimated (but still probably being lower than $\sim 5 - 10$ in the case of DMSO). For water, no model compatible with the data contained in Fig. 47 was found so far. Also the volume-dependent intensity profile is more difficult to obtain and correctly interpret in this case due to very quick droplet evaporation in the case of very small droplets (< 1 μl). We expect that addressing these issues will constitute a matter of further experiments as well as theoretical calculations.

[11] This model is actually an extreme case of the Langmuir adsorption model (Langmuir isotherm), which predicts the surface coverage $\sigma$ to depend on concentration $c$ as $\sim \frac{Bc}{1+Bc}$, where $B$ is a constant.

As already mentioned, quenching effect should be observed for substrates without the PTFE overlay used. From this point of view, the distance-dependent SEF intensity for both water and DMSO is rather unexpected. For DMSO, both fluorescence characteristics (intensity and lifetime) for sufficiently thick PTFE overlay (22 nm) are almost identical to that for 0 nm PTFE, which suggests that the quenching effect is almost not observed. Vice versa, although the fluorescence intensity of riboflavin in water has a decreasing trend for PTFE thicknesses > 5 nm, the lowest intensity is still well above the intensity measured without the PTFE overlay used where the quenching effect is clearly observed. In other words, the enhancement effect of riboflavin in water is rather poor, but the quenching effect is more dominant in comparison to DMSO. Whether or not this finding has a more general application remains an issue for further research.

It may seem strange that although the total signal obtained with the focus placed on the interface is likely to come from two contributions, all lifetime curves obtained in our experiments were nicely fitted using a single exponential model, whereas attempts to apply double exponential models resulted in degradation of the final fit. We hypothesize that this could be caused by low sensitivity of the measured technique to a possible presence of extremely low lifetime components (according to literature, typical lifetimes of molecules attached on an interface can be as low as ~ 0.2 ns [55]). Thus, also the shortened lifetimes presented in Figs. 43, 44 and Table 2 (and corresponding quantities calculated using the information on lifetime shortening) should be interpreted as averaged quantities over an ensemble of both bound and "free" molecules within the focal volume. Since our frequency-domain technique may not provide sufficient sensitivity in this case, we suggest that using pulse methods of lifetime determination could enable gain better insight into the possible existence of extremely small lifetime components and consequently on the proportion of the two contributions [7].

Preliminary SEF measurements were also performed with the aim of determining the dependence of SEF intensity on the deposition time of Ag nanoislands (and consequently spectral position of the LSPR peak) using both "normal" nanoislands as well as gradient nanostructures, similarly to the case of SERS (not shown here). These measurement could reveal whether the extinction peak of the nanostructures favours being overlapped by the absorption or emission

band of the fluorophore for maximum signal enhancement and to possibly identify the contribution of absorption enhancement and quantum yield enhancement, which is an issue not yet fully understood in literature. Unfortunately, due to bad batch-to-batch reproducibility of obtained data (along with rather poor enhancement factor), this effect could not have been systematically explored. Thus, more detailed investigation of the SEF enhancement factor with respect to mutual position of the absorption and emission band of the fluorophore and extinction peak of the nanostructures remains a challenge for future research.

# Conclusions

In this thesis, main focus was placed on testing regular metal plasmonic nanostructures for enhanced optical processes, mainly surface-enhanced Raman scattering (SERS) and surface-enhanced fluorescence (SEF). Two main groups of metal nanostructures, fabricated at the Department of Macromolecular Physics, were used: Silver nanorods and metal nanoislands growing on magnetron-sputtered polytetrafluoroethylene film.

Step-by-step optimization process was performed on the silver nanoislands, resulting in the SERS enhancement factor about 2 orders of magnitude larger than commonly reported in literature for comparable SERS-active system. Detailed SERS intensity profiles were also measured using gradient silver nanoislands, i.e. structures where the localized surface plasmon resonance (LSPR) varies across the sample length. Two different mask speeds and three different excitation wavelengths were tested using riboflavin as the model biomolecule. Results were interpreted in terms of a superposition of the electromagnetic enhancement mechanism (i.e. the degree of spectral overlap between the excitation wavelength and the LSPR band along with the scattering cross section of the nanostructures) and position of molecular resonance with respect to the excitation wavelength. We also developed an approach consisting of fabrication of mixed gold/silver nanoislands, which enabled to vary spectral position of the LSPR band and LSPR intensity simultaneously, which is not attainable for single silver coatings. This method provided the enhancement $\sim 4\times$ bigger in comparison to single silver coatings.

Silver nanorods prepared by means of oblique angle vapor deposition (OAD) were used mainly for the study of polarization- and angular- dependences of the SERS signal. SERS experiments were supported by ellipsometry measurements, which showed very good correspondence with the SERS enhancement. Both the SERS intensities as well as the ellipsometric parameters were found to exhibit strong dependence on rotating the sample by 90°, although they were fairly insensitive to flipping the sample by 180°. A theoretical model based on optical (pseudo)parameters was applied on the data, enabling quantitative analysis of MB Raman tensor elements. These results indicated that the MB molecules adsorb predominantly with the symmetry axis perpendicular to the surface.

Finally, silver nanoislands supported by magnetron-sputtered PTFE film, were used for the study of surface-enhanced fluorescence. We systematically measured riboflavin SEF intensity in dependence on the thickness of the PTFE spacer using different solutions (water and DMSO). Stationary fluorescence spectra were supported by time-resolved measurements in frequency domain, which revealed very good correlation between fluorescence enhancement and lifetime shortening.

To sum up, results of this dissertation thesis contribute to better theoretical understanding of the enhancement mechanism, polarization characteristics of anisotropic plasmonic nanostructures and point out the need for careful optimization of plasmon-based sensors for maximum signal enhancement. It was shown that due to sufficient sensitivity and excellent spectral reproducibility, the plasmonic substrates used are very promising candidates for biomolecular quantitative (sensing) applications. Last but not least, experience gathered during the experimental part open the way for investigation of other plasmon-enhanced phenomena for future research.

# Bibliography


[1] Stratton, J. A. (1941). *Electromagnetic Theory*. McGraw-Hill Book Company, New York and London. ISBN 978-1443730549.

[2] Aroca, R. (2006). *Surface-enhanced Vibrational Spectroscopy*. John Wiley & Sons Ltd, Chichester. ISBN 978-0-471-60731-1.

[3] Le Ru, E. C., Etchegoin, P. G. (2009). *Principles of Surface Enhanced Raman Spectroscopy and related plasmonic effects*. Elsevier, Amsterdam. ISBN 978-0-444-52779-0.

[4] Demtröder, W. (2010). *Atoms, Molecules and Photons: An Introduction to Atomic-, Molecular- and Quantum-Physics*. Second edition. Springer, Heidelberg. ISBN 978-3-642-10297-4.

[5] Šubr, M., Procházka, M. (2018). Polarization- and Angular-Resolved Optical Response of Molecules on Anisotropic Plasmonic Nanostructures. *Nanomaterials*, **8**, 418.

[6] Ferraro J. R., Nakamoto K., Brown C. W. (2003). *Introductory Raman Spectroscopy*. Second edition. Elsevier. ISBN 978-0-12-254105-6.

[7] Lakowicz, J. R. (2006). *Principles of Fluorescence Spectroscopy*. Third edition. Springer, Singapore. ISBN 0-387-31278-1.

[8] Long, D. A. (2002). *The Raman Effect. A Unified Treatment of the Theory of Raman Scattering by Molecules.* John Wiley & Sons Ltd, Chichester. ISBN 0-471-49028-8.

[9] Smith, E., Dent, G. (2005). *Modern Raman Spectroscopy – A Practical Approach*. John Wiley & Sons Ltd, Chichester. ISBN 0-471-49794-0.

[10] Cotton, F. A. (1990). *Chemical Applications of Group Theory*. Third edition. John Wiley & Sons, Chichester. ISBN 0-471-51094-7.

[11] Fleischmann, M., Hendra, P. J., McQuillan, A. J. (1974). Raman-Spectra of Pyridine Adsorbed at a Silver Electrode. *Chemical Physics Letters*, **26**, 163-166.

[12] Jeanmaire, D. L., Van Duyne, R. P. (1977). Surface Raman Spectroelectrochemistry .1. Heterocyclic, Aromatic, and Aliphatic-Amines Adsorbed on Anodized Silver Electrode. *Journal of Electroanalytical Chemistry*, **84**, 1-20.

[13] Moskovits, M. (1985). Surface-Enhanced Spectroscopy. *Reviews of Modern Physics*, **57**, 783-826.

[14] Moskovits, M. (2005). Surface-enhanced Raman spectroscopy: A brief retrospective. *Journal of Raman Spectroscopy*, **36**, 485-496.

[15] Barber, P. W., Chang, R. K., Massoudi, H. (1983). Surface-Enhanced Electric Intensities on Large Silver Spheroids. *Physical Review Letters*, **50**, 997-1000.

[16] Kelly, K. L., Coronado, E., Zhao, L. L., Schatz, G. C. (2003). The Optical Properties of Metal Nanoparticles: The Influence of Size, Shape, and Dielectric Environment. *Journal of Physical Chemistry B*, **107**, 668-677.

[17] Gucciardi, P. G., de la Chapelle, M. L., Lidgi-Guigui, N. (2016). *Handbook of Enhanced Spectroscopy*. Pan Stanford Publishing Pte. Ltd, Singapore. ISBN 978-981-4613-32-3.

[18] Laurent, G., Félidj, N., Aubard, J., Lévi, G., Krenn, J. R., Hohenau, A., Schider, G., Leitner, A., Aussenegg, F. R. (2005). Evidence of multipolar excitations in surface enhanced Raman scattering. *Physical Review B*, **71**, 045430.

[19] Brolo, A. G., Irish, D. E., Smith, B. D. (1997). Applications of surface enhanced Raman scattering to the study of metal-adsorbate interactions. *Journal of Molecular Structure* **405**, 29-44.

[20] Lin, W.-C., Liao, L.-S., Chen, Y.-H., Chang, H.-C., Tsai, D.-P., Chiang, H.-P. (2011). Size Dependence of Nanoparticle-SERS Enhancement from Silver Film over Nanosphere (AgFON) Substrate. *Plasmonics*, **6**, 201-206.

[21] Stranik, O., Nooney, R., McDonagh, C., MacCraith, D. (2007). Optimization of Nanoparticle Size for Plasmonic Enhancement of Fluorescence. *Plasmonics*, **2**, 15-22.

[22] Njoki, P. N., Lim, I-I. S., Mott, D., Park, H.-Y., Khan, B., Mishra, S., Sujakumar, R., Luo, J., Zhong, C.-J. (2007). Size Correlation of Optical and Spectroscopic Properties for Gold Nanoparticles. *Journal of Physical Chemistry C*, **111**, 14664-14669.

[23] Evanoff, D. D., Chumanov, G. (2004). Size-Controlled Synthesis of Nanoparticles. 2. Measurement of Extinction, Scattering, and Absorption Cross Sections. *Journal of Physical Chemistry B*, **108**, 13957-13962.

[24] Le Ru, E. C., Blackie, E., Meyer, M., Etchegoin, P. G. (2007). Surface Enhanced Raman Scattering Enhancement Factors: A Comprehensive Study. *Journal of Physical Chemistry C*, **111**, 13794-13803.

[25] Etchegoin, P. G., Le Ru, E. C., Meyer, M. (2006). An analytic model for the optical properties of gold. *Journal of Chemical Physics*, **125**, 164705.

[26] Šubr, M. (2014). Diploma thesis: SERS Spectroscopy of Model Biomolecules for SERS Biosensing. MFF UK, Prague.

[27] Johnson, P. B., Christy, R. W. (1972). Optical Constants of Noble Metals. *Physical Review B*, **6**, 4370-4379.

[28] Aravind, P. K., Nitzan, A., Metiu, H. (1981). The Interaction between Electromagnetic Resonances and its Role in Spectroscopic Studies of Molecules Adsorbed on Colloidal Particles or Metal Spheres. *Surface Science*, **110**, 189-204.

[29] Aravind, P. K., Metiu, H. (1983). The Effects of the Interaction between Resonances in the Electromagnetic Response of a Sphere-Plane Structure; Applications to Surface Enhanced Spectroscopy. *Surface Science*, **124**, 506-528.

[30] Xu, H., Bjerneld, E. J., Käll, M., Börjesson, L. (1999). Spectroscopy of Single Hemoglobin Molecules by Surface Enhanced Raman Scattering. *Physical Review Letters*, **83**, 4357-4360.

[31] Xu, H., Aizpurua, J., Käll, M., Apell, P. (2000). Electromagnetic contributions to single-molecule sensitivity in surface-enhanced Raman scattering. *Physical Review E*, **62**, 4318-4324.

[32] Xu, H., Käll, M. (2003). Polarization-Dependent Surface-Enhanced Raman Spectroscopy of Isolated Silver Nanoaggregates. *ChemPhysChem*, **4**, 1001-1005.

[33] Kneipp, K., Wang, Y., Kneipp, H., Perelman, L. T., Itzkan, I., Dasari, R., Feld, M. S. (1997). Single Molecule Detection Using Surface-Enhanced Raman Scattering (SERS). *Physical Review Letters*, **78**, 1667-1670.

[34] Nie, S., Emory, S. R. (1997). Probing Single Molecules and Single Nanoparticles by Surface-Enhanced Raman Scattering. *Science*, **275**, 1102-1106.

[35] Moskovits, M. (2013). Persistent misconceptions regarding SERS. *Physical Chemistry Chemical Physics*, **15**, 5301-5311.

[36] Camden, J. P., Dieringer, J. A., Wang, Y., Masiello, D. J., Marks, L. D., Schatz, G. C., Van Duyne, R. P. (2008). Probing the Structure of Single-Molecule Surface-Enhanced Raman Scattering Hot Spots. *Journal of the American Chemical Society*, **130**, 12616-12617.

[37] Wustholz, K. L., Henry, A.-I., McMahon, J. M., Freeman, R. G., Valley, N., Piotti, M. E., Natan, M. J., Schatz, G. C., Van Duyne, R. P. (2010). Structure-Activity Relationships in Gold Nanoparticle Dimers and Trimers for Surface-

Enhanced Raman Spectroscopy. *Journal of the American Chemical Society*, **132**, 10903-10910.

[38] Šubr, M., Petr, M., Peksa, V., Kylián, O., Hanuš, J., Procházka, M. (2015). Ag Nanorod Arrays for SERS: Aspects of Spectral Reproducibility, Surface Contamination, and Spectral Sensitivity. *Journal of Nanomaterials*, **2015**, 729231.

[39] Šubr, M., Kuzminova, A., Kylián, O., Procházka, M. (2018). Surface-enhanced Raman scattering (SERS) of riboflavin on nanostructured Ag surfaces: The role of excitation wavelength, plasmon resonance and molecular resonance. *Spectrochimica Acta Part A: Molecular and Biomolecular Spectroscopy,* **197**, 202-207.

[40] McFarland, A. D., Young, M. A., Dieringer, J. A., Van Duyne, R. P. (2005). Wavelength-Scanned Surface-Enhanced Raman Excitation Spectroscopy. *Journal of Physical Chemistry B,* **109**,11279-11285.

[41] Šubr, M., Petr, M., Kylián, O., Štěpánek, J., Veis, M., Procházka, M. (2017). Anisotropic Optical Response of Silver Nanorod Arrays: Surface Enhanced Raman Scattering Polarization and Angular Dependences Confronted with Ellipsometric Parameters. *Scientific Reports*, **7**, 4293.

[42] Le Ru, E. C., Galloway, C., Etchegoin, P. G. (2006). On the connection between optical absorption/extinction and SERS enhancements. *Physical Chemistry Chemical Physics,* **8**, 3083-3087.

[43] Zuloaga, J., Nordlander, P. (2011). On the Energy Shift between Near-Field and Far-Field Peak Intensities in Localized Plasmon Systems. *Nano Letters*, **11**, 1280-1283.

[44] Zhao, Y.-P., Chaney, S. B., Shanmukh, S., Dluhy, R. A. (2006). Polarized Surface Enhanced Raman and Absorbance Spectra of Aligned Silver Nanorod Arrays. *Journal of Physical Chemistry B,* **110**, 3153-3157.

[45] Kleinman, S. L., Sharma, B., Blaber, M. G., Henry, A.-I., Valley, N., Freeman, R. G., Natan, M. J., Schatz, G. C., Van Duyne, R. P. (2013). Structure Enhancement Factor Relationships in Single Gold Nanoantennas by Surface-Enhanced Raman Excitation Spectroscopy. *Journal of the American Chemical Society*, **135**, 301-308.

[46] Kambhampati, P., Child, C. M., Foster, M. C., Campion, A. (1998). On the chemical mechanism of surface enhanced Raman scattering: Experiment and theory. *Journal of Chemical Physics*, **108**, 5013-5026.

[47] Otto, A. (2005). The 'chemical' (electronic) contribution to surface-enhanced Raman scattering. *Journal of Raman Spectroscopy*, **36**, 497-509.

[48] Lombardi, J. R., Birke, R. L. (2008). A Unified Approach to Surface-Enhanced Raman Spectroscopy. *Journal of Physical Chemistry C*, **112**, 5605-5617.

[49] Campion, A., Kambhampati, P. (1998). Surface-enhanced Raman scattering. *Chemical Society Reviews*, **27**, 241-250.

[50] Aroca, R. F. (2013). Plasmon enhanced spectroscopy. *Physical Chemistry Chemical Physics*, **15**, 5355-5363.

[51] Weitz, D. A., Garoff, S., Gersten, J. I., Nitzan, A. (1983). The enhancement of Raman scattering, resonance Raman scattering, and fluorescence from molecules adsorbed on a rough silver surface. *Journal of Chemical Physics*, **78**, 5324-5338.

[52] Wokaun, A., Lutz, H.-P., King, A.-P., Wild, U.-P., Ernst, R. R. (1983). Energy transfer in surface enhanced luminescence. *Journal of Chemical Physics*, **79**, 509-514.

[53] Lakowicz, J.R. (2001). Radiative Decay Engineering: Biophysical and Biomedical Applications. *Analytical Biochemistry*, **298**, 1-24.

[54] Sun, G., Khurgin, J. B. (2012). Origin of giant difference between fluorescence, resonance, and nonresonance Raman scattering enhancement by surface plasmons. *Physical Review A*, **85**, 063410.

[55] Li, J.-F., Li, C.-Y., Aroca, R. F. (2017). Plasmon-enhanced fluorescence spectroscopy. *Chemical Society Reviews*, **46**, 3962-3979.

[56] Waldeck, D. H., Alivisatos, A. P., Harris, C. B. (1985). Nonradiative damping of molecular electronic excited states by metal surfaces. *Surface Science*, **158**, 103-125.

[57] Mishra, H., Mali, B. L., Karolin, J., Dragan, A. I., Geddes, C. D. (2013). Experimental and theoretical study of the distance dependence of metal-enhanced fluorescence, phosphorescence and delayed fluorescence in a single system. *Physical Chemistry Chemical Physics*, **15**, 19538-19544.

[58] Asselin, J., Legros, P., Grégorie, A., Boudreau, D. (2016). Correlating Metal-Enhanced Fluorescence and Structural Properties in Ag@$SiO_2$ Core-Shell Nanoparticles. *Plasmonics*, **11**, 1369-1376.

[59] Ferreira, M., Constantino, C. J. L., Olivati, C. A., Vega, M. L., Balogh, D. T., Aroca, R. F., Faria, R. M., Oliveira, O. N. Jr. (2003). Langmuir and Langmuir-Blodgett Films of Poly[2-methoxy-5-(*n*-hexyloxy)-*p*-phenylenevinylene]. *Langmuir*, **19**, 8835-8842.

[60] Constantino, C. J. L., Aroca, R. F., Mendonca, C. R., Mello, S. V., Balogh, D. T., Oliveira, O. N. (2001). Surface enhanced fluorescence and Raman imaging of Langmuir-Blodgett azopolymer films. *Spectrochimica Acta Part A: Molecular and Biomolecular Spectroscopy*, **57**, 281-289.

[61] Tam, F., Goodrich, G. P., Johnson, B. R., Halas, N. J. (2007). Plasmonic Enhancement of Molecular Fluorescence. *Nano Letters*, **7**, 496-501.

[62] Bardhan, R., Grady, N. K., Cole, J. R., Joshi, A., Halas, N. J. (2009). Fluorescence Enhancement by Au Nanostructures: Nanoshells and Nanorods. *ACS Nano*, **3**, 744-752.

[63] Chen, Y., Munechika, K., Ginger, D. S. (2007). Dependence of Fluorescence Intensity on the Spectral Overlap between Fluorophores and Plasmon Resonant Single Silver Nanoparticles. *Nano Letters*, **7**, 690-696.

[64] Dragan, A. I., Bishop, E. S., Casas-Finet, J. R., Strouse, R. J., McGivney J., Schenerman, M. A., Geddes, C. D. (2012). Distance Dependence of Metal-Enhanced Fluorescence. *Plasmonics*, **7**, 739-744.

[65] Zhang, J., Fu, Y., Chowdhury, M. H., Lakowicz, J. R. (2007). Metal-Enhanced Single-Molecule Fluorescence on Silver Particle Monomer and Dimer: Coupling Effect between Metal Particles. *Nano Letters*, **7**, 2101-2107.

[66] Sun, G., Khurgin, J. B., Bratkovsky, A. (2011). Coupled-mode theory of field enhancement in complex metal nanostructures. *Physical Review B*, **84**, 045415.

[67] Mueller, N. S., Heeg, S., Reich, S. (2016). Surface-enhanced Raman scattering as a higher-order Raman process. *Physical Review A*, **94**, 023813.

[68] Natan, M. J. (2006). Concluding Remarks – Surface enhanced Raman scattering. *Faraday Discussions*, **132**, 321-328.

[69] Thomsen, V., Schatzlein, D., Mercuro, D. (2003). Limits of Detection in Spectroscopy. *Spectroscopy*, **18**, 112-114.

[70] Peksa, V., Lebrušková, P., Šípová, H., Štěpánek, J., Bok, J., Homola, J., Procházka, M. (2016). Testing gold nanostructures fabricated by hole-mask colloidal lithography as potential substrates for SERS sensors: sensitivity, signal variability, and the aspect of adsorbate deposition. *Physical Chemistry Chemical Physics*, **18**, 19613-19620.

[71] Kopecký, V. Jr., Baumruk, V. (2006). Structure of the ring in drop coating deposited proteins and its implication for Raman spectroscopy of biomolecules. *Vibrational Spectroscopy*, **42**, 184-187.

[72] Yaffe, N. R., Blanch, E. W. (2008). Effects and anomalies that can occur in SERS spectra of biological molecules when using a wide range of aggregating agents for hydroxylamine-reduced and citrate-reduced silver colloids. *Vibrational Spectroscopy*, **48**, 196-201.

[73] Sánchez-Cortés, S., García-Ramos, J. V. (1998). Anomalous Raman bands appearing in surface-enhanced Raman Spectra. *Journal of Raman Spectroscopy*, **29**, 365-371.

[74] Lin, X.-M., Cui, Y., Xu, Y.-H., Ren, B., Tian, Z.-Q. (2009). Surface-enhanced Raman spectroscopy: substrate-related issues. *Analytical and Bioanalytical Chemistry*, **7**, 1729-1745.

[75] Negri, P., Marotta, N. E., Bottomley, L. A., Dluhy, R. A. (2011). Removal of Surface Contamination and Self-Assembled Monolayers (SAMs) from Silver (Ag) Nanorod Substrates by Plasma Cleaning with Argon. *Applied Spectroscopy*, **65**, 66-74.

[76] Nuntawong, N., Eiamchai, P., Wong-ek, B., Horprathum, M., Limwichean, K., Patthanasettakul, V., Chindaudom, P. (2013). Shelf time effect on SERS effectiveness of silver nanorod prepared by OAD technique. *Vacuum*, **88**, 23-27.

[77] Bachenheimer, L., Scherzer, R., Elliott, P., Stagon, S., Gasparov, L., Huang, H. (2017). Degradation Mechanism of Ag Nanorods for Surface Enhanced Raman Spectroscopy. *Scientific Reports*, **7**, 16282.

[78] Norrod, K. L., Rowlen, K. L. (1998). Removal of Carbonaceous Contamination from SERS-Active Silver by Self-Assembly of Decanethiol. *Analytical Chemistry*, **70**, 4218-4221.

[79] Creighton, J. A., Blatchford, C. G., Albrecht, M. G. (1979). Plasma resonance enhancement of Raman scattering by pyridine adsorbed on silver or gold sol particles of size comparable to the excitation wavelength. *Journal of the Chemical Society-Faraday Transactions II*, **75**, 790-798.

[80] Lee, P. C., Meisel, D. (1982). Adsorption and Surface-Enhanced Raman of Dyes on Silver and Gold Sols. *Journal of Physical Chemistry*, **86**, 3391-3395.

[81] Leopold, N., Lendl, B. (2003). A New Method for Fast Preparation of Highly Surface-Enhanced Raman Scattering (SERS) Active Silver Colloids at Room Temperature by Reduction of Silver Nitrate with Hydroxylamine Hydrochloride. *Journal of Physical Chemistry B*, **107**, 5723-5727.

[82] Chaney, S. B., Shanmuhk, S., Dluhy, R. A., Zhao, Y.-P. (2005). Aligned silver nanorod arrays produce high sensitivity surface-enhanced Raman spectroscopy substrates. *Applied Physics Letters*, **87**, 031908.

[83] Robbie, K., Brett, M. J. (1997). Sculptured thin films and glancing angle deposition: Growth mechanics and applications. *Journal of Vacuum Science & Technology A-Vacuum Surfaces and Films*, **15**, 1460-1465.

[84] Robbie, K., Sit, J. C., Brett, M. J. (1998). Advanced techniques for glancing angle deposition. *Journal of Vacuum Science & Technology B*, **16**, 1115-1122.

[85] Song, C., Abell, J. L., He, Y., Murph, S. H., Cui, Y., Zhao, Y. (2012). Gold-modified silver nanorod arrays: growth dynamics and improved SERS properties. *Journal of Materials Chemistry*, **22**, 1150-1159.

[86] Fu, J., Zhao, Y. (2010). Au nanoparticle based localized surface plasmon resonance substrates fabricated by dynamic shadowing growth. *Nanotechnology*, **21**, 175303.

[87] Tait, R. N., Smy, T., Brett, M. J. (1993). Modelling and characterization of columnar growth in evaporated films. *Thin Solid Films*, **226**, 196-201.

[88] Choukourov, A., Solar, P., Polonskyi, O., Hanus, J., Drabik, M., Kylian, O., Pavlova, E., Slavinska, D., Biederman, H. (2010). Structured Ti/Hydrocarbon Plasma Polymer Nanocomposites Produced By Magnetron Sputtering with Glancing Angle Deposition. *Plasma Processes and Polymers*, **7**, 25-32.

[89] Solař, P., Kylián, O., Petr, M., Hanuš, J., Choukourov, A., Slavínská, D., Biederman, H. (2015). Glancing Angle Deposition of Silver Promoted by Pre-Deposited Nanoparticles. *Plasma Processes and Polymers*, **12**, 486-492.

[90] Fu, J., Cao, Z., Yobas, L. (2011). Localized oblique-angle deposition: Ag nanorods on microstructured surfaces and their SERS characteristics. *Nanotechnology*, **22**, 505302.

[91] Negri, P., Dluhy, R. A. (2013). Ag nanorod based surface-enhanced Raman spectroscopy applied to bioanalytical sensing. *Journal of Biophotonics*, **6**, 20-35.

[92] Zhou, Q., Li, Z., Yang, Y., Zhang, Z. (2008). Arrays of aligned, single crystalline silver nanorods for trace amount detection. *Journal of Physics D-Applied Physics*, **41**, 152007.

[93] Liu, Y., Fan, J., Zhao, Y.-P., Shanmukh, S., Dluhy, R.-A. (2006). Angle dependent surface enhanced Raman scattering obtained from a Ag nanorod array substrate. *Applied Physics Letters*, **89**, 173134.

[94] Schlegel, V. L., Cotton, T. M. (1991). Silver-island films as substrates for enhanced Raman scattering: effect of deposition rate on intensity. *Analytical Chemistry*, **63**, 241-247.

[95] Šubr, M., Petr, M., Kylián, O., Kratochvíl, J., Procházka, M. (2015). Large-scale Ag nanoislands stabilized by a magnetron-sputtered polytetrafluoroethylene film as substrates for highly sensitive and reproducible surface-enhanced Raman scattering (SERS). *Journal of Materials Chemistry C*, **3**, 11478-11485.

[96] Haynes, C. L., McFarland, A. D., Van Duyne, R. P. (2005). Surface-Enhanced Raman Spectroscopy. *Analytical Chemistry*, **77**, 338A-346A.

[97] Procházka, M. (2016). *Surface-Enhanced Raman Spectroscopy. Bioanalytical, Biomolecular and Medical Applications*. Springer, Cham, Switzerland. ISBN 978-3-319-23990-3.

[98] Jahn, M., Patze, S., Hidi, I. J., Knipper, R., Radu, A. I., Mühlig, A., Yüksel, S., Peksa, V., Weber, K., Mayerhöfer, T., Cialla-May, D., Popp, J. (2016). Plasmonic nanostructures for surface enhanced spectroscopic methods. *Analyst*, **141**, 756-793.

[99] Jensen, T. R., Malinsky, M. D., Haynes, C. L., Van Duyne, R. P. (2000). Nanosphere Lithography: Tunable Localized Surface Plasmon Resonance Spectra of Silver Nanoparticles. *Journal of Physical Chemistry B*, **104**, 10549-10556.

[100] Štolcová, L., Peksa, V., Proška, J., Procházka, M. (2018). Gold film over very small (107 nm) spheres as efficient substrate for sensitive and reproducible surface-enhanced Raman scattering (SERS) detection of biologically important molecules. *Journal of Raman Spectroscopy*, **49**, 499-505.

[101] Hulteen, J. C., Van Duyne, R. P. (1995). Nanosphere lithography: A materials general fabrication process for periodic particle array surfaces. *Journal of Vacuum Science & Technology A-Vacuum Surfaces and Films*, **13**, 1553-1558.

[102] Fredriksson, H., Alaverdyan, Y., Dmitriev, A., Langhammer, C., Sutherland, D. S., Zäch, M., Kasemo, B. (2007). Hole-Mask Colloidal Lithography. *Advanced Materials*, **19**, 4297-4302.

[103] Malinowski, E. R. (2002). *Factor Analysis in Chemistry*. Third edition. John Wiley & Sons, New York. ISBN 0-471-13479-1.

[104] Procházka, M., Šimáková, P., Hajduková-Šmídová, N. (2012). SE(R)RS microspectroscopy of porphyrins on immobilized Au nanoparticles: Testing

spectral sensitivity and reproducibility. *Colloids and Surfaces A: Physicochemical and Engineering Aspects*, **402**, 24-28.

[105] Kočišová, E., Praus, P., Bok, J., Bonneau, S., Sureau, F. (2015). Intracellular Monitoring of AS1411 Aptamer by Time-Resolved Microspectrofluorimetry and Fluorescence Imaging. *Journal of Fluorescence*, **25**, 1245-1250.

[106] Woolam, J. A. (2014). *CompleteEase Software Manual*. J. A. Woolam Co., Inc., Lincoln.

[107] Jellison, G. E. (1998). Spectroscopic ellipsometry data analysis: measured versus calculated quantities. *Thin Solid Films*, **313**, 33-39.

[108] Ossikovski, R., Anastasiadou, M., Ben Hatit, S., Garcia-Caurel, E., De Martino, A. (2008). Depolarizing Mueller matrices: how to decompose them? *Physica Status Solidi A-Applications and Materials Science*, **205**, 720-727.

[109] Cheng, H.-W., Huan, S.-Y., Yu, R.-Q. (2012). Nanoparticle-based substrates for surface-enhanced Raman scattering detection of bacterial spores. *Analyst*, **137**, 3601-3608.

[110] Kadish, K., Smith, K. M., Guilard, R. (2010). *Handbook of porphyrin science: with applications to chemistry, physics, materials science, engineering, biology and medicine*. World Scientific Publishing, Singapore.

[111] Roy, S. D., Ghosh, M., Chowdhury, J. (2015). Adsorptive parameters and influence of hot geometries on the SER(R)S spectra of methylene blue molecules adsorbed on gold nanocolloidal particles. *Journal of Raman Spectroscopy*, **46**, 451-461.

[112] Le Ru, E. C., Meyer, S. A., Artur, C., Etchegoin, P. G., Grand, J., Lang, P., Maurel, F. (2011). Experimental demonstration of surface selection rules for SERS on flat metallic surfaces. *Chemical Communications*, **47**, 3903-3905.

[113] Moskovits, M. (1982). Surface selection rules. Journal of Chemical Physics, **77**, 4408-4416.

[114] Zhao, Y.-P., Chaney, S. B., Zhang, Z.-Y. (2006). Absorbance spectra of aligned Ag nanorod arrays prepared by oblique angle deposition. *Journal of Applied Physics*, **100**, 063527.

[115] Zhong, L., Hu, Y.-J., Xing, D., Gu, H.-M. (2010). Adsorption of Methylene Blue on Colloidal Silver-A Surface-Enhanced Raman Spectroscopy Study Combined with Density Functional Theory Calculations. *Spectroscopy and Spectral Analysis*, **30**, 90-94.

[116] Nuntawong, N., Horprathum, M., Eiamchai, P., Wong-ek, K., Patthanasettakul, V., Chindaudom, P. (2010). Surface-enhanced Raman

scattering substrate of silver nanoparticles depositing on AOO template fabricated by magnetron sputtering. *Vacuum*, **84**, 1415-1418.

[117] Nagai, Y., Yamaguchi, T., Kajikawa, K. (2012). Angular-Resolved Polarized Surface Enhanced Raman Spectroscopy. *Journal of Physical Chemistry C*, **116**, 9716-9723.

[118] Shoute, L. C. T., Bergren, A. J., Mahmoud, A. M., Harris, K. D., McCreery, R. L. (2009). Optical Interference Effects in the Design of Substrates for Surface-Enhanced Raman Spectroscopy. *Applied Spectroscopy*, **63**, 133-140.

[119] Hanuš, J., Libenská, H., Khalakhan, I., Kuzminova, A., Kylián, O., Biederman, H. (2017). Localized surface plasmon resonance tuning via nanostructured gradient Ag surfaces. *Materials Letters*, **192**, 119-122.

[120] Kokaislová, A., Matějka, P. (2012). Surface-enhanced vibrational spectroscopy of B vitamins: what is the effect of SERS-active metals used? *Analytical and Bioanalytical Chemistry*, **403**, 985-993.

[121] Liu, F., Gu, H., Lin, Y., Qi, Y., Dong, X., Gao, J., Cai, T. (2012). Surface-enhanced Raman scattering study of riboflavin on borohydride-reduced silver colloids: Dependence of concentration, halide anions and pH values. *Spectrochimica Acta Part A: Molecular and Biomolecular Spectroscopy*, **85**, 111-119.

[122] Qin, L., Liu, J., Kang, S.-Z., Li, G., Li, X. (2017). The strong dependence of the bi-functionalities of core-shell-like gold-based nanocomposites on the size of gold nanoparticles. *Journal of Materials Chemistry C*, **5**, 11411-11415.

[123] Sugawa, K., Akiyama, T., Tanoue, Y., Harumoto, T., Yanagida, S., Yasumori, A., Tomita, S., Otsuki, J. (2015). Particle size dependence of the surface-enhanced Raman scattering properties of densely arranged two-dimensional assemblies of Au(core)-Ag(shell) nanospheres. *Physical Chemistry Chemical Physics*, **17**, 21182-21189.

[124] dos Santos, D. P., Temperini, M. L. A., Brolo, A. G. (2012). Mapping the Energy Distribution of SERRS Hot Spots from Anti-Stokes to Stokes Intensity Ratios. *Journal of the Americal Chemical Society*, **134**, 13492-13500.

[125] Brolo, A. G., Sanderson, A. C., Smith, A. P. (2004). Ratio of the surface-enhanced anti-Stokes scattering to the surface-enhanced Stokes-Raman scattering for molecules adsorbed on a silver electrode. *Physical Review B*, **69**, 045424.

[126] Kuzminova, A., Šubr, M., Kylián, O., Kúš, P., Hanuš, J., Procházka, M. Nanostructured metal coatings for surface-enhanced Raman spectroscopy

(SERS) prepared by means of low-pressure plasma. Under consideration for publication in *Vacuum.*

[127] Kočišová, E., Procházka, M. (2011). Drop-coating deposition Raman spectroscopy of liposomes. *Journal of Raman Spectroscopy*, **42**, 1606-1610.

[128] Drössler, P., Holzer, W., Penzkofer, A., Hegemann, P. (2003). Fluorescence quenching of riboflavin in aqueous solution by methionin and cystein. *Chemical Physics*, **286**, 409-420.

[129] Zirak, P., Penzkofer, A., Mathes, T., Hegemann, P. (2009). Photo-dynamics of roseoflavin and riboflavin in aqueous and organic solvents. *Chemical Physics*, **358**, 111-122.

[130] Everall, N. J (2009). Confocal Raman Microscopy: Performance, Pitfalls, and Best Practice. *Applied Spectroscopy*, **63**, 245A-262A.

[131] Bridges, T. E., Houlne, M. P., Harris, J. M. (2004). Spatially Resolved Analysis of Small Particles by Confocal Raman Microscopy: Depth Profiling and Optical Trapping. *Analytical Chemistry*, **76**, 576-584.

# List of abbreviations

| | |
|---|---|
| AFM | Atomic force microscopy |
| DPA | Dipicolinic acid |
| EF | Enhancement factor |
| FA | Factor analysis |
| FON | Film over nanospheres |
| FWHM | Full width at half of maximum |
| HCL | Hole-mask colloidal lithography |
| HOMO | Highest occupied molecular orbital |
| LM | Longitudinal plasmon mode |
| LSPR | Localized surface plasmon resonance |
| LUMO | Lowest unoccupied molecular orbital |
| MB | Methylene blue |
| NA | Numerical aperture |
| NSL | Nanosphere lithography |
| OAD | Oblique angle vapor deposition |
| PTFE | Polytetrafluoroethylene |
| RSD | Relative standard deviation |
| SEF | Surface-enhanced fluorescence |
| SEM | Scanning electron microscopy |
| SEIRA | Surface-enhanced infrared absorption |
| SERS | Surface-enhanced Raman scattering |
| SERRS | Surface-enhanced resonance Raman scattering |
| SVD | Singular value decomposition |
| TM | Transverse plasmon mode |
| XPS | X-ray photoelectron spectra |

# List of publications

**M. Šubr**, M. Petr, V. Peksa, O. Kylián, J. Hanuš, M. Procházka: Ag Nanorod Arrays for SERS: Aspects of Spectral Reproducibility, Surface Contamination, and Spectral Sensitivity. *Journal of Nanomaterials*, 2015, vol. 2015, 729231.

Author's contribution: Doing the SERS experiments, analysing the results and writing the manuscript.

**M. Šubr**, M. Petr, O. Kylián, J. Kratochvíl, M. Procházka: Large-scale Ag nanoislands stabilized by a magnetron-sputtered polytetrafluoroethylene film as substrates for highly sensitive and reproducible surface-enhanced Raman scattering (SERS). *Journal of Materials Chemistry C*, 2015, vol. 3, 11478-11485.

Author's contribution: Doing the SERS experiments, analysing the results and writing the manuscript.

**M. Šubr**, M. Petr, O. Kylián, J. Štěpánek, M. Veis, M. Procházka: Anisotropic Optical Response of Silver Nanorod Arrays: Surface Enhanced Raman Scattering Polarization and Angular Dependences Confronted with Ellipsometric Parameters. *Scientific Reports*, 2017, vol. 7, 4293.

Author's contribution: Doing the SERS and ellipsometry experiments, analysing the results and writing the manuscript.

**M. Šubr**, A. Kuzminova, O. Kylián, M. Procházka: Surface-enhanced Raman scattering (SERS) of riboflavin on nanostructured Ag surfaces: The role of excitation wavelength, plasmon resonance and molecular resonance. *Spectrochimica Acta Part A: Molecular and Biomolecular Spectroscopy*, 2018, vol. 197, 202-207.

Author's contribution: Doing the SERS experiments, analysing the results and writing the manuscript.

**M. Šubr**, M. Procházka: Polarization- and Angular-Resolved Optical Response of Molecules on Anisotropic Plasmonic Nanostructures. *Nanomaterials,* 2018, vol. 8, 418.

Author's contribution: Review of the literature, preparation of figures and writing the manuscript.

A. Kuzminova, **M. Šubr**, O. Kylián, P. Kúš, J. Hanuš, M. Procházka: Nanostructured metal coatings for surface-enhanced Raman spectroscopy (SERS) prepared by means of low-pressure plasma. Under consideration for publication in *Vacuum.*

Author's contribution: Participation in the SERS testing and analysis of the SERS results, writing respective parts of the manuscript.

# List of conference contributions: [12]

**M. Šubr**, M. Petr, O. Kylián, J. Kratochvíl, M. Procházka: New substrates for Highly Sensitive and Reproducible Surface-enhanced Raman Scattering of Biomolecules: Metal Nanoislands Growing on Magnetron-sputtered Polytetrafluoroethylene Film. ECSBM, September 2015, Bochum, Germany (poster).

**M. Šubr**, M. Petr, O. Kylián, J. Štěpánek, M. Procházka: Polarization and Angular Characteristics of Molecules Adsorbed on Silver Nanorod Arrays: A Relationship between SE(R)RS Intensities and Ellipsometric Parameters. ICORS 2016, August 2016, Fortaleza, Brazil (poster).

**M. Šubr,** M. Petr, O. Kylián, J. Štěpánek, M. Veis, M. Procházka: Anisotropic Optical Response of Silver Nanorod Arrays: SERS Polarization and Angular Dependences Confronted with Ellipsometric Parameters. Faraday Discussions, August 2017, Glasgow, United Kingdom (poster).

**M. Šubr,** A. Kuzminova, P. Praus, O. Kylián, M. Procházka: Silver Nanoislands Growing on Magnetron-Sputtered Polytetrafluoroethylene Film with Gradient Plasmon Resonance for the Surface-Enhanced Spectroscopies of Biomolecules. ECSBM 2017, Amsterdam, the Netherlands (poster).

**M. Šubr**, A. Kuzminova, O. Kylián, M. Procházka: Nanostructured Gradient Metal Surfaces for Surface-Enhanced Raman Spectroscopy of Biomolecules. ICORS, August 2018, Jeju, South Korea (poster).

[12] Only contributions presented by the author himself are included.

# Attachments

# Attachment A1

**M. Šubr**, M. Petr, V. Peksa, O. Kylián, J. Hanuš, M. Procházka: Ag Nanorod Arrays for SERS: Aspects of Spectral Reproducibility, Surface Contamination, and Spectral Sensitivity. Journal of Nanomaterials, 2015, vol. 2015, 729231.

Hindawi Publishing Corporation
Journal of Nanomaterials
Volume 2015, Article ID 729231, 7 pages
http://dx.doi.org/10.1155/2015/729231

*Research Article*

# Ag Nanorod Arrays for SERS: Aspects of Spectral Reproducibility, Surface Contamination, and Spectral Sensitivity

**Martin Šubr,[1] Martin Petr,[2] Vlastimil Peksa,[1] Ondřej Kylián,[2] Jan Hanuš,[2] and Marek Procházka[1]**

[1] *Institute of Physics, Faculty of Mathematics and Physics, Charles University in Prague, Ke Karlovu 5, 121 16 Prague, Czech Republic*
[2] *Department of Macromolecular Physics, Faculty of Mathematics and Physics, Charles University in Prague, V Holešovičkách 2, 180 00 Prague, Czech Republic*

Correspondence should be addressed to Marek Procházka; prochaz@karlov.mff.cuni.cz

Received 25 November 2014; Accepted 17 February 2015

Academic Editor: Weihai Ni



Ag nanorod arrays prepared by oblique angle vapor deposition (OAD) represent regular, large area substrates for surface-enhanced Raman scattering (SERS) spectroscopy. We studied uniformity and spectral reproducibility of silver OAD-fabricated substrates (AgOADs) by spectral mapping of methylene blue. The results demonstrate good reproducibility apart from occasional "hot-spot" sites where the intensity is higher. The number of "hot-spots" represents 2%–6% of SERS-active sites of mapping substrate area. We were able to obtain good SERS spectra of testing amino acid tryptophan at $1 \times 10^{-5}$ M concentration and three different free-base porphyrins down to ~$10^{-7}$ M concentration. We found out that keeping the AgOADs in a vacuum chamber overnight prevents the surface from binding any contaminants from the ambient atmosphere, without significant reduction in the SERS enhancement. Such substrates provide stable SERS enhancement even when stored for 1 year after preparation.

## 1. Introduction

Surface-enhanced Raman scattering (SERS) is a spectroscopic technique capable of detecting specific molecules at low concentrations [1, 2]. It yields to enormous enhancement (above $10^5$) of Raman scattering of molecules placed in the vicinity of certain metal nanostructures. It is generally recognized that the dominant contribution to the SERS enhancement is due to the electromagnetic effect. This phenomenon is based on the resonance excitation of localized conduction-electron oscillations at the metal surface, which are termed surface plasmons [3]. The conditions for localized surface plasmon resonance (LSPR) are given by, namely, the size, shape, and degree of the aggregation of metal nanostructures [1, 3]. In bioanalytical, medical, and biosensing applications of SERS (e.g., [2, 4–6]), the most commonly used metals are silver and gold because of their highly effective LSPR in the visible spectral region. The advantage of silver is the strongest enhancement allowing very low concentrations of analytes to be detected. Gold is due to its chemical inactivity more suitable for incorporation inside biological systems and/or designing of bioassay and biosensor platforms.

Roughened metal electrodes, metal island films, and metal colloids have been used in SERS spectroscopy since its discovery in the 70s. In attempts to fabricate more uniform and spectrally reproducible substrates, close attention has been paid to more sophisticated control of substrate morphology in the last 10–15 years. The wide variety of employed preparation methods, including nanoparticle immobilization, nanoimprinting, templating, and nanosphere or nanocolloidal lithography, is reviewed, for example, in [7–9]. Chaney and coworkers developed a nanofabrication technique based on oblique angle vapor deposition (OAD) to obtain a versatile, simple, and inexpensive way of producing regular Ag nanorod arrays for SERS applications [10]. OAD utilizes an effect of self-shadowing

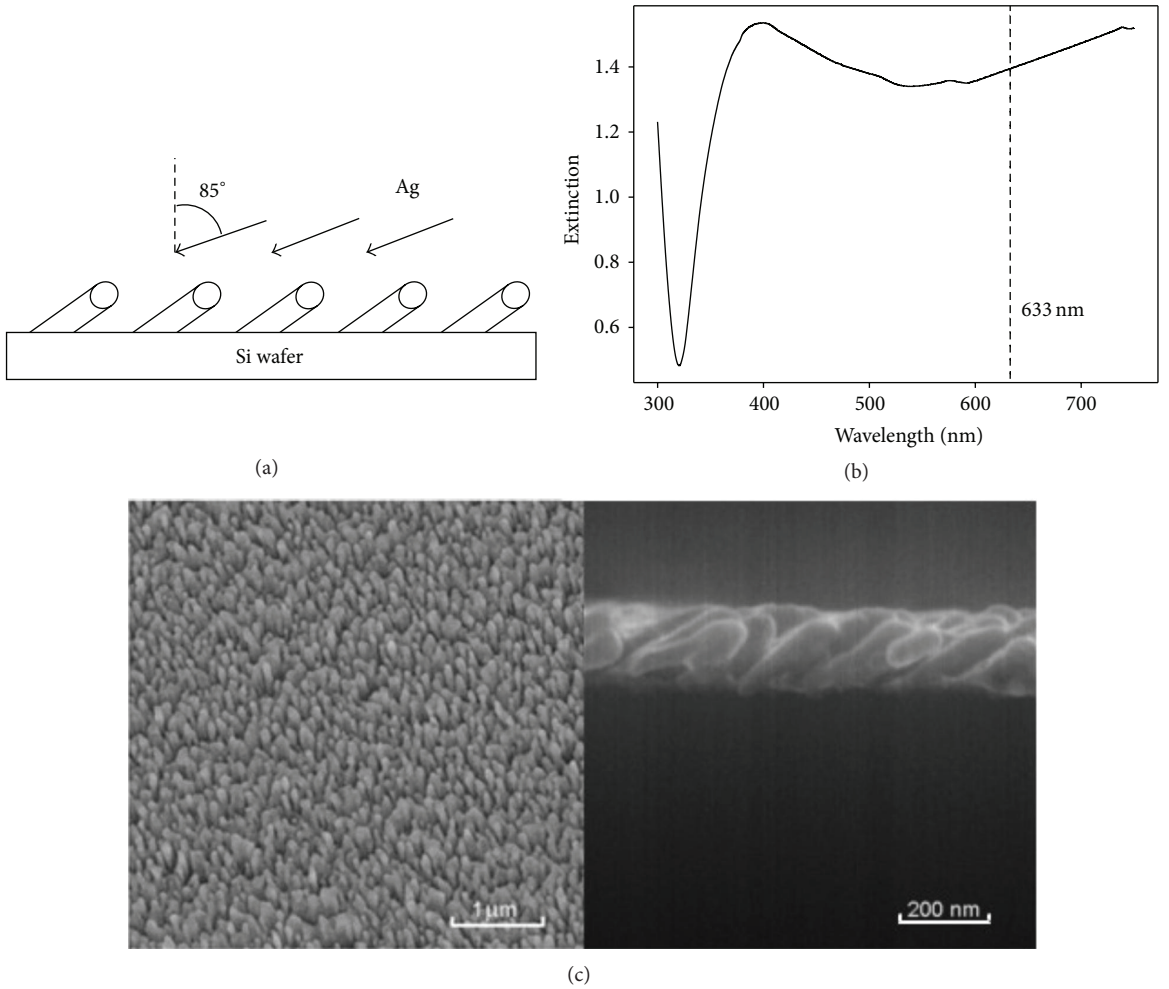


Figure 1: (a) Scheme of the OAD procedure, (b) extinction spectrum of prepared structures with excitation wavelength used for SERS measurements indicated by a dashed line, and (c) SEM images of a typical Ag nanorod array (top and side view).

which occurs when a collimated flux of vaporized atoms arrives at a substrate at an oblique angle with respect to the substrate normal. In this case, the growing nuclei shadow the area opposite to the incoming flux, and therefore the film grows through the formation of columnar structures separated from each other by voids and inclined towards the source of the flux (Figure 1(a)). The main advantage of OAD preparation is its simplicity. It is a one-step, vacuum-based process and, since no chemical substances are required, is also environmentally friendly. It was proved that OAD offers uniform, reproducible, large area SERS-active substrates with high SERS enhancement [11]. Ag nanorod arrays fabricated by OAD have been investigated as SERS-active substrates for the detection of pathogens, including viruses and bacteria, as well as assessing the potential of nucleotide-modified Ag nanorod arrays in a variety of biorecognition and biosensing applications [11].

In spite of recent advances in substrate fabrication suitable for SERS applications, employed metal nanostructures still pose a serious drawback for routine SERS quantitative analysis. In the case of Ag substrates, surface contamination irrespective of the nature of the fabrication method is often observed. It comes either from the preparation procedure or from the ambient atmosphere during storage and involves mainly organic (carbonaceous) species that are adsorbed on Ag surface. In the case of studied molecules with weak affinity to Ag surface, it can make their adsorption on the contaminated surface difficult or even impossible. Moreover, the surface contaminants (or impurities) manifest themselves, even in very small concentrations, by their anomalous SERS bands that overlap the SERS signal of a studied molecule. Such problems were previously reported in the case of both colloidal NPs [12, 13] and solid substrates [9, 14, 15]. Thus, special care must be exercised when analyzing any spectral pattern in an effort to reliably distinguish the bands coming from the analyte from those of the contaminants or, better still, to develop a method for preventing the contamination. There have been numerous ways to clean SERS-active surfaces from contaminants under ambient conditions, including electrochemical [9], plasma [14, 15], or ozone cleaning [16], but none have been uniformly successful [11]. Unfortunately, a side result of some electrochemical desorption

techniques can be the introduction of surface defects where the carbon contamination was present or strong oxidation due to the high chemical reactivity of Ag [16, 17]. In the case of Ag nanorod arrays prepared by the OAD technique, it was demonstrated that under controlled plasma conditions and exposure times (<4 min.) the Ar plasma cleaning procedure essentially eliminated any detectable background organic and carbonaceous contamination from the surface without substantially changing their morphology [14]. Moreover, it was demonstrated that the process of ion etching was able to recover SERS effectiveness of such substrates even after 1-month storage [15].

In this paper, we focused on testing of silver OAD-fabricated nanorod array substrates (AgOADs) for SERS spectroscopy. We studied uniformity and spectral reproducibility of AgOADs by spectral mapping of methylene blue. We were able to obtain SERS spectra of biomolecules tryptophan down to $1 \times 10^{-5}$ M concentration and porphyrins down to ~$10^{-7}$ M. We found out that keeping the substrates in a vacuum chamber overnight prevents it from binding any further contaminants from the ambient air, moreover, without significant reduction in the SERS enhancement.

## 2. Materials and Methods

*2.1. Materials.* Methylene blue (MB), L-tryptophan, 5, 10,15,20-tetrakis(1-methyl-4-pyridyl)-21H,23H-porphine ($H_2$TMPyP), 5,10,15,20-tetrakis(4-trimethylammoniophenyl)-21H,23H-porphine ($H_2$TMAP), and 5,10,15,20-tetrakis(4-sulfonatophenyl)-21H,23H-porphine ($H_2$TSPP) were purchased from Sigma-Aldrich.

*2.2. Preparation and Characterization of AgOADs.* For preparation of the AgOADs, a magnetron sputtering of silver target was used (Figure 1(a)). Depositions were performed in a cylindrical stainless steel vacuum chamber (40 l) pumped by scroll and turbomolecular pumps to base pressure lower than $10^{-3}$ Pa. Films were deposited onto Si wafer support introduced into the deposition chamber by a load-lock system. Ar (purity 99.99%) was used as a working gas. The pressure during deposition was 0.18 Pa, magnetron current was 300 mA, distance between magnetron and substrate was 10 cm, deposition angle was 85°, and deposition time was 15 minutes. Under these conditions the mean diameter of individual Ag nanorods was 60 nm, the mean distance between their centers was 150 nm, and the height of the nanorod array was around 200 nm as can be seen in Figure 1(c) where top and side views of Ag nanorods acquired by scanning electron microscopy (SEM, TESCAN Mira 3, 15 kV accelerating voltage) are presented. For the sake of characterization of the surface plasmon properties of the AgOADs, silver deposition was performed on glass and extinction spectra of structures fabricated in this way were obtained (UV-Vis spectrophotometer Hitachi U-3300). From Figure 1(b) it follows that the AgOADs exhibit plasmon resonance over a very broad range of wavelengths.

*2.3. SERS Measurements.* For spectral reproducibility measurements, the AgOADs (deposited on Si wafer) were cut into ~0.5 cm × 0.5 cm pieces, immersed in $1 \times 10^{-6}$ M stock solution of MB for 1 hour, and then removed and dried with an air stream. For SERS measurements of tryptophan and porphyrins, a small drop of sample was deposited on the Ag surface and left to dry. SERS spectra were collected at room temperature using an integrated confocal Raman microscopic system LabRam HR800 (Horiba Jobin-Yvon), equipped with a diffraction grating with 300 grooves/mm and a liquid nitrogen cooled CCD detector. We tried 514.5 nm, 632.8 nm, and 785 nm excitation wavelengths, but the 632.8 nm one provided the best SERS signal. Thus, He-Ne laser, operating at the wavelength 632.8 nm, was used as an excitation source for all SERS measurements. Laser power at the sample was 0.07 mW, 0.02 mW, and 0.002 mW for MB, tryptophan, and porphyrins, respectively. The laser beam was focused to a spot of about 1 $\mu$m diameter using 100x objective; NA = 0.9. Scattered radiation was collected in a back-scattering geometry and filtered by an edge filter for Rayleigh rejection before focusing it onto the 100 $\mu$m entrance slit of the spectrometer. Acquisition times were 1 s, 10 s, and 60 s for MB, tryptophan, and porphyrins, respectively.

## 3. Results and Discussion

*3.1. Aspects of Spectral Reproducibility.* Uniformity and spectral reproducibility of the prepared AgOADs were evaluated by spectral mapping of MB, which is a well-established SERS probe molecule and a very efficient Raman scatterer (for its chemical structure see Figure 2). We tested different batches of AgOADs by mapping of random places at the samples covering $10 \times 10$ spectral points. Spectral maps were processed by in-house developed software based on factor analysis (FA), using a singular value decomposition (SVD) algorithm [18]. This procedure provides a set of singular values $W_j$, orthonormal subspectra $S_j(t)$, and a unitary matrix of corresponding $V_{ij}$ coefficients. A particular experimental spectrum $Y_i(t)$ within the treated series ($i = 1, \ldots, N$) can be expressed as

$$Y_i(t) = \sum_{j=1}^{m} W_j V_{ij} S_j(t). \quad (1)$$

The factor dimension $m$ can be determined as the number of independent components (subspectra) resolvable in the analyzed spectral set and its value can be derived from the plot of the residual error values against the subspectra numbers. The $W_j$ is a vector representing the relative statistical weight of each subspectrum and the $V_{ij}$ is a unitary matrix representing relative contents of a subspectrum $S_j(t)$ in a particular spectrum $Y_i(t)$. In our case, spectra obtained in different mapping points may vary in intensities but not in the shape of the basic spectral profile (in an ideal case, all spectra in different mapping points are just multiples of one basic spectral profile). That is why we may assume with sufficient preciseness that $m = 1$ with only the first subspectrum $S_1$ being relevant for our further calculations, whereas other subspectra represent only noise or at most slight changes in the background, traces of parasitic signal, and other artifacts. Thus, we used the coefficients $V_{i1}$ to construct spectral maps of MB.

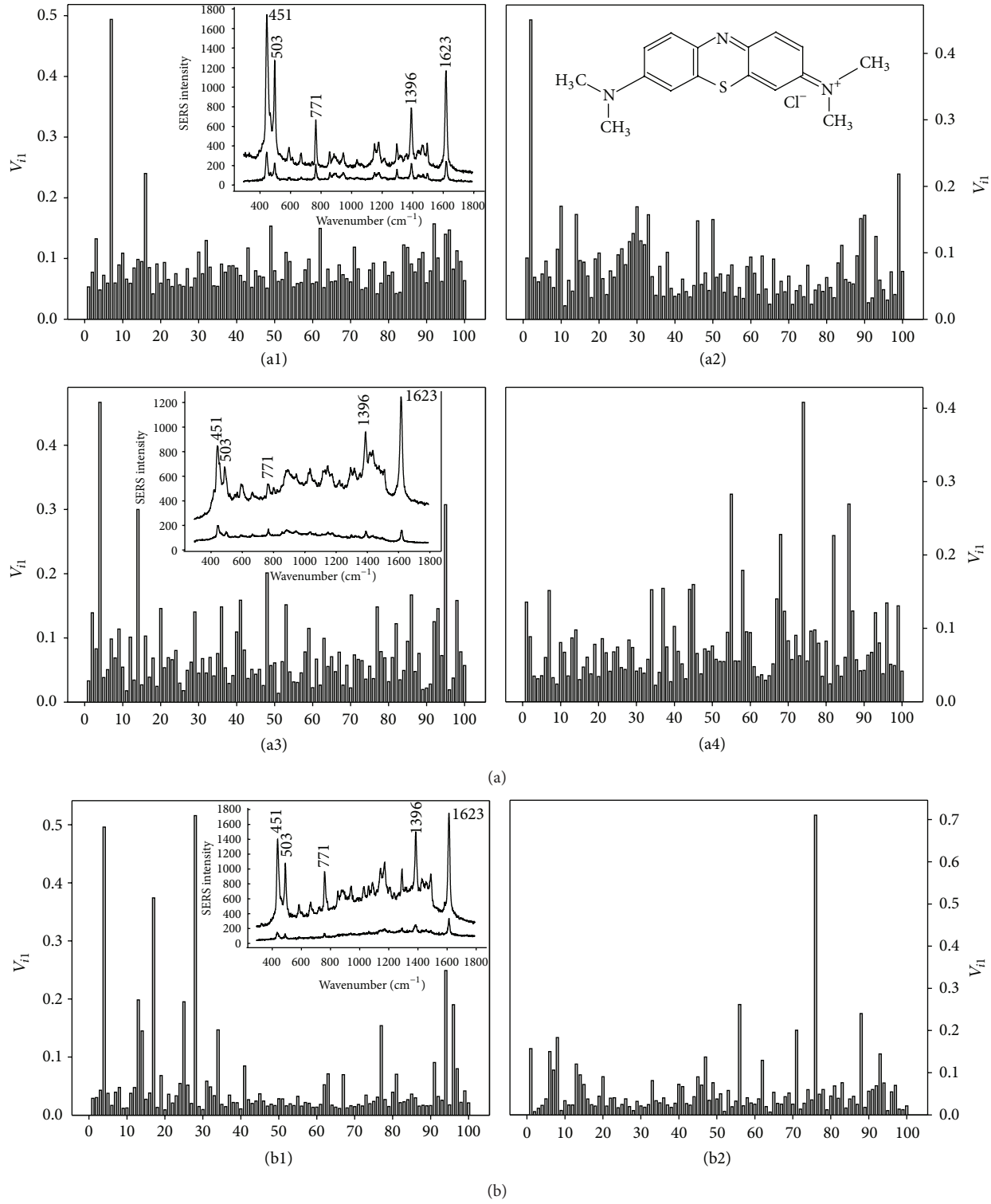


Figure 2: Reproducibility of spectral maps of MB on two different batches of AgOADs ((a) and (b)) in terms of coefficients $V_{i1}$. Steps between mapping points were 5 $\mu$m. Spectral maps on the batch (a) were taken two days after their fabrication ((a1), (a2)) and after 1-year storage ((a3), (a4)). Examples of MB spectra with an average enhancement and spectra obtained from "hot-spot" sites are depicted as insets of graphs (a1), (a3), and (b1). Chemical structure of MB is depicted as inset of graph (a2).

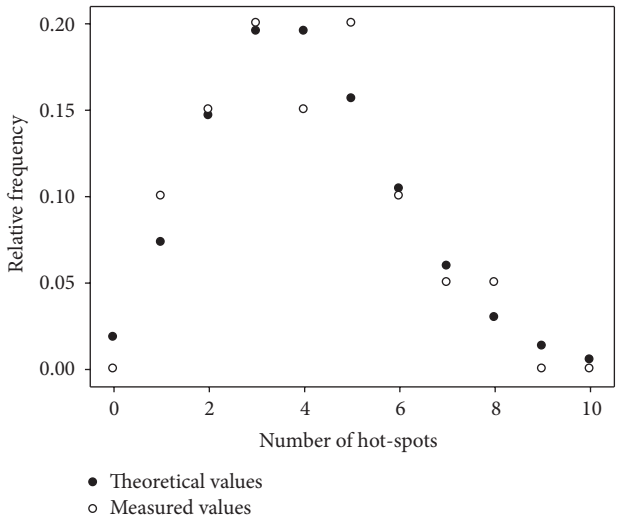


Figure 3: Comparison of the relative frequency of number of "hot-spots" in a given map of 10 × 10 spectral points (out of 20 maps in total) with the values predicted by the Poisson distribution with fixed mean value of 4.

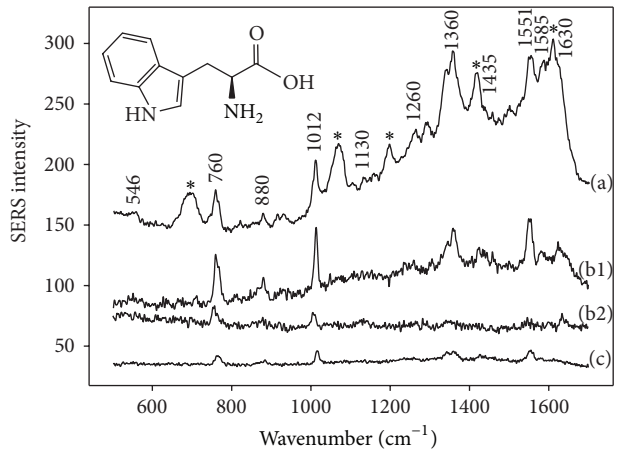


Figure 4: SERS spectra of tryptophan on two different AgOADs and demonstration of the effect of cleaning: (a) $1 \times 10^{-4}$ M tryptophan on contaminated substrate, (b) tryptophan on clean substrate kept in vacuum overnight, $1 \times 10^{-4}$ M (1) and $1 \times 10^{-5}$ M concentration (2), and (c) $1 \times 10^{-4}$ M tryptophan on contaminated substrate after 5 min. ultrasonic cleaning. Positions of main anomalous bands are marked with asterisks. Inset: chemical structure of tryptophan.

Comparison of spectral reproducibility and SERS effectiveness of two different batches of AgOADs ((a), (b)) and after different storage times (2 days and 1 year) on a given batch are depicted in Figure 2. It is clear that both batches as well as 2-day and 1-year aged substrates provide reproducible SERS enhancement, signal variation up to 20% apart from occasional points where the intensity is higher. Higher SERS intensity obviously comes from excitation of "hot-spot" sites, which are sparsely distributed over the surface. Thus, reproducibility of a given spectral map is influenced mainly by the presence of occasional "hot-spots"; however, the actual number of "hot-spots" in a given set of 10 × 10 spectral points fluctuates (see maps (a) and (b) in Figure 2). We determined the relative frequency of number of "hot-spots" in a mapping area (10 × 10 spectral points) using 20 spectral maps of MB, exhibiting the expected Poisson distribution (Figure 3). We assumed that "hot-spot" is a point where the intensity was at least 3 times the average intensity of a given spectral map. The mean number of "hot-spots" in a given set is ~4 and the mean deviation is ~2. Thus, we conclude that the number of "hot-spots" represents 2%–6% of SERS-active sites of the mapping substrate area.

*3.2. Aspects of Surface Contamination and SERS Sensitivity.* In order to evaluate the SERS sensitivity of AgOADs, we tested amino acid tryptophan and porphyrins. They represent biomolecules widely studied by means of SERS. We measured their SERS spectra by depositing a droplet of a stock solution on the AgOADs and left it to dry. This process resulted in rather irregular distribution of molecules on the metal surface, leading to the loss of reproducibility of obtained spectra across different mapping points (in comparison to Figure 2). On the other hand, increased concentration of the analyte in certain regions of the substrate can increase the SERS sensitivity.

As already mentioned, one of the major limitations of exploiting AgOADs for SERS applications is the contamination of their surface by organic contaminants. This problem may be overcome by specific cleaning of the substrate, for example, by Ar plasma [14, 15] or ozone [16] treatment. However, the success of these methods strongly depends on the time of the applied cleaning and may lead to a reduction in SERS effectiveness due to suffered oxidation damage or distortion of the surface nanostructures. In the case of MB measurements no anomalous SERS bands of impurities were observed probably because MB molecules have a high affinity to silver and are able to replace the contaminants from the surface. On the other hand, when tryptophan was measured, we found a strong interference of surface contaminant bands with the tryptophan spectrum. Thus, we tried to find a way of cleaning the Ag surface before deposition of tryptophan. Figure 4 demonstrates the SERS spectra of tryptophan on (a) substrates exposed to the ambient atmosphere immediately after their fabrication, exhibiting anomalous bands marked with asterisks, (b) substrates kept in vacuum overnight, and (c) substrates after a 5 min. ultrasonic treatment.

Although the ultrasonic treatment did in some cases lead to the disappearance of anomalous bands from the spectra, the SERS effectiveness was approximately 4x worse. Keeping the substrates several hours in vacuum immediately after the deposition managed to reduce the spectra of contaminants significantly without a significant decrease in the SERS enhancement. By extending the time for which the substrates were kept in a vacuum after the deposition, SERS intensity of anomalous bands was gradually decreasing with almost complete suppression of a parasitic signal after overnight storage in a vacuum. We suggest that keeping the substrates in a vacuum chamber for at least 16 hours prevents it from binding any further contaminants in the ambient air. Such

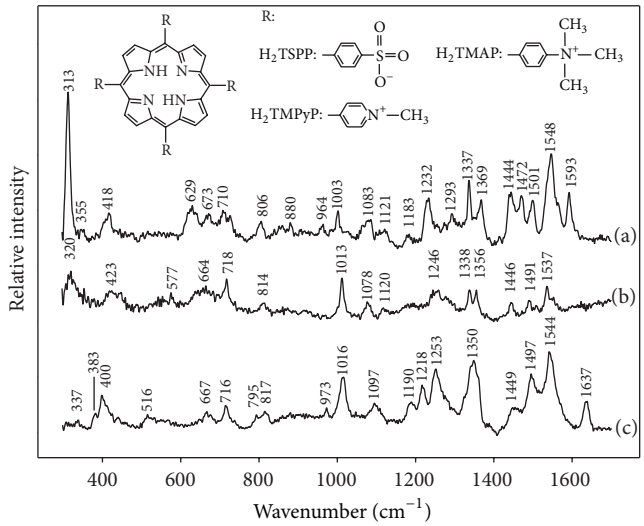


Figure 5: SERS spectra of three free-base porphyrins on AgOADs: (a) $H_2$TSPP, $3 \times 10^{-7}$ M, (b) $H_2$TMAP, $3 \times 10^{-7}$ M, and (c) $H_2$TMPyP, $5 \times 10^{-7}$ M concentrations. Spectra are baseline corrected and shifted in vertical scale for the sake of clarity. Inset: chemical structure of porphyrins.

substrates provide stable enhancement even 3 months after their fabrication. We consider this method of keeping the substrates in a vacuum immediately after the deposition convenient due to the possibility of not using any other chemicals or further cleaning procedures whose influence on the surface morphology may be arguable.

The SERS spectra of tryptophan are dominated by two intense bands around 760 and 1012 cm$^{-1}$ (Figure 4), which are assigned to the ring-breathing vibrations of the indole ring [19]. These two bands remain obvious down to $1 \times 10^{-5}$ M concentration. Our tryptophan spectra are analogous to those reported previously using Ag nanoparticles [19, 20].

The final step of this study was testing of capability of fabricated clean AgOADs, that is, substrates that were kept 16 hours in vacuum after their deposition, to detect different porphyrins. The chemical structures of studied free-base porphyrins are depicted as inset of Figure 5. Two porphyrins ($H_2$TMPyP and $H_2$TMAP) are positively charged and one is charged negatively ($H_2$TSPP). SERS spectra of these three porphyrins of the order of $10^{-7}$ M concentration were obtained from clean AgOADs (Figure 5). Our SERS spectra have a very good signal-to-noise ratio and positions of bands correspond very well with the spectra obtained previously using Ag nanoparticles [21, 22]. No anomalous bands of surface contaminants were observed.

## 4. Conclusions

We studied uniformity and spectral reproducibility of Ag nanorod arrays prepared by an oblique angle vapor deposition (OAD) technique. SERS spectra of methylene blue were used for spectral mapping through the AgOADs. The results demonstrated good reproducibility apart from occasional "hot-spot" sites where the intensity is higher. The number of "hot-spots" represents 2%–6% of SERS-active sites of mapping substrate area. Freshly prepared substrates exhibited strong anomalous bands from surface contaminants, often overlapping SERS spectra of the studied molecules. We found out that keeping the substrates in a vacuum chamber overnight after the preparation is a simple way to avoid this effect without a significant reduction in the SERS enhancement. Such substrates provide stable enhancement even after 1-year storage. We demonstrate that, by such substrate treatment, appropriate choice of laser power with respect to a given molecule, and reduced time of exposure to the laser beam, we were able to obtain SERS spectra of tryptophan at $1 \times 10^{-5}$ M concentration and as low as ~$10^{-7}$ M for porphyrins.

## Conflict of Interests

The authors declare that there is no conflict of interests regarding the publication of this paper.

## Acknowledgments

Funding of research Projects P205/13/20110S from the Czech Science Foundation and no. SVV 260092 from the Charles University in Prague is gratefully acknowledged.

## References

[1] E. C. Le Ru and P. G. Etchegoin, *Principles of Surface-Enhanced Raman Spectroscopy and Related Plasmonic Effects*, Elsevier, Amsterdam, The Netherlands, 2009.

[2] S. Schlücker, "Surface-enhanced Raman spectroscopy: concepts and chemical applications," *Angewandte Chemie International Edition*, vol. 53, no. 19, pp. 4756–4795, 2014.

[3] M. Moskovits, "Surface-enhanced spectroscopy," *Reviews of Modern Physics*, vol. 57, no. 3, pp. 783–826, 1985.

[4] K. C. Bantz, A. F. Meyer, N. J. Wittenberg et al., "Recent progress in SERS biosensing," *Physical Chemistry Chemical Physics*, vol. 13, no. 24, pp. 11551–11567, 2011.

[5] D. Cialla, A. März, R. Böhme et al., "Surface-enhanced Raman spectroscopy (SERS): progress and trends," *Analytical and Bioanalytical Chemistry*, vol. 403, no. 1, pp. 27–54, 2012.

[6] M. Procházka and J. Štěpánek, "Surface-enhanced Raman scattering (SERS) and its application to biomolecular and cellular investigation," in *Applications of Raman Spectroscopy to Biology—From Basic Studies to Disease Diagnosis*, M. Ghomi, Ed., IOS Press, Amsterdam, The Netherlands, 2012.

[7] M. J. Banholzer, J. E. Millstone, L. D. Qin, and C. A. Mirkin, "Rationally designed nanostructures for surface-enhanced Raman spectroscopy," *Chemical Society Reviews*, vol. 37, no. 5, pp. 885–897, 2008.

[8] M. Fan, G. F. S. Andrade, and A. G. Brolo, "A review on the fabrication of substrates for surface enhanced Raman spectroscopy and their applications in analytical chemistry," *Analytica Chimica Acta*, vol. 693, no. 1-2, pp. 7–25, 2011.

[9] X.-M. Lin, Y. Cui, Y.-H. Xu, B. Ren, and Z.-Q. Tian, "Surface-enhanced Raman spectroscopy: substrate-related issues," *Analytical and Bioanalytical Chemistry*, vol. 394, no. 7, pp. 1729–1745, 2009.

[10] S. B. Chaney, S. Shanmukh, R. A. Dluhy, and Y.-P. Zhao, "Aligned silver nanorod arrays produce high sensitivity surface-enhanced Raman spectroscopy substrates," *Applied Physics Letters*, vol. 87, no. 3, Article ID 031908, 2005.

[11] P. Negri and R. A. Dluhy, "Ag nanorod based surface-enhanced Raman spectroscopy applied to bioanalytical sensing," *Journal of Biophotonics*, vol. 6, no. 1, pp. 20–35, 2013.

[12] S. Sánchez-Cortés and J. V. García-Ramos, "Anomalous Raman bands appearing in surface-enhanced Raman spectra," *Journal of Raman Spectroscopy*, vol. 29, no. 5, pp. 365–371, 1998.

[13] N. R. Yaffe and E. W. Blanch, "Effects and anomalies that can occur in SERS spectra of biological molecules when using a wide range of aggregating agents for hydroxylamine-reduced and citrate-reduced silver colloids," *Vibrational Spectroscopy*, vol. 48, no. 2, pp. 196–201, 2008.

[14] P. Negri, N. E. Marotta, L. A. Bottomley, and R. A. Dluhy, "Removal of surface contamination and self-assembled monolayers (SAMs) from silver (Ag) nanorod substrates by plasma cleaning with argon," *Applied Spectroscopy*, vol. 65, no. 1, pp. 66–74, 2011.

[15] N. Nuntawong, P. Eiamchai, B. Wong-Ek et al., "Shelf time effect on SERS effectiveness of silver nanorod prepared by OAD technique," *Vacuum*, vol. 88, no. 1, pp. 23–27, 2013.

[16] K. L. Norrod and K. L. Rowlen, "Removal of carbonaceous contamination from SERS-active silver by self-assembly of decanethiol," *Analytical Chemistry*, vol. 70, no. 19, pp. 4218–4221, 1998.

[17] S. Z. Zou, Y. X. Chen, B. W. Mao, B. Ren, and Z. Q. Tian, "SERS studies on electrode/electrolyte interfacial water I. Ion effects in the negative potential region," *Journal of Electroanalytical Chemistry*, vol. 424, no. 1-2, pp. 19–24, 1997.

[18] J. Hanzlíková, M. Procházka, J. Štěpánek, J. Bok, V. Baumruk, and P. Anzenbacher Jr., "Metalation of 5,10,15,20-tetrakis(1-methyl-4-pyridyl)porphyrin in silver colloids studied via time dependence of surface-enhanced resonance Raman spectra," *Journal of Raman Spectroscopy*, vol. 29, no. 7, pp. 575–584, 1998.

[19] C.-H. Chuang and Y.-T. Chen, "Raman scattering of L-tryptophan enhanced by surface plasmon of silver nanoparticles: vibrational assignment and structural determination," *Journal of Raman Spectroscopy*, vol. 40, no. 2, pp. 150–156, 2009.

[20] P. Šimáková, M. Procházka, and E. Kočišová, "SERS microspectroscopy of biomolecules on dried Ag colloidal drops," *Spectroscopy*, vol. 27, no. 5-6, pp. 449–453, 2012.

[21] M. Procházka, J. Hanzliková, J. Štěpánek, and V. Baumruk, "Metalation of positively charged water soluble mesoporphyrins studied via time-resolved SERRS spectroscopy," *Journal of Molecular Structure*, vol. 410-411, pp. 77–79, 1997.

[22] M. Itabashi, K. Kato, and K. Itoh, "Electrochemical processes of meso-tetrakis (4-sulfonatophenyl) porphine at a silver electrode studied by surface-enhanced resonance Raman spectroscopy," *Chemical Physics Letters*, vol. 97, no. 6, pp. 528–532, 1983.

# Attachment A2

**M. Šubr**, M. Petr, O. Kylián, J. Kratochvíl, M. Procházka: Large-scale Ag nanoislands stabilized by a magnetron-sputtered polytetrafluoroethylene film as substrates for highly sensitive and reproducible surface-enhanced Raman scattering (SERS). Journal of Materials Chemistry C, 2015, vol. 3, 11478-11485.

Journal of Materials Chemistry C

PAPER

Cite this: DOI: 10.1039/c5tc02919h

# Large-scale Ag nanoislands stabilized by a magnetron-sputtered polytetrafluoroethylene film as substrates for highly sensitive and reproducible surface-enhanced Raman scattering (SERS)†

Martin Šubr,*[a] Martin Petr,[b] Ondřej Kylián,[b] Jiří Kratochvíl[b] and Marek Procházka*[a]

Fabrication of surface-enhanced Raman scattering (SERS) nanostructures with both high sensitivity and spectral reproducibility, which are key requirements for routine SERS quantitative (sensing) applications, is a great challenge. Here we report on the multilayered design of SERS-active substrates formed by uniform Ag nanoislands stabilized by a magnetron-sputtered polytetrafluoroethylene (msPTFE) film of nanometre thickness. The preparation of large scale (~20 $cm^2$) nanostructures with long (~months) time stability was fast (~minutes), cheap and repeatable. SERS performance of our substrates was subsequently improved by step-by-step optimisation of the fabrication procedure and introduction of the additional silver layer, separating the supporting glass from the msPTFE film, which contributed to the total enhancement factor by another order of magnitude. Such substrates provided high SERS sensitivity with a SERS enhancement factor of about 2 orders of magnitude larger than commonly reported in the literature for Ag nanoislands grown directly on glass. The limits of detection were determined as $\sim 1 \times 10^{-10}$ M, $1 \times 10^{-7}$ M and $1 \times 10^{-6}$ M for testing analytes methylene blue (MB), 5,10,15,20-tetrakis(1-methyl-4-pyridyl)porphyrin ($H_2$TMPyP) and cysteine, respectively. SERS substrates showed excellent spectral reproducibility both across a single substrate and different substrate batches. The relative standard deviation (RSD) of the SERS signal did not exceed 20% for different concentrations of MB and $H_2$TMPyP, respectively. Therefore, Ag nanoislands stabilized by the msPTFE film are due to high sensitivity, stability and excellent spectral reproducibility very promising substrates for SERS biomolecular quantitative (sensing) applications.

Received 15th September 2015,
Accepted 30th September 2015

DOI: 10.1039/c5tc02919h

www.rsc.org/MaterialsC

## 1. Introduction

Surface-enhanced Raman scattering (SERS) is a spectroscopic technique based on an enormous (above $10^4$) enhancement of Raman scattering of molecules situated in close proximity to nanostructured metallic substrates.[1,2] The main enhancement mechanism, so-called electromagnetic, is based on the resonance excitation of surface plasmons, localized in the metallic nanostructure, which enhances both the incident radiation and the radiation scattered by the molecules.[3] In order to maximize the Raman signal enhancement, it is necessary to use nanostructured surfaces or nanoparticles of noble metals with suitable optical properties. The conditions for localized surface plasmon resonance (LSPR) are given by the size, shape and degree of aggregation of applied metallic nanostructures.[1,3] In SERS applications, the commonly used metals are Ag and Au because of their highly effective LSPR in the visible spectral region.[1]

Although recent advances have turned SERS to a wide variety of bioanalytical, medical and biosensing applications,[2,4–6] employed metallic nanostructures still pose a serious drawback for routine quantitative analysis. That is because not only high sensitivity, but also spatial and temporal uniformity and spectral reproducibility of used metallic nanostructures are crucial. For example, commonly used SERS substrates such as Ag and Au hydrosols provide very poor reproducibility with fluctuant SERS enhancement that may vary across several orders of magnitudes, which hinders quantitative SERS measurements.[1,6]

Generally, metallic nanostructures for quantitative SERS applications (sensing) should: (i) possess high Raman enhancement,

[a] Charles University in Prague, Faculty of Mathematics and Physics, Institute of Physics, Ke Karlovu 5, 121 16 Prague, Czech Republic. E-mail: subr.Martin@seznam.cz, prochaz@karlov.mff.cuni.cz
[b] Charles University in Prague, Faculty of Mathematics and Physics, Department of Macromolecular Physics, V Holešovičkách 2, 180 00 Prague, Czech Republic

† Electronic supplementary information (ESI) available. See DOI: 10.1039/c5tc02919h

(ii) be uniform so that the SERS signal will not deviate remarkably over the whole surface (generally signal variation not exceed 20%), (iii) provide good spectral stability and reproducibility, and (iv) be clean enough from stray SERS signals.[7] Moreover, simplicity, high throughput and low cost are also essential requirements for the development of methods for nanostructure fabrication, which can subsequently be used on a large scale. A big effort has been made to improve the uniformity and SERS reproducibility of metallic substrates, most notably by rational design of highly ordered array nanostructures that can fulfil the above mentioned criteria.[8–10] Unfortunately, the most widely used metallic array nanostructure preparation techniques, such as nanoparticle immobilization,[11] electron and ion beam lithography,[12] nanoimprinting,[13] and nanosphere[14,15] or nanocolloidal[16] lithography, are limited by the high costs, the enormous difficulties to extend to large scales or complicated preparation steps.[8–10]

Metal nanoislands have been used as SERS-active substrates for a long time.[17] The main advantage of nanoislands is the simplicity of the fabrication process and the possibility of tuning the LSPR wavelength by varying the film's thickness and confluence. Although the enhancement factor (EF) of Au and Ag nanoislands is generally considered to be rather modest ($10^4$–$10^5$),[14] additional Raman intensity on SERS substrates can arise as a result of optical interference effects on a given structure by utilizing an underlying reflective layer.[18] Polymers were commonly used to improve the mechanical stability of nanoparticles[19] and better signal reproducibility *via* embossing surfaces and lithographic techniques.[20] Polytetrafluoroethylene (PTFE) is a polymer with high thermal stability and low degradation after exposure to a focused laser beam. PTFE foil has great surface roughness with improved adhesive properties of sputtering gold overlay and can be positive for the electromagnetic mechanism. Gold overlay can suppress the Raman background signal of the PTFE substrate.[19] Previously, the SERS-active surfaces were prepared by short (30 s) sputtering deposition of the gold layer on the standard PTFE foil of 50 μm thickness.[21] With the use of Au/Ag sandwich nanostructures the SERS spectra of testing adsorbate biphenyl-4,4′-dithiol at $10^{-8}$ M concentration were obtained. The analytical EF between $10^6$ and $10^7$ was determined for such substrates. The standard PTFE film was also used as a concentrator for both Ag nanoparticles and the analyte (rhodamine 6G) to achieve higher SERS enhancement.[22]

In this paper, we focused on the preparation of Ag nanostructures stabilized by a magnetron-sputtered polytetrafluoroethylene (msPTFE) film of nanometre thickness, which are schematically depicted in Fig. 1. These layer structures are supported on a standard microscopic glass slide. The topmost layer of these structures is formed by Ag nanoislands (responsible for the SERS effect) grown on an underlying dielectric film made of msPTFE. The msPTFE film also works as a dielectric separation layer (see layout in Fig. 1). To further improve the SERS performance of our substrates, the supporting glass slide was decorated by an additional reflective smooth metal layer (prior to the deposition of the msPTFE film), serving as a mirror for the incident laser beam. The fabrication procedure was

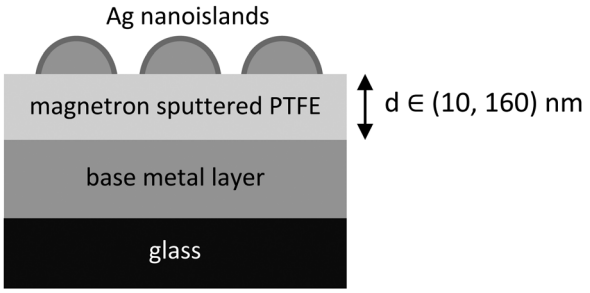


Fig. 1 Schematic representation of the prepared nanostructures.

optimised with respect to the following parameters: (i) deposition time of the Ag nanoislands, (ii) utilization of the metal back-reflector and its type, and (iii) variation in the thickness of the msPTFE film. We demonstrate that careful control of each of the aforementioned parameters enables an additional 5–10 times increase in Raman intensity (in comparison to the parameters which were not optimised) and thus deserves special attention at the stage of substrate fabrication in order to achieve maximum SERS enhancement. The SERS activity and stability of our substrates were tested by methylene blue (MB), which is an often used SERS probe providing strong SERS signals, and two biomolecules: 5,10,15,20-tetrakis(1-methyl-4-pyridyl)porphyrin ($H_2$TMPyP) and amino acid cysteine.

## 2. Experimental section

### 2.1 Chemicals

Methylene blue (MB), 5,10,15,20-tetrakis(1-methyl-4-pyridyl)-porphyrin ($H_2$TMPyP) and amino acid cysteine were purchased from Sigma-Aldrich.

### 2.2 Preparation of SERS substrates

The SERS substrates were prepared on standard microscopic glass slides (76 mm × 26 mm).

For deposition of Ag nanoislands a DC, planar, water-cooled magnetron was used. This magnetron was equipped with the silver target (81 mm diameter, 3 mm thickness, Safina a.s., declared purity 99.99%) and attached onto a vacuum deposition chamber pumped by scroll and turbomolecular pumps (base pressure lower than $1 \times 10^{-2}$ Pa). DC current was 0.04 A, which corresponded to the magnetron voltage of 239 V, and the deposition time was varied in the range of 20−200 s. After nanoisland deposition, the substrates were kept in a vacuum chamber overnight to prevent contamination from the ambient atmosphere.[23]

The msPTFE interlayer was deposited in another deposition chamber equipped by a RF planar magnetron with the PTFE target (81 mm diameter, 3 mm thickness, Goodfellow). The magnetron operated at a frequency of 13.56 MHz and the applied RF power was 40 W. Argon was used as a working gas with the flow of 3 sccm and the pressure of 3 Pa. Deposition time was varied between 1.5 and 30 min, which led to the

 

thicknesses between 10 and 160 nm as measured by spectral ellipsometry (Woolam M-2000DI).

The base metal layers (Ag, Au, Al and Cu) were deposited onto glass in an argon atmosphere (3 sccm, 3 Pa). In the case of Ag and Al base layers 3″ magnetron powered by DC power supply was used, and magnetron current was 0.3 A. Au and Cu base layers were deposited using 2″ DC planar magnetron (magnetron current 0.04 A). The thickness of these layers was 120 nm as measured using an Atomic Force Microscope (AFM, Ntegra Prima, NT-MDT).

### 2.3 Instrumentation and measurements

The extinction spectra of the prepared structures (without additional metal layer) were obtained using a UV-Vis spectrophotometer Hitachi U-3300. The surface morphology of the prepared structures was investigated by scanning electron microscopy (SEM, TESCAN Mira 3, 15 kV accelerating voltage). Topography of the samples was analyzed by AFM in a semi-contact mode with standard silicon cantilevers (Multi75DLC, Budget Sensors).

All SERS spectra were recorded at room temperature using an integrated confocal Raman microscopic system LabRam HR800 (Horiba Jobin-Yvon), equipped with a diffraction grating with 300 grooves per mm and a liquid nitrogen cooled CCD detector. He–Ne laser, operating at the wavelength of 632.8 nm, was used as an excitation source. The beam was focused onto the sample to a spot of approximately a 1 μm diameter using a 100× objective, NA = 0.9. Scattered radiation was collected in a back-scattering geometry and filtered by an edge filter for Rayleigh rejection before focusing it onto the 100 μm entrance slit of the spectrometer.

SERS testing was carried out using MB in the concentration range between $1 \times 10^{-7}$ M and $1 \times 10^{-10}$ M, $H_2$TMPyP in concentrations $2 \times 10^{-6}$ M and $10^{-7}$ M and cysteine in the concentration range between $1 \times 10^{-4}$ M and $1 \times 10^{-6}$ M. In the case of MB and porphyrin SERS measurements, the Ag substrate was dipped in adsorbate aqueous solution for 30 min, then removed from the solution and dried in an air stream. Since the 632.8 nm excitation wavelength falls into the slope of the electronic absorption bands of MB and $H_2$TMPyP, SERS spectra of both analytes should be considered as surface-enhanced (resonance) Raman scattering spectra. SERS spectra of cysteine were obtained by dropping 2 μl of a cysteine stock solution on the Ag nanoislands structures and left to dry. SERS spectra of MB were collected using 0.02 mW laser power at the sample and 5 s acquisition time (5 averaged accumulations). The same laser power and 3 s acquisition time were used for cysteine. Porphyrin SERS spectra were obtained with a laser power of 0.07 mW and 60 s acquisition time (60 averaged accumulations).

## 3. Results and discussion

### 3.1 Optimisation of the fabrication process and SERS testing

Fig. 1 shows the scheme of the prepared SERS-active structures. Their topmost layer is formed by Ag nanoislands that are responsible for the SERS effect, stabilized by a dielectric film made of msPTFE. Our optimisation strategy of the fabrication procedure was carried out in the following way: the first parameter varied was the deposition time of the Ag nanoislands, while the thickness of the msPTFE film was kept constant (40 nm) and no back-reflector layer was utilized. Then, a smooth layer of metal was introduced between the supporting glass slide and the msPTFE film, while the thickness of the msPTFE film (40 nm) and the deposition time of Ag nanoislands (100 s) remained unchanged. The final step of the optimisation process involved variation in the thickness of the dielectric msPTFE film between 10 and 160 nm in an effort to further maximize the SERS signal. The evaluation of the SERS performance during this process was carried out on the basis of averaged measured spectral maps (including maps obtained both across a single substrate as well as on different substrate batches) constructed from the height of the strongest SERS peak at around 1624 $cm^{-1}$ above the spectral background for different MB concentrations.

In the first stage of the fabrication procedure deposition time of the Ag nanoislands was optimised. By changing the deposition time we were able to obtain different morphologies ranging from small individual Ag nanoparticles of dozens of nm at short deposition times to an interconnected Ag network observed at longer deposition times (Fig. 2a–d). Different morphologies of Ag coatings consequently resulted in different extinction spectra, and thus different LSPR conditions (Fig. 3A). For further SERS testing, the deposition time was set to 100 s, corresponding to the surface composed of individual Ag nanoislands in close proximity to each other. In this case, the average height of Ag nanoislands was $\sim$6 nm, the root-mean-square roughness was $\sim$1.1 nm (Fig. 2e–g) and the extinction maximum wavelength (673 nm) slightly red-shifted with respect to the incident laser wavelength (632.8 nm). The rightmost part of the obtained SERS spectral region ($\sim$1700 $cm^{-1}$) corresponds to the wavelength of approximately 710 nm, which means that both the incident and the scattered radiation may be optimally enhanced. The position and the shape of the extinction band were found to be unchanged within 6 weeks storage after deposition (Fig. 3B).

In the second step of the optimisation process, a smooth layer of the metal back-reflector was introduced in the structures as sketched in Fig. 1, expected to provide stronger SERS signals on account of the optical interference effect.[18] Different metal back-reflectors (Ag, Au, Al and Cu) were tested as can be seen in Fig. 4A. Our results clearly show the role of the bottom layer of metal, suggesting that it acts like a mirror for the incident laser beam, reflecting part of the incoming radiation back to the surface. The maximum signal increase was found for Ag, which is consistent with the fact that Ag is the most reflective metal in the 600–700 nm region.[1]

Finally, the thickness of the dielectric msPTFE film was adjusted. Changes in the msPTFE thicknesses were accompanied by changes in the SERS signal as can be seen in Fig. 4B. Fig. 4B demonstrates that the SERS signal rises very sharply as the thickness $d$ of the msPTFE film increases up to $d \sim 80$ nm and

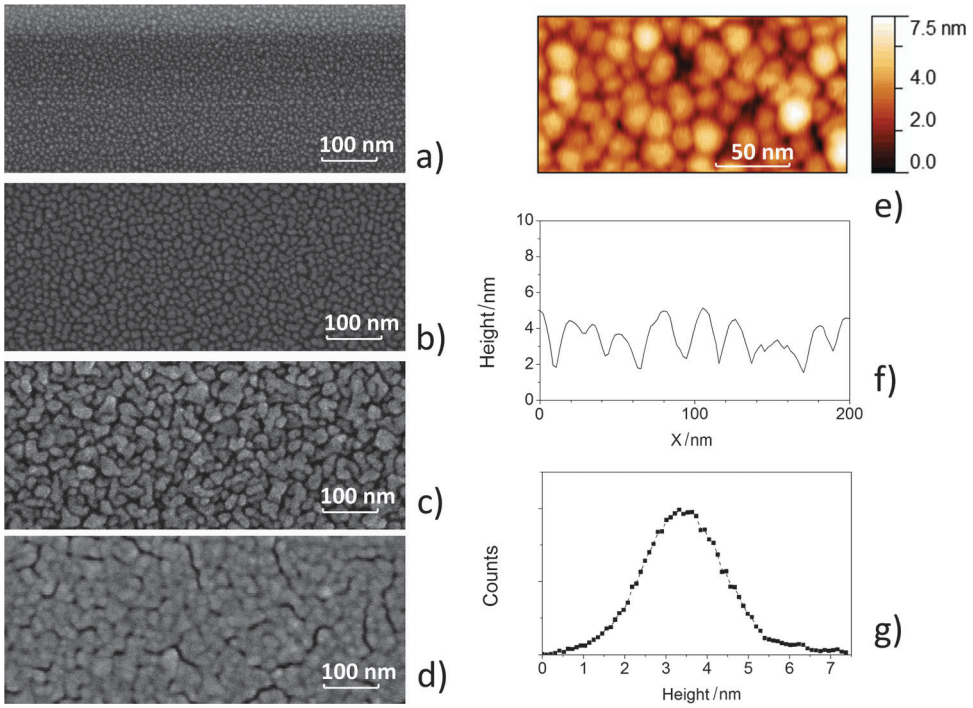


Fig. 2 SEM images of Ag sputtered onto msPTFE. Deposition time was (a) 20 s, (b) 50 s, (c) 100 s and (d) 200 s; (e) 100 nm × 200 nm section of the AFM image of Ag deposited onto msPTFE for 100 s, (f) corresponding height profile and (g) height histogram.

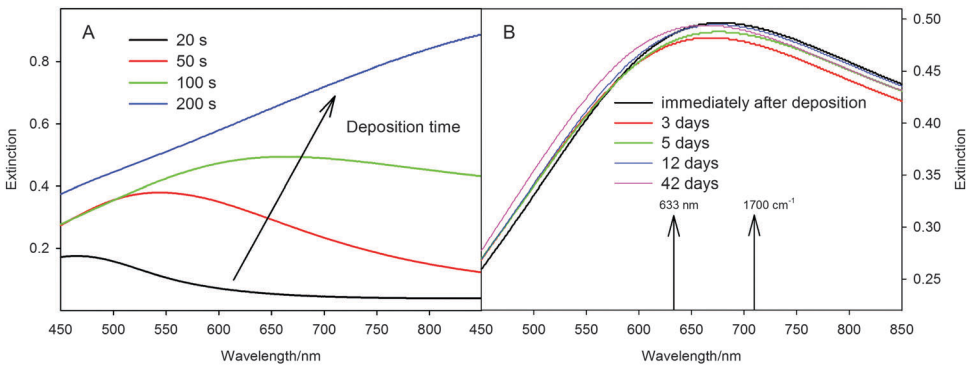


Fig. 3 (A) Extinction spectra of Ag sputtered onto msPTFE under different deposition times, (B) extinction spectra evolution with storage time (100 s deposition). The excitation wavelength (633 nm) and the rightmost part of the measured SERS spectral region (corresponding to 1700 $cm^{-1}$) are marked by arrows.

reaches a plateau for $d > 80$ nm (corresponding MB intensities for $d = 80$ nm and $d = 160$ nm tend to be the same within the experimental error).

### 3.2 Determination of the limit of detection of MB

Concentration dependence of MB SERS spectra on optimised structures (100 s nanoislands deposition, underlying Ag back-reflector) is displayed in Fig. 4C and D. For MB concentrations lower than $10^{-10}$ M the signal is overlapped by strong PTFE background and that is why we conclude that the $10^{-10}$ M concentration is the detection limit of MB. Indeed, spectral background intensity for $c_{SERS} = 10^{-10}$ M is ~900, corresponding to $\sigma \sim 900^{1/2} = 30$ noise level, whereas the MB intensity is ~100 above the spectral background. This is in agreement with the commonly established definition of the limit of detection (LOD), according to which $c_{LOD} = 3\sigma$.[24]

The exact number of MB molecules present in the measured spot is difficult to determine precisely, however, we tried to estimate the surface coverage of the Ag substrate in the following way: after 30 min soaking in the $10^{-7}$ M stock solution, the number of molecules in the stock solution must be diminished by the number of molecules that adsorbed on the substrate. That is why the final concentration of the stock solution is $(1 - \delta) \times 10^{-7}$ M after 30 min soaking for a certain $\delta \in (0, 1)$. Therefore, we soaked another substrate in the $(1 - \delta) \times 10^{-7}$ M stock solution and investigated the drop in the SERS intensity with respect to the intensity of the $10^{-7}$ M soaking concentration. This experiment was repeated twice and in both cases

 

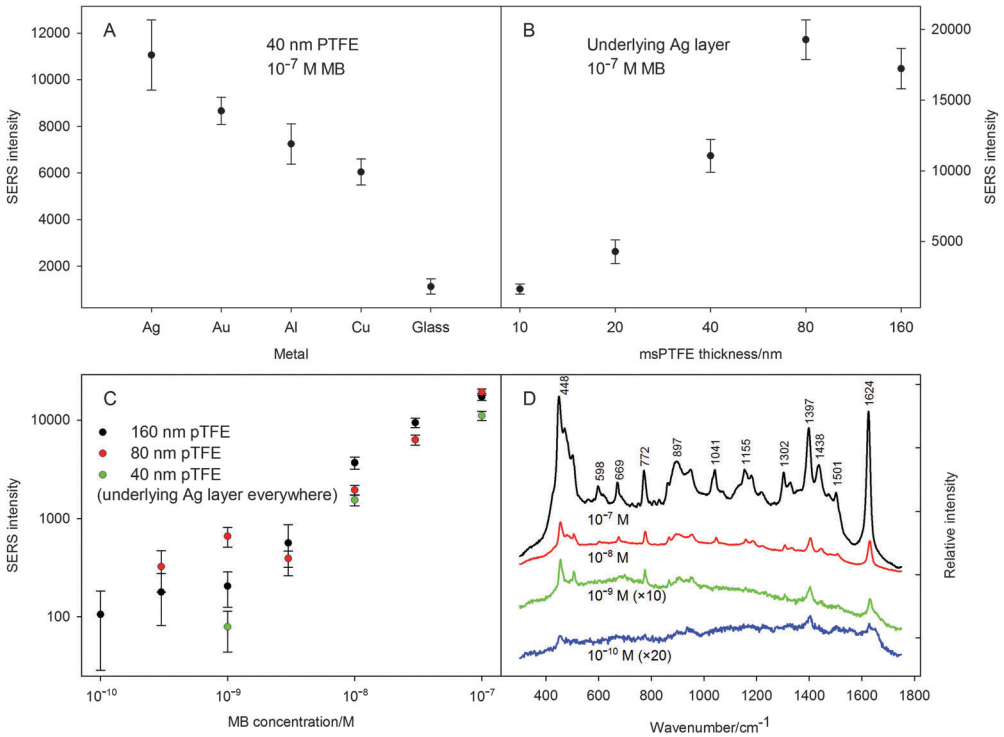


Fig. 4 (A) Dependence of the SERS signal on the type of the underlying metal layer, (B) dependence of the MB SERS signal on the msPTFE thickness with the underlying Ag layer, (C) concentration dependence of MB SERS spectra on different structures with the underlying Ag layer (intensity determined as the height of the peak at 1624 $cm^{-1}$ above spectral background), (D) MB spectra on the optimised structures – concentration dependence (80 nm PTFE, underlying Ag layer). Note logarithmic axes in graphs (B) and (C), the spectra in graph (D) are offset for clarity.

the SERS intensity decreased to ~80% of the original value. Therefore, we estimate $\delta$ to be ~0.2 (assuming constant sensitivity at a certain small vicinity of the $10^{-7}$ M MB concentration as the first approximation). The volumes of respective stock solutions were $V_{SERS}$ = 1 ml and the dimensions of immersed substrates $x^2$ ~ 3 mm × 3 mm, which means that the $1 \times 10^{-7}$ M stock solution of MB contained $1 \times 10^{-10}$ moles of MB, *i.e.* $6 \times 10^{13}$ MB molecules and thus the surface coverage is ~$10^{14}$ molecules per $cm^2$ for the highest measured MB concentration. Although the equilibrium constant between the number of adsorbed molecules and the number of molecules in the solution may be a bit different for different concentrations, it makes the surface coverage of ~$10^{11}$ molecules per $cm^2$ for the lowest measured ($10^{-10}$ M) MB concentration and ~$10^3$ MB molecules in selected measured spots that we are able to detect.

### 3.3 Evaluation of the spectral reproducibility

The evaluation of the spectral reproducibility of optimised SERS substrates was performed on the basis of at least 4 measured spectral maps for each measured MB concentration (including maps obtained both across a single substrate and on different substrate batches). Signal homogeneity in each of these maps, each of them covering 10 × 10 spectral points, was evaluated using in-house developed software based on the 'singular value decomposition' algorithm of factor analysis.[25] This approach allows a rapid and precise analysis of spectral intensities of very large sets of spectra. This procedure provides a set of singular values $W_j$, orthonormal subspectra $S_j(t)$ and a unitary matrix of the corresponding $V_{ij}$ coefficients. A particular experimental spectrum $Y_i(t)$ within the treated series can be expressed as

$$Y_i(t) = \sum_{j=1}^{m} W_j V_{ij} S_j(t).$$

The factor dimension $m$ represents the number of independent components (subspectra) resolvable in the analysed spectral set, and its value can be derived from the plot of the residual error values against the subspectra numbers. $W_j$ is a vector representing the relative statistical weight of each subspectrum and $V_{ij}$ is a unitary matrix representing the relative contents of subspectrum $S_j(t)$ in a particular spectrum $Y_i(t)$. In our case, spectra obtained in different mapping points may vary in intensities, but not in the shape of the basic spectral profile (in an ideal case, all spectra in different mapping points are just multiples of one basic spectral profile). That is why we may assume with sufficient preciseness that $m$ = 1 with only the first subspectrum $S_1$ being relevant for our further calculations. Other subspectra represent only noise or, at most, slight changes in the background, traces of parasitic signal or other artifacts. The main reason for this approximation is that coefficients $W_j$ decrease rapidly with the increasing ordering number $j$, which justifies the negligence of subspectra $S_j(t), j > 2$.

Uniformity and spectral reproducibility of employed substrates was determined from the set of coefficients $V_{ij}$ of each map.

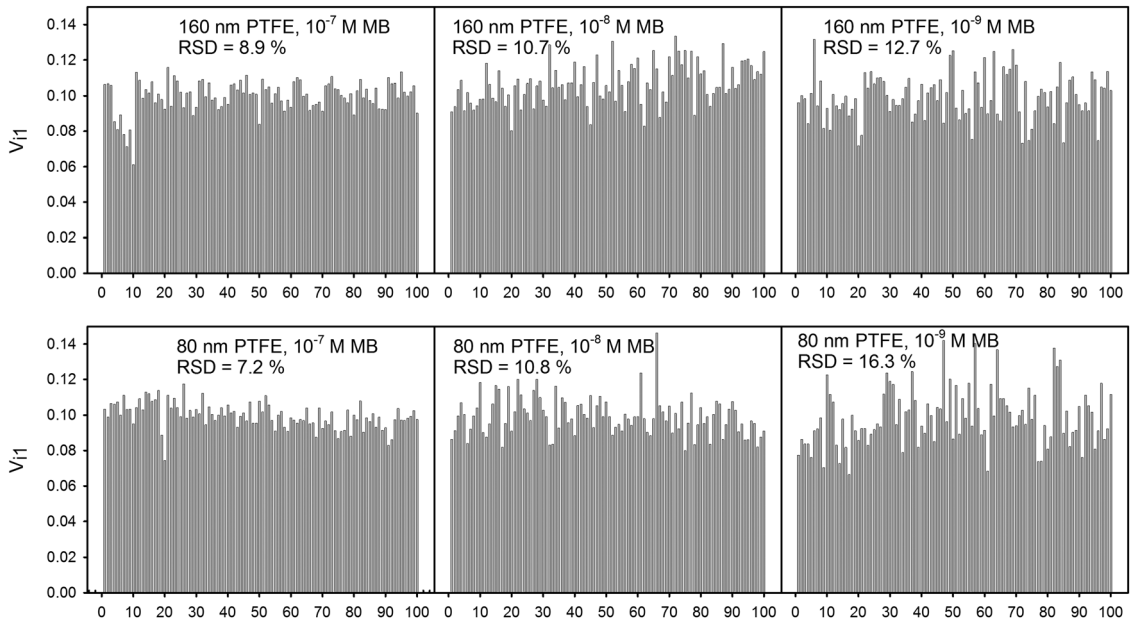


Fig. 5 RSD of six representative spectral maps for various MB concentrations measured under the same experimental conditions in terms of coefficients $V_{i1}$. The coefficients are calculated within the whole spectral range (*i.e.* ~400–1700 $cm^{-1}$) and normalized so that the sum of their squares for each map equals one.

Representative examples of measured maps for 3 MB concentrations, calculated in the spectral range ~400–1700 $cm^{-1}$ where the most prominent Raman bands of MB can be found, are shown in Fig. 5. For all the measured maps on optimised structures down to $10^{-9}$ M MB concentration, the RSD calculated over the whole spectral range did not consistently exceed 20% (Fig. 5), which demonstrates excellent spectral reproducibility. It is worth noting that even repetitive attempts of obtaining spectral maps of MB in the concentration range between $10^{-7}$ and $10^{-9}$ M, carried out within 5 months after sample fabrication, whether on the same batch or on different substrate batches, did not lead to significant worsening of spectral reproducibility nor to the diminishing of the limit of detection (for details see ESI,† Fig. S1 and S2). We suppose that the excellent temporal stability of our structures is due to (i) keeping the substrates in a vacuum chamber overnight immediately after the deposition,[23] and (ii) stabilizing effect of the supporting msPTFE film of nanometre thickness.[21] It makes these types of SERS substrates less susceptible to oxidation and the presence of contaminants in an ambient environment.

### 3.4 Determination of the EF

To evaluate the SERS performance of our optimised structures, the EF (referred to as substrate EF[1]) was calculated for MB as the probe molecule considering the intensity ratio of the strongest MB band at SERS spectra ($I_{SERS}$) and at non-SERS (resonant Raman) spectrum ($I_{RRS}$) acquired from a $1.5 \times 10^{-2}$ M MB solution dropped onto a glass slide and left to dry, measured under the same experimental conditions and normalized to number of respective molecular scatterers:

$$\mathrm{EF} = \frac{I_{\mathrm{SERS}}/N_{\mathrm{SERS}}}{I_{\mathrm{RRS}}/N_{\mathrm{RRS}}}$$

where $N_{SERS}$ is the number of molecules participating in SERS measurements and $N_{RRS}$ in the non-SERS case. Obviously, the quantities $N_{SERS}$ and $N_{RRS}$ are proportional to the SERS soaking concentration $c_{SERS}$ and the dropping concentration $c_{RRS}$, respectively, however, the exact determination of the number of participating molecules in both cases is a bit more challenging task. The MB drop on the glass surface had a diameter of $a \sim 2.6$ mm and the pipetted volume was $V_{RRS} = 2$ μl, which implies that the surface coverage in the case of non-SERS measurements was $\sim 3 \times 10^{17}$ molecules per $cm^2$. Substituting these values in the EF definition yields

$$\mathrm{EF} = \frac{I_{\mathrm{SERS}}/N_{\mathrm{SERS}}}{I_{\mathrm{RRS}}/N_{\mathrm{RRS}}} = \frac{4}{\pi\delta}\frac{x^2}{a^2}\frac{c_{\mathrm{RRS}}V_{\mathrm{RRS}}}{c_{\mathrm{SERS}}V_{\mathrm{SERS}}}\frac{I_{\mathrm{SERS}}}{I_{\mathrm{RRS}}}.$$

The biggest uncertainty of the previous formula lies in the determination of $I_{RRS}$ and in the factor $\delta$ representing the efficiency of binding the molecules in the solution to the Ag substrate. Unlike the SERS case with molecules evenly distributed on the Ag surface (as can be inferred from Fig. 5), the distribution of MB molecules on glass is rather nonuniform due to creation of molecular aggregates. That is why $I_{RRS}$ (~24) was determined on the basis of averaging of ~1000 spectra (and verified by multiple separate calculations carried out on different areas of the drop) (see ESI,† Fig. S3). The exact value of $\delta$ is unknown, but since $\delta \in (0, 1)$, $1/\delta$ must be >1 with the most likely value of ~5 as discussed in Section 3.2. Putting the numerical values in the EF definition (taking the aforementioned uncertainties into account) leads to the biggest EF (for $10^{-10}$ M concentration) between $2 \times 10^6$ and $10^7$. Thus, the EF of our substrates is about 2 orders of magnitude higher than the EF commonly reported in the literature for Ag nanoislands growing directly on glass.[14]

 

### 3.5 SERS of testing biomolecules

The potential of our substrates for quantitative SERS analysis of biomolecules was further tested using $H_2$TMPyP and amino acid cysteine.

Porphyrins are important biomolecules and their derivatives are applied in the photodynamic therapy of cancer, antiviral treatments, molecular biology, specific sensing of DNA sequences, selective cleavage of nucleic acids, transport of oligonucleotides into the cell *etc.* The SERS spectra of $H_2$TMPyP were obtained using the optimised structures (80 nm msPTFE) dipped in a $2 \times 10^{-6}$ M and $1 \times 10^{-7}$ $H_2$TMPyP stock solution for 30 min. As well as in the case of MB, reproducibility of obtained data was evaluated by means of factor analysis in the measured spectral range ~400–1700 $cm^{-1}$. Typical SERS spectra of $H_2$TMPyP and typical $H_2$TMPyP spectral maps are shown in Fig. 6. The positions of bands in the spectrum correspond well with those obtained using standard Ag colloids[26] although two broad peaks of graphitic carbon can be seen in the 1200–1600 $cm^{-1}$ region.[27]

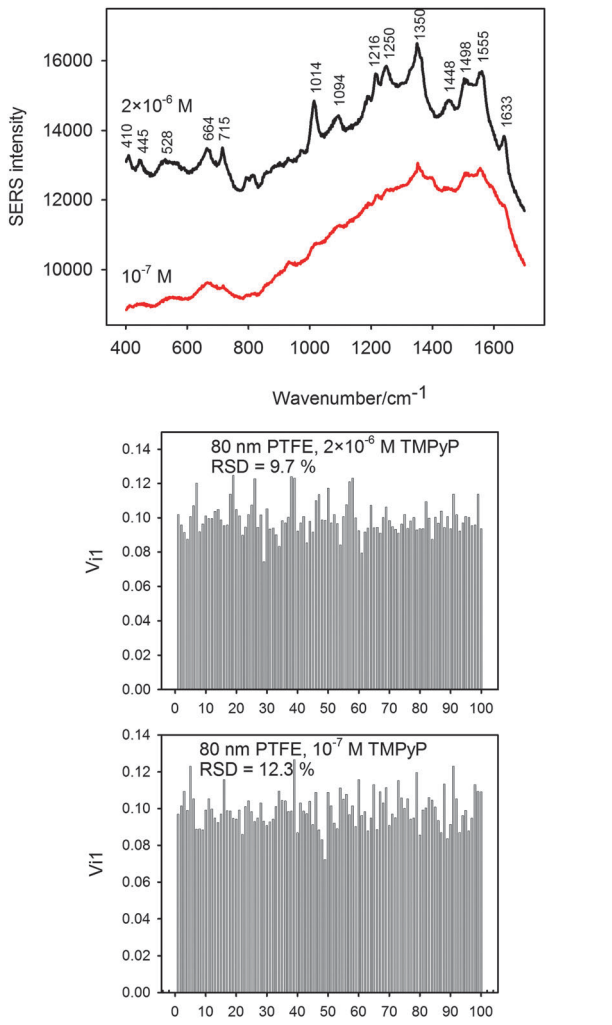


Fig. 6 SERS spectra of $H_2$TMPyP on optimised nanostructures (underlying Ag layer, 80 nm msPTFE) and two representative spectral maps for two different concentrations. The meaning of the $V_{i1}$ coefficients is the same as in Fig. 5.

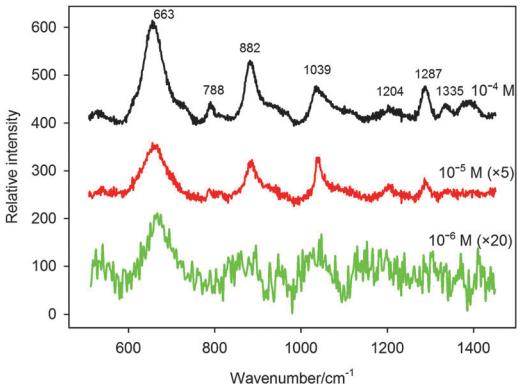


Fig. 7 SERS spectra of cysteine on optimised nanostructures (underlying Ag layer, 80 nm msPTFE). Presented spectra are averaged from 100 spectra across a mapping array and offset for clarity.

The RSD was <20% for all the measured maps, which demonstrates excellent spectral reproducibility.

Cysteine is an important structural and functional component of many proteins and enzymes and one out of two amino acids containing a sulphur atom. The SERS spectra of cysteine were obtained by dropping a 2 μl drop of a cysteine stock solution on the optimised Ag nanoisland structures. A common problem when analysing the SERS spectra of various biomolecules is analyte heating and photodecomposition due to prolonged exposure to laser illumination, resulting in a strong spectral background, temporal spectral fluctuations, diminishing of the obtained signal with time and the occurrence of broad amorphous carbon bands between ~1350 and 1600 $cm^{-1}$ that often overlap with the spectrum of the molecule to be studied.[27] All these reasons lead to the loss of the enhancing capabilities of the adsorption site and hamper efforts to fully exploit the potential of the SERS technique. That is why a compromise between the laser power and the acquisition time usually has to be settled to keep the spectral degradation at a bare minimum. To partly make up for this problem, SERS spectra of cysteine were collected from multiple nonoverlapping points at the sample, each of which was irradiated only for 3 s. The final cysteine spectrum was computed by averaging of 100 spectra of a given map instead of increasing the accumulation time at a given spectral spot. The 3 s acquisition time was chosen low enough to compensate for the strong spectral degradation in longer exposition times but still high enough with respect to the readout noise. Typical SERS spectra of cysteine in the $10^{-4}$–$10^{-6}$ M concentration range are shown in Fig. 7. Our cysteine concentration range is comparable to that using Ag colloids[28,29] and positions of Raman bands correspond well with spectra reported previously, dominated by the band at 663 $cm^{-1}$, attributed to the C–S stretching vibrational mode.[29] It is apparent from Fig. 7 that the limit of detection of cysteine is about $10^{-6}$ M dropping concentration.

## 4. Conclusions

In this study, we focused on the fabrication of Ag nanostructures stabilized by magnetron-sputtered PTFE as highly

uniform and sensitive SERS-active substrates. The fabrication procedure was optimised with respect to the deposition time of the Ag nanoislands and thickness of the supporting msPTFE film. Moreover, introducing a smooth Ag layer between the supporting glass slide and the msPTFE film increased the SERS performance by another order of magnitude. The preparation of large-scale ($\sim$20 cm$^2$) nanostructures is fast ($\sim$minutes), simple and repeatable and they exhibit long ($\sim$months) time stability.

The evaluation of spectral reproducibility was performed on the basis of obtained spectral maps measured for the MB testing analyte. Signal homogeneity in each of these maps, each of them covering 10 $\times$ 10 spectral points, was evaluated using in-house developed software based on factor analysis. The RSD of the SERS signal was found to be $<$20% for different concentrations of MB and $H_2$TMPyP without substantial deviation both across a single substrate and different substrate batches. The limits of detection were $\sim 1 \times 10^{-10}$ M, $1 \times 10^{-7}$ M and $1 \times 10^{-6}$ M for testing analytes MB, $H_2$TMPyP and cysteine, respectively. The substrate EF was computed to be between $2 \times 10^6$ and $10^7$, which is about 2 orders of magnitude higher than the EF commonly reported in the literature for Ag nanoislands grown directly on glass. In conclusion, the major advantages of our substrates are fast and cheap large-scale fabrication and excellent spectral reproducibility and therefore these structures hold great promise for SERS quantitative (sensing) applications.

## Acknowledgements

Funding of research projects No. P205/13/20110S from the Czech Science Foundation and No. SVV 260214 (M. Šubr) and GAUK No. 382313 (M. Petr) from the Charles University in Prague is gratefully acknowledged.

## References

1 E. C. Le Ru and P. G. Etchegoin, *Principles of Surface-Enhanced Raman Spectroscopy and related plasmonic effects*, Elsevier, Amsterdam, 2009.
2 S. Schlücker, *Angew. Chem., Int. Ed.*, 2014, **53**, 4756.
3 M. Moskovits, *Rev. Mod. Phys.*, 1985, **57**, 783.
4 K. C. Bantz, A. F. Meyer, N. J. Wittenberg, H. Im, Ö. Kurtulus, S. H. Lee, N. C. Lindquist, S. H. Oh and C. L. Haynes, *Phys. Chem. Chem. Phys.*, 2011, **13**, 11551.
5 D. Cialla, A. März, R. Böhme, F. Theil, K. Weber, M. Schmitt and J. Popp, *Anal. Bioanal. Chem.*, 2012, **403**, 27.
6 M. Procházka and J. Štěpánek, in *Applications of Raman Spectroscopy to Biology – From Basic Studies to Disease Diagnosis*, ed. M. Ghomi, IOS Press, Amsterdam, 2012, pp. 1–30.
7 M. J. Natan, *Faraday Discuss.*, 2006, **132**, 321.
8 M. J. Banholzer, J. E. Millstone, L. D. Qin and C. A. Mirkin, *Chem. Soc. Rev.*, 2008, **37**, 885.
9 M. K. Fan, G. F. S. Andrade and A. G. Brolo, *Anal. Chim. Acta*, 2011, **693**, 7.
10 X. M. Lin, Y. Cui, Y. H. Xu, B. Ren and Z. Q. Tian, *Anal. Bioanal. Chem.*, 2009, **394**, 1729.
11 N. Hajduková, M. Procházka, P. Molnár and J. Štěpánek, *Vib. Spectrosc.*, 2008, **48**, 142.
12 M. Kahl, E. Voges, S. Kostrewa, C. Viets and W. Hill, *Sens. Actuators, B*, 1998, **51**, 285.
13 G. M. Zhang, J. Zhang, G. Y. Xie, Z. F. Liu and H. B. Shao, *Small*, 2006, **2**, 1440.
14 C. L. Haynes, A. D. McFarland and R. P. Van Duyne, *Anal. Chem.*, 2005, **77**, 338.
15 L. Baia, M. Baia, J. Popp and S. Astilean, *J. Phys. Chem. B*, 2006, **110**, 23982.
16 H. Fredriksson, Y. Alaverdyan, A. Dmitriev, C. Langhammer, D. S. Sutherland, M. Zäch and B. Kasemo, *Adv. Mater.*, 2007, **19**, 4297.
17 V. L. Schlegel and T. M. Cotton, *Anal. Chem.*, 1991, **63**, 241.
18 L. C. T. Shoute, A. J. Bergren, A. M. Mahmoud, K. D. Harris and R. L. McCreery, *Appl. Spectrosc.*, 2009, **63**, 133.
19 S. G. Jang, D. G. Choi, C. J. Heo, S. Y. Lee and S. M. Yang, *Adv. Mater.*, 2008, **20**, 4862.
20 M. Geissler, K. Li, B. Cui, L. Clime and T. Veres, *J. Phys. Chem. C*, 2009, **113**, 17296.
21 P. Žvátora, P. Řezanka, V. Prokopec, J. Siegel, V. Švorčíik and V. Král, *Nanoscale Res. Lett.*, 2011, **6**, 366.
22 L.-Q. Lu, Y. Zheng, W.-G. Qu, H.-Q. Yu and A.-W. Xu, *J. Mater. Chem.*, 2012, **22**, 20986.
23 M. Šubr, M. Petr, V. Peksa, O. Kylián, J. Hanuš and M. Procházka, *J. Nanomater.*, 2015, **ID**, 729231.
24 V. Thomsen, D. Schatzlein and D. Mercuro, *Spectroscopy*, 2003, **18**, 112.
25 E. R. Malinowski, *Factor Analysis in Chemistry*, J. Wiley & Sons, New York, 2002.
26 M. Procházka, B. Vlčková, J. Štěpánek and P.-Y. Turpin, *Langmuir*, 2005, **21**, 2956.
27 A. Kudelski and B. Pettinger, *Chem. Phys. Lett.*, 2000, **321**, 356.
28 N. R. Yaffe, A. Ingram, D. Graham and E. W. Blanch, *J. Raman Spectrosc.*, 2010, **41**, 618.
29 G. D. Fleming, J. J. Finnerty, M. Campos-Vallette, F. Célis, A. E. Aliaga, C. Fredes and R. Koch, *J. Raman Spectrosc.*, 2009, **40**, 632.

 

Electronic Supplementary Material (ESI) for Journal of Materials Chemistry C.


## Supplementary information:

# Large-scale Silver Nanoislands Stabilized by Magnetron-sputtered Polytetrafluoroethylene Film as Substrates for Highly Sensitive and Reproducible Surface-enhanced Raman Scattering (SERS)

Martin Šubr, Martin Petr, Ondřej Kylián, Jiří Kratochvíl, and Marek Procházka

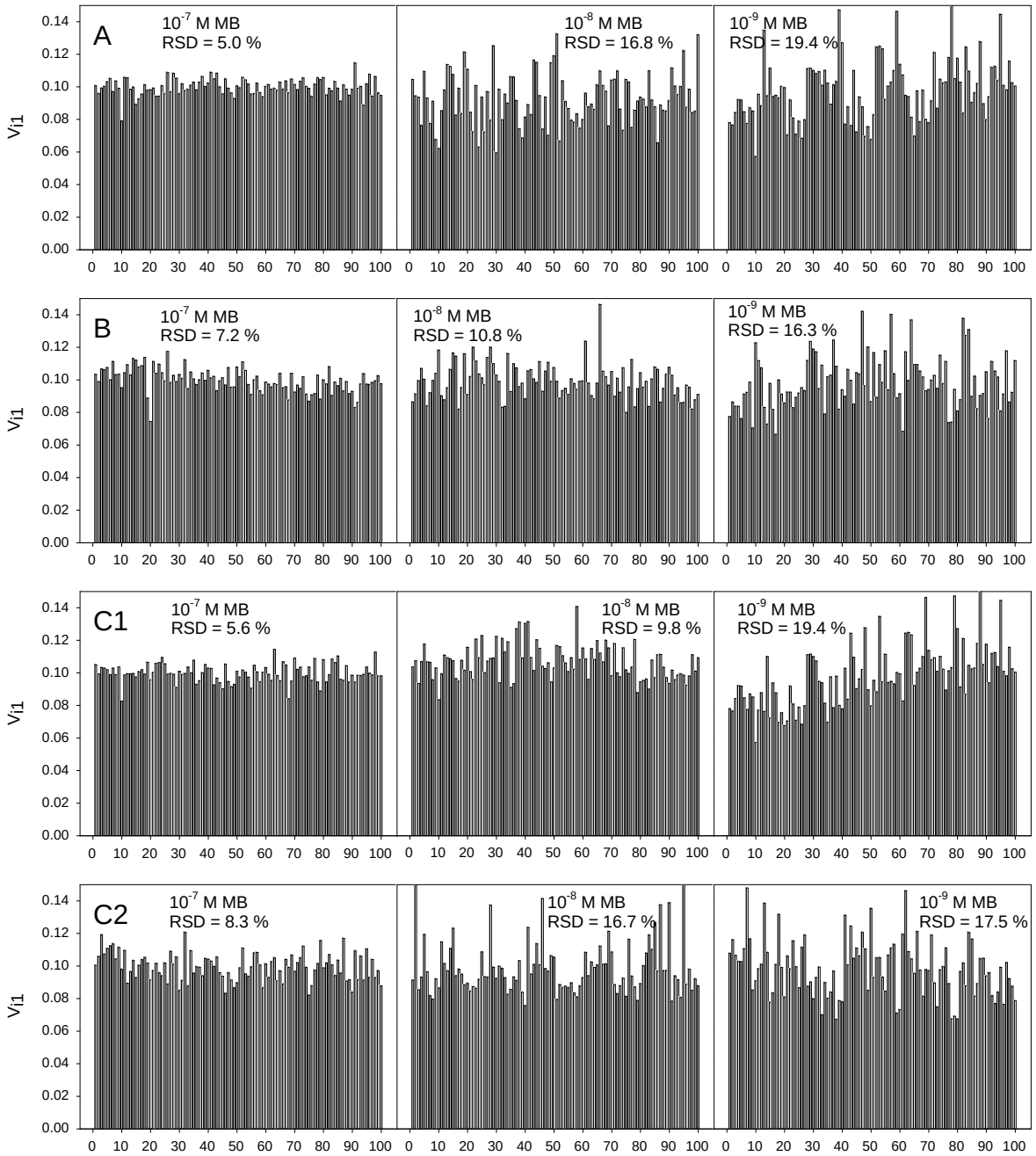


Fig. S1. RSD of spectral maps taken for different MB concentrations on different substrate batches (A, B and C) with all parameters optimised. The maps in graphs A, B and C1 were measured 2 days after the substrate preparation and the maps in graph C2 were measured 5 months after the substrate preparation (being stored in normal laboratory conditions). The meaning of the $V_{i1}$ coefficients is the same as in Fig. 5.

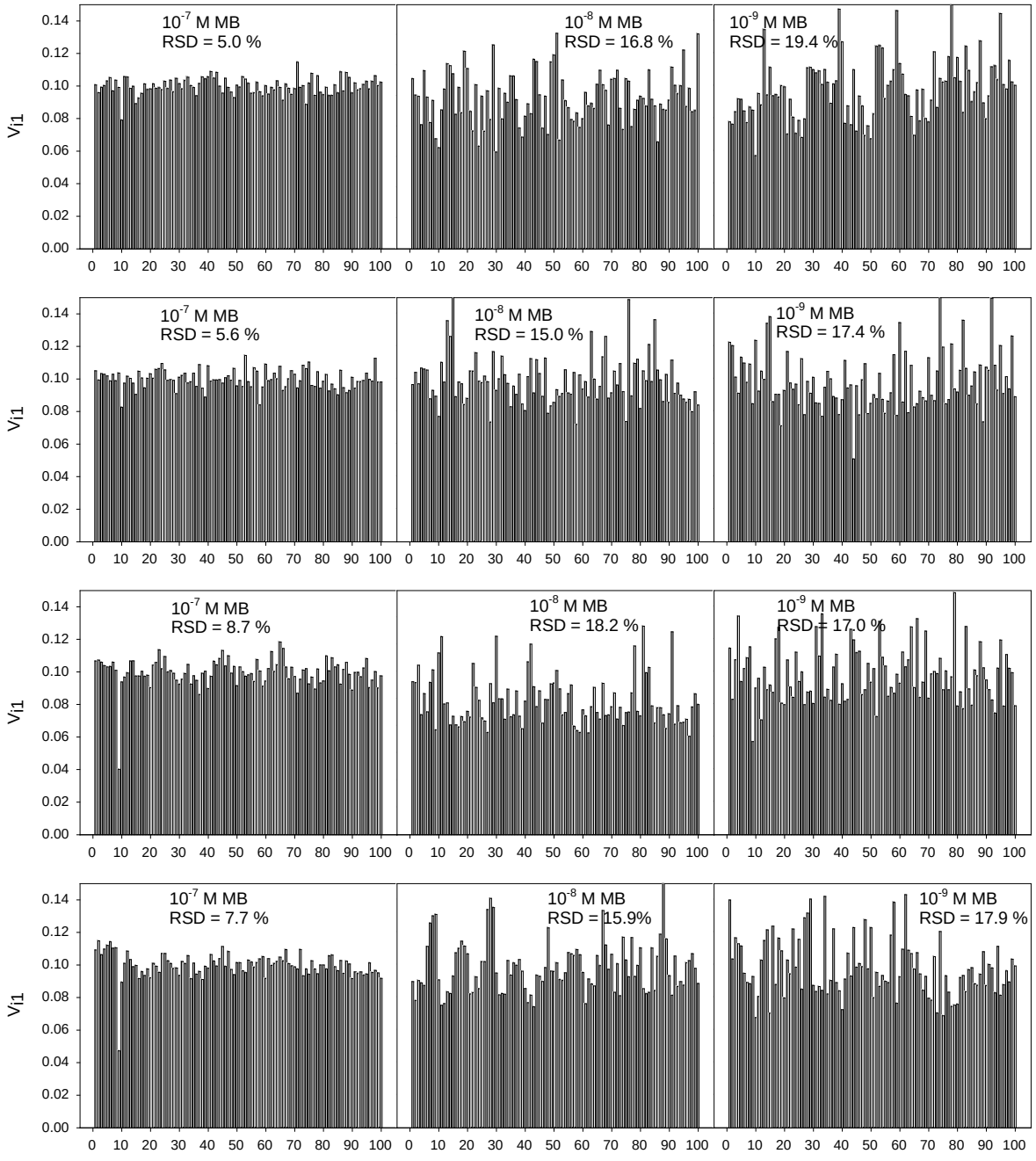


Fig. S2. RSD of spectral maps taken on different areas of the A batch for different MB concentrations. The meaning of the $V_{i1}$ coefficients is the same as in Fig. 5.

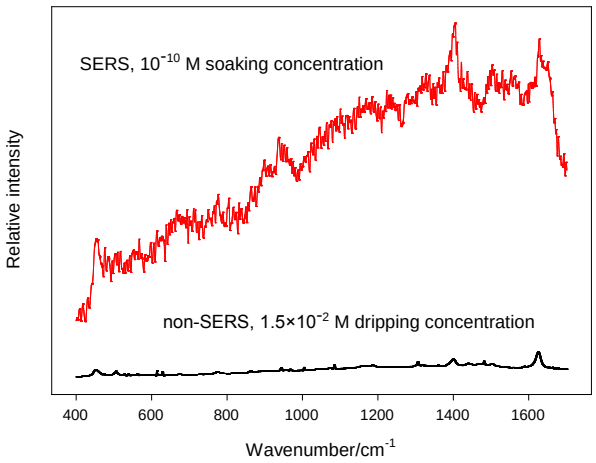


Fig. S3. Comparison of SERS and non-SERS (resonance Raman) spectra of MB. Non-SERS spectrum is averaged from 1000 spectra taken across the drop. Spectra are offset for clarity, but the relative proportion between corresponding band intensities (above spectral background) is maintained.

# Attachment A3

**M. Šubr**, M. Petr, O. Kylián, J. Štěpánek, M. Veis, M. Procházka: Anisotropic Optical Response of Silver Nanorod Arrays: Surface Enhanced Raman Scattering Polarization and Angular Dependences Confronted with Ellipsometric Parameters. Scientific Reports, 2017, vol. 7, 4293.

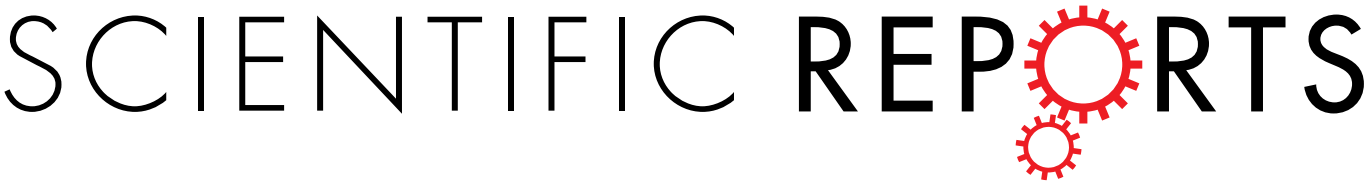

OPEN

Received: 28 December 2016
Accepted: 17 May 2017
Published online: 27 June 2017

# Anisotropic Optical Response of Silver Nanorod Arrays: Surface Enhanced Raman Scattering Polarization and Angular Dependences Confronted with Ellipsometric Parameters

Martin Šubr[1], Martin Petr[2], Ondřej Kylián[2], Josef Štěpánek[1], Martin Veis[1] & Marek Procházka[1]

**Silver nanorod arrays prepared by oblique angle deposition (AgOADs) represent versatile, simple and inexpensive substrates for high sensitivity surface enhanced Raman scattering (SERS) applications. Their anisotropic nature suggests that their optical responses such as the SERS signal, the depolarization ratio, reflectivity and ellipsometric parameters critically depend on the states of polarization, nanorod angular arrangement and specific illumination-observation geometry. SERS polarization and angular dependences of AgOADs were measured using methylene blue (MB) molecule. Our study constitutes, to our knowledge, the most detailed investigation of such characteristics of plasmonic nanostructures to date. This is due to the 90°-scattering geometry used in which two out of three Euler angles determining the nanorod spatial orientation and four polarization combinations can be varied simultaneously. We attributed the anisotropic optical response to anisotropic (pseudo) refractive index caused by different periodicity of our structures in different directions since the plasmonic properties were found rather isotropic. For the first time we demonstrate very good correspondence between SERS intensities and ellipsometric parameters for all measured configurations as compared on the basis of the surface selection rules. Obtained results enable quantitative analysis of MB Raman tensor elements, indicating that the molecules adsorb predominantly with the symmetry axis perpendicular to the surface.**

Plasmonic nanostructures possessing anisotropic morphology are expected to be anisotropic in terms of localized surface plasmon resonances, which implies that their optical responses such as absorbance or the enhancement factor should depend on the incident as well as the scattered polarization. In a typical Raman experiment, measurements employing combinations of different polarizations (or possibly different scattering angles) allow to compute the Raman depolarization ratio[1–3] which gives information on the orientation-averaged components of the Raman tensor of the analyte and consequently on the symmetry of the vibration involved or on the preferential molecular orientation on smooth surfaces ("surface selection rules")[4,5]. However, in SERS, the relationship between the symmetry of the Raman tensor of the analyte and the SERS depolarization ratio is often completely overwhelmed by polarization-dependent coupling of the incident (or scattered) field to a given nanostructure[3,6,7]. This effect is probably most pronounced for dimers[8–11], *i.e.* two closely spaced nanoparticles between which a molecule is embedded. It was found that the field component parallel to the dimer axis exceeds the perpendicular component by up to ~5 orders of magnitude[9,10,12], which was explained by strong interparticle coupling between adjacent nanoparticles (however, in practice, a factor around 5–20 is more likely)[8,13–15]. Thus, denoting $\alpha$ as the

[1]Charles University, Faculty of Mathematics and Physics, Institute of Physics, Ke Karlovu 5, 121 16, Prague, Czech Republic. [2]Charles University, Faculty of Mathematics and Physics, Department of Macromolecular Physics, V Holešovičkách 2, 180 00, Prague, Czech Republic. Correspondence and requests for materials should be addressed to M.Š. (email: subr.Martin@seznam.cz) or M.P. (email: prochaz@karlov.mff.cuni.cz)

angle between the dimer axis and the incident polarization wavevector, the local field should scale as ~cos $\alpha$, the local intensity as ~cos$^2$ $\alpha$ and the SERS enhancement factor as ~cos$^4$ $\alpha$ in the most common $E^4$ approximation, which was verified experimentally many times. A more in-depth approach was derived in the literature[2,3] where a formula linking the Raman and SERS depolarization ratios beyond the $E^4$ approximation was derived. However, the possibility of using SERS to probe the Raman tensor of molecules or their spatial arrangement still remains in question since it is difficult to verify the formula experimentally[2,16,17].

Polarization characteristics of SERS spectra have already been investigated for a wide range of plasmonic platforms possessing anisotropic morphology, besides nanoparticle dimers Ag nanocubes[18], arrays of silver nanoparticle rows[13], gold nanoassemblies[19] etc. Frequently-studied are also arrays of elongated nanoparticles such as nanorods[20–23], nanowires[17,24–26], nanoantennas[27] and nanorattles[28]. Experimental results published so far suggest that the optical response for light polarized parallel/perpendicular to the long axis of the nanoobjects (related to excitation of transverse plasmon modes (TM) or longitudinal plasmon modes (LM), respectively) is indeed different. However, the SERS intensity profile with varying angle/polarization is a function of a wide range of parameters, such as the dimensions of the metallic objects, their aspect ratios and spatial arrangement, material (Ag or Au), the exciting wavelength or orientation of the probe molecules on the surface, which resulted in the last years in some seemingly contradictory results. For example, according to Dluhy and co-workers[21], the ratio of SERS responses in the directions parallel/perpendicular to the nanorods was found to be around 0.8, which was attributed to the lateral arrangement of the nanorod lattice and strong electromagnetic coupling between adjacent metallic nanorods instead of preferential molecular orientation of the probe molecule on the surface. Similar trends were observed for Ag and Au nanowires[17,24–26] where the SERS intensity ratios for light polarized perpendicular/parallel with respect to the nanorod axes was found around 5 and explained by excitation of a new plasmon mode trapped in the interstices between adjacent, parallel wires, similarly to the case of a dimer. However, this only happens if the interwire distance is sufficiently small ($<$10 nm)[24]. By contrast, the response of nanorods or antenna-like structures[22,23,27,28] were all found to be dominated by the longitudinal plasmon modes. Such results were, on the other hand, usually rationalized by intense local electromagnetic fields emanating from points of high curvature, such as nanorod tips ("lightning rod effect").

Since the vast majority of experiments have been performed only in the backscattering geometry, a detailed inspection on the angular dependence of the SERS signal is still missing. However, possible optimization of plasmon-based sensors for maximum signal enhancement relies, among other things, on the right choice of the exciting and/or the scattering angle[29–33]. A modified Greenler model based on classical electrodynamic dipole radiation was used to explain the anisotropic nature of the Ag nanorods, producing maximum SERS intensities at approximately 45° relative to the surface normal as measured in a backscattering geometry[20,34]. This model was treating the surface of the nanorod (length ~868 nm) as planar, neglecting the diffraction effect and calculating near-field intensities using the Fresnel equations. However, nanorods of subwavelength dimensions can be tricky to treat as planar as demonstrated by Benson and co-workers[35] where a strong difference between the optical constants of the nanorod films and those of the constituent materials was found using generalized ellipsometry. Such nanorods exhibited biaxial properties with the complex refractive index different for different orientations of the incident angle with respect to the nanorods. The anisotropy is most significant predominantly at plasmonic resonances[36].

In spite of numerous studies and approaches aiming to elucidate the optimum conditions for SERS signal enhancement and studies dealing with ellipsometry characteristics of plasmonic substrates, a detailed relationship between SERS intensities and ellipsometry parameters is still missing in the literature. In this paper, polarization and angular characteristics of methylene blue (MB) adsorbed on silver nanorod arrays prepared by oblique angle deposition (AgOADs) are investigated. These nanostructures represent uniform, reproducible, large-area SERS-active substrates with high SERS enhancement and exhibit plasmon resonance over a very broad range of wavelengths[37,38]. We demonstrate very good correspondence between SERS intensities, interpreted in terms of the surface selection rules, and ellipsometric parameters for all polarization states and angular arrangements used. Information on the relative magnitudes of the Raman tensor elements is extracted and a possible adsorptive stance of the MB molecules on the nanorod surface is inferred.

## Methods

**Preparation of AgOADs.** Fabrication of AgOADs was performed by low-pressure magnetron sputtering of a silver target onto Si wafer support using the procedure described in more detail in our previous work[39]. The deposition angle was 70° with respect to the surface normal, corresponding to nanocolumns tilted at an angle $\beta$ around 55° as predicted by the Tait's rule[40]. The deposition time was 15 minutes, which led to the mean diameter of individual Ag nanorods of 60 nm, the mean distance between their centers 150 nm and the height of the nanorod array around 300 nm as can be seen in Fig. 1. There, a cross-sectional and top view of AgOADs acquired by scanning electron microscopy (SEM, TESCAN Mira 3, 15 kV accelerating voltage) are presented. All substrates were kept in a vacuum chamber overnight to prevent their contamination from ambient environment.

**SERS Measurements.** SERS spectra were acquired using a custom-built Raman spectroscopic system operating in the 90°-scattering geometry according to the scheme in Fig. 2. This system was equipped with a frequency-doubled Nd:$YVO_4$ laser providing the excitation wavelength 532 nm, an 1800 grooves/mm grating and a liquid-nitrogen-cooled CCD detector (Princeton Instruments). The laser beam was partly focused using an anti-reflective coated lens (BK7 glass, focal length 400 mm) to a spot of ~10 mm$^2$ at an angle $\theta = 45°$. The SERS signal was collected using the Pentacon objective 1.8/50. Since the 532 nm excitation wavelength approaches the slope of the electronic absorption band of MB, obtained SERS spectra should be considered as pre-resonance ones. A holographic notch-plus filter (Kaiser) was placed in front of the entrance slit of the monochromator to remove the Rayleigh line from the scattered light. Light polarization falling on the sample was altered by a

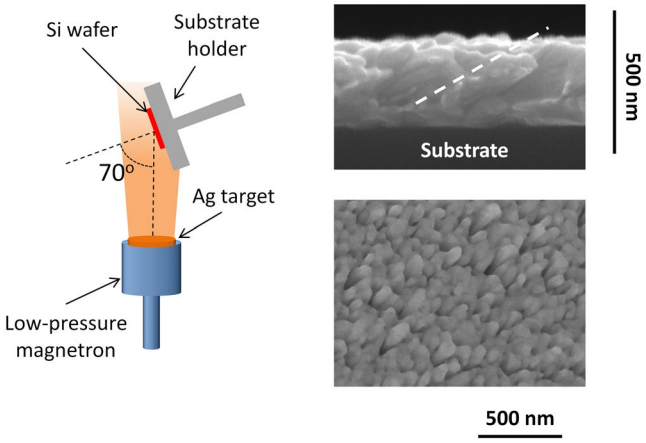


**Figure 1.** Schematic illustration of the oblique angle deposition and SEM images of a Ag nanorod array (cross-sectional and top view). In the cross-sectional view, direction of the nanorod growth is indicated by a dashed line.

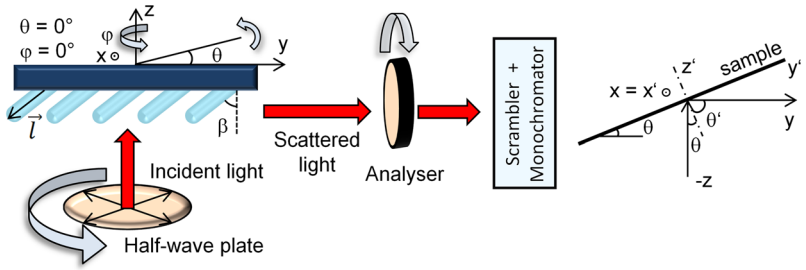


**Figure 2.** Scheme of the experimental geometry.

half-wave plate (Thorlabs) and an analyser was placed between the sample and the monochromator to allow only the light polarized in one plane fall on the detector. In order to overcome different grating responses for different light polarizations, a scrambler was inserted between the analyser and the monochromator. Correct function of the scrambler and other optical components was checked using $CCl_4$ bands (measured in a cuvette) with a well-known polarization-dependent behaviour[1].

For better description of the experiments, we adopted the laboratory-fixed coordinate system with axes lined up as sketched in Fig. 2. We call the direction along the wavevector of the incident beam ("vertical") the $z$ direction, analogously the $y$ direction along the wavevector of the scattered beam and the $x$ direction perpendicular to $y$ and $z$ (perpendicular to the plane of sheet). In this notation, $yz$ determines the scattering plane. SERS spectra of MB were retrieved with varying tilting angle of the substrate $\theta$ (corresponding to rotation about the $x$ axis) and the azimuthal angle $\varphi$ (corresponding to rotation about the $z$ axis). Four angles $\varphi$ were used in our measurements (0°, 90°, 180° and 270°) with the angle $\theta$ bound between 20° and 70° (increment 4°; with exclusion of the interval between ~40°–50° in order to avoid direct reflection from the surface falling on the detector). The unit vector $\vec{l}$ lying in the direction of growing nanorods takes under 4 respective orientations of the angle $\varphi$ in the laboratory-fixed coordinate system the following form:

$$\varphi = 0°: \ \vec{l_1} = (0, \ \sin(\theta - \beta), -\cos(\theta - \beta)), \tag{1}$$

$$\varphi = 90°: \ \vec{l_2} = (\sin\beta, \ \sin\theta\cos\beta, -\cos\theta\cos\beta), \tag{2}$$

$$\varphi = 180°: \ \vec{l_3} = (0, \ \sin(\theta + \beta), -\cos(\theta + \beta)), \tag{3}$$

$$\varphi = 270°: \ \vec{l_4} = (-\sin\beta, \ \sin\theta\cos\beta, -\cos\theta\cos\beta). \tag{4}$$

To better describe changes in SERS intensities with both angles, we further introduce the primed (sample-fixed) Cartesian coordinate system $x'$, $y'$, $z'$ where $x = x'$ and $z'$ specifies at any instant the substrate normal. Since there are two basic possibilities of setting the polarization of the incident beam as well as the scattered beam, a total of 4 different polarization combinations arise, which we will abbreviate as:

$$I(e_x^{exc}, e_x^{det}) = I_{vv}, \quad I(e_y^{exc}, e_x^{det}) = I_{hv}, \quad I(e_x^{exc}, e_z^{det}) = I_{vh}, \quad I(e_y^{exc}, e_z^{det}) = I_{hh}$$

with the first subscript standing for the exciting light and the second subscript standing for the scattered (detected) light; $v$ stands for vertical (with respect to the scattering plane) and $h$ for horizontal polarization. One of the four above-mentioned polarization arrangements together with angles $\theta$ and $\varphi$ unambiguously define the experimental configuration for SERS response measurements.

Before SERS measurements, the AgOADs were cut into ~1 cm × 1 cm pieces, immersed in $1 \times 10^{-6}$ M MB solution (Sigma-Aldrich) for 1 hour, then removed and dried with an air stream. The samples were glued to a supporting glass slide and fixed to a substrate holder capable of rotation about the $x$ axis (see Fig. 2). The exact $y$ position of the holder was set so that the incident beam would intersect the $x$ axis to achieve optimal focus. Moreover, its $z$ position was slightly readjusted after each change in the angle $\theta$ if needed to retain the laser spot at any instant exactly in the objective axis and to obtain the highest SERS signal. To keep the sample heating and photodecomposition at a bare minimum, the laser power was set to 100 mW, which resulted in the power density around 1 W/cm$^2$. To increase precision of our measurements, measurement in each of the 4 polarization arrangements was repeated twice (4 spectra $I_{vv}$, $I_{hv}$, $I_{vh}$, $I_{hh}$ were measured in a given order and immediately after in the exactly opposite order) and the geometric mean of two corresponding spectra was used for further analysis to account for slight signal diminishment with time. All spectra were recorded using 30 s acquisition time (1 s exposition × 30 accumulations) and calibrated against a neon lamp.

**Spectral Ellipsometry Measurements.** AgOADs were characterized using a commercially available spectroscopic ellipsometer Woollam RC2. This ellipsometer employs dual rotating compensator enabling standard ellipsometry, generalized ellipsometry, Mueller-matrix ellipsometry and reflectivity measurements in the energy spectral range from 0.7 to 6 eV. The reflectivity spectra were calibrated with respect to the oxidized silicon wafer. Woollam ellipsometric software CompleteEase was used to analyse the experimental data.

**Theoretical Description of the SERS Response.** According to Moskovits' surface selection rules, an adsorbed molecule may be thought to be illuminated by two beams, a direct beam and the beam reflected from the surface, which superimpose coherently[4,5]. By analogy, the total scattered radiation results from interference between a directly scattered beam and the one experiencing a reflection from the surface. Having adopted the system of coordinates $x'$, $y'$, $z'$ as shown in Fig. 2, the surface selection rules for the 90°-scattering geometry read (see Supplementary Information for more details):

$$\rho_1 = \frac{I_{hv}}{I_{vv}} = \frac{\left|\alpha'_{xy}(1+r'_s)(1-r_p)\cos\theta + \alpha'_{xz}(1+r'_s)(1+r_p)\sin\theta\right|^2}{\left|\alpha'_{xx}(1+r_s)(1+r'_s)\right|^2}, \tag{5}$$

$$\rho_2 = \frac{I_{vh}}{I_{vv}} = \frac{\left|\alpha'_{yx}(1+r_s)(r'_p-1)\cos\theta' + \alpha'_{zx}(1+r_s)(1+r'_p)\sin\theta'\right|^2}{\left|\alpha'_{xx}(1+r_s)(1+r'_s)\right|^2}, \tag{6}$$

$$\rho_3 = \frac{I_{hh}}{I_{vv}} = \frac{\left|\alpha'_{yy}(1-r_p)(r'_p-1)\cos\theta\cos\theta' + \alpha'_{yz}(1+r_p)(r'_p-1)\sin\theta\cos\theta'\right|}{\left|\alpha'_{xx}(1+r_s)(1+r'_s)\right|^2} + \frac{\alpha'_{zy}(1-r_p)(1+r'_p)\sin\theta'\cos\theta + \alpha'_{zz}(1+r_p)(1+r'_p)\sin\theta\sin\theta'\right|^2}{\left|\alpha'_{xx}(1+r_s)(1+r'_s)\right|^2}, \tag{7}$$

where $\theta$ is the incident angle, identical to the inclination angle sketched in Fig. 2, $\theta' = 90° - \theta$ in our geometry, $r_s$ and $r_p$ are the Fresnel reflection coefficients related to the frequency of the incident radiation, their primed counterparts refer to the frequency of the scattered radiation and $\alpha'_{ij}$ refers to orientation-averaged components of the Raman tensor of the adsorbed molecule in the primed frame of reference. In Eqs 5–7, we introduced the depolarization ratios $\rho_1$, $\rho_2$ and $\rho_3$, all of them normalised to $I_{vv}$ since this polarization arrangement provides information only on one term of the Raman tensor. This approach is more convenient because it enables to exclude the insignificant multiplicative constant relating Raman intensities to specific combinations of squares of Raman tensor elements[1]. The Fresnel coefficients were retrieved from optical (pseudo)parameters of the sample as measured by spectral ellipsometry and used for fitting the experimentally measured depolarization ratios on the left side of Eqs 5–7 via relative ratios of respective Raman tensor elements.

## Results and Discussion

**SERS Polarization and Angular Dependences.** Examples of MB SERS spectra obtained under different configurations are given in Fig. 3. A more detailed account of varying SERS intensities with varying angles $\theta$, $\varphi$ and polarization arrangement is given in Fig. 4. These intensities, assumed as height of the 1628-cm$^{-1}$ peak above spectral background, vary up to ~1 order of magnitude when measured under different configurations. Since the surface area is covered with occasional hot-spot sites, we tried to estimate the uncertainty in the SERS intensities. Occurrence frequency of hot-spot sites complies well with the Poisson distribution[38], however, the actual number of hot-spot sites affected by the laser spot is expected to average out on the mm-scale. Supposing 4 hot-spot sites over 2500 μm$^2$ as determined in our previous work, it makes ~16000 hot-spot sites across the

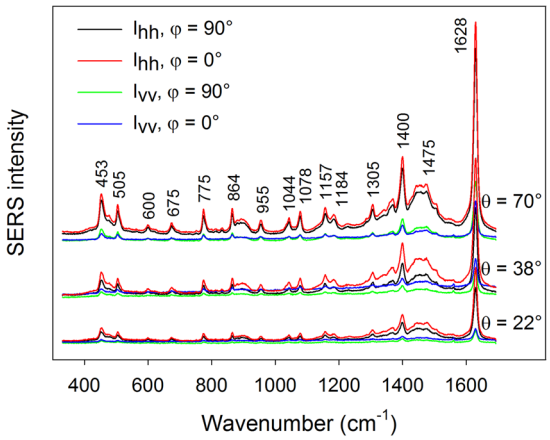


**Figure 3.** Examples of MB SERS spectra obtained under different configurations. Spectra for different angles $\theta$ are offset for clarity.

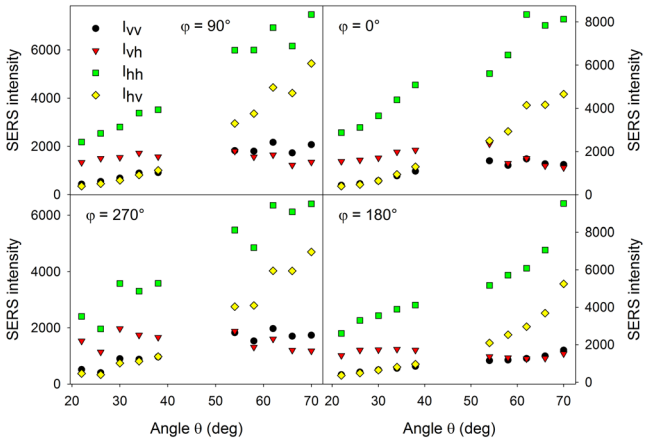


**Figure 4.** Variation in MB SERS intensities with angles $\theta$, $\varphi$ and polarization arrangement for the 1628-cm$^{-1}$ band.

laser spot with the standard deviation of $16000^{1/2} = 126$ and the relative standard deviation of the SERS intensity $<1\%$. Uncertainty in our measurements was therefore caused mainly by slight sample photodecomposition in the course of our measurements, estimated at ~5% (i.e. ~10% uncertainty in the depolarization ratios). In order to obtain a deeper understanding of varying SERS intensities with different experimental configurations and to possibly identify subtle spectral changes such as varying relative intensities across different bands, factor analysis (FA) was employed (see Supplementary Information, Fig. S1). FA results suggest that only the first subspectrum is sufficient so that the original spectral information is retained within the noise level. Therefore, all observable MB bands in Fig. 3 exhibit the same polarization and angular-dependent behaviour. This is in agreement with the fact that most observable bands in the spectrum are of the same symmetry[41]. For the sake of comparison, absorption spectra of MB, polarization-resolved Raman spectra measured in a water solution under non-SERS conditions and corresponding depolarization ratios were also retrieved (see Supplementary Information, Fig. S2).

Obtained polarization and angular characteristics may be attributed to many different factors, such as: (i) different surface plasmon coupling efficiency between the incident/scattered laser field and silver nanorods with changing polarization/wavevector direction ("plasmonic anisotropy"), (ii) interference between the incident/scattered and reflected radiation as dictated by the surface selection rules, (iii) effectiveness of collection of the scattered radiation and different laser spot size with a given angle $\theta$ (scaling approximately as ~cos$\theta$)[42]. In order to better understand intensity changes with varying angle $\theta$, Raman spectrum of a Si wafer was measured as a reference (see Supplementary Information, Fig. S3). Comparison between Raman intensities as measured using a Si wafer and corresponding theoretical values predicted by the surface selection rules revealed that the point (iii) plays a crucial role in the observable characteristics. Therefore, in order to diminish the effect of the geometrical layout, to highlight the difference between different angles $\varphi$ and since we are interested rather in the relative ratios of MB Raman tensor elements instead of their magnitudes, the depolarization ratios $\rho_1$, $\rho_2$ and $\rho_3$ were further analysed instead of intensities. Obtained results for these 3 depolarization ratios with varying angles $\theta$ and $\varphi$ are shown as colour points in Fig. 5.

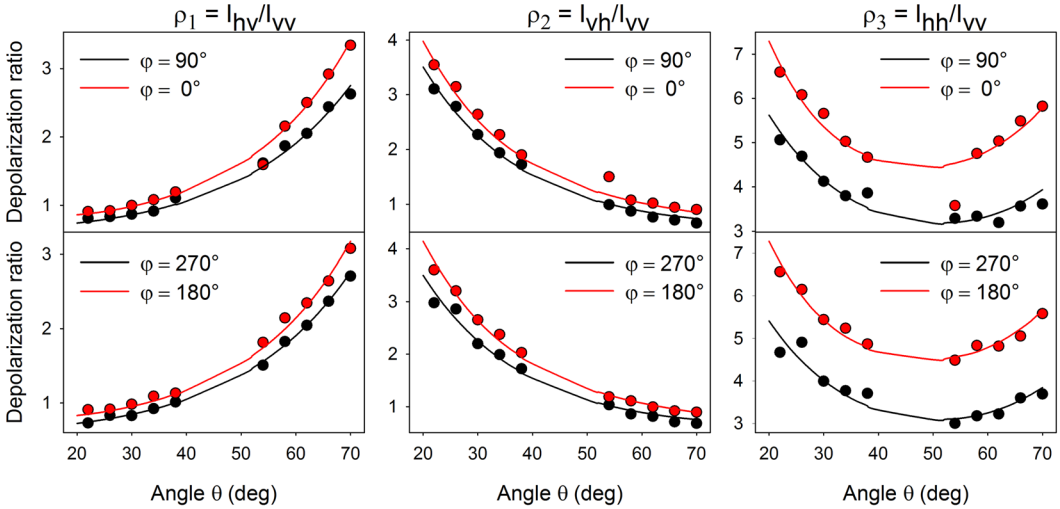


**Figure 5.** Depolarization ratios of the 1628-cm$^{-1}$ MB band for different angular arrangements (colour points) and their fit by the surface selection rules with pseudo-refractive indices obtained from ellipsometry measurements (lines).

In order to determine the effect of the "plasmonic anisotropy", a simple model based on "competition" between the enhancement provided by longitudinal plasmon modes (excited by polarization parallel to the long axis of the nanorods) and by transverse plasmon modes (excited by polarization perpendicular to the long axis of the nanorods) was employed at the first stage. The primary reason for this competition (and consequently alteration of the incident/scattered polarization caused by the nanostructures) is the presence of hot-spots, which may be distributed both at the edges of nanowires and at the gaps among adjacent nanorods. Knowing the long axes orientation under given angular arrangement in the laboratory-fixed coordinate system (determined by Eqs 1–4), intensities obtained in respective configurations are expected to be[6,10,11,17,21]

$$I_j \sim [a_{\|}(\vec{e_1}\cdot\vec{l_j})^2 + a_{\perp}(1-(\vec{e_1}\cdot\vec{l_j})^2)][a'_{\|}(\vec{e_2}\cdot\vec{l_j})^2 + a'_{\perp}(1-(\vec{e_2}\cdot\vec{l_j})^2)], \tag{8}$$

where $\vec{e_1}$ is the unit incident field vector, $\vec{e_2}$ is the unit scattered field vector, $j \in \{1, 2, 3, 4\}$ and $a_{\perp}$ and $a_{\|}$ are factors determining the plasmonic response to polarization parallel/perpendicular to the long axis of the nanorods for the exciting light (unprimed values) and the scattered light (primed values). The first bracket in Eq. 8 accounts for the enhancement of the incident radiation and the latter accounts for the enhancement of the scattered radiation. Since we analyse the depolarization ratios instead of intensities, the final formulas will depend only on the ratio $r = a_{\perp}/a_{\|}$. We tried to fit the obtained depolarization ratios using the Eq. 8, but no value of $r$ consistent for all three depolarization ratios and any of the four angles $\varphi$ and copying the shape of the experimentally measured depolarization ratios (Fig. 5) was found (see section 4 in Supplementary Information for more details). An insightful view on failure of such a fit is provided by the depolarization ratios in Fig. 5, which exhibit marked distinction after rotating the sample by 90° about the $z'$ axis while upon rotating the sample by 180° the depolarization ratios change very little. This was expected for $\varphi = 90°$ and 270° since in both cases the angle between the axes of the nanorods and incident/scattered wavevector is the same. More surprisingly, even the ratios for $\varphi = 0°$ and 180° are similar (but still distinct from $\varphi = 90°$ and 270°), truly indicating that different surface plasmon coupling efficiency of light polarized rather parallel/rather perpendicular to the nanorods has very little effect on the observable characteristics. In other words, although our nanostructures are morphologically anisotropic, the plasmonic properties around the wavelength used (532 nm) are rather isotropic and therefore it can not be the main reason for the anisotropic behaviour we observed in the SERS experiments. It suggests that hot-spots, which are primarily responsible for altering the polarization of the SERS photons, are evenly distributed both at the edges of nanowires and at the gaps among adjacent nanorods. This result indicates that the majority of the difference in the depolarization ratios after rotating the sample by 90° is attributable to different refractive indices along different directions and may be explained within the framework of the surface selection rules.

**Ellipsometry Characteristics.** In order to theoretically describe the SERS response, ellipsometry measurements were performed on the nanostructures with the aim of retrieving their optical constants which enter Eqs 5–7. Ellipsometry measurements of AgOADs were carried out after MB adsorption with varying angles $\theta$ and $\varphi$ in the same range as in the case of SERS measurements. From ellipsometry measurements several basic conclusions were drawn: As expected, the optical (pseudo)parameters of the nanostructured layers are strongly different from the optical constants of the constituent materials. Unlike optical constants of homogeneous materials, optical constants of silver nanorods depend (due to the presence of subwavelength structures) on the incident angle $\theta$ and are strongly influenced by rotating the sample by 90° about the $z'$ axis (see Fig. 6 or the section 5 in Supplementary Information for more details). On the other hand, the optical constants are virtually insensitive

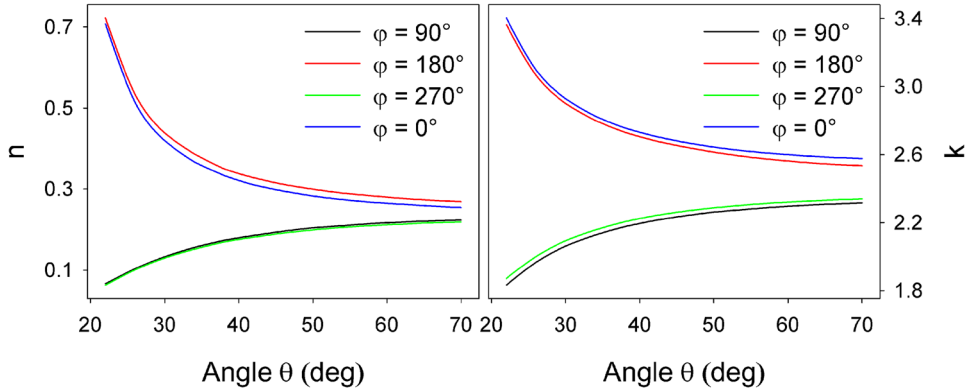


**Figure 6.** Real and imaginary part of pseudo-refractive index $\tilde{n} = n + ik$ of AgOADs and their variation with angles $\theta$ and $\varphi$ as measured by standard ellipsometry. The values pertain to substrates after MB adsorption, $\lambda = 532$ nm. To compare, the refractive index of the bulk silver is $\tilde{n}_{Ag} \sim 0.05 + 3.4i$[43].

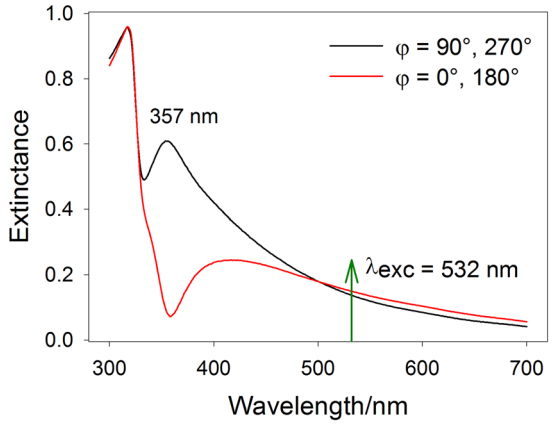


**Figure 7.** Extinctance of the AgOADs for angles $\varphi = 90°$ (virtually identical to $\varphi = 270°$) and $\varphi = 0°$ (virtually identical to $\varphi = 180°$). Extinctance ($E$) was calculated as $E = 1 - R$, where the reflectivity $R$ was obtained based on the values $\tilde{n} = n + ik$ from Fig. 6. The exciting wavelength is marked with a green arrow, the angle $\theta$ was 45°.

to rotating the sample by 180°, which is in full compliance with the SERS results. Comparison between optical (pseudo)refractive indices, obtained in standard ellipsometry measurement mode, and total reflected intensity, measured in the reflection mode (together with Mueller-matrix measurements) revealed that the structures may be treated as non-depolarizing (with only ~5% of the reflected light exhibiting depolarization, see Supplementary Information, Fig. S6) and thus analysed by the standard Jones formalism[35,36]. Moreover, further analysis showed that the off-diagonal elements of the Jones matrix are ~$10^2\times$ smaller than the diagonal elements and thus may also be dismissed. This justifies application of the surface selection rules in the form given by Eqs 5–7 for theoretical analysis of the SERS response.

Another purpose of ellipsometry measurements was that it can reveal more detailed information on the plasmonic properties of the AgOADs. Calculated extinction spectra of our structures for given angles $\varphi$ are depicted in Fig. 7. The extinctance presented there ($E$) was computed as $E = 1 - R$, where the reflectivity $R$ was obtained based on the values contained in Fig. 6. Extinctance features a sharp transverse plasmon peak around 357 nm and a broad band above ~400 nm, attributed to the longitudinal plasmon mode[21,44]. The latter is less intense than expected, probably due to very high reflectivity of the sample above ~400 nm, which may be partly attributed to the supporting Si wafer. We suppose that the distinction between these two profiles may be attributed to different periodicity of our structures in the $x'/y'$ direction. As can be seen in Fig. 1, the nanorods are almost perfectly aligned in the direction perpendicular to the nanorod axes (the deviation of the nanorod axes from the $x'$ axis is negligible from 90°) while the tilting angle of the nanorods $\beta$ exhibits a certain distribution around the value of ~55°. Since the $\varphi = 90°/270°$ configuration is sensitive predominantly to the former case, the corresponding plasmonic resonance is expected to be rather sharp. On the other hand, in the $\varphi = 0°/180°$ arrangement, the angle made between the polarization vector and axes of respective nanorods exhibits a certain distribution which is reflected in the inhomogeneously broadened longitudinal plasmon peak above ~400 nm. Figure 7 indeed confirms that the coupling efficiency for $\lambda = 532$ nm is almost identical for all four angles $\varphi$ and therefore the difference in the SERS responses when rotating the sample about the $z'$ axis is mostly dictated by interference between

| $\varphi$ | 90° | 0° | 270° | 180° | |
|---|---|---|---|---|---|
| $\alpha'_{xx}$ | 1 | 1 | 1 | 1 | |
| $\alpha'_{xy}$ | 0.81 | 0.84 | 0.80 | 0.85 | *a* |
| $\alpha'_{xz}$ | 0.06 | 0.10 | 0.08 | 0.04 | |
| $\alpha'_{yx}$ | 0.80 | 0.89 | 0.81 | 0.91 | *b* |
| $\alpha'_{zx}$ | 0.18 | 0.12 | 0.17 | 0.12 | |
| $\alpha'_{yy}$ | 0.91 | 0.97 | 0.90 | 0.92 | *c* |
| $\alpha'_{zz}$ | 0.01 | 0.05 | 0.01 | 0.06 | |
| $\alpha'_{yz}$ | 0.01 | 0.09 | 0.01 | 0.01 | |
| $\alpha'_{zy}$ | 0.24 | 0.16 | 0.23 | 0.16 | |

**Table 1.** Relative magnitudes of Raman tensor elements (normalised to $\alpha'_{xx}$) of the 1628-cm$^{-1}$ MB band for different angles $\varphi$. The values were obtained by fitting the SERS depolarization ratios using the surface selection rules. Values revealed by the fit of $\rho_1$ are labelled as *a*, by $\rho_2$ as *b* and by $\rho_3$ as *c*.

the incident/scattered and reflected radiation. "Higher plasmonic anisotropy" is more likely to arise at shorter wavelengths as can be seen in Fig. 7 where the two curves differ more obviously, although more extensive research is required to confirm this. We have to note, however, that the relationship between the near-field (Raman-enhancing) properties and the far-field properties (such as extinctance of reflectance) is not straighforward in SERS and in the case of anisotropic SERS substrates no correlation between these two phenomena was found[21,45].

**Determination of Molecular Orientation on the Surface.** Knowing the optical (pseudo)parameters of the sample, it is possible to use Eqs 5–7 to fit the measured SERS depolarization ratios (colour points in Fig. 5). Unlike the former model based on different surface plasmon coupling efficiency for different light polarization, the model using optical (pseudo)parameters fits the experimentally measured depolarization ratios very well. Moreover, these fits provide information on the relative ratios of Raman tensor elements of the probe molecule and are represented by solid lines in Fig. 5. The obtained results are summarized in Table 1.

Table 1 clearly demonstrates basically comparable values of $\alpha'_{xx}$, $\alpha'_{yy}$, $\alpha'_{xy}$ and $\alpha'_{yx}$ and considerably lower values of $\alpha'_{zz}$, $\alpha'_{xz}$, $\alpha'_{zx}$, $\alpha'_{yz}$ and $\alpha'_{zy}$. MB belongs to the $C_2$ point group symmetry with the vibrational representation $\Gamma^{3N-6} = 54\,A + 54\,B$[41]. The strongest MB band at 1628 cm$^{-1}$ belongs to the *A* species which transform as $x'^2$, $y'^2$, $z'^2$ and $x'y'$ ($z'$ being the axis of symmetry of the molecule)[41]. Moreover, almost all the other observable bands in the SERS spectrum exhibit very similar intensity profile and thus very similar relative magnitudes of Raman tensor elements as already discussed using FA. This conclusion is also justified by the fact that the pseudo-refractive indices change very little within the Raman shift wavelengths. Thus, for the MB orientation on the surface with the symmetry axis along the $z'$ direction (the plane of the fused phenyl rings perpendicular to the substrate), the $\alpha'_{xx}$, $\alpha'_{yy}$, $\alpha'_{xy}$ and $\alpha'_{yx}$ Raman tensor elements are expected to be enhanced most while the $\alpha'_{xz}$, $\alpha'_{zx}$, $\alpha'_{yz}$ and $\alpha'_{zy}$ elements should tend to zero. Therefore, we conclude that the orientation of the MB molecule on the surface is predominantly edge-on and possibly a small proportion of the molecules may take also different orientations (since the $\alpha'_{xz}$, $\alpha'_{zx}$ $\alpha'_{yz}$ and $\alpha'_{zy}$ elements are not exactly zero but still much lower than $\alpha'_{xy}$ and $\alpha'_{yx}$). This is in agreement with the literature since at higher concentrations the MB is supposed to take rather edge-on adsorptive stance on the surface with the face-on orientation preferable at lower concentrations[41,46]. The concentration used in our experiments ($10^{-6}$ M) is expected to be slightly above the complete surface coverage[41,47]. We have to note, though, that the group theory (together with experimentally measured depolarization ratios) provides information only on the orientation of the molecular symmetry axis with respect to the surface, but says nothing about the distribution of the planes of the fused phenyl rings of the molecules with respect to $x'$ or $y'$. Thus, the non-diagonal elements of the MB Raman tensor should be viewed as orientation-averaged for an ensemble of MB molecules possessing predominantly edge-on adsorptive stance on the surface.

The similarity between the MB Raman tensor elements for four angles $\varphi$ is rather peculiar since it indicates that the molecules do not follow the curved orientation of the nanostructured surface. It suggests that the molecules actually do not cover the lateral surface of the nanowires and probably aggregate in the vicinity of the nanorod tips. This may be caused by rather densely-packed nanocolumns, low porosity of the AgOADs and surface tension of the solution[31], but obviously more in-depth experiments are required to confirm this. We propose that this could be further validated by testing different solvents, different analytes and their concentration-dependence or by preparing different nanocolumn height, porosity or constituent materials. Some of these aspects will be addressed in our further research.

Results of our fits also reveal that $\alpha'_{xy} \sim \alpha'_{yx}, \alpha'_{xx} \sim \alpha'_{yy}$ and the remaining components are very small for all angles $\varphi$. This follows directly from tensor rotational transformation formulas and confirms the success of our fitting procedures since different tensor components were obtained from different fits. For example, when rotating the system by 90° about the $z'$ axis, the $\alpha'_{xx}$ component becomes $\alpha'_{yy}$, the $\alpha'_{xy}$ component becomes $\alpha'_{yx}$, the $\alpha'_{xz}$ component becomes $\alpha'_{yz}$ and the $\alpha'_{zx}$ component becomes $\alpha'_{zy}$ and vice versa (for details see section 7 in Supplementary Information). Table 1 demonstrates the agreement between MB Raman tensor elements even across different angles $\varphi$, although obviously not all elements are obtained with the same accuracy which causes slight discrepancies. Unfortunately, that tensor components containing $z'$ in at least one of its indices suffer from

higher uncertainty, especially those obtained from the fit of $\rho_3$, which presents rather an ill-posed problem since it aims to fit four values of the Raman tensor simultaneously. In order to obtain a better criterion for reliability of our fits, we further computed the usual Raman tensor invariants (see the section 7 in Supplementary Information for more details), the corresponding depolarization ratio of MB adsorbed on AgOADs and compared these values with the values retrieved from MB Raman spectra measured in a solution. Raman tensor elements in Table 1 give the usual Raman tensor invariants for each of the angles $\varphi$ as follows: $a^2 = 0.43 \pm 0.02$, $\gamma^2 = 3.1 \pm 0.1$ and $\delta^2 = 0.03 \pm 0.01$. The corresponding depolarization ratio is $\rho = 0.29 \pm 0.01$. To compare, the depolarization ratio of MB as measured in a water solution (see the section 2 in Supplementary Information for more details) is $\rho_M = 0.21 \pm 0.01$ for all symmetric vibrations involved. We suppose that the difference may be attributable either to the presence of hot-spot sites or to formation of dimers/trimers at the surface which could feature a different depolarization ratio with respect to the monomers that are analysed in liquid (or possibly to a combination of the two factors). Hot-spot sites are sparsely distributed over the surface as demonstrated by spectral mapping of the surface in our previous work[38]. These sites may occur either at the edges of nanowires or at the gap among nanoparticles (with completely different polarization characteristics), but since no significant difference between efficiency of excitation of longitudinal/transverse plasmon modes was observed, we hypothesize that the hot-spot occurrences in these two locations are approximately equal. On the other hand, for a collection of randomly oriented hot-spots such as colloids, the measured depolarization ratio of all modes under SERS conditions will be $\rho_{SERS} = 1/3$, virtually independent of the symmetry of a given Raman mode[7, 17]. When measuring in a macro-mode (with the laser spot in the order of several mm$^2$), a large number of hot-spots is affected, which may still cover rather negligible proportion of the illuminated area but have a non-negligible share of the total intensity, difficult to estimate precisely. Thus, for SERS-active systems where only a certain proportion of the signal (say 50%) comes from randomly-oriented hot-spots, one can expect that the depolarization ratio of the vibrations (for which the depolarization ratio under non-SERS conditions is ~0.21) will be shifted towards 1/3. Supposedly the depolarization ratio as computed using values in Table 1 is bound between these two extremes ($\rho_M < \rho < \rho_{SERS}$).

In summary, a detailed analysis of the SERS polarization and angular dependences was performed on MB adsorbed on silver nanorod arrays prepared by oblique angle deposition (AgOADs). The main advantage of our approach is employment of the 90°-scattering geometry in which two out of three Euler angles determining the nanorod spatial orientation and four polarization combinations can be varied simultaneously. This enabled us to carry out the most in-depth investigation of polarization- and angular-resolved characteristics of AgOADs to date, as far as we know. Ellipsometry measurements were carried out on the nanostructures to characterize their plasmonic properties and to retrieve their optical constants which enter the surface selection rules. A detailed relationship between the SERS intensities and corresponding ellipsometric parameters was elucidated, which was still missing in the literature. Both the SERS intensities as well as ellipsometric parameters were found to exhibit strong dependence on rotating the sample by 90°, although being fairly insensitive to flipping the sample by 180°. We suppose that this distinction may be attributed to slightly different periodicity of our structures in different directions instead of different surface plasmon coupling efficiency for light polarized parallel/perpendicular to the nanorod arrays as reported in numerous studies where a comparable approach was employed for other SERS-active systems. The theoretical description of the SERS response on the basis of the surface selection rules was therefore well applicable. Fit of the obtained depolarization ratios against the optical (pseudo)parameters of the sample obtained by means of spectral ellipsometry provided relative magnitudes of MB Raman tensor elements. These results enable to gain insight into the adsorptive stance of the molecule on the surface, indicating that the MB adsorbs predominantly with the symmetry axis perpendicular to the surface. Our experimental findings contribute to better theoretical understanding of the SERS enhancement mechanism and may be useful for optimization of plasmon-based sensors for maximum signal enhancement.

## References


1. Long, D. A. *The Raman Effect: A Unified Treatment of the Theory of Raman Scattering by Molecules* (John Wiley & Sons Ltd, 2002).
2. Gucciardi, P. G., Chapelle, M. L. d. l. & Lidgi-Guigui, N. *Handbook of Enhanced Spectroscopy* (Pan Stanford Publishing Pte. Ltd, 2016).
3. Foti, A. *et al.* On the SERS depolarization ratio. *Nanospectroscopy* **1**, 26–62 (2015).
4. Moskovits, M. Surface-Enhanced Spectroscopy. *Rev. Mod. Phys.* **57**, 783–826 (1985).
5. Moskovits, M. Surface Selection-Rules. *J. Chem. Phys.* **77**, 4408–4416 (1982).
6. Etchegoin, P. G., Galloway, C. & Le Ru, E. C. Polarization-dependent effects in surface-enhanced Raman scattering (SERS). *Phys. Chem. Chem. Phys.* **8**, 2624–2628 (2006).
7. Le Ru, E. C., Meyer, M., Blackie, E. & Etchegoin, P. G. Advanced aspects of electromagnetic SERS enhancement factors at a hot spot. *J. Raman. Spectrosc.* **39**, 1127–1134 (2008).
8. Xu, H. & Käll, M. Polarization-Dependent Surface-Enhanced Raman Spectroscopy of Isolated Silver Nanoaggregates. *ChemPhysChem* **4**, 1001–1005 (2003).
9. Moskovits, M. Surface-enhanced Raman spectroscopy: a brief perspective. *J. Raman Spectrosc.* **36**, 485–496 (2005).
10. Xu, H., Aizpurua, J., Käll, M. & Apell, P. Electromagnetic contributions to single-molecule sensitivity in surface-enhanced Raman scattering. *Phys. Rev. E* **62**, 4318–4324 (2000).
11. Shegai, T. *et al.* Managing light polarization via plasmon-molecule interactions within an asymmetric metal nanoparticle trimer. *Proc. Natl. Acad. Sci. USA* **105**, 16448–16453 (2008).
12. Jiang, J., Bosnick, K., Maillard, M. & Brus, L. Single Molecule Raman Spectroscopy at the Junctions of Large Ag Nanocrystals. *J. Phys. Chem. B* **107**, 9964–9972 (2003).
13. Luo, W. *et al.* Polarization-Dependent Surface Enhanced Raman Scattering from Silver 1D Nanoparticle Arrays. *J. Phys. Chem. C* **112**, 11609–11613 (2008).
14. Wei, H. *et al.* Polarization Dependence of Surface-Enhanced Raman Scattering in Gold Nanoparticle-Nanowire Systems. *Nano Lett.* **8**, 2497–2502 (2008).
15. Theiss, J., Pavaskar, P., Echternach, P. M., Muller, R. E. & Cronin, S. B. Plasmonic Nanoparticle Arrays with Nanometer Separation for High-Performance SERS Substrates. *Nano Lett.* **10**, 2749–2754 (2010).
16. Le Ru, E. C. *et al.* Experimental Verification of the SERS Electromagnetic Model beyond the $|E|^4$ Approximation: Polarization Effects. *J. Phys. Chem. C* **112**, 8117–8121 (2008).

17. Fazio, B. *et al*. Re-radiation Enhancement in Polarized Surface-Enhanced Resonant Raman Scattering of Randomly Oriented Molecules on Self-Organized Gold Nanowires. *ACS Nano* **5**, 5945–5956 (2011).
18. McLellan, J. M., Li, Z.-Y., Siekkinen, A. R. & Xia, Y. The SERS Activity of a Supported Ag Nanocube Strongly Depends on Its Orientation Relative to Laser Polarization. *Nano Lett.* **7**, 1013–1017 (2007).
19. Hossain, M. K., Huang, G. G., Tanaka, Y., Kaneko, T. & Ozaki, Y. Anisotropic gold nanoassembly: a study on polarization-dependent and polarization-selective surface-enhanced Raman scattering. *Phys. Chem. Chem. Phys.* **17**, 4268–4276 (2015).
20. Liu, Y. J., Fan, J. G., Zhao, Y.-P., Shanmukh, S. & Dluhy, R. A. Angle dependent surface enhanced Raman scattering obtained from a Ag nanorod array substrate. *Appl. Phys. Lett.* **89**, 173134 (2006).
21. Zhao, Y.-P., Chaney, S. B., Shanmukh, S. & Dluhy, R. A. Polarized Surface Enhanced Raman and Absorbance Spectra of Aligned Silver Nanorod Arrays. *J. Phys. Chem. B* **110**, 3153–3157 (2006).
22. Suzuki, M. *et al*. In-line aligned and bottom-up Ag nanorods for surface-enhanced Raman spectroscopy. *Appl. Phys. Lett.* **88**, 203121 (2006).
23. Ming, T. *et al*. Strong Polarization Dependence of Plasmon-Enhanced Fluorescence on Single Gold Nanorods. *Nano Lett.* **9**, 3896–3903 (2009).
24. Tao, A. R. & Yang, P. Polarized Surface-Enhanced Raman Spectroscopy on Coupled Metallic Nanowires. *J. Phys. Chem. B* **109**, 15687–15690 (2005).
25. Jeong, D. H., Zhang, Y. X. & Moskovits, M. Polarized Surface Enhanced Raman Scattering from Aligned Silver Nanowire Rafts. *J. Phys. Chem. B* **108**, 12724–12728 (2004).
26. Zhou, W., Hu, A., Bai, S., Ma, Y. & Bridges, D. Anisotropic optical properties of large-scale aligned silver nanowire films via controlled coffee ring effects. *RSC Adv* **5**, 39103–39109 (2015).
27. Chen, L. *et al*. Polarization-dependent SERS effects of laser-generated sub-100 nm antenna structures. *Nanotechnology* **25**, 265302 (2014).
28. Liu, K.-K. *et al*. Polarization-Dependent Surface-Enhanced Raman Scattering Activity of Anisotropic Plasmonic Nanorattles. *J. Phys. Chem. C* **120**, 16899–16906 (2016).
29. Hu, Q., Tay, L.-L., Noestheden, M. & Pezacki, J. P. Mammalian Cell Surface Imaging with Nitrile-Functionalized Nanoprobes: Biophysical Characterization of Aggregation and Polarization Anisotropy in SERS Imaging. *J. Am. Chem. Soc.* **129**, 14–15 (2007).
30. Stranahan, S. M., Titus, E. J. & Willets, K. A. SERS Orientational Imaging of Silver Nanoparticle Dimers. *J. Phys. Chem. Lett.* **2**, 2711–2715 (2011).
31. Nagai, Y., Yamaguchi, T. & Kajikawa, K. Angular-Resolved Polarized Surface Enhanced Raman Spectroscopy. *J. Phys. Chem. C* **116**, 9716–9723 (2012).
32. Shegai, T., Brian, B., Miljković, V. D. & Käll, M. Angular Distribution of Surface-Enhanced Raman Scattering from Individual Au Nanoparticle Aggregates. *ACS Nano* **5**, 2036–2041 (2011).
33. Baumberg, J. J. *et al*. Angle-Resolved Surface-Enhanced Raman Scattering on Metallic Nanostructured Plasmonic Crystals. *Nano Lett.* **5**, 2262–2267 (2005).
34. Liu, Y.-J. & Zhao, Y.-P. Simple model for surface-enhanced Raman scattering from tilted silver nanorod array substrates. *Phys. Rev. B* **78**, 075436 (2008).
35. Benson, M., Shah, P., Marciniak, M., Sarangan, A. & Urbas, A. Optical Characterization of Silver Nanorod Thin Films Grown Using Oblique Angle Deposition. *J. Nanomater*. 694982 (2014).
36. Oates, T. W. H., Ranjan, M., Facsko, S. & Arwin, H. Highly anisotropic effective dielectric functions of silver nanoparticle arrays. *Opt. Express* **19**, 2014–2028 (2011).
37. Negri, P. & Dluhy, R. A. Ag Nanorod Based Surface-Enhanced Raman Spectroscopy Applied to Bioanalytical Sensing. *J. Biophotonics* **6**, 20–35 (2013).
38. Šubr, M. *et al*. Ag Nanorod Arrays for SERS: Aspects of Spectral Reproducibility, Surface Contamination, and Spectral Sensitivity. *J. Nanomater*. 729231 (2015).
39. Solař, P. *et al*. Glancing Angle Deposition of Silver Promoted by Pre-Deposited Nanoparticles. *Plasma Process. Polym.* **12**, 486–492 (2015).
40. Tait, R. N., Smy, T. & Brett, M. J. Modeling and characterization of columnar growth in evaporated films. *Thin Solid Films* **226**, 196–201 (1993).
41. Roy, S. D., Ghosh, M. & Chowdhury, J. Adsorptive parameters and influence of hot geometries on the SER(R) S spectra of methylene blue molecules adsorbed on gold nanocolloidal particles. *J. Raman Spectrosc.* **46**, 451–461 (2015).
42. Le Ru, E. C. *et al*. Experimental demonstration of surface selection rules for SERS on flat metallic surfaces. *Chem. Commun.* **47**, 3903–3905 (2011).
43. Johnson, P. B. & Christy, R. W. Optical Constants of the Noble Metals. *Phys. Rev. B* **6**, 4370–4379 (1972).
44. Zhao, Y.-P., Chaney, S. B. & Zhang, Z.-Y. Absorbance spectra of aligned Ag nanorod arrays prepared by oblique angle deposition. *J. Appl. Phys*. **100** (2006).
45. Kleinman, S. L. *et al*. Structure Enhancement Factor Relationships in Single Gold Nanoantennas by Surface-Enhanced Raman Excitation Spectroscopy. *J. Am. Chem. Soc.* **135**, 301–308 (2013).
46. Zhong, L., Hu, Y. J., Xing, D. & Gu, H. M. Adsorption of Methylene Blue on Colloidal Silver-A Surface-Enhanced Raman Spectroscopy Study Combined with Density Functional Theory Calculations. *Spectrosc. Spectr. Anal.* **30**, 90–94 (2010).
47. Nuntawong, N. *et al*. Surface-enhanced Raman scattering substrate of silver nanoparticles depositing on AAO template fabricated by magnetron sputtering. *Vacuum* **84**, 1415–1418 (2010).


## Acknowledgements

The study was supported by the Charles University, project GA UK No. 572216, and the Czech Science Foundation (P205/12/G118). The authors thank Vlastimil Peksa from Institute of Physics, Charles University, for help with Raman measurements.

## Author Contributions

M.Š. carried out both SERS and ellipsometry measurements under the supervision of M. Procházka (SERS; J.Š. was the consultant) and M.V. (ellipsometry), analysed the results and wrote the manuscript. M. Petr fabricated the SERS substrates under the supervision of O.K. All authors have given permission to the final version of the manuscript.

## Additional Information

**Supplementary information** accompanies this paper at doi:10.1038/s41598-017-04565-0

**Competing Interests:** The authors declare that they have no competing interests.

**Publisher's note:** Springer Nature remains neutral with regard to jurisdictional claims in published maps and institutional affiliations.

Supplementary Information

# Anisotropic Optical Response of Silver Nanorod Arrays: Surface Enhanced Raman Scattering Polarization and Angular Dependences Confronted with Ellipsometric Parameters

Martin Šubr,[*†] Martin Petr,[§] Ondřej Kylián,[§] Josef Štěpánek,[†] Martin Veis,[†] and Marek Procházka[*†]

† Charles University, Faculty of Mathematics and Physics, Institute of Physics, Ke Karlovu 5, 121 16 Prague, Czech Republic

§ Charles University, Faculty of Mathematics and Physics, Department of Macromolecular Physics, V Holešovičkách 2, 180 00 Prague, Czech Republic

Corresponding authors:

* M. Šubr: e-mail subr.Martin@seznam.cz

* M. Procházka: e-mail prochaz@karlov.mff.cuni.cz

## 1. Factor Analysis

In order to obtain a deeper understanding of varying SERS intensities with different experimental configurations and to possibly identify subtle spectral changes such as varying relative intensities across different bands, factor analysis (FA) was employed. In the singular value decomposition (SVD) algorithm, a set or $N$ background-corrected MB SERS spectra $Y_i(\nu)$ ($i = 1$ corresponding to $\vartheta = 22°$,… $i = N$ corresponding to $\vartheta = 70°$; angle $\varphi$ playing the role of a parameter) are projected into orthonormal set of functions $S_i(\nu)$ (referred to as subspectra) as

$$Y_i(\nu) = \sum_j W_j V_{ij} S_j(\nu), \quad \text{(S1)}$$

where $W_j$ ($j = 1,2, \ldots N$) is the *j*th singular value, representing relative statistical weight of the *j*th subspectrum, and $V_{ij}$ is a unitary matrix determining relative spectral contribution of $S_j(\nu)$ in $Y_i(\nu)$.[1] FA results for spectra measured for $\varphi = 0°$ are given in Fig. S1 and suggest that only the first subspectrum is sufficient so that the original spectral information is retained within the noise level (factor dimension is 1). In other words, eq S1 simplifies to

$$Y_i(\nu) = W_1 V_{i1} S_1(\nu), \quad \text{(S2)}$$

because higher $V_{ij}$ coefficients ($j \geq 2$) exhibit rather random behaviour and were not reproducible in our measurements. Corresponding subspectra $S_j(\nu)$, $j \geq 2$, describe only fluctuating spectral background, extremely sensitive to slight changes in baseline subtraction, and even higher subspectra only the white noise. This is in agreement with the fact that all observable bands in the spectrum are of the same symmetry.[2]

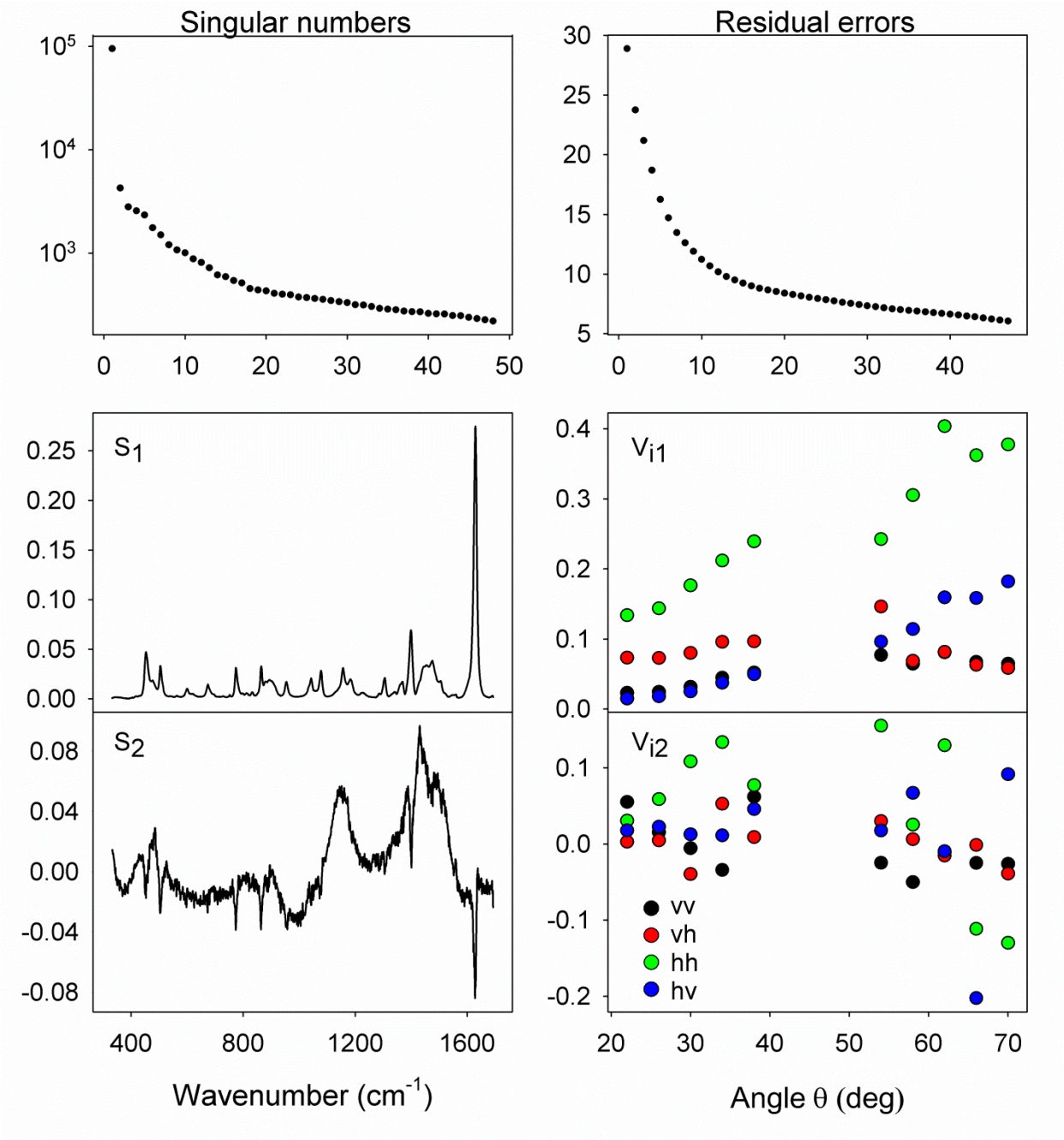


Figure S1. FA results of baseline-corrected MB SERS spectra measured at an angle $\varphi = 0°$. The subspectrum $S_1$ represents the basic spectral profile and the profile of the $V_{i1}$ coefficients very well fits the intensity profile of the 1628-cm$^{-1}$ MB band given in Fig. 4. Different polarization arrangements are distinguished by different colours. Shape of the subspectrum $S_2$ and profile of the $V_{i2}$ coefficients were not reproducible in our measurements and were both extremely sensitive to slight changes in background subtraction.

## 2. Raman Spectra of Methylene Blue

For the sake of comparison, polarization-resolved Raman spectra of MB measured in a water solution under non-SERS conditions were retrieved. These spectra are depicted in Fig. S2. In the case of randomly oriented molecules and the 90°-scattering geometry, the ratio of cross-polarized (in principle, any of $I_{hv}$, $I_{vh}$ or $I_{hh}$ polarization arrangements) to parallel-polarized ($I_{vv}$ arrangement) Raman intensities defines the molecular depolarization ratio $\rho_M$. The depolarization ratios of the most intense A-type bands were computed to be $\rho_M = 0.21 \pm 0.01$.

Absorption spectra of MB in the same concentration were also retrieved. MB absorption spectra feature a maximum at 665 nm and a shoulder around 618 nm, both of them being characteristic of a monomeric form[3].

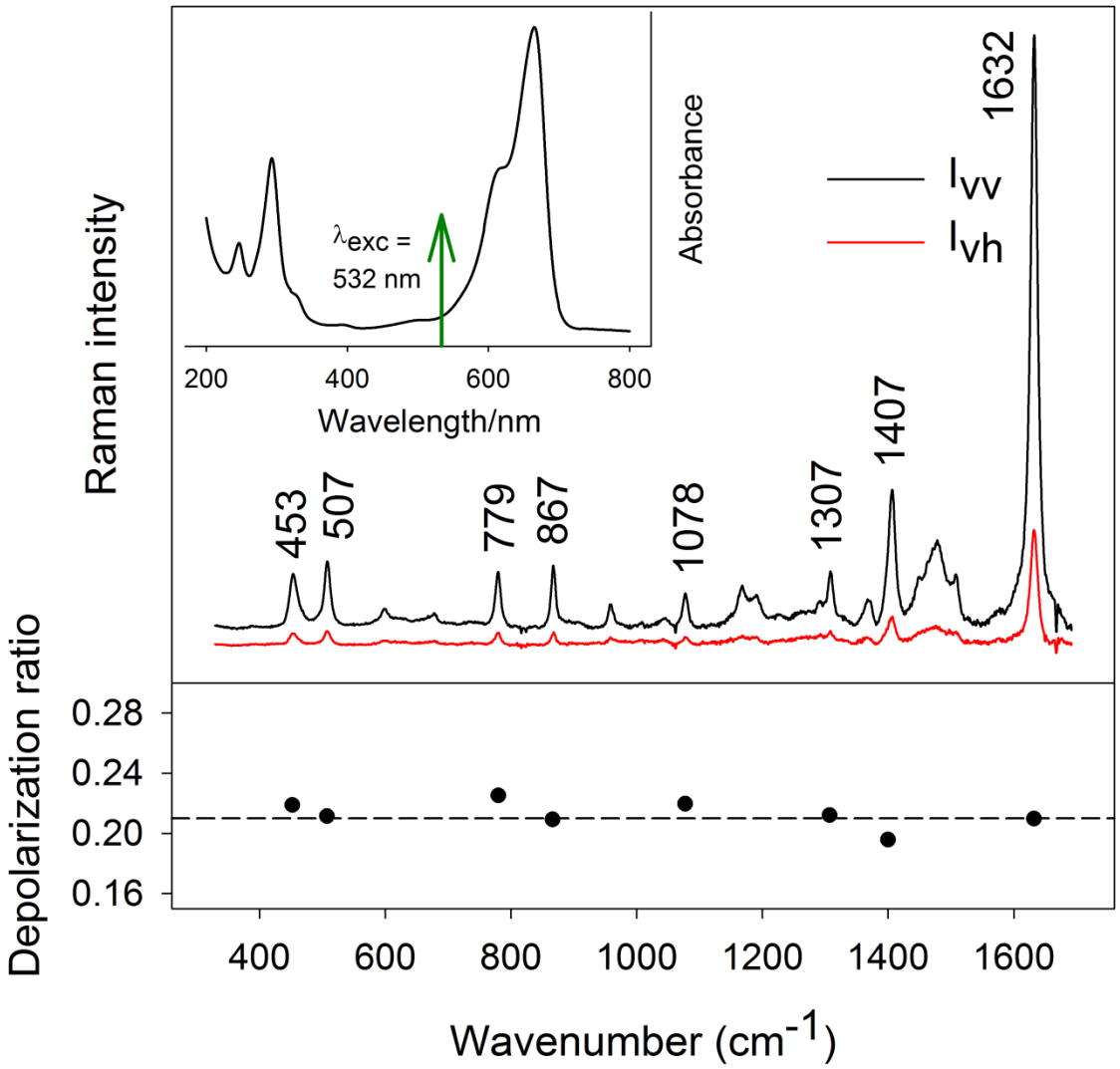

Figure S2. Pre-resonance Raman spectra of MB measured under non-SERS conditions in the $vv$ (parallel-polarized) and $vh$ (cross-polarized) arrangement. Presented spectra are after fluorescence background subtraction and offset for clarity. The MB concentration was $10^{-5}$ M, Inset: Absorption spectra of MB with the exciting wavelength marked with a green arrow. The depolarization ratios of the most intense A-type bands are presented below and take the value $\rho_M = 0.21 \pm 0.01$ as indicated by the dashed line.

## 3. Details of Raman Experiments

Since the obtained polarization and angular characteristics depend on a wide range of factors, we first investigated the effect of the geometrical layout, *i.e.* effectiveness of collection of the scattered radiation and the effect of the laser spot size with a given angle $\theta$. Fig. S3 demonstrates the difference between experimentally measured Raman intensities of a Si wafer and corresponding theoretical values predicted by the surface selection rules, both with the changing inclination angle $\theta$ measured in the $vv$ arrangement. For this purpose, optical pseudo-refractive index of a Si wafer $\tilde{n} = n + ik$ was obtained using spectral ellipsometry as $n = 4.11$, $k = 0.35$ (for $\lambda = 532$ nm) and $n' = 4.05$, $k' = 0.33$ for $\lambda' = 547$ nm (corresponding to the wavelength of the scattered radiation of the 520-cm$^{-1}$ silicon mode). The $vv$ arrangement was chosen due to the fact that corresponding intensities depend only on one term of the Raman tensor. Comparison between experimental and theoretical values implies that their ratio can be well fitted by an expected $\cos\theta$ function[4] and suggests that very similar effect (variation in the laser spot size with the angle $\theta$) will play a dominant role also in the case of AgOADs. To eliminate this effect, SERS depolarization ratios were further analyzed instead of intensities (see the main text).

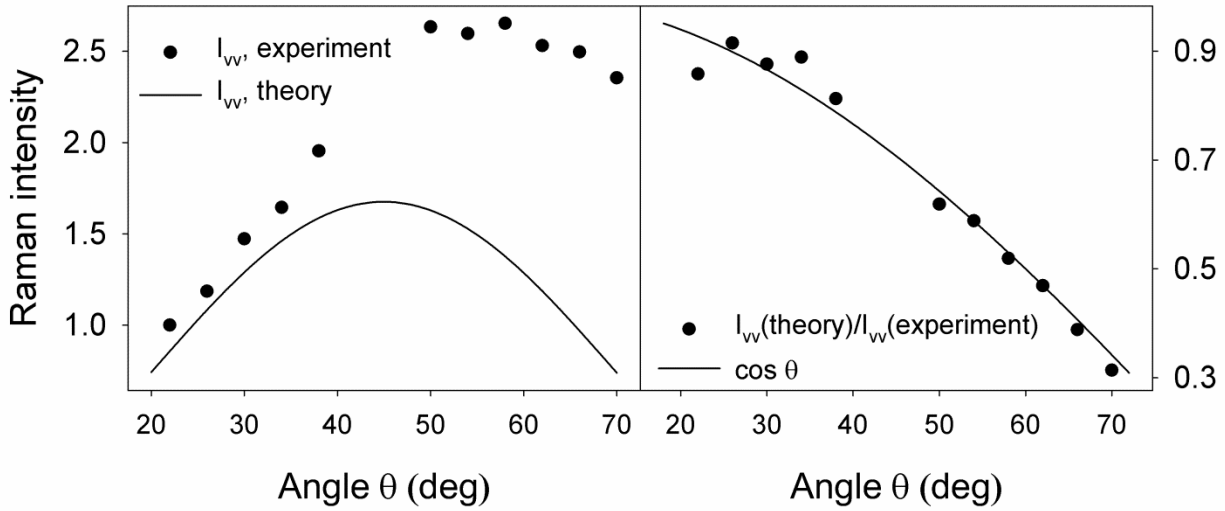

Figure S3. Left: Comparison between Raman intensities of a Si wafer (black points) and (normalised) theoretical values predicted by the surface selection rules (line) with the varying inclination angle $\theta$ as measured in the $vv$ arrangement. Right: The ratios of theoretical/experimental values from the left graph and their fit by a $\cos\theta$ function.

## 4. Modelling of the Plasmonic Anisotropy

At the first stage of the analysis of the optical response of the AgOADs, a simple model based on "competition" between the enhancement provided by longitudinal plasmon modes and by transverse plasmon modes was employed. This model makes use of the fact that the plasmonic response of light polarized parallel/perpendicular to the nanorod axis should be different. Since the projection of incident/scattered polarization to the direction of growing nanorods is given by the scalar product between these two vectors, the intensities obtained in respective cases (varying angles θ and φ) are expected to be proportional to the right side of eq 8 (for simplicity, we will now suppose the factors $a_{||}$ and $a_{\perp}$ the same both for the exciting wavelength and the Raman-shifted wavelength). Since we analyse the depolarization ratios instead of intensities, the final formulas are expected to depend only on the ratio $r = a_{\perp}/a_{||}$. Fig. S4 clearly demonstrates that no value of r consistent for all experimental configurations can be found. The reasons are as follows: (i) any possible value of $r$ (irrespective whether $r < 1$ or $r > 1$) is able to consistently copy the shape of all 3 experimentally measured depolarization ratios, (ii) for $r > 1$, the depolarization ratios for $\varphi = 0°$ and $\varphi = 180°$ lie below the depolarization ratios corresponding to $\varphi = 90°$ and $\varphi = 270°$, while from experiment the depolarization ratio curves for $\varphi = 0°$ and $\varphi = 180°$ are above those for $\varphi = 90°$ and $\varphi = 270°$, (iii) even for $r < 1$, the two depolarization ratio curves especially for $\varphi = 0°$ and $\varphi = 180°$ are (supposedly) distinct (the distinction being the more pronounced the lower is $r$), although in experiment they are almost identical, (iv) the increasing/decreasing trend in the depolarization ratio curves for $\rho_1/\rho_2$ is not compatible with the model supposing plasmonic anisotropy of our structures. Nor is the U-shaped trend in the case of experimentally measured $\rho_3$ since the model supposing plasmonic anisotropy predicts very little dependence on the angle $\theta$ in this case. Most importantly, the model based on plasmonic anisotropy predicts the existence of three different trends for the experimentally measured depolarization ratio curves (since the angles $\varphi = 90°$ and $\varphi = 270°$ provide the same response in the plasmonic anisotropy model) while in reality only two distinct trends were measured (see Fig. 5). In conclusion, we suggest that although our nanostructures are morphologically anisotropic, the plasmonic properties around the wavelength used (532 nm) are rather isotropic and therefore they are not responsible for the anisotropic behaviour we observed in the SERS experiments.

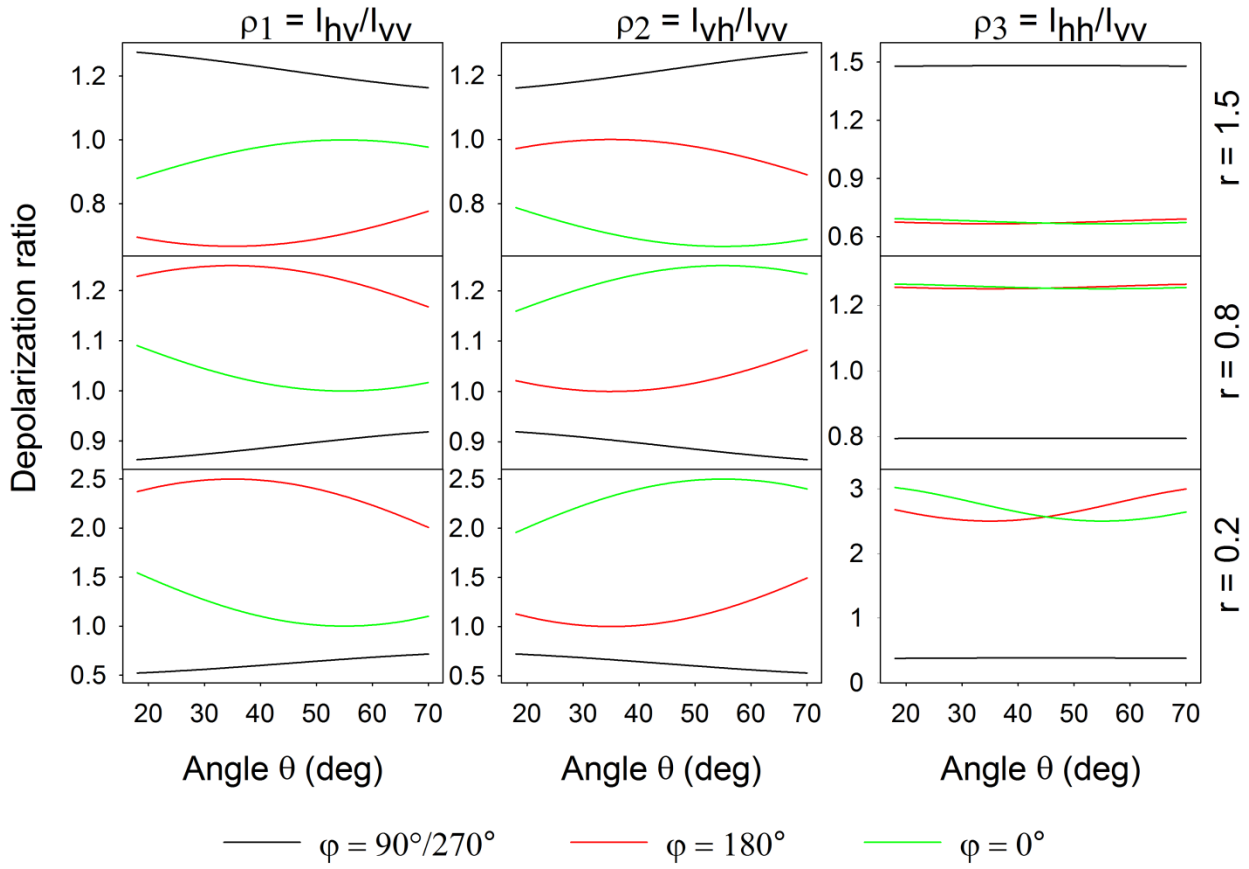


Figure S4. Theoretical shapes of the depolarization ratio curves in the case of plasmonic anisotropy described by the $r$ value. Three values of $r$, three depolarization ratios and three angles $\varphi$ (since the angles $\varphi = 90°$ and $\varphi = 270°$ provide the same response in the plasmonic anisotropy model) are presented. Since obviously no value of $r$ is able to fit the experimentally measured depolarization curves, the plasmonic anisotropy around the wavelength 532 nm is not the main reason for anisotropic behaviour observed in the SERS experiments.

## 5. Spectral Ellipsometry Measurements

Spectral ellipsometry measures changes in light polarization after reflecting from a material structure. To describe reflection from the surface, it is traditional to resolve the electric field into two orthogonal components: parallel (p) and perpendicular (s) with respect to the plane of incidence. Both the amplitude and the phase of both field components undergo a change upon reflection as determined by the Fresnel reflection coefficients

$$\tilde{r}_s = \frac{\cos\theta - \sqrt{\tilde{n}^2 - \sin^2\theta}}{\cos\theta + \sqrt{\tilde{n}^2 - \sin^2\theta}}, \qquad \text{(S3)}$$

$$\widetilde{r_p} = \frac{\tilde{n}^2 \cos\theta - \sqrt{\tilde{n}^2 - \sin^2\theta}}{\tilde{n}^2 \cos\theta + \sqrt{\tilde{n}^2 - \sin^2\theta}}, \tag{S4}$$

where $\theta$ denotes the angle of incidence. Complex quantities are marked with a tilde. A commonly measured ellipsometric quantity describing changes in polarization upon reflection is the complex reflectance ratio, defined as

$$\tilde{\rho} = \frac{\widetilde{r_s}}{\widetilde{r_p}}. \tag{S5}$$

The inverse transformation is

$$\tilde{n}^2 = \sin^2\theta \left[1 + \tan^2\theta \left(\frac{1-\tilde{\rho}}{1+\tilde{\rho}}\right)^2\right], \tag{S6}$$

which allows to compute the pseudo-refractive index of the structure, knowing the complex reflectance ratio $\tilde{\rho}$. Both $\tilde{\rho}$ and $\tilde{n}$ depend inherently on light frequency.

For semi-infinite, homogeneous and isotropic samples, the pseudo-refractive index is independent of the incident angle, which means it is sufficient to measure $\tilde{\rho}$ only for one angle $\theta$ for unique description of the reflective properties of the material. Then, the pseudo-refractive index becomes identical with the refractive index of the material. However, the above-mentioned criteria are hardly ever met, often due to surface roughness, native oxide layers (the case of a Si wafer) or presence of other films and overlays. Therefore, the pseudo-refractive index of silicon may be different from its refractive index. Moreover, in the case of nanostructured materials, the assumption that the pseudo-refractive index is independent of the incident angle does not have to hold anymore, which is due to the presence of subwavelength structures (see Figs. 6 and S5).

In a more general case such as anisotropic, but still non-depolarizing materials, it is convenient to make use of the Jones formalism and express the components of the reflected light in the matrix form

$$\begin{pmatrix} E_r^p \\ E_r^s \end{pmatrix} = \begin{pmatrix} r_{pp} & r_{ps} \\ r_{sp} & r_{ss} \end{pmatrix} \begin{pmatrix} E_i^p \\ E_i^s \end{pmatrix}, \tag{S7}$$

where the subscript $i$ stands for the incident and $r$ for the reflected radiation. Generalized ellipsometry measures the ratios of the Jones matrix elements, *i.e.*

$$\frac{r_{pp}}{r_{ss}}, \frac{r_{ps}}{r_{pp}}, \frac{r_{sp}}{r_{ss}}, \tag{S8}$$

the two latter of them being identically zero in the case of homogeneous and isotropic samples.

Finally, samples which exhibit depolarization are not compatible with standard or generalized ellipsometry measurements and thus should be treated by the Mueller-matrix formalism. This formalism employs Stokes vectors and 4×4 matrices to account for depolarization, *i.e.* loss of

coherence of the phase and amplitude of the electric field.[5] The conversion of the polarized light into partially polarized or unpolarized happens due to surface roughness, film thickness inhomogeneity or presence of plasmonic resonances. Occurring depolarization may be surmised from the comparison between Mueller-matrix and Jones-matrix elements or between reflection intensities and corresponding intensities calculated using Jones-matrix elements.

Generalized ellipsometry measurements of AgOADs showed that the ratios $\frac{r_{ps}}{r_{pp}}$, $\frac{r_{sp}}{r_{ss}}$ are < 0.01 (not shown here) and thus the non-diagonal terms of the Jones matrix were neglected in our calculations. We expect that this is due to rather densely packed nanocolumns and low porosity of the AgOADs. Measurements in the reflection mode further revealed that our structures may be treated (around the wavelength of 532 nm) as non-depolarizing and thus analyzed by the standard Jones formalism. Fig. S6 demonstrates the difference between total reflectivity as measured in the reflection mode and reflectivity computed via optical pseudo-parameters retrieved from standard ellipsometry measurements using the Fresnel equations. As expected, the values obtained by direct reflection measurements are for most angles slightly higher than that computed, which do not take depolarization into account. The average difference between these two methods is around 5%. The slight discrepancy at small angles $\theta$ and $\varphi = 90°/270°$ may be caused by the low values of the imaginary part of the refractive index which implies high penetration depth of the incident angle through the nanostructures, which means that the effective reflection does not occur only at the interface Ag/air, but also at the interface Ag/Si. Upon reflection, however, the part of the light reflected from the Si interface is absorbed in the material structure and that is why the approach based on the effective medium approximation somewhat overestimates the total reflectivity.

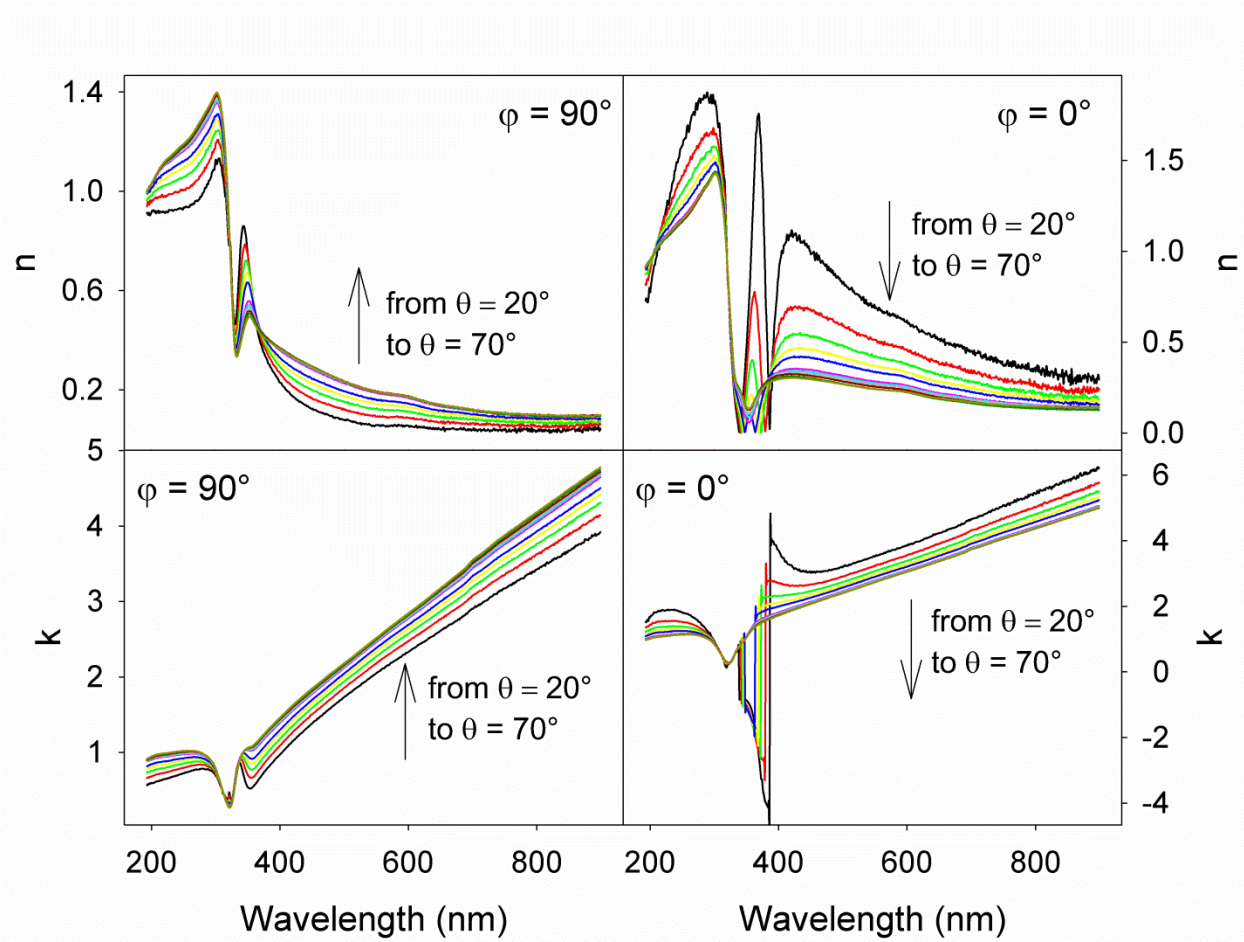


Figure S5. Wavelength dependence of the real and imaginary part of the pseudo-refractive index of AgOADs for different angles of incidence $\theta$. Left: $\varphi = 90°$ (virtually identical to $\varphi = 270°$), right: $\varphi = 0°$ (virtually identical to $\varphi = 180°$). Variation with the angle of incidence $\theta$ around $\lambda = 500$ nm is indicated by arrows.

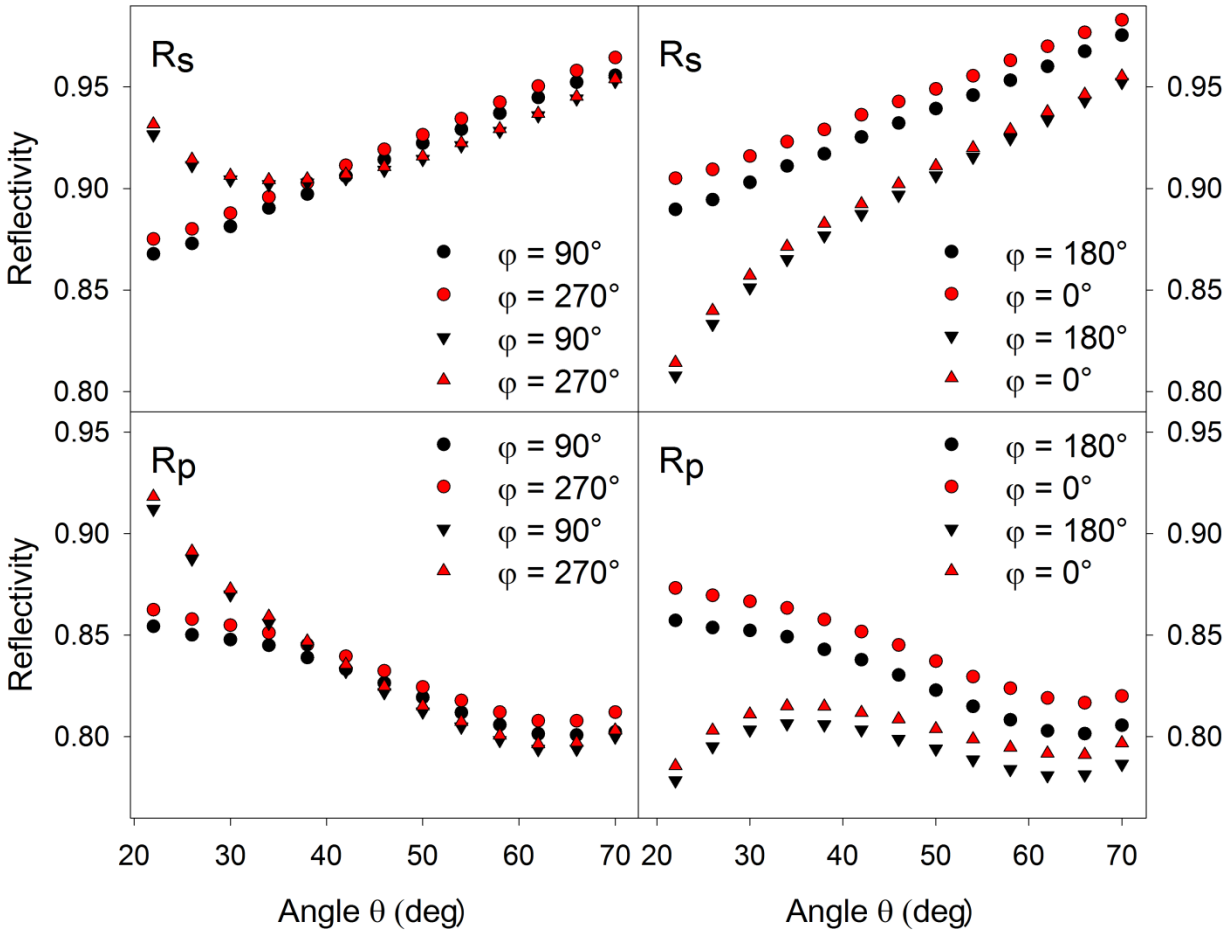


Figure S6. Reflectivity of the AgOADs as measured using reflection mode (circles) and as computed using pseudo-refractive indices measured in the standard ellipsometry mode (triangles). The values $R_s$ are in the two graphs above, the values $R_p$ are below; $\lambda = 532$ nm.

## 6. Surface Selection Rules

Let us consider the situation when a molecule adsorbed on a surface (determined by the $x'y'$ plane and $z$' specifying the substrate normal) is irradiated by a light beam at an incident angle $\theta$ with the wavevector perpendicular to the $x'$ axis. Let the scattered radiation be collected at an angle $\theta'$, again with the wavevector perpendicular to $x'$. The molecule may be thought of as being irradiated by two beams: The direct (incident) and the reflected one, which superimpose coherently, and a similar process applies in the case of the scattered radiation. In the following, we will denote $\vec{e}$ the unit electric field vector, the subscripts $i$ and $r$ stand for the incident and reflected radiation respectively, and primed quantities pertain to the scattered radiation. This situation is depicted in Fig. S7.

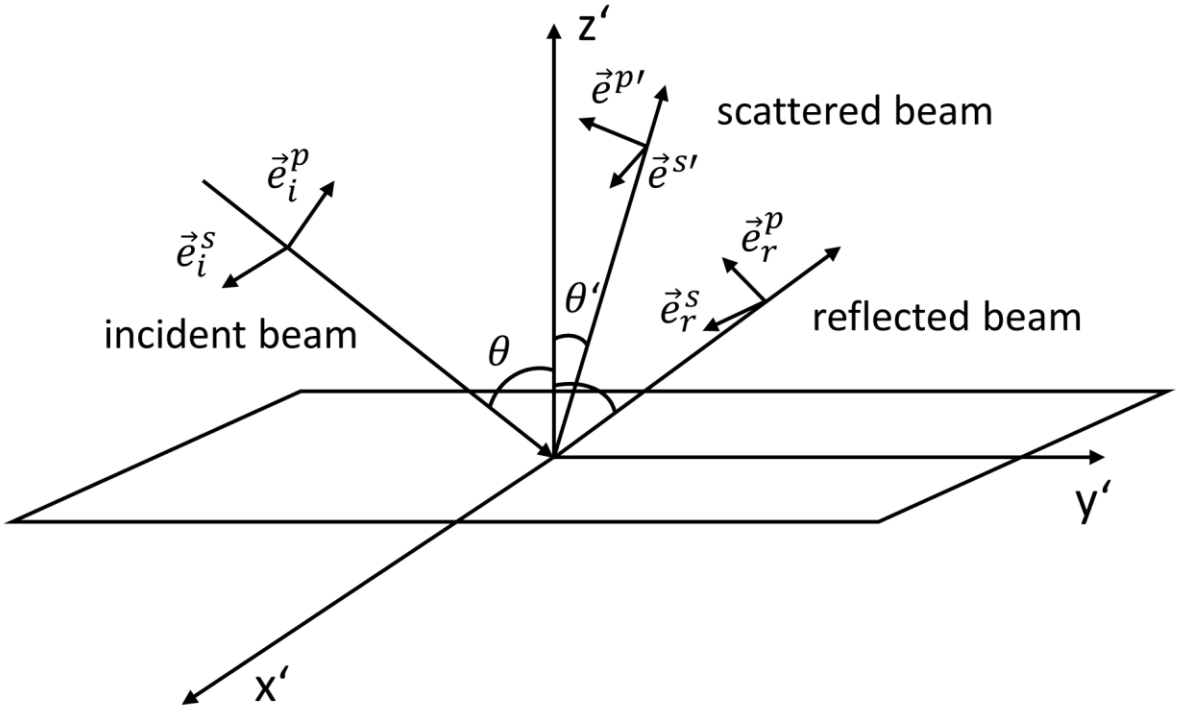


Figure S7. Scheme of the geometrical layout and definition of the coordinates. All symbols have usual meanings as described in the text. The components of the scattered field experiencing a reflection from the surface ($\vec{e}_r^{s'}$ and $\vec{e}_r^{p'}$) are not included in the scheme for simplicity.

First, we will address the description of the incident beam. In the case of s-polarization, we have

$$\vec{e}_i^{s} = (1,0,0),\ \vec{e}_r^{s} = (r_s,0,0), \tag{S9}$$

and thus the total field felt by the molecule is

$$\vec{e}^{s} = (1+r_s,0,0). \tag{S10}$$

In the case of p-polarization, we have

$$\vec{e}_i^{p} = (0,\cos\theta,\sin\theta),\ \vec{e}_r^{p} = \left(0,-r_p\cos\theta,r_p\sin\theta\right), \tag{S11}$$

and the total field felt by the molecule is

$$\vec{e}^{p} = \left(0,\left(1-r_p\right)\cos\theta,(1+r_p)\sin\theta\right). \tag{S12}$$

Very similar principle applies in the case of the scattered radiation. Supposing an analyser allows only the detection of the s-polarized light, we have

$$\vec{e}^{s'} = (1,0,0),\ \vec{e}_r^{s'} = (r_s',0,0), \tag{S13}$$

and the total detected field is

$$\vec{e}^{\,s'} = (1 + r_s^{'}, 0, 0). \tag{S14}$$

Finally, for the p-polarized light entering the detector, we have

$$\vec{e}^{\,p'} = (0, -\cos\theta', \sin\theta'),\ \vec{e}_r^{\,p'} = \left(0, r_p^{'}\cos\theta', r_p^{'}\sin\theta'\right), \tag{S15}$$

and the total detected field is

$$\vec{e}^{\,p'} = \left(0, \left(r_p^{'} - 1\right)\cos\theta', (1 + r_p^{'})\sin\theta'\right). \tag{S16}$$

Raman scattering intensity is proportional to

$$(e_j^{'}\,\alpha_{jk}^{'}\,e_k)^2, \tag{S17}$$

which means that, for example, the Raman scattering intensity of the p-polarized light excited by the s-polarized light will be proportional to

$$\left|\left(0, \left(r_p^{'} - 1\right)\cos\theta', (1 + r_p^{'})\sin\theta'\right) \cdot \begin{pmatrix} \alpha_{xx}^{'} & \alpha_{xy}^{'} & \alpha_{xz}^{'} \\ \alpha_{yx}^{'} & \alpha_{yy}^{'} & \alpha_{yz}^{'} \\ \alpha_{zx}^{'} & \alpha_{zy}^{'} & \alpha_{zz}^{'} \end{pmatrix} \cdot \begin{pmatrix} 1 + r_s \\ 0 \\ 0 \end{pmatrix}\right|^2, \tag{S18}$$

which produces the result given in eq 6. We abbreviate this intensity as $I_{vh}$ with the first subscript standing for the exciting light (*i.e.* "vertical" with respect to the scattering plane) and the second subscript standing for the scattered light (*i.e.* "horizontal" with respect to the scattering plane). Intensity profiles for the three remaining polarization combinations may be derived in a very similar fashion and are summarized in the main text.

## 7. Raman Tensor Invariants and the Depolarization Ratio

Tensor elements are transformed upon rotation of axes. Denoting $\alpha_{ij}^{'}$ Raman tensor elements in a certain (primed) system of Cartesian coordinates and $\alpha_{ij}^{''}$ Raman tensor elements in another (double primed) system of Cartesian coordinates, the 9 components of the 3×3 matrix will be transformed according to the formula[6]

$$\alpha_{kl}^{''} = R_{ki}\,R_{lj}\,\alpha_{ij}^{'}. \tag{S19}$$

More explicitly, assuming that $R$ is the rotational matrix about the $z'$ axis by 90°, *i.e.* taking the form

$$R = \begin{pmatrix} \cos\omega & \sin\omega & 0 \\ -\sin\omega & \cos\omega & 0 \\ 0 & 0 & 1 \end{pmatrix}_{\omega=90°} = \begin{pmatrix} 0 & 1 & 0 \\ -1 & 0 & 0 \\ 0 & 0 & 1 \end{pmatrix}, \quad \text{(S20)}$$

then, the transformation relation (S19) reads

$$\begin{pmatrix} \alpha''_{xx} & \alpha''_{xy} & \alpha''_{xz} \\ \alpha''_{yx} & \alpha''_{yy} & \alpha''_{yz} \\ \alpha''_{zx} & \alpha''_{zy} & \alpha''_{zz} \end{pmatrix} = \begin{pmatrix} 0 & 1 & 0 \\ -1 & 0 & 0 \\ 0 & 0 & 1 \end{pmatrix} \cdot \begin{pmatrix} \alpha'_{xx} & \alpha'_{xy} & \alpha'_{xz} \\ \alpha'_{yx} & \alpha'_{yy} & \alpha'_{yz} \\ \alpha'_{zx} & \alpha'_{zy} & \alpha'_{zz} \end{pmatrix} \cdot \begin{pmatrix} 0 & -1 & 0 \\ 1 & 0 & 0 \\ 0 & 0 & 1 \end{pmatrix} =$$

$$\begin{pmatrix} \alpha'_{yy} & -\alpha'_{yx} & \alpha'_{yz} \\ -\alpha'_{xy} & \alpha'_{xx} & -\alpha'_{xz} \\ \alpha'_{zy} & -\alpha'_{zx} & \alpha'_{zz} \end{pmatrix}. \quad \text{(S21)}$$

Leaving aside the unimportant signs in the final matrix product in eq S21, we see that the Raman tensor component $\alpha'_{xx}$ for $\varphi = 90°/270°$ becomes identical to $\alpha'_{yy}$ for $\varphi = 0°/180°$ and vice versa, the Raman tensor component $\alpha'_{xz}$ for $\varphi = 90°/270°$ becomes $\alpha'_{yz}$ for $\varphi = 0°/180°$ (and vice versa) etc.

In the case of resonance Raman scattering, a total of 3 independent combinations of Raman tensor elements can be found that remain invariant after rotation of the system of coordinates. These are usually referred to as:[6]

The square of the mean polarizability $a$:

$$a^2 = \frac{(\alpha_{xx}+\alpha_{yy}+\alpha_{zz})^2}{9}, \quad \text{(S22)}$$

the anisotropy $\gamma$:

$$\gamma^2 = \frac{(\alpha_{xx}-\alpha_{yy})^2+(\alpha_{yy}-\alpha_{zz})^2+(\alpha_{xx}-\alpha_{zz})^2}{2} + 3\frac{(\alpha_{xy}+\alpha_{yx})^2+(\alpha_{yz}+\alpha_{zy})^2+(\alpha_{zx}+\alpha_{xz})^2}{4}, \quad \text{(S23)}$$

and the antisymmetric anisotropy $\delta$:

$$\delta^2 = 3\frac{(\alpha_{xy}-\alpha_{yx})^2+(\alpha_{yz}-\alpha_{zy})^2+(\alpha_{zx}-\alpha_{xz})^2}{4}. \quad \text{(S24)}$$

The relative proportion between these 3 invariants (especially between $a^2$ and $\gamma^2$ since $\delta^2$ tends to zero in the case of non-resonance Raman scattering) helps to surmise the symmetry of the vibration involved. In a typical experiment, this information is accessible with the use of polarized light. For the sake of simplicity, we limit our attention here to the 90°-scattering geometry, although some of the following results may be easily generalized to other geometries too. As already mentioned in the section 2, in the case of randomly oriented molecules, the ratio of cross-polarized (in principle, any of $I_{hv}$, $I_{vh}$ or $I_{hh}$ polarization arrangements) to parallel-polarized ($I_{vv}$ arrangement) Raman intensities defines the Raman depolarization ratio $\rho$.

Equivalently, it involves the ratio of the orientation-averaged non-diagonal Raman tensor components to the diagonal ones, which may be expressed using the three above-mentioned invariants as

$$\rho = \frac{\langle \alpha_{ij}^2 \rangle}{\langle \alpha_{ii}^2 \rangle} = \frac{3\gamma^2 + 5\delta^2}{4\gamma^2 + 45a^2}. \quad \text{(S25)}$$

We expect that the difference between the depolarization ratio of MB as measured in a water solution ($\rho_M = 0.21 \pm 0.01$) and that computed for MB adsorbed on AgOADs using eq S25 and values from table 1 ($\rho = 0.29 \pm 0.01$) is attributable mainly to the presence of hot-spot sites. Briefly, in the following, we will assume random orientation of dimers (which are generally agreed to be the principal sources of hot-spot sites) between which a molecule may be embedded. Then, the local field scales as ~ $\cos\alpha$ where $\alpha$ is the angle between polarization vector and the dimer axis. Introducing standard spherical coordinates $(x,\ y,\ z) = (\sin u \cos v\,, \sin u \sin v, \cos u)$, we obtain

$$\rho_{SERS} = \frac{I_{vh}}{I_{vv}} = \frac{I\left(e_x^{exc}, e_z^{det}\right)}{I\left(e_x^{exc}, e_x^{det}\right)} = \frac{\iint (\sin u \cos u \cos v)^2 \mathrm{d}\Omega}{\iint (\sin u \cos v)^4 \mathrm{d}\Omega}, \quad \text{(S26)}$$

where $\mathrm{d}\Omega = \sin u\, \mathrm{d}u\mathrm{d}v,\ u \in (0, \pi)$ and $v \in (0, 2\pi)$. Simple integration yields the value of $\rho_{SERS} = 1/3$ as verified experimentally many times.[7,8] As expected, the depolarization ratio as computed using values in table 1 is bound between these two extremes ($\rho_M < \rho < \rho_{SERS}$). Another reason for the difference between $\rho$ and $\rho_M$ may be formation of dimers/trimers at the surface, which could feature a different depolarization ratio with respect to the monomers that are analyzed in liquid (or possibly a combination of the two factors mentioned above).

## References


1. Malinowski, E.R. *Factor Analysis in Chemistry* (J. Wiley & Sons. 2002).
2. Roy, S. D., Ghosh, M. & Chowdhury, J. Adsorptive parameters and influence of hot geometries on the SER(R) S spectra of methylene blue molecules adsorbed on gold nanocolloidal particles. *J. Raman Spectrosc.* **46**, 451-461 (2015).
3. Heger, D., Jirkovský, J. & Klán, P. Aggregation of Methylene Blue in Frozen Aqueous Solutions Studied by Absorption Spectroscopy. *J. Phys. Chem. A* **109**, 6702-6709 (2005).
4. Le Ru, E. C. *et al*. Experimental demonstration of surface selection rules for SERS on flat metallic surfaces. *Chem. Commun.* **47**, 3903-3905 (2011).
5. Jellison, G. E. Spectroscopic ellipsometry data analysis: measured versus calculated quantities. *Thin Solid Films* **313**, 33-39 (1998).
6. Long, D. A. *The Raman Effect: A Unified Treatment of the Theory of Raman Scattering by Molecules* (John Wiley & Sons Ltd, 2002).

7. Le Ru, E. C., Meyer, M., Blackie, E. & Etchegoin, P. G. Advanced aspects of electromagnetic SERS enhancement factors at a hot spot. *J. Raman Spectrosc.* **39**, 1127-1134 (2008).
8. Fazio, B. *et al*. Re-radiation Enhancement in Polarized Surface-Enhanced Resonant Raman Scattering of Randomly Oriented Molecules on Self-Organized Gold Nanowires. *ACS Nano* **5**, 5945-5956 (2011).

# Attachment A4

**M. Šubr**, A. Kuzminova, O. Kylián, M. Procházka: Surface-enhanced Raman scattering (SERS) of riboflavin on nanostructured Ag surfaces: The role of excitation wavelength, plasmon resonance and molecular resonance. Spectrochimica Acta Part A: Molecular and Biomolecular Spectroscopy, 2018, vol. 197, 202-207.

Spectrochimica Acta Part A: Molecular and Biomolecular Spectroscopy 197 (2018) 202–207

Contents lists available at ScienceDirect

Spectrochimica Acta Part A: Molecular and Biomolecular Spectroscopy

journal homepage: www.elsevier.com/locate/saa

# Surface-enhanced Raman scattering (SERS) of riboflavin on nanostructured Ag surfaces: The role of excitation wavelength, plasmon resonance and molecular resonance

Martin Šubr [a,*], Anna Kuzminova [b], Ondřej Kylián [b], Marek Procházka [a,*]

[a] Institute of Physics, Faculty of Mathematics and Physics, Charles University, Ke Karlovu 5, 121 16 Prague, Czech Republic
[b] Department of Macromolecular Physics, Faculty of Mathematics and Physics, Charles University, V Holešovičkách 2, 180 00 Prague, Czech Republic

ARTICLE INFO

*Article history:*
Received 28 November 2017
Received in revised form 16 January 2018
Accepted 19 January 2018
Available online 3 February 2018

*Keywords:*
SERS
Riboflavin
Ag nanoislands
Excitation profile
LSPR

ABSTRACT

Optimization of surface-enhanced Raman scattering (SERS)-based sensors for (bio)analytical applications has received much attention in recent years. For optimum sensitivity, both the nanostructure fabrication process and the choice of the excitation wavelength used with respect to the specific analyte studied are of crucial importance. In this contribution, detailed SERS intensity profiles were measured using gradient nanostructures with the localized surface-plasmon resonance (LSPR) condition varying across the sample length and using riboflavin as the model biomolecule. Three different excitation wavelengths (633 nm, 515 nm and 488 nm) corresponding to non-resonance, pre-resonance and resonance excitation with respect to the studied molecule, respectively, were tested. Results were interpreted in terms of a superposition of the enhancement provided by the electromagnetic mechanism and intrinsic properties of the SERS probe molecule. The first effect was dictated mainly by the degree of spectral overlap between the LSPR band, the excitation wavelength along with the scattering cross-section of the nanostructures, while the latter was influenced by the position of the molecular resonance with respect to the excitation wavelength. Our experimental findings contribute to a better understanding of the SERS enhancement mechanism.



## 1. Introduction

Fabrication of plasmonic platforms for surface-enhanced spectroscopic methods, such as surface-enhanced Raman scattering (SERS), surface-enhanced fluorescence (SEF) or surface-enhanced infrared absorption (SEIRA), has been under thorough investigation for the last ~20 years [1]. To date, close attention has been devoted to optimization of the SERS efficiency by tuning the nanoparticle dimensions, geometry, composition, degree of aggregation as well as their dielectric environment [2–5]. Correlation between the maximum SERS enhancement and details of the nanoobject fabrication procedure mentioned above was in place already in the 1990s [6]. Supposing the size of the metallic nanoobjects is much smaller than the laser wavelength (electrostatic approximation), the oscillating charge density at the metal-dielectric interface may be viewed as an oscillating electric dipole and the term dipolar plasmon resonance is often used. However, when the dimensions of the nanoobjects become comparable to the excitation wavelength, other terms of the multipole expansion have to be taken into account. This gives rise to higher order plasmon resonances (usually quadrupolar) that do not couple to light very effectively [2]. For this reason, it is generally recognized that there exist optimum dimensions of the metallic objects that provide the biggest enhancement, usually in the range ~5–200 nm. This is evidenced by a vast body of experimental data using both metallic colloids [7,8] as well as regular SERS-active platforms [9,10]. Generally, with the increasing size of the metallic nanoobjects and/or reducing the mutual distance, the LSPR is shifted to longer wavelengths and progressively broadens, accompanied by reduced local field enhancements due to retardation effects. Moreover, special care should be devoted to the proper choice of the excitation wavelength used. Information on the plasmonic properties of the substrate is very often derived from extinction [6,11] or reflection [9,12] spectra, although this approach has led to several misconceptions found in literature [13,14]. This confusion stems from overseeing the difference between the "near-field" (Raman-enhancing) and the "far-field" properties of a given substrate. In the average SERS regime, spectral position of the highest SERS enhancement was found near the spectral position of the localized surface-plasmon resonance (LSPR) maximum. In this case, the optimum excitation wavelength tends to be slightly blue-shifted with respect to the LSPR with the LSPR peaking approximately halfway between the incident and the Raman frequency so that both fields can be optimally enhanced [15]. However, this relationship may no longer be true for hot-spot dominated SERS-active

* Corresponding authors.
*E-mail addresses:* Martin.Subr@mff.cuni.cz (M. Šubr), prochaz@karlov.mff.cuni.cz (M. Procházka).

https://doi.org/10.1016/j.saa.2018.01.055
1386-1425/

systems (such as colloids) where the maximum enhancement is often red-shifted with respect to the LSPR maximum [2,13]. In the case of more complicated SERS-active platforms, no correlation between these two phenomena was found [16–18]. Moreover, the SERS enhancement may be coupled with molecular resonance enhancement or charge transfer effects, which in turn influences the SERS excitation profile (dependence of the SERS intensity on the excitation wavelength) [19–21].

In this contribution, we use gradient nanostructured silver surfaces, i.e. surfaces with gradually changing optical properties in one direction, to study the dependence of the SERS enhancement factor on the excitation wavelength and the LSPR position in the range from 450 nm to 700 nm. We show that not only the scattering cross-section of the nanostructures, but also the spectral position of the molecular resonance of the analyte used (riboflavin in this study) and its relation to the excitation wavelength used possess a key role in the observable characteristics. Our approach facilitates the way for modern analytical techniques, biosensing and medical applications [22,23].

## 2. Experimental Section

### 2.1. Fabrication of the SERS Nanostructures

The SERS nanostructures were prepared on polished Si wafers (~3 cm × 1 cm). The fabrication procedure was carried out based on a step-by-step optimization process described in our previous work [11]. The produced coatings had a three-layer structure schematically depicted in Fig. 1a.

The topmost layer consisted of Ag nanoislands (responsible for the SERS effect) deposited by means of DC magnetron sputtering of a silver target in argon atmosphere (pressure 0.1 Pa, magnetron current 200 mA). The gradient character of properties of silver nanoislands was achieved using a movable mask introduced in between the substrate and the magnetron during the process of deposition of nanoislands (Fig. 1b) [24]. The mask initially shielded the entire substrate area from the flux of incoming silver atoms emitted from the magnetron target. The position of the edge of the mask in this situation is denoted as 0 mm. The mask was subsequently moved with the constant speed along the sample length which in turn gradually diminished the shielded fraction of the substrate. As a result of this, different locations on the samples experienced different fluence of silver atoms that led to Ag structures with different morphologies at different spots on the substrate.

The intermediate, 80 nm thick layer in the SERS active samples was composed of magnetron-sputtered polytetrafluoroethylene (PTFE) film. This film, that was produced using applied RF power of 40 W and argon as the working gas (pressure 1 Pa), served as a dielectric separation layer between the Ag nanoislands and the continuous smooth silver that represented the bottom layer of the produced structure. As we demonstrated in our previous study, the introduction of such a base layer, which acts as a mirror for the incoming laser beam during SERS measurements, contributes to the total enhancement factor by approximately an order of magnitude [11].

The morphology of prepared surfaces along the sample length was investigated by scanning electron microscopy (SEM, TESCAN Mira 3, 15 kV accelerating voltage). Optical properties of silver nanoislands deposited onto glass slides were investigated by UV–Vis spectrophotometry (Hitachi U-2910). No metallic back-reflector was used in this case.

### 2.2. Raman Measurements

SERS spectra were recorded at room temperature using an integrated confocal Raman microscopic system LabRam HR800 (Horiba Jobin-Yvon), equipped with a diffraction grating with 300 grooves per mm and a liquid nitrogen cooled CCD detector. Two excitation sources were used: He–Ne laser, operating at the wavelength of 633 nm, and $Ar^+$ laser with the lines at 488 and 515 nm. The laser beam was focused onto the sample at a spot of approximately a 1 μm diameter using a 100× objective, NA = 0.9. Laser powers were adjusted using grey filters to approximately the same laser power around 0.05 mW for all three wavelengths used. Scattered radiation was collected in a back-scattering geometry and filtered by an edge filter for Rayleigh rejection before focusing it onto the 100 μm entrance slit of the spectrometer. SERS intensities were determined as height of the Raman band centered around 1077 $cm^{-1}$ above spectral background and normalized using a Si wafer as an external intensity standard.

### 2.3. Studied Biomolecule

Riboflavin (vitamin B2) was used as the model biomolecule. Riboflavin serves as a cofactor of many key enzymes and absorbs light in the spectral region between ~400–500 nm. Thus, it is a suitable molecule for the study of both SERS and resonance SERS in the spectral region determined by the LSPR of our structures. Riboflavin powder was dissolved in deionized water. Final riboflavin concentration $3 \times 10^{-5}$ M was obtained by subsequent dilution of the stock solution and used for SERS testing.

## 3. Results and Discussion

The first step of this study involved characterization of produced SERS-active surfaces from the point of view of their morphology and

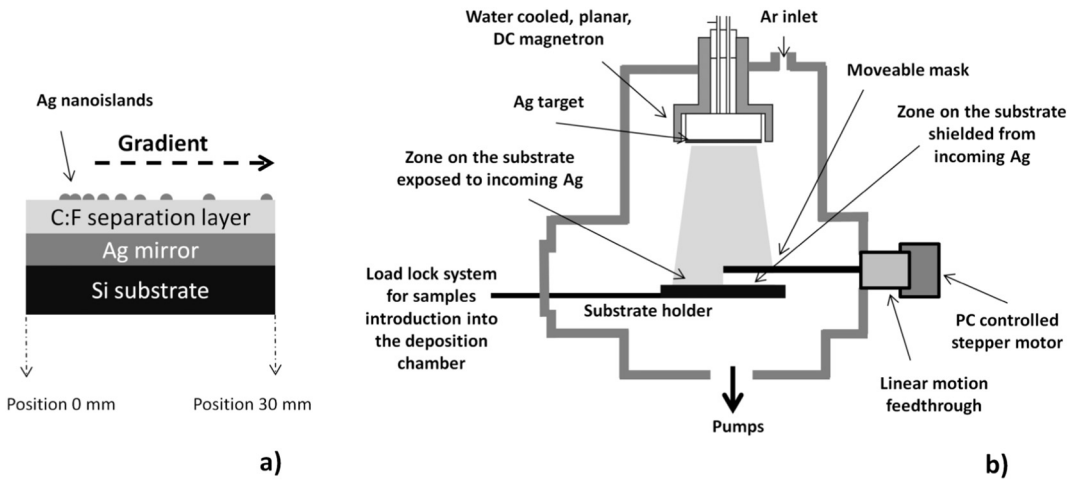


**Fig. 1.** a) Schematic illustration of the substrate, b) schematic representation of the setup used for production of gradient nanoislands.

optical properties. As can be seen in Fig. 2 where sections of SEM images recorded at different positions on the sample prepared with the mask speed 1 cm/30 s are presented, different morphologies along the sample length arise. They range from small individual Ag nanoparticles of dozens of nm at positions that correspond to short exposure times of the substrate to the Ag flux to an interconnected Ag network observed at the locations exposed to incoming Ag for longer time period.

The gradual changes in morphology of silver nanostructures (size and separation of individual nanoparticles, see Fig. 2) naturally result in significant appearance variation of the LSPR. For small and well-separated Ag nanoislands the LSPR band has maxima at shorter wavelengths (450–500 nm). An increase in nanoisland size and a decrease in their mean distances causes red-shift of the wavelength of the LSPR maximum (see Fig. 3). In addition, the course and the range in which LSPR changes its position on a single sample may be varied by alternation of the mask speed. As expected, lower speed of the mask caused bigger differences in the amount of incoming atoms. Thus, also bigger differences in interparticle distances on particular positions on the sample and consequently bigger differences in LSPR were observed [24]. This made possible to cover the range of the LSPR band maxima from approximately 450 nm up to 700 nm. However, it has to be emphasized that the shape and the wavelength of the LSPR maximum is the same for the spots on the samples with the same exposure time to Ag flux (Fig. 3c).

SERS spectra were retrieved by dropping 2 μl of a riboflavin stock solution on the Ag nanoisland structures and letting dry. 3–4 drops were deposited evenly along the sample length, each of the droplets possessing a different LSPR condition. Although this approach often results in rather inhomogeneous drying patterns, SERS reproducibility in each of the droplets (diameter ~ 2 mm) was found to be better than 10% as determined by spectral mapping. For reproducibility determination, we used an approach based on singular value decomposition algorithm, described in more detail in our previous work [11]. The spatial resolution, determined by the diameter of the droplet, imposes an uncertainty in the determination of the LSPR maximum in respective positions on the sample of up to ~20–30 nm in the leftmost part of the sample (that experienced the highest fluence of Ag). This uncertainty is comparable to the uncertainty in LSPR maxima determination on respective positions on the sample and plays relatively a minor role in further considerations. In order to enable intensity comparison across different wavelengths used, Si wafer was employed as an external intensity standard. This approach accounts for fluctuating laser power as well as the $f^4$-dependence imposed by using different excitation wavelengths [2,22].

Absorption spectrum of riboflavin solution and examples of riboflavin SERS spectra taken with different laser wavelengths under the optimized conditions are depicted in Fig. 4. It is obvious from Fig. 4a that using the excitation wavelength 488 nm, the SERS may be considered as resonance SERS (SE(R)RS), in the case of the excitation wavelength 515 nm as pre-resonance and as out-of-resonance in the case of the 633-nm excitation wavelength. Spectral positions of respective riboflavin vibrational modes are virtually identical for all three excitation wavelengths and correspond well with riboflavin SERS spectra reported in literature [25,26]. The SERS spectrum is dominated by bands centered around 1342 and 1624 $cm^{-1}$, attributed to the vibrational motion of the isoalloxazine ring, which interacts with Ag surface [25,26]. These two bands have also obviously biggest contribution from the molecular resonance as their relative proportion with respect to other observable bands is most significant in the case of 488-nm excitation wavelength (to a lesser extent, this effect can be attributable to the $f^4$-dependence of different vibrational modes). Most importantly, the effect of the wavelength used is expected to be reflected in the SERS intensity profile when measured along the sample length (in different positions possessing different LSPR conditions). This situation is depicted in Fig. 5.

As already mentioned in Section 1, in the average SERS regime (which is the case of Ag nanoislands), the spectral position of the LSPR

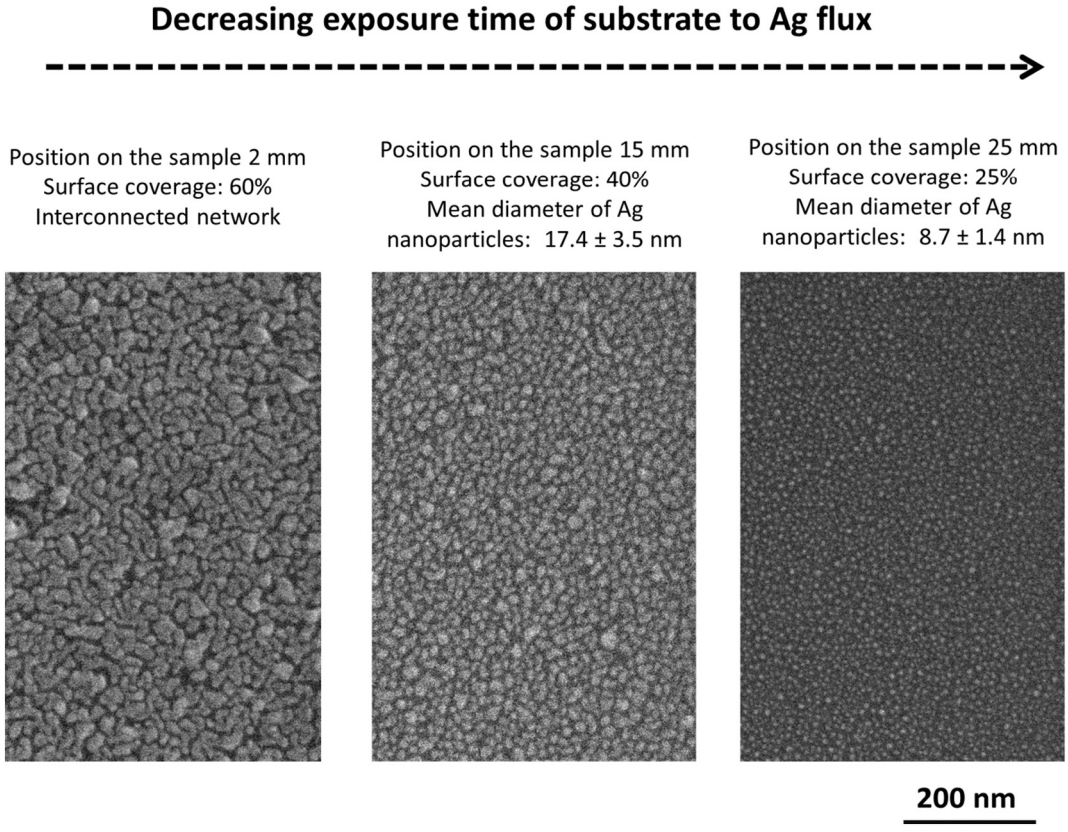


**Fig. 2.** SEM images of Ag nanoislands measured on different positions on the sample (mask speed 1 cm/30 s). Surface coverage and mean diameter of Ag nanoparticles were determined by analysis of SEM images.

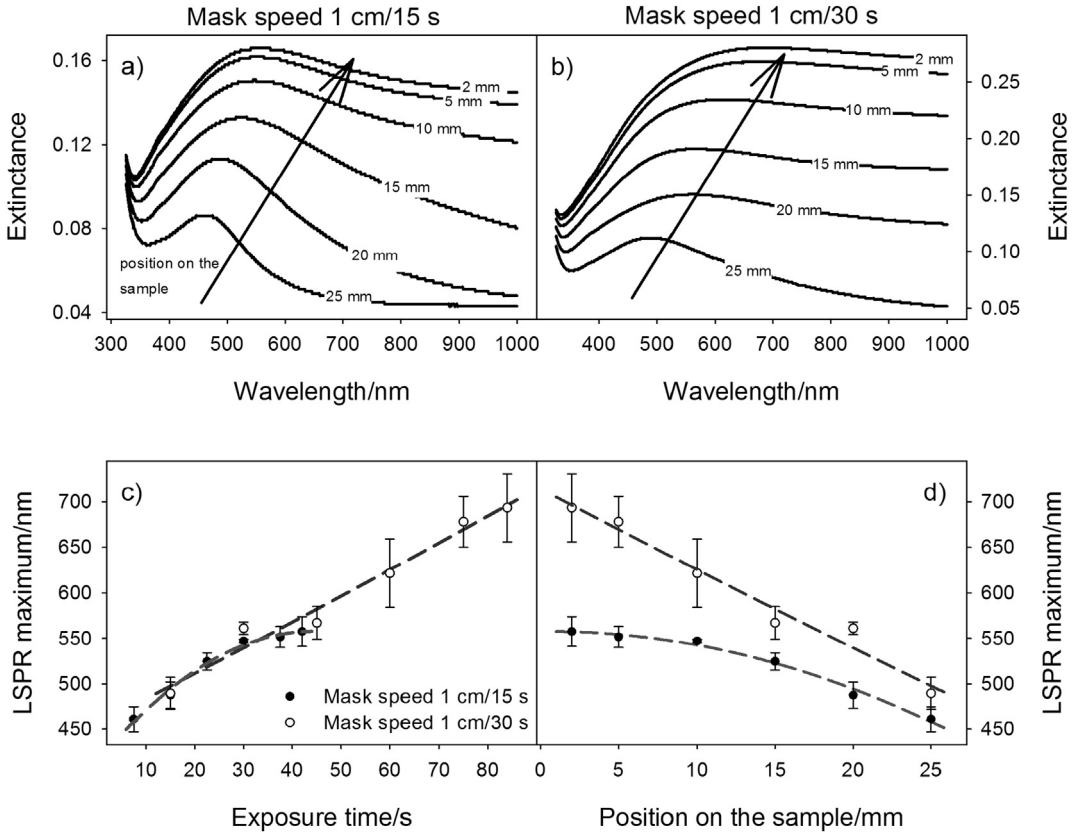


**Fig. 3.** Extinction spectra on gradient samples prepared at mask speed of a) 1 cm/15 s and b) 1 cm/30 s, dependence of the wavelength of the LSPR maximum on c) exposure time and on d) position on the sample.

band on particular position of the sample should possess maximum overlap with the excitation wavelength used in order to achieve optimum SERS enhancement. However, this matter is further complicated by the fact that the studied molecule (riboflavin) exhibits a broad absorption band between ~400 and 500 nm and its molecular resonance contributes to the total enhancement when the excitation wavelength approaches the slope of this absorption band. This causes the SERS intensity profile of riboflavin with different positions on the sample to deviate from the expected dependence under the conditions of non-resonance excitation (with respect to the studied molecule) where the electromagnetic contribution to the total enhancement is dominant. To sum up, the resultant SERS intensity profile with respect to the LSPR maximum position may be thought of as a superposition of two contributions: the scattering cross-section of the nanostructures (depending on the exposure time of a particular position on the sample to the Ag flux and consequently different extinction profile and LSPR condition) and intrinsic properties of the SERS probe molecule. The latter contribution is affected predominantly by the position of molecular resonance with respect to the excitation wavelength.

From Fig. 5, several conclusions can be drawn: for the excitation wavelengths 515 nm and 633 nm, the electromagnetic enhancement mechanism is the most dominant. In these instances, the SERS intensity is dictated mainly by (i) the degree of spectral overlap between the LSPR band and the excitation wavelength, and (ii) the scattering cross-section on the nanostructures. The scattering cross-section is (in a certain range) an increasing function of the nanoparticle size and a decreasing function of the inter-particle distance. In other words, the scattering cross-section of the nanostructures rises when the LSPR position shifts

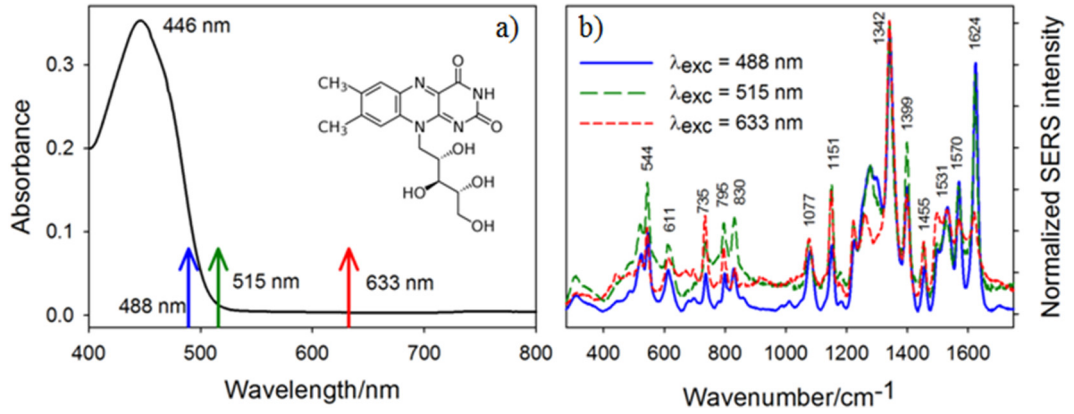


**Fig. 4.** a) Absorption spectrum of riboflavin and the structure of riboflavin, b) examples of riboflavin SERS spectra taken with different excitation wavelengths. Riboflavin concentration was $3 \times 10^{-5}$ M, SERS spectra were normalized with respect to the most intense Raman band.

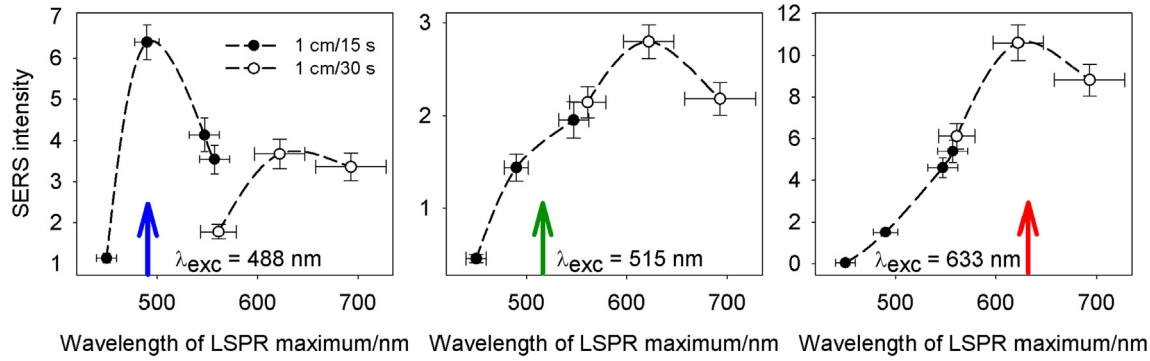


**Fig. 5.** SERS intensity profile with different wavelengths of LSPR maxima across the sample. 2 different mask speeds and 3 different excitation wavelengths were tested. SERS intensities were normalized using a Si wafer as an external intensity standard. The horizontal error bars represent uncertainty the in LSPR maxima determination (drop size). The vertical error bars were determined from spectral mapping.

to the red and starts to decrease when a certain size limit is reached. The maximum enhancement in this case was found around the position of LSPR maximum of ~630 nm, irrespective of the excitation wavelength used. This can be possibly explained by the fact that using the mask speed 1 cm/30 s, extinction maxima are rather broad and all wavelengths (partly including also the 488-nm wavelength) fall into the LSPR band. It suggests that not only spectral position of LSPR maximum, but also the shape and width of the LSPR band is decisive for the optimum SERS enhancement. Under the conditions of optimum excitation (position of LSPR maximum around 630 nm), the SERS intensity in the case of 633-nm excitation wavelength is about 4× higher in comparison to the 515-nm and 488-nm wavelengths. The shape of the SERS intensity profile well copies the Lorentz curve with a small shoulder around 500 nm in the case of the 515-nm excitation wavelength, which is obviously due to the fact that this excitation wavelength approaches the slope of the riboflavin absorption band (pre-resonance SERS). In Fig. 6, this intensity profile is correlated with the dependence of the extinction maximum on the LSPR position. It is obvious that both curves follow the same trend except for the wavelengths above ~650 nm when the SERS nanostructures turn into a smooth film, resulting in a decrease in the SERS signal. A very similar trend is followed using the 515-nm excitation wavelength.

For the resonance SERS (excitation wavelength 488 nm), however, a sharp maximum was found close to the excitation wavelength. This most likely is because of the decisive role of the molecular resonance, which decays rapidly when shifting the LSPR condition of a particular position on the sample off resonance. Local maximum around LSPR position around 630 nm may again be due to the biggest scattering cross-section of the nanostructures around this wavelength and broad and shallow maximum, partly overlapping with the excitation wavelength 488 nm.

Completely different SERS intensity profiles for the excitation wavelengths 488 nm and 515 nm suggest that a possible effect of the silver substrate on a red-shift in riboflavin absorption spectrum with respect to the situation in an aqueous solution may be considered negligible. This is in agreement with the literature [27] where no such shift was observed. On the other hand, contradictory studies [28] reveal that after formation of riboflavin-Ag complex, absorption spectrum can be red-shifted as much as ~50 nm. The precise elucidation of the effect of silver nanoislands on riboflavin absorption spectrum and a possible role of the molecular enhancement mechanism is still unclear in our model and will be addressed in our future research.

It is worth noting that although the enhancement effect is different for different riboflavin modes depending on the excitation wavelength (Fig. 4), the trend followed by the graphs in Fig. 5 is almost identical for all riboflavin modes. No significant difference was observed for larger or smaller Raman shifts (not shown here). For example, the difference between the excitation wavelength and the Raman-shifted wavelength ranges from ~42 to 72 nm across the excitation wavelengths used in the case of the 1624-$cm^{-1}$ mode. This effect is obviously too little with respect to the width of the LSPR curves (FWHM ~ 100–300 nm) and their shallow maxima to be observable.

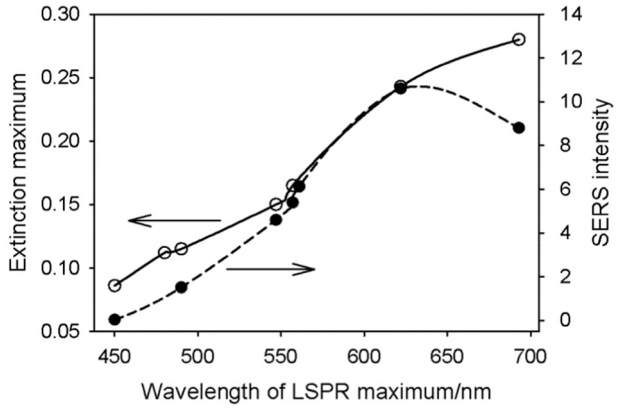


**Fig. 6.** Dependence of the extinction maximum on the LSPR position (solid line) and its correlation with the SERS intensity profile (non-resonance excitation 633 nm, dashed line).

## 4. Conclusions

In this contribution, detailed SERS intensity profiles were measured using gradient nanostructures with the LSPR condition varying across the sample length using 3 different excitation wavelengths (633 nm, 515 nm and 488 nm) corresponding to non-resonance, pre-resonance and resonance excitation with respect to the studied molecule, respectively. Results were interpreted in terms of a superposition of the enhancement provided by the electromagnetic mechanism and intrinsic properties of the SERS probe molecule. The first effect was dictated mainly by the degree of spectral overlap between the LSPR band and the excitation wavelength along with the scattering cross-section on the nanostructures, while the latter was influenced by the position of the molecular resonance with respect to the excitation wavelength. Highest SERS intensity was obtained either when the position of the LSPR maximum of the nanostructures was around 630 nm, closely matching the 633-nm excitation wavelength, or when the position of the LSPR maximum matched both the riboflavin absorption band and the 488-nm excitation wavelength. Our results point out the need for careful optimization of the nanostructure fabrication process and excitation wavelength used and may be useful for optimization of SERS-based sensors for (bio)analytical applications.

## Funding

The research was supported by grants No. 16-14024S and P205/13/20110S from the Czech Science Foundation and GAUK No. 572216 from Charles University. Authors would like to thank also I. Khalakhan for SEM measurements.

## References

[1] M. Jahn, S. Patze, I.J. Hidi, R. Knipper, A.I. Radu, A. Mühlig, S. Yüksel, V. Peksa, K. Weber, T. Mayerhöfer, D. Cialla-May, J. Popp, Analyst 141 (2016) 756–793.
[2] E.C. Le Ru, P.G. Etchegoin, Principles of Surface-enhanced Raman Spectroscopy and Related Plasmonic Effects, Elsevier, Amsterdam, 2009.
[3] K.L. Kelly, E. Coronado, L.L. Zhao, G.C. Schatz, J. Phys. Chem. B 107 (2003) 668–677.
[4] P.W. Barber, R.K. Chang, H. Massoudi, Phys. Rev. Lett. 50 (1983) 997–1000.
[5] P.K. Jain, K.S. Lee, I.H. El-Sayed, M.A. El-Sayed, J. Phys. Chem. B 110 (2006) 7238–7248.
[6] V.L. Schlegel, T.M. Cotton, Anal. Chem. 63 (1991) 241–247.
[7] P.N. Njoki, I.-I.S. Lim, D. Mott, H.-Y. Park, B. Khan, S. Mishra, R. Sujakumar, J. Luo, C.-J. Zhong, J. Phys. Chem. C 111 (2007) 14664–14669.
[8] D.E. Evanoff Jr., G. Chumanov, J. Phys. Chem. B 108 (2004) 13948–13956.
[9] W.-C. Lin, L.-S. Liao, Y.-H. Chen, H.-C. Chang, D.P. Tsai, H.-P. Chiang, Plasmonics 6 (2011) 201–206.
[10] K. Sugawa, T. Akiyama, Y. Tanoue, T. Harumoto, S. Yanagida, A. Yasumori, S. Tomita, J. Otsuki, Phys. Chem. Chem. Phys. 17 (2015) 21182–21189.
[11] M. Šubr, M. Petr, O. Kylián, J. Kratochvíl, M. Procházka, J. Mater. Chem. C 3 (2015) 11478–11485.
[12] M. Šubr, M. Petr, O. Kylián, J. Štěpánek, M. Veis, M. Procházka, Sci. Rep. 7 (2017) 4293.
[13] E.C. Le Ru, C. Galloway, P.G. Etchegoin, Phys. Chem. Chem. Phys. 8 (2006) 3083–3087.
[14] M. Moskovits, Phys. Chem. Chem. Phys. 15 (2013) 5301–5311.
[15] A.D. McFarland, M.A. Young, J.A. Dieringer, R.P. Van Duyne, J. Phys. Chem. B 109 (2005) 11279–11285.
[16] S.L. Kleinman, B. Sharma, M.G. Blaber, A.-I. Henry, N. Valley, R.G. Freeman, M.J. Natan, G.C. Schatz, R.P. Van Duyne, J. Am. Chem. Soc. 135 (2013) 301–308.
[17] Y.-P. Zhao, S.B. Chaney, S. Shanmukh, R.A. Dluhy, J. Phys. Chem. B 110 (2006) 3153–3157.
[18] M.D. Doherty, A. Murphy, J. McPhillips, R.J. Pollard, P. Dawson, J. Phys. Chem. C 114 (2010) 19913–19919.
[19] N. Hajduková-Šmídová, M. Procházka, M. Osada, Vib. Spectrosc. 62 (2012) 115–120.
[20] I. Srnová-Šloufová, B. Vlčková, T.L. Snoeck, D.J. Stufkens, P. Matějka, Inorg. Chem. 39 (2000) 3551–3559.
[21] J. Zhao, J.A. Dieringer, X.Y. Zhang, G.C. Schatz, R.P. Van Duyne, J. Phys. Chem. C 112 (2008) 19302–19310.
[22] M. Procházka, Surface-enhanced Raman Spectroscopy: Bioanalytical, Biomolecular and Medical Applications, Springer, Switzerland, 2016.
[23] Y. Ozaki, K. Kneipp, R. Aroca, Frontiers of Surface-enhanced Raman Scattering: Single Nanoparticles and Single Cells, John Wiley & Sons Ltd., Chichester, United Kindgdom, 2014.
[24] J. Hanuš, H. Libenská, I. Khalakhan, A. Kuzminova, O. Kylián, H. Biederman, Mater. Lett. 192 (2017) 119–122.
[25] A. Kokaislová, P. Matějka, Anal. Bioanal. Chem. 403 (2012) 985–993.
[26] F. Liu, H. Gu, Y. Lin, Y. Qi, X. Dong, J. Gao, T. Cai, Spectrochim. Acta Part A 85 (2012) 111–119.
[27] M.B.R. Aiello, J.J. Romero, S.G. Bertolotti, M.C. Gonzalez, D.O. Mártire, J. Phys. Chem. C 120 (2016) 21967–21975.
[28] M. Voicescu, D.G. Angelescu, S. Ionescu, V.S. Teodorescu, J. Nanopart. Res. 15 (2013) 1555.

# Attachment A5

**M. Šubr**, M. Procházka: Polarization- and Angular-Resolved Optical Response of Molecules on Anisotropic Plasmonic Nanostructures. Nanomaterials, 2018, vol. 8, 418.

nanomaterials

MDPI

*Review*

# Polarization- and Angular-Resolved Optical Response of Molecules on Anisotropic Plasmonic Nanostructures

**Martin Šubr * and Marek Procházka ***

Faculty of Mathematics and Physics, Institute of Physics, Charles University, 121 16 Prague 2, Czech Republic

* Correspondence: subr.Martin@seznam.cz (M.S.); prochaz@karlov.mff.cuni.cz (M.P.); Tel.: +420-221-911-463 (M.S.); +420-221-911-474 (M.P.)

Received: 10 May 2018; Accepted: 7 June 2018; Published: 9 June 2018

**Abstract:** A sometimes overlooked degree of freedom in the design of many spectroscopic (mainly Raman) experiments involve the choice of experimental geometry and polarization arrangement used. Although these aspects usually play a rather minor role, their neglect may result in a misinterpretation of the experimental results. It is well known that polarization- and/or angular-resolved spectroscopic experiments allow one to classify the symmetry of the vibrations involved or the molecular orientation with respect to a smooth surface. However, very low detection limits in surface-enhancing spectroscopic techniques are often accompanied by a complete or partial loss of this detailed information. In this review, we will try to elucidate the extent to which this approach can be generalized for molecules adsorbed on plasmonic nanostructures. We will provide a detailed summary of the state-of-the-art experimental findings for a range of plasmonic platforms used in the last ~ 15 years. Possible implications on the design of plasmon-based molecular sensors for maximum signal enhancement will also be discussed.

**Keywords:** SERS; Raman; plasmonics; metallic nanostructures; polarization and angular dependences; molecular orientation; ellipsometry

## 1. Introduction

Methods of optical spectroscopy, such as absorption spectroscopy, Raman scattering spectroscopy or fluorescence spectroscopy, can be performed in a wide range of experimental setups relying on a proper choice of instrumentation, light sources, waveguides, monochromators, detectors etc. Interplay between all the factors mentioned above determines the final spectral pattern observed in spectroscopic experiments. An obvious degree of freedom in the experimental design is the polarization and (especially in the case of Raman experiments) angular arrangement used. Although for many types of experiments this additional information is not required, variation in light polarization and/or the scattering angle give rise to a family of phenomena that both theoreticians and experimentalists should be aware of when interpreting their results. For example, confusion of laser polarization may lead to very strong Raman bands to appear as rather weak in the Raman spectra, and vice versa. Thus, understanding these effects helps to obtain deeper insight into the properties of the system studied.

In this review, the main emphasis is placed on polarization and directional/angular characteristics occurring in Raman spectroscopy and surface-enhanced Raman spectroscopy (SERS). However, it briefly touches on the polarization and angular dependences of other optical phenomena such as absorbance, reflectance or fluorescence. It is well known that polarization- and/or angular-resolved Raman experiments allow one to classify the symmetry of the vibrations involved [1–3] or

molecular orientation with respect to a smooth surface [4–6]. We will try to extend some of these results to molecules adsorbed on plasmonic nanostructures. Generalizing these results to the case of SERS is not straightforward due to the existence of one more element—the nanostructure, which imposes its own anisotropic pattern in the polarization and directional properties of the SERS signal.

Although some reviews focusing on anisotropic metallic nanostructures for SERS and their fabrication already exist in literature [7–10], our review covers the topic from a rather untraditional point of view, focusing primarily on their polarization and directional properties. The review is organized as follows. Firstly, basic overview of polarization and angular dependences in classical Raman spectroscopy will be introduced. Different experimental geometries for Raman scattering measurements will be presented and consequences for the Raman signal coming from randomly oriented molecules as well as crystals will be derived. We will summarize basic results of the group theory, allowing classification of normal vibrational modes depending on the symmetry of the vibration involved. Theoretical predictions will be briefly compared to the experimental results measured in our laboratory. It is important to note that we will focus only on the phenomena within the dipole approximation, leaving aside the vast body of experimental techniques such as dichroic methods or Raman optical activity [11]. Secondly, we will concentrate on the polarization effects for molecules adsorbed on smooth surfaces. We will show that interference between the incident and the reflected radiation must be taken into account in order to correctly describe the observed spectral pattern. The crucial part will involve the derivation of the surface-selection rules, allowing determination of molecular orientation on smooth surfaces. Although this approach may seem to go far beyond the original scope of this review, we will show that a very similar principle also applies on roughened metallic surfaces and contributes to the SERS enhancement. Finally, we will try to generalize previous considerations to the case of surface-enhanced Raman scattering. We will summarize the up-to-date findings regarding polarization- and angular-resolved SERS experiments and survey the contributions to this field from the last 15 years. The influence of both different coupling efficiency of different laser polarizations to plasmons as well as symmetry of the Raman tensor of the analyte on polarized SERS will be critically discussed. Described phenomena will be supported by our own experimental results as well as by published ones.

## 2. The Origin of Polarization Characteristics in Spectroscopy

Before going deeply into the definitions of the depolarization ratios or formulations of the selection rules, we devote a short paragraph to the theoretical description of the polarization of the light waves. A monochromatic plane wave travelling along the $z$ axis in a given Cartesian coordinate system can be characterized by its electric field vector in any instant restricted to the $xy$ plane. Thus, the variables in an equation describing a plane wave can be decoupled in the form [12]:

$$\vec{E}(x,y,z,t) = E_{0x}\cos(\omega t - kz)\vec{e}_x + E_{0y}\cos(\omega t - kz + \delta)\vec{e}_y, \quad (1)$$

where $E_{0x}$ and $E_{0y}$ denote amplitudes of the electric field intensities in the $x$ and $y$ direction, respectively (traditionally, the polarization direction is assumed to be determined by the electric field vector instead of the magnetic field vector), $k$ denotes the wavevector and $\omega$ the angular frequency. The way that the electric field vector oscillates in space and time defines the light polarization. In the simplest case, these oscillations are confined to a single spatial direction, which is termed linear polarization. In this case, there does not exist any phase shift between the $x$ and $y$ constituents of the electric field vector. If there does exist a phase shift $\delta$ between these constituents ($\delta \neq k\pi, k \in Z$), the electric field vector experiences a more complex motion in the $xy$ plane, which gives rise to circular polarization ($E_{0x} = E_{0y}, \delta = \frac{\pi}{2} + k\pi, k \in Z$) or elliptical polarization (otherwise). Vice versa, any polarization state can be built up from two mutually perpendicular linearly polarized components.

Further, it is instructive to delve somewhat into a brief theoretical description of the interaction between (polarized) light and matter. Absorption is an optical process whereby energy of an electromagnetic wave (a photon) is absorbed in a medium, accompanied by a transition of the atom/molecule in a higher energetic state. Depending on the photon energy and quantum states participating in the process, one can distinguish the infrared (IR) absorption, which is connected with

a molecular transfer to a higher vibrational level within a given electronic state, and the UV/Vis absorption, which involves an electron excitation to a higher electronic state. In the context of this review, absorption will be mainly understood as the UV/Vis absorption. In order to restore the thermodynamic equilibrium, a molecule in an elevated electronic state can lose its energy and return to the ground state, which can be basically performed via one of the two processes: (i) The energy excess may dissipate in the form of heat (non-radiative crossing); or (ii) by a spontaneous emission of radiation, which is termed luminescence (fluorescence). Raman scattering belongs to the group of light scattering processes including annihilation of a primary photon and creation of a secondary photon with the frequency shifted from the primary photon by frequency of a molecular vibration. Thus, Raman scattering is a two-photon, inelastic process, which does not require the participating photons match the resonance frequency. For this reason, Raman scattering is a very weak process, but can be greatly amplified for molecules adsorbed in the vicinity of nanostructured metallic surfaces. This technique is called surface-enhanced Raman scattering (SERS) and it provides enhancement of the Raman scattering by a factor of $10^4$ or higher due to resonance excitation of plasmons localized in the metallic nanostructures [13]. Due to its high sensitivity, SERS has found use in numerous bio-related applications [14,15], e.g., for the detection of pharmaceuticals and drugs [16–18], food additives [19,20], explosives [21,22], disease biomarkers [23–25] and many others.

Although "classical" models of the interaction between light and matter appeared already in the 1900s [12] (followed by a semi-classical theory of Raman scattering in 1930s by Placzek [26]), interaction of light with atoms or molecules cannot be fully described unless quantum theory comes into play. In the lowest degree of approximation, transition probability (to which intensity of a given spectral line is proportional) between two quantum states of an atom/molecule is governed by the Fermi's golden rule. This rule says that in order for the transition to be allowed, the matrix element

$$\langle 2|\widehat{W}|1\rangle \tag{2}$$

must be different from zero. In Equation (2), $|1\rangle$ represents the wavefunction of the initial state, $\langle 2|$ the wavefunction of the final state and $\widehat{W}$ is a perturbation operator, which usually corresponds to the presence of the electromagnetic wave.

In the case of absorption spectroscopy, the perturbation operator can be rewritten using the electric dipole moment of the molecule ($\vec{d}$) and the probability of the transition then derives from the transition dipole moment matrix element:

$$\langle 2|\hat{d}|1\rangle. \tag{1}$$

In the case of Raman spectroscopy, the situation is more complex because in order to obtain the non-zero contribution, second-order perturbation theory has to be employed. The transition probability then derives from the second-rank tensor [27,28]:

$$\alpha_{pq}^{12} = \sum_{s\neq 1,2}\left[\frac{\langle 2|\hat{d}_p|s\rangle\langle s|\hat{d}_q|1\rangle}{E_1 - E_s + \hbar\omega_i} + \frac{\langle 2|\hat{d}_q|s\rangle\langle s|\hat{d}_p|1\rangle}{E_2 - E_s - \hbar\omega_i}\right], \tag{2}$$

where $E_1$ and $E_2$ denote the energies of the initial ($|1\rangle$) and final ($|2\rangle$) quantum states of the molecule, $\hat{\vec{d}}$ is the electric dipole moment operator and the *s*-indices refer to all remaining quantum states of the molecule. $\hbar$ denotes the reduced Planck's constant and $\omega_i$ is the angular frequency of the incident radiation.

Equations (3) and (4) demonstrate basic differences between absorption and Raman measurements. While the molecular dipole moment is a vector quantity, the transition probability is expected to scale with the projection of the light polarization in the direction of the transition dipole moment of the molecule. However, Raman scattering is a two-photon process, which means that both the polarization of the incident beam as well as that of the scattered beam dictate the total Raman intensity.

In the case of absorption spectroscopy, polarization effects in an ensemble of many randomly oriented molecules, such as liquid samples, are averaged out. That is because the total absorption

intensity is given by spatial averaging over positions of all absorbing molecules. This can be computed explicitly in azimuthal coordinates:

$$x = \sin\vartheta\cos\varphi\,,\ \ y = \sin\vartheta\sin\varphi\,,\ \ z = \cos\vartheta \tag{3}$$

as:

$$\langle(\vec{E}\cdot\vec{d})^2\rangle = (Ed)^2\langle\cos^2\vartheta\rangle = (Ed)^2\frac{\int\cos^2\vartheta\mathrm{d}\Omega}{\int\mathrm{d}\Omega} \tag{4}$$

where $\mathrm{d}\Omega = \sin\vartheta\,\mathrm{d}\vartheta\mathrm{d}\varphi$ , $\vartheta \in (0,\pi)$ and $\varphi \in (0,2\pi)$ are standard azimuthal coordinates. After standard integration, we obtain:

$$\langle\cos^2\vartheta\rangle = \frac{1}{3}, \tag{5}$$

which implies that for many randomly oriented molecules, the absorbance does not depend on the direction of polarization. Since any polarization state can be built up from two mutually perpendicular linearly polarized components, absorbance of randomly oriented molecules never depends on the state of polarization including unpolarized (natural) radiation. This is not the case for molecules exhibiting some preferential orientation (linear dichroism) or phenomena beyond the dipole approximation in the case of chiral molecules (circular dichroism). Both of these effects are, however, beyond the scope of this paper.

In the case of the Raman scattering, intensity of a given spectral line is given by a combination of the molecular Raman tensor and unit vectors of both the incident field $\vec{e}^{\,i}$ and the scattered field $\vec{e}^{\,sc}$:

$$I \sim (e_p^{sc}\alpha_{pq}^{12}e_q^i)^2. \tag{6}$$

Directions $\vec{e}^{\,i}$ and $\vec{e}^{\,sc}$ are determined by the illumination-observation geometry, including the scattering angle and polarization of the incident beam (and possibly also polarization of the collected beam). Unlike in absorption spectroscopy, Raman measurements allow much wider choice of the experimental geometry including the polarization arrangement used as well as the scattering angle. Equation (8) naturally explains why the molecular quantity describing the disposition to Raman transition must intrinsically be of tensorial nature and also predicts that detected Raman intensities depend on the polarization arrangement used even in the case of liquids, i.e., randomly oriented molecules.

In both absorption and Raman measurements, molecular symmetry imposes certain restrictions on the number of vibrational modes being active or non-active in respective spectroscopic techniques. According to the number of symmetry elements characterizing a given isolated molecule, molecules can be classified into one out of 32 molecular point groups [29]. Having assigned a molecule to a point group, the methods of group theory allow one to decompose the vibrational signature of the molecule into so-called irreducible representations. The number of normal modes belonging to each irreducible representation (out of the $3N-6$ normal modes in total) is calculated using a well-established algorithm, making use of character tables of molecular point groups [29,30]. For the purpose of spectroscopy, it is important to note that each irreducible representation may transform as a particular linear or quadratic function of coordinates. Since the constituents of the electric dipole moment have the same transformation properties as $x, y$ and $z$ and elements of a Raman tensor as $x^2$, $y^2, z^2, xy, xz$ and $yz$, it is relatively easy to predict which vibrations will be active in Raman/IR absorption spectra: In order for a given vibrational mode to be allowed in IR absorption spectra, its irreducible representation must span at least one of $x$, $y$ and $z$ species (in the case of randomly-oriented molecules). For the transition to be allowed in Raman spectra, its irreducible representation must span at least one of the quadratic ($x^2$, $y^2, z^2, xy, xz$ and $yz$) species (again in the case of randomly-oriented molecules).

## 3. Polarization and Angular Dependences in Raman Spectroscopy

### *3.1. Derivation of Raman Intensities as a Function of the Polarization and Angular Arrangement*

Let us consider a general experimental geometry for Raman scattering measurements, depicted in Figure 1. Let us suppose that a Cartesian coordinate system is chosen so that the sample is placed in its origin, the excitation beam travels along the $x$ direction with polarization along the $z$ direction and the detector is oriented to collect light scattered in the $xy$ plane at an angle $\vartheta$ with respect to the $x$ axis. The angle $\vartheta$ is termed the scattering angle and it can take any value from 0° to 180°. The $xy$ plane is termed the scattering plane. In the following, we will refer to the $z$ components of the electric field as to the normal or vertical (with respect to the scattering plane, denoted as $v$ or $\perp$) and the components lying in the scattering plane as to the horizontal (denoted as $h$ or ||). In general, the scattered light contains both vertical and horizontal components—that is why an analyser is often inserted between the monochromator and the sample to distinguish these two polarizations. In order to overcome different grating responses for different light polarizations, a scrambler must be inserted between the analyser and the monochromator (not shown in Figure 1 for simplicity).

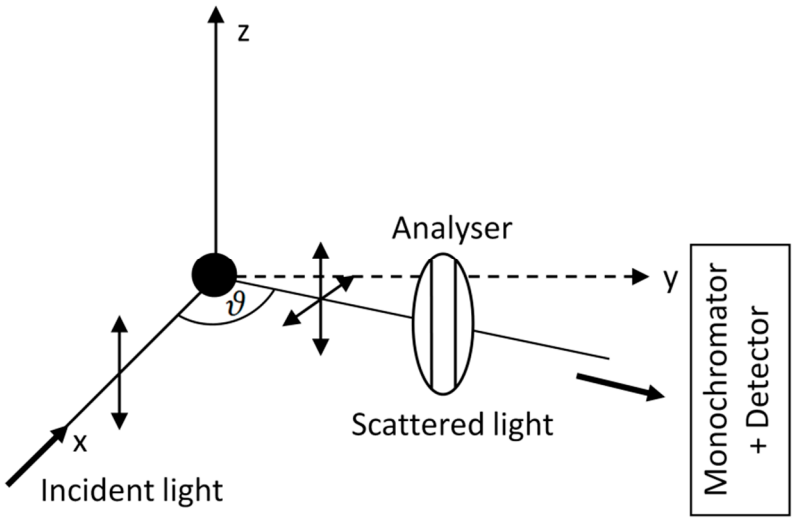


**Figure 1.** Scheme of a general Raman scattering geometry. The excitation beam travels along the $x$ direction with polarization in the $z$ direction and the detector collects light scattered in the $xy$ plane at an angle $\vartheta$ with respect to the $x$ axis. An analyser may be inserted between the sample and the monochromator to allow only one specific Raman polarization enter the detector.

With the fixed angle $\vartheta$, 4 different polarization combinations can be thought of to retrieve Raman spectra: There are two basic possibilities of setting the polarization of the incident beam (either perpendicular to the scattering plane as depicted in Figure 1, i.e., in the $z$ direction, or lying in the scattering plane, i.e., in the $y$ direction) as well as two basic possibilities of rotating the analyser to pick out either horizontal or vertical polarization. Thus, we adopt the symbols:

$$I\left(\vartheta, \perp^{sc}, \perp^{i}\right) = I_{vv}, \quad I\left(\vartheta, \|^{sc}, \perp^{i}\right) = I_{vh}, \quad I\left(\vartheta, \perp^{sc}, \|^{i}\right) = I_{hv}, \quad I\left(\vartheta, \|^{sc}, \|^{i}\right) = I_{hh} \tag{9}$$

to account for each of these polarization arrangements. The first symbol in each bracket denotes the scattering angle, the second symbol refers to polarization of the scattered beam (with respect to the scattering plane) and the third one refers to polarization of the incident beam. Sometimes the scattering angle is unimportant and as a shorthand we introduce the notation $I_{vv}$, $I_{vh}$, $I_{hv}$ and $I_{hh}$ with the first subscript standing for polarization of the incident beam and the latter standing for polarization of the scattered beam. Our task is to derive expressions for intensities of a given Raman line, measured under respective arrangements. It is important to note that for $\vartheta = 0°$ or $\vartheta = 180°$ the scattering plane is not well-defined. Nevertheless, we will show that the general considerations above will become trivial in these special cases.

Equation (8) says that each of the 4 possible polarization arrangements mentioned above picks out different elements of the Raman tensor of the molecules. In other words, specific illumination-observation geometry determines which elements of the Raman tensor will appear in the final expressions dictating the intensity of a given Raman line. The Cartesian components of the electric field vector of the scattered beam are:

$$E_x^{sc} = E(\vartheta, \|^{sc}) \sin\vartheta\,, \qquad E_y^{sc} = E(\vartheta, \|^{sc}) \cos\vartheta\,, \qquad E_z^{sc} = E(\vartheta, \perp^{sc}), \tag{10}$$

where $E(\vartheta, \|^{sc})$ and $E(\vartheta, \perp^{sc})$ denote components of the amplitude of the scattered beam lying in the scattering plane and in the direction perpendicular to the scattering plane, respectively. By combination of Equations (8), (9) and (10), the following explicit formulas can be obtained (for simplicity, we further omit the upper indices 12 in denomination of the molecular Raman tensor $\alpha$):

$$I\left(\vartheta, \perp^{sc}, \perp^{i}\right) \sim \alpha_{zz}^2, \qquad I\left(\vartheta, \|^{sc}, \perp^{i}\right) \sim (\alpha_{xz} \sin\vartheta + \alpha_{yz} \cos\vartheta)^2, \tag{11}$$

$$I\left(\vartheta, \perp^{sc}, \|^{i}\right) \sim \alpha_{zy}^2, \qquad I\left(\vartheta, \|^{sc}, \|^{i}\right) \sim (\alpha_{xy} \sin\vartheta + \alpha_{yy} \cos\vartheta)^2. \tag{12}$$

In the case of an ensemble of randomly oriented molecules, respective squares or Raman tensor elements in Equations (11) and (12) are to be replaced with their spatially-averaged values as contributions from each individual molecule sum up incoherently. This can be performed in a manner analogous to Equation (6), however, molecular polarizability responsible for the Raman scattering is a tensor rather than a vector quantity, which makes the determination of spatially-averaged tensor elements a more tedious procedure. Any spatial rotation of the molecule with respect to a given reference frame can be expressed unambiguously by a rotational matrix associated with 3 Euler angles, whose elements must be averaged in a manner analogous to Equation (6) [31]. An alternative and less time-consuming approach involves computation of isotropic averages of respective products of direction cosines between two Cartesian axis systems (again only 3 out of 9 direction cosines are independent) [27,32]. For an ensemble of many randomly oriented molecules, intensity of a given Raman line in a given experimental geometry may be expressed as a linear combination of Raman tensor invariants. These are usually referred to as:

The square of the mean polarizability $a$:

$$a^2 = \frac{(\alpha_{xx} + \alpha_{yy} + \alpha_{zz})^2}{9}, \tag{13}$$

the anisotropy $\gamma$:

$$\gamma^2 = \frac{\left(\alpha_{xx} - \alpha_{yy}\right)^2 + \left(\alpha_{yy} - \alpha_{zz}\right)^2 + (\alpha_{zz} - \alpha_{xx})^2}{2} + 3\frac{(\alpha_{xy} + \alpha_{yx})^2 + (\alpha_{yz} + \alpha_{zy})^2 + (\alpha_{zx} + \alpha_{xz})^2}{4}, \tag{14}$$

and the antisymmetric anisotropy $\delta$:

$$\delta^2 = 3\frac{\left(\alpha_{xy} - \alpha_{yx}\right)^2 + \left(\alpha_{yz} - \alpha_{zy}\right)^2 + (\alpha_{zx} - \alpha_{xz})^2}{4}. \tag{15}$$

For non-resonance Raman scattering only the isotropic invariant $a$ and the anisotropic invariant $\gamma$ are relevant since in this case the Raman tensor is symmetric and the antisymmetric invariant $\delta$ is identically zero. The result of the averaging procedure is [27,32]:

$$\langle\alpha_{xx}^2\rangle = \langle\alpha_{yy}^2\rangle = \langle\alpha_{zz}^2\rangle = \frac{45a^2 + 4\gamma^2}{45}, \qquad \langle\alpha_{xy}^2\rangle = \langle\alpha_{xz}^2\rangle = \langle\alpha_{yz}^2\rangle = \frac{3\gamma^2 + 5\delta^2}{45}, \tag{16}$$

$$\langle\alpha_{xz}\alpha_{yz}\rangle = \langle\alpha_{xy}\alpha_{yy}\rangle = 0. \tag{17}$$

This result shows the intuitive notion that the average values of all diagonal elements of the Raman tensor are equal and also all off-diagonal elements are equal, irrespective of a specific choice of the system of coordinates. Also all Raman tensor products which involve one common subscript are zero. Putting these values in Equations (11) and (12) yields:

$$I\left(\vartheta,\perp^{sc},\perp^{i}\right)\sim\frac{45a^2+4\gamma^2}{45},\qquad I\left(\vartheta,\|^{sc},\perp^{i}\right)\sim\frac{3\gamma^2+5\delta^2}{45},\tag{18}$$

$$I\left(\vartheta,\perp^{sc},\|^{i}\right)\sim\frac{3\gamma^2+5\delta^2}{45},\qquad \left(\vartheta,\|^{sc},\|^{i}\right)\sim\frac{45a^2+4\gamma^2}{45}\cos^2\vartheta+\frac{3\gamma^2+5\delta^2}{45}\sin^2\vartheta.\tag{19}$$

Equations (18) and (19) reveal that actually the only polarization arrangement in which the intensity of a given line will depend on the scattering angle $\vartheta$ is the arrangement in which both the incident beam as well as the scattered beam are polarized in the scattering plane.

In order to avoid misunderstanding, it is important to realize that any combination of Raman tensor invariants (13)–(15) is again an invariant. In literature, many alternative definitions of Raman tensor invariants may be found [27]. For example, Raman tensor invariants used by Placzek [26] are:

$$G^0=3a^2,\qquad G^a=\frac{2}{3}\delta^2,\qquad G^s=\frac{2}{3}\gamma^2.\tag{20}$$

A quantity which can be very easily measured experimentally is the Raman depolarization ratio, which is defined as the ratio of Raman intensities measured under two selected configurations. Most commonly, the depolarization ratio $\rho$ is assumed as the ratio between the intensity of the Raman field polarized orthogonal to the incident field and the intensity of the Raman field polarized parallel to the laser field [27,28]. The most common way of retrieving the depolarization ratio is fixing the incident polarization and rotating the analyser. In our notation, this yields to:

$$\rho\left(\vartheta,\perp^{i}\right)=\frac{I\left(\vartheta,\|^{sc},\perp^{i}\right)}{I\left(\vartheta,\perp^{sc},\perp^{i}\right)}=\frac{I_{vh}}{I_{vv}}.\tag{21}$$

Although many textbooks resort only to the definition of the depolarization ratio given by Equation (21) [28,30], this formula can be easily generalized and many alternative definitions of the depolarization ratio can be found in the literature [27], such as:

$$\rho\left(\vartheta,\|^{i}\right)=\frac{I\left(\vartheta,\perp^{sc},\|^{i}\right)}{I\left(\vartheta,\|^{sc},\|^{i}\right)}=\frac{I_{hv}}{I_{hh}},\qquad \rho\left(\vartheta,\perp^{sc}\right)=\frac{I\left(\vartheta,\perp^{sc},\|^{i}\right)}{I\left(\vartheta,\perp^{sc},\perp^{i}\right)}=\frac{I_{hv}}{I_{vv}},\tag{22}$$

$$\rho\left(\vartheta,\perp^{sc},\perp^{i},\|^{sc},\|^{i}\right)=\frac{I\left(\vartheta,\perp^{sc},\perp^{i}\right)}{I\left(\vartheta,\|^{sc},\|^{i}\right)}=\frac{I_{vv}}{I_{hh}},\tag{23}$$

etc. The depolarization ratio provides unique information on the Raman polarizability tensor of a given molecular vibration and is therefore a very useful tool. Indeed, in the case of randomly oriented molecules, we have:

$$\rho\left(\vartheta,\perp^{i}\right)=\frac{I_{vh}}{I_{vv}}=\frac{3\gamma^2+5\delta^2}{45a^2+4\gamma^2}.\tag{24}$$

Similar formulas can be derived for the depolarization ratios given by Equations (22) and (23). It is obvious that the introduction of the depolarization ratios is very convenient because it allows to exclude the insignificant multiplicative constant relating Raman intensities to specific combinations of squares of Raman tensor elements. The depolarization ratio defined by Equation (24) is usually termed the molecular depolarization ratio since it is an intrinsic property of the Raman probe (contrary to the depolarization ratio measured in presence of smooth/nanostructured metallic surfaces where the mutual interaction between light/analyte/metal substantially affect the measured depolarization ratio). From Equation (24) it immediately follows that for non-resonance Raman scattering ($\delta=0$) the molecular depolarization ratio is always bound between 0 and 3/4. A specific value of $\rho$ will depend on the symmetry of the vibration involved. For totally symmetric vibrations $\gamma^2=0$ and the depolarization ratio tends to zero. Conventionally, such a Raman line is said to be completely polarized. This aspect can be explained straightforwardly from a classical point of view: For totally symmetric vibrations, the polarizability tensor will become a scalar and the direction of the oscillating dipole will match the direction of the incident field polarization. Since total Raman

intensity is proportional to the scalar product of the oscillating dipole moment and the detected field, one would expect that when setting the analyser parallel to the direction of the oscillating dipole (the incident polarization), the intensity will reach its maximum, while after rotating the analyser about 90° the intensity will drop to its minimum. On the other hand, for non-totally symmetric vibrations $a^2 = 0$ and the depolarization ratio is 3/4 [27,28]. Conventionally, such a Raman line is said to be depolarized. When $0 < \rho < 3/4$, the Raman line is said to be (partially) polarized [27].

Previous considerations are valid for any angle $\vartheta$ apart from $\vartheta = 0°$ (forward scattering) and $\vartheta = 180°$ (backscattering). In this instance the scattering plane is not well-defined and the symbols $\perp^{sc}, \perp^{i}$, $\|^{sc}$ and $\|^{i}$ as well as $I_{vv}$, $I_{vh}$, $I_{hv}$ and $I_{hh}$ lose their sense. Nevertheless, the situation is trivial in this case. Let us resketch the experimental geometry in Figure 2, adopting the direction of the $z$ axis parallel to the wavevector of the incident (scattered) light. After illuminating the sample with light with a given polarization, confined to the $xy$ plane, the analyser may be set to collect Raman field polarized parallel or orthogonal to the laser field. Alternatively, Raman measurements may be performed with a fixed position of the analyser and varying polarization of the incident beam. Respective arrangements lead to probing of the averages of the squares of the diagonal/off-diagonal Raman tensor elements. In this case, the $z$ components of the Raman tensor do not figure in the equations. Formally, the 4 respective polarization combinations discussed above split into two groups since $I(0°, \perp^{sc}, \perp^{i}) = I(0°, \|^{sc}, \|^{i})$ and $I(0°, \|^{sc}, \perp^{i}) = I(0°, \perp^{sc}, \|^{i})$ in this case, the same holding also for $\vartheta = 180°$. The depolarization ratio for $\vartheta = 0°$ or $\vartheta = 180°$ can be expressed simply as the ratio of intensities obtained with crossed polarizations to intensities obtained with parallel polarizations. Formally:

$$\rho = \frac{I(0° \text{ or } 180°, \|^{sc}, \perp^{i})}{I(0° \text{ or } 180°, \|^{sc}, \|^{i})}, \tag{25}$$

which takes the form given by Equation (24) in the case of randomly oriented molecules.

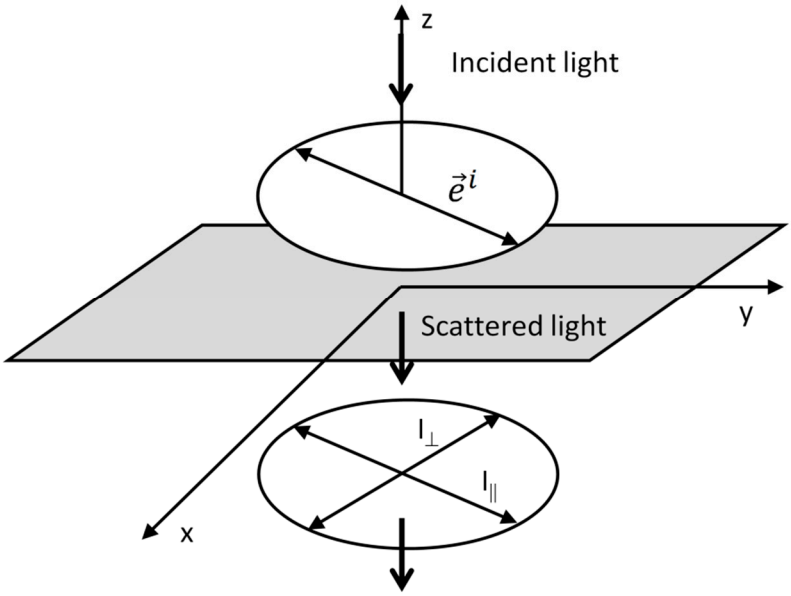


**Figure 2.** Scheme of a forward-scattering geometry. Linearly polarized light is falling on the plane of the sample ($xy$) from above. Analyser can be set to retrieve either a perpendicular component of the laser field ($I_{\perp}$) or a parallel one ($I_{\|}$). Analogous situation occurs in the case of a backscattering geometry.

Further, let us inspect another widely-used geometry in which $\vartheta = 90°$ (right-angle geometry). After inserting $\vartheta = 90°$ in Equation (19), we obtain:

$$I(90°, \|^{sc}, \perp^{i}) = I(90°, \perp^{sc}, \|^{i}) = I(90°, \|^{sc}, \|^{i}) \neq I(90°, \perp^{sc}, \perp^{i}), \tag{26}$$

$$I_{vh} = I_{hv} = I_{hh} \neq I_{vv}. \quad (27)$$

It means that for retrieving information on the Raman depolarization ratio (and consequently on the symmetry of the vibration involved), $I_{vv}$ and any of $I_{vh}$, $I_{hv}$ and $I_{hh}$ are required.

### 3.2. Simple Illustration of the Depolarization Ratio Measurement

In this paragraph, we demonstrate previous considerations on a simple example of liquid $CCl_4$ measured in our laboratory in the right-angle geometry (excitation wavelength 532 nm). The default polarization of the incident beam in this experimental setup is perpendicular to the scattering plane, but may be rotated by 90° using a half-wave plate or a Fresnel rhomb retarder. The $CCl_4$ is a highly symmetric molecule belonging to the $T_d$ point group. Polarized Raman spectra obtained in all four polarization arrangements are displayed in Figure 3.

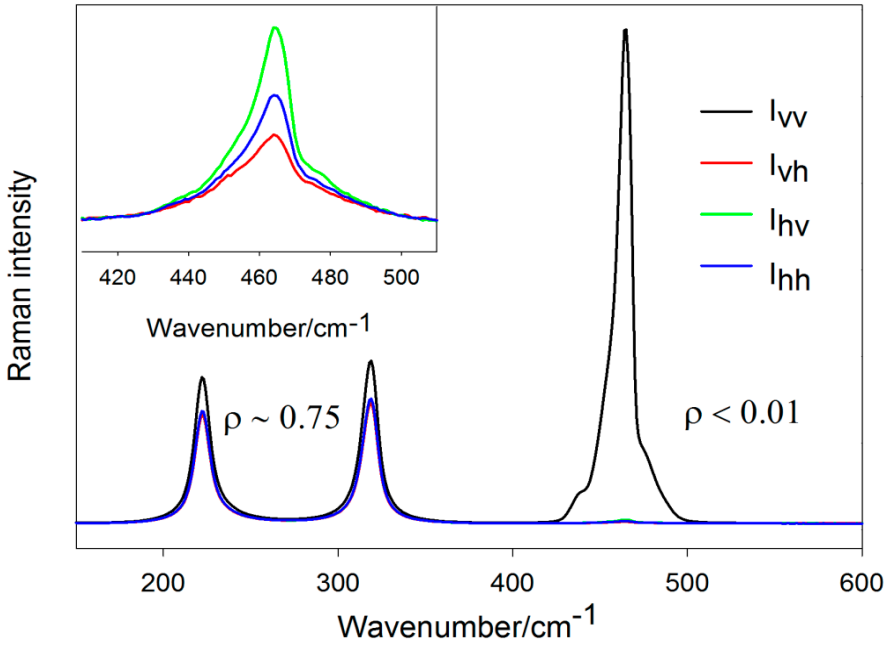


**Figure 3.** Polarized Raman spectra of $CCl_4$. The excitation wavelength was 532 nm, laser power 100 mW and the accumulation time 1 min. No further corrections have been made.

Analysis of respective depolarization ratios suggests that the band centered around 465 $cm^{-1}$ can be classified as totally symmetric (the "disrupted" structure of the 465-$cm^{-1}$ band is owed to different Cl isotopes which lift the degeneracy of this peak) while the bands around 222 and 319 $cm^{-1}$ as non-totally symmetric modes. Indeed, group theory predicts the $\Gamma^{3N-6}$ representation of $CCl_4$ to be $A_1 \oplus E \oplus 2F_2$ (E being doubly degenerate and F being triply degenerate, making $3 \cdot 5 - 6 = 9$ vibrational modes in total).

Basically, those values obtained from the experiment confirm that $I_{vh}$, $I_{hv}$ and $I_{hh}$ configurations are equivalent. However, closer analysis (inset of Figure 3) reveals slight differences in respective polarization arrangements, which is obviously attributable to transfer optics imperfections. The depolarization ratios obtained from measurements with varying incident polarization are larger than from the measurements where the incident polarization was kept constant, which shows some subtle imperfection of the half-wave plate, transmitting a small fraction of orthogonal polarization as well (making the relative error particularly large for highly polarized lines where $\rho \approx 0$). Thus, polarization-dependent Raman spectra of $CCl_4$ serve well for checking the correct function of the scrambler and other optical components used for more complex polarization-dependent measurements.

Last but not least, the literature is not consistent about whether peak heights (above spectral background) or rather integrated areas should actually enter Equations (21)–(23). In many instances

(such as in the case of $CCl_4$) these two ways produce almost identical results as the line width is not expected to change with polarization. On the other hand, in the case of several overlapping bands, determination of the spectral background and delimiting the peak area may be difficult and the two methods may give somewhat different results. In these cases, fitting the spectrum with the sum of the Lorentz curves would be advisable.

### *3.3. Other Possible Polarization Arrangements Used*

Previous survey of the most widely-used geometries for the depolarization ratio measurements is still not exhaustive. All other possible geometries can be resolved exploiting the fact that any polarization state can be decomposed into a superposition of two independent, linearly polarized waves with their electric field vectors perpendicular to each other. Other possible experimental geometries (maybe even the most frequent) involve the situations when no analyser is used, i.e., the excitation field is either vertical or horizontal, but polarization of the detected field is not characterized (or a far less common case when the excitation field is unpolarized and respective scattered field components are detected). For the sake of completeness, we adopt the symbols:

$$I\left(\vartheta, n^{sc}, \perp^{i}\right) = I\left(\vartheta, \perp^{sc}, \perp^{i}\right) + I\left(\vartheta, \parallel^{sc}, \perp^{i}\right), \tag{28}$$

$$I\left(\vartheta, n^{sc}, \parallel^{i}\right) = I\left(\vartheta, \perp^{sc}, \parallel^{i}\right) + I\left(\vartheta, \parallel^{sc}, \parallel^{i}\right), \tag{29}$$

and the less commonly used symbols:

$$I(\vartheta, \perp^{sc}, n^{i}) = I\left(\vartheta, \perp^{sc}, \perp^{i}\right) + I\left(\vartheta, \perp^{sc}, \parallel^{i}\right), \tag{30}$$

$$I(\vartheta, \parallel^{sc}, n^{i}) = I\left(\vartheta, \parallel^{sc}, \perp^{i}\right) + I\left(\vartheta, \parallel^{sc}, \parallel^{i}\right). \tag{31}$$

Equations (28) and (29) show that investigating a total Raman intensity without an analyser is equivalent to performing two experiments in a row: setting the analyser to collect the horizontal polarization, then rotating the analyser by 90° to collect the vertical polarization and summing up both results. An analogous situation is true for Equations (30) and (31). Moreover, respective left-hand sides of Equations (28)–(31) can be combined and yield further alternative depolarization ratio definitions. Surprisingly, information on the orientation-averaged squares of the Raman tensor elements (and consequently information on the symmetry of molecular vibrations involved) can be extracted even without an analyser—all that one needs to do is to record the Raman spectra with the incident field polarization perpendicular to the scattering plane and parallel to the scattering plane, respectively. Let us, for instance, determine the expected depolarization ratio in the right-angle geometry with varying incident polarization and no analyser used. By combining Equations (18), (19), (28) and (29), we obtain:

$$\rho(90°, n^{sc}) = \frac{I\left(90°, n^{sc}, \parallel^{i}\right)}{I\left(90°, n^{sc}, \perp^{i}\right)} = \frac{6\gamma^2 + 10\delta^2}{45a^2 + 7\gamma^2 + 5\delta^2}. \tag{32}$$

The depolarization ratio for non-resonance Raman scattering ($\delta^2 = 0$), defined in the manner of Equation (32), is always bound between 0 and 6/7.

### *3.4. Directional Properties in Raman Spectroscopy*

At the end of this section, implications of previous considerations on the angular dependences in Raman spectroscopy will be discussed. We have already seen that out of the 4 basic polarization arrangements, the only one where the Raman intensity actually depends on the angle $\vartheta$ is the $I\left(\vartheta, \parallel^{sc}, \parallel^{i}\right)$ arrangement (Equation (19)). Thus, let us resketch the Raman measurement scheme as in Figure 4. Supposing the scattering process takes place in the plane of the sheet, different Raman intensities are expected to arise when moving the detector about the axis perpendicular to the scattering plane. This intensity modulation occurs only if both the excitation and the detected field are polarized parallel to the scattering plane, or when the detected field is unpolarized (or a far less common case when the excitation field is unpolarized and parallel field component is detected). If at

least one of the excitation/detected field components is perpendicular to the scattering plane, Raman intensity will no longer be the function of $\vartheta$ as follows directly from Equation (18). By contrast, if both the excitation and detected fields were perpendicular to the plane of the sheet, Raman intensity would be modulated when moving the detector in the plane perpendicular to the sheet.

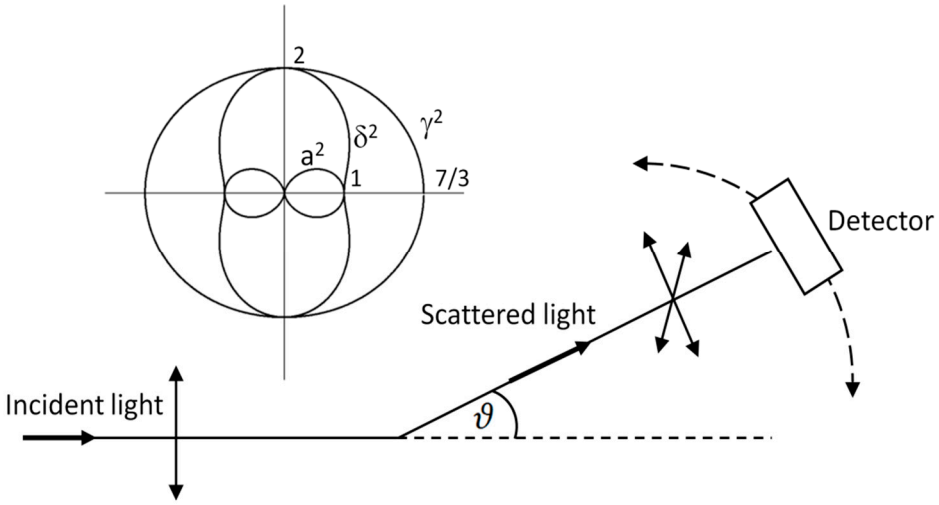


**Figure 4.** Angular dependence of the Raman signal. When both the incident and scattered fields are polarized parallel to the scattering plane or when one field is polarized parallel and the latter is unpolarized, the detected Raman intensity will be angular-dependent. Angular dependences for molecules with a dominant contribution of $a^2$, $\gamma^2$ and $\delta^2$ respectively when moving the detector by an angle $\vartheta$ from 0° to 360° and no analyser is used are indicated in the inset.

Let us explore in more detail the case when the excitation line is polarized parallel to the scattering plane and polarization of the scattered beam is not characterized, i.e., the analyser is missing. Again, we will suppose that the Raman scatterers are randomly oriented molecules. In our notation:

$$I(\vartheta, n^{sc}, \|^i) = I(\vartheta, \perp^{sc}, \|^i) + I(\vartheta, \|^{sc}, \|^i) \sim \frac{3\gamma^2 + 5\delta^2}{45} + \frac{45a^2 + 4\gamma^2}{45}\cos^2\vartheta + \frac{3\gamma^2 + 5\delta^2}{45}\sin^2\vartheta. \quad (33)$$

Rearranging Equation (33), we obtain:

$$I(\vartheta, n^{sc}, \|^i) \sim a^2\cos^2\vartheta + \frac{\gamma^2}{45}(6 + \cos^2\vartheta) + \frac{\delta^2}{9}(1 + \sin^2\vartheta). \quad (34)$$

Angular dependence of the three terms on the right-hand side of Equation (34) is displayed in the inset of Figure 4. From here it follows that the angular dependence of a totally symmetric vibration ($a \neq 0, \gamma = 0, \delta = 0$) is dictated by the $\cos^2\vartheta$ function, i.e., the same as encountered in investigating the angular dependence of the dipole radiation in classical physics [12]. For a vibration whose dominant invariant is $\gamma^2$, the detected intensity will only slightly depend on the angle $\vartheta$ via the term $6 + \cos^2\vartheta$. Finally, in the case of resonance Raman scattering, the anisotropic contribution will scale as $1 + \sin^2\vartheta$. It is the only term which experiences its maximum for $\vartheta = 90°$ (anomalous angular dependence).

## 4. Polarization Effects for Crystals and Molecules Adsorbed on Smooth Surfaces

We have demonstrated that Raman scattering measurements of systems consisting of freely rotating molecules allow retrieving only spatially-averaged values of respective squares of Raman tensor elements. However, more detailed information can be extracted from anisotropic systems such as single crystals [33] or molecules adsorbed on planar surfaces possessing some sort of preferential orientation. In single crystals, all molecular axes are lined up within the unit cell in the same direction for each cell. Under these circumstances, polarization of the incident light set to $\vec{e}_q$ and polarization of the scattered light set to $\vec{e}_p$ will pick out only the $\alpha_{pq}$ component of the Raman tensor (see Equation

(8)). Thus, it is possible to analyse each of the Raman tensor elements separately by employing different polarization arrangements. According to Porto's notation, each configuration for Raman scattering measurements of single crystals is unambiguously described by four symbols, such as $i(jk)l$ (where $i,j,k,l = x,y,z$). The symbols inside the parentheses are, left to right, the polarization of the incident and the scattered light, the leftmost symbol denotes the wavevector of the incident light and the rightmost symbol the wavevector of the scattered light [33]. However, in the case of anisotropic systems such as single crystals, the selection rules are a bit stricter in some sense. In the geometry determined by the Porto's notation $i(j,k)l$, only those vibrations covering the same irreducible representation as $jk$ ($j,k = x,y,z$) will be allowed. As a consequence, symmetry species of single crystals of known orientation may be distinguished with the use of polarized radiation. In this paper, we will not deal further with crystal samples, but we will demonstrate how exploiting the formalism of the group theory together with experimental observation can determine the orientation of molecules on (whether planar or rough) surfaces.

In 1982, Moskovits coined the term "surface selection rules" to account for modification of the absorption, emission and Raman scattering intensities of molecules in the vicinity of planar metallic surfaces [34,35], although some considerations concerning variation in near-field intensities with the angle of incidence/polarization had been made before [4,5]. A year later, Creighton derived expressions enabling him to determine the orientation of molecules adsorbed at the surface of a small metallic sphere [36]. Both results show that depending on the molecular orientation with respect to the surface, differences in the relative enhancement of modes belonging to different irreducible representations (symmetry classes) may be expected. Let us first consider the situation on a flat surface and proceed further to molecules adsorbed on plasmonic nanostructures. The latter is a more complicated case due to the fact that in this instance both the symmetry of the Raman tensor and coupling efficiency of the laser light to nanostructures influence the final spectral pattern.

What lies behind the surface selection rules for molecules adsorbed on planar (metallic) surfaces is the fact that the field felt by the analyte may be viewed as a superposition of the incident wave and the reflected wave. In principle, this interference can be both constructive and destructive and the total intensity of a given optical process will depend, among other things, on reflectivity of the substrate (and thus wavelength, of which reflectivity is a function), angle of incidence and polarization. For molecules adsorbed on planar surfaces, the surface selection rules may be interpreted simply in the framework of the Fresnel coefficients. Briefly, when light in vacuum (air) is incident on a planar interface between two different media, the latter possessing a (complex) refraction index $\tilde{n} = n + ik$, it is common procedure to resolve the electric field vectors of both the incident and the reflected wave into two orthogonal components. Assuming that the interface lies in the $xy$ plane, the plane of incidence is $yz$ and light of frequency $\omega$ falls on the interface at an angle $\vartheta$ with respect to the surface normal, the wavevectors of both the incident and the reflected light may be expressed as:

$$\vec{k}_i = \frac{\omega}{c}(0,\ \sin\vartheta\,, -\cos\vartheta), \qquad \vec{k}_r = \frac{\omega}{c}(0,\ \sin\vartheta\,,\ \cos\vartheta), \tag{35}$$

and their electric field vectors as:

$$\vec{E}_i = (E_i^s,\ E_i^p\cos\vartheta\,,\ E_i^p\sin\vartheta), \tag{36}$$

$$\vec{E}_r = \left(E_r^s,\ -E_r^p\cos\vartheta\,,\ E_r^p\sin\vartheta\right) = (r_sE_i^s,\ -r_pE_i^p\cos\vartheta\,,\ r_pE_i^p\sin\vartheta), \tag{37}$$

where the amplitude of the electric field vector of the incident beam projected on the plane of incidence is denoted as $E_i^p$ and on the direction perpendicular to the plane of incidence as $E_i^s$, similarly $E_r^p$ and $E_r^s$ are amplitudes of the electric field vector of the reflected beam projected on the plane of incidence and on the direction perpendicular to the plane of incidence, respectively. $r_s$ and $r_p$ are the Fresnel reflection coefficients for s- and p- polarized light. By applying boundary conditions to the solutions of Maxwell's equations, it can be shown that [12,13]:

$$r_s = \frac{\cos\vartheta - \sqrt{\tilde{n}^2 - \sin^2\vartheta}}{\cos\vartheta + \sqrt{\tilde{n}^2 - \sin^2\vartheta}}, \qquad r_p = \frac{\tilde{n}^2\cos\vartheta - \sqrt{\tilde{n}^2 - \sin^2\vartheta}}{\tilde{n}^2\cos\vartheta + \sqrt{\tilde{n}^2 - \sin^2\vartheta}}. \tag{38}$$

In general, both Fresnel reflection coefficients become complex, thus $r_s \equiv \tilde{r}_s$ and $r_p \equiv \tilde{r}_p$. Interference between the incident and the reflected beam at the interface suggests that the electric field intensity felt by the adsorbed molecules has the components:

$$E_x = E_i^s(1 + r_s), \qquad E_y = E_i^p\cos\vartheta\,(1 - r_p), \qquad E_z = E_i^p\sin\vartheta\,(1 + r_p). \tag{39}$$

Since the real part of $r_s$ is negative and the real part of $r_p$ is usually positive, it is clear that only the $z$ (normal) component of the electric field at the surface will benefit from constructive interference, whereas the other two (tangential) components exhibit rather destructive interference. For most metals, $r_s$ approaches −1 and $r_p$ approaches 1 in the IR and the visible spectral region at angles around ~ 60°. For example, for silver, light intensity associated with the field in the $z$ direction ($E_z^2$) can be as much as ~ 6× stronger than the intensity in other directions ($E_x^2 + E_y^2$) around the wavelength of 500 nm (Figure 5). The difference tends to be even more pronounced in the IR [37].

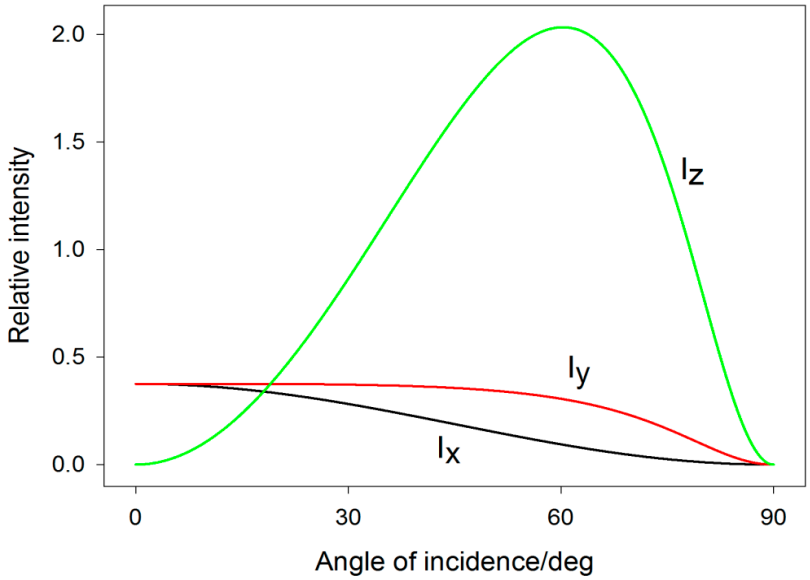


**Figure 5.** Calculated near-field intensities in the vicinity of a smooth Ag surface for an arbitrarily polarized light wave, $\lambda$ = 500 nm. Calculations were performed for different angles of incidence and the refractive index $\tilde{n}_{Ag} = 0.05 + 3.09\mathrm{i}$ [38].

Since IR absorption intensity derives from the scalar product of the transition dipole moment and direction of light polarization, one can deduce that the IR absorption by molecular vibrations with a nonzero component of the transition dipole moment perpendicular to the surface will be strengthened, whereas the absorption by vibrations with the only nonzero component parallel to the surface will be weakened with respect to a "free" molecule [37]. This observation together with the aid of the group theory becomes useful when aiming to elucidate molecular orientation on the surface. Let us illustrate this aspect with a simple example. For each individual molecule, a local Cartesian system of coordinates $x'$, $y'$ $z'$ may be introduced to describe its orientation in space (with z' usually being the principal axis of symmetry). Providing that the molecule binds to the surface so that $x = x', y = y'$ and $z = z'$, the strongest modes observed in the IR spectrum will be those belonging to the irreducible representation with the same transformation properties as $z$. By contrast, in case the molecule is positioned on the surface so that its $z'$ axis lies parallel to the surface, the modes spanning $z$ coordinate are expected to be very weak.

In the case of Raman scattering of molecules adsorbed on flat surfaces, a very similar principle applies in the case of the scattered radiation. Providing that the scattered radiation is collected at an arbitrary angle $\vartheta'$ as shown in Figure 6, the wavevector of the scattered light will be:

$$\vec{k}_{sc} = \frac{\omega}{c}(0,\ \sin\vartheta',\ \cos\vartheta'), \tag{40}$$

the directly scattered laser field is:

$$\vec{E}_{sc} = (E^s_{sc},\ -E^p_{sc}\cos\vartheta',\ E^p_{sc}\sin\vartheta'), \tag{41}$$

and the contribution to the total detected field experiencing a single reflection from the surface will be:

$$(r'_s E^s_{sc},\ r'_p E^p_{sc}\cos\vartheta',\ r'_p E^p_{sc}\sin\vartheta'). \tag{42}$$

Thus, the total detected field will have the components:

$$E_x = E^s_{sc}(1 + r'_s), \qquad E_y = E^p_{sc}\cos\vartheta'\left(r'_p - 1\right), \qquad E_z = E^p_{sc}\sin\vartheta'\left(1 + r'_p\right). \tag{43}$$

As usual, $E^p_{sc}$ and $E^s_{sc}$ denote the amplitudes of the electric field vector of the scattered radiation projected on the plane of incidence and on the direction perpendicular to the plane of incidence, respectively. The prime in $r'_s$ and $r'_p$ refers to the fact that the scattered radiation is slightly shifted in frequency and thus also the Fresnel reflection coefficients may be slightly shifted. Combination of Equations (8), (39) and (43) gives:

$$I_{vv} \sim |\alpha_{xx}(1 + r_s)(1 + r'_s)|^2, \tag{44}$$

$$I_{hv} \sim \left|\alpha_{xy}(1 + r'_s)\left(1 - r_p\right)\cos\vartheta + \alpha_{xz}(1 + r'_s)\left(1 + r_p\right)\sin\vartheta\right|^2, \tag{45}$$

$$I_{vh} \sim \left|\alpha_{yx}(1 + r_s)\left(r'_p - 1\right)\cos\vartheta' + \alpha_{zx}(1 + r_s)(1 + r'_p)\sin\vartheta'\right|^2, \tag{46}$$

$$\begin{aligned} I_{hh} \sim |&\alpha_{yy}(1 - r_p)(r'_p - 1)\cos\vartheta\cos\vartheta' \\ &+ \alpha_{yz}(1 + r_p)(r'_p - 1)\sin\vartheta\cos\vartheta' + \alpha_{zy}(1 - r_p)(1 + r'_p)\sin\vartheta'\cos\vartheta \\ &+ \alpha_{zz}(1 + r_p)(1 + r'_p)\sin\vartheta\sin\vartheta'|^2. \end{aligned} \tag{47}$$

Equations (44)–(47) are known as the surface selection rules [34,35].

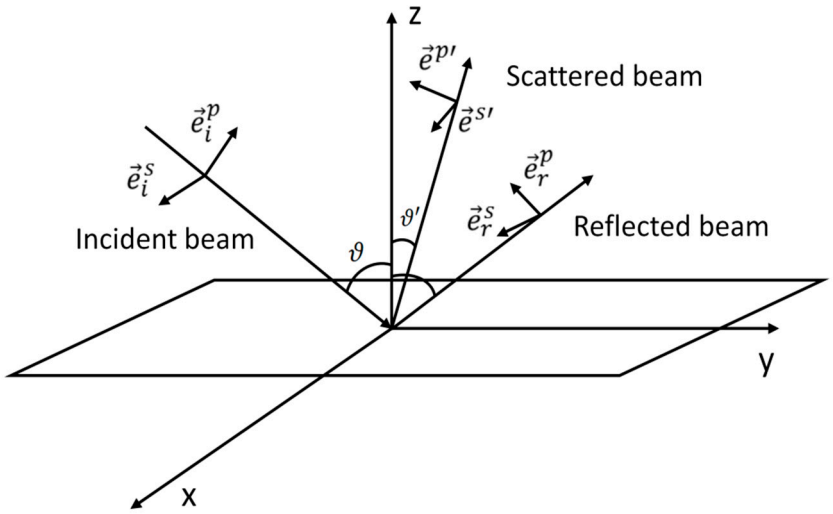


**Figure 6.** Scheme of the geometrical layout and definition of the coordinates. All symbols have usual meanings as described in the text. The components of the scattered field experiencing a reflection from the surface ($\vec{E}^{s\prime}_r$ and $\vec{E}^{p\prime}_r$) are not included in the scheme for simplicity.

## 5. Polarization Effects for Molecules on Plasmonic Nanostructures

Polarization-dependent effects for molecules located in presence of plasmonic nanostructures are much more complex in comparison to "free" molecules. The principal reason is that the enhancement provided by plasmonic nanostructures is polarization-sensitive and is therefore commonly accompanied by dramatic alteration of polarizations of both the incident beam as well as of the scattered beam. Local field polarization is dictated mainly by coupling of the given light polarization in the metallic nanostructures and the similar process applies in the case of the scattered field. As a result, polarization felt by the molecule can be drastically different from polarization of the incident beam. It causes the depolarization ratio to no longer depend only on the intrinsic properties of the Raman tensor of the analyte, but also (and often mainly) on the geometry of the given nanostructure [39–41]. This difference occurs even in the simplest nanostructure geometries, such as a small sphere in the dipole approximation, it can be commonly observed in arrays of elongated nanoparticles (NPs) and is most pronounced for molecules in the location of hot-spots which exhibit anisotropic behaviour [40,42]. Since different polarizations couple to metallic nanostructures with different efficiency, the enhancement factor (EF) can no longer be regarded as a scalar but it takes the form of a tensor. In this case, the polarization and angular dependence of the SERS signal is therefore mostly dictated by the coupling of the laser to the plasmons while symmetry of the Raman tensor of the analyte often plays a minor role [39,40,43].

### *5.1. Polarization Properties of Isolated Spherical Particles*

The case of an isolated metallic sphere in the dipole approximation was theoretically studied in [36,44]. Theoretical analysis reveals that the enhanced local field in the vicinity of a small metallic sphere after illumination with a light wave may be expressed in the electrostatic approximation in spherical coordinates as:

$$\vec{E} = E_0\big(1 + 2g(\omega)\big)\cos\vartheta\,\vec{e}_r - E_0\big(1 - g(\omega)\big)\sin\vartheta\,\vec{e}_\vartheta, \tag{48}$$

i.e., the normal field components with respect to the sphere undergo the enhancement by the factor of $A_r = 1 + 2g(\omega)$ while the tangential component is enhanced by the factor of $A_\vartheta = 1 - g(\omega)$, where $g(\omega) = \frac{\varepsilon(\omega)-\varepsilon_r}{\varepsilon(\omega)+2\varepsilon_r}$ is the geometrical factor for a sphere. The relative permittivity of the surrounding medium is denoted as $\varepsilon_r$. Therefore, amplification of the surface field for any point on the surface of the sphere is determined by the matrix:

$$\overleftrightarrow{A}_{r,\vartheta,\varphi} = \begin{pmatrix} 1 + 2g(\omega) & 0 & 0 \\ 0 & 1 - g(\omega) & 0 \\ 0 & 0 & 1 - g(\omega) \end{pmatrix}. \tag{49}$$

As a consequence, molecules with certain elements of symmetry and preferential orientation with respect to the surface will exhibit differences in the relative enhancements of modes belonging to different symmetry classes. Averaging over all solid angles (all positions on the metallic sphere) reveals that the ratio of tangential to normal intensities is:

$$\frac{\langle E_r^2\rangle}{\langle E_\vartheta^2\rangle} = \left|\frac{1 + 2g(\omega)}{1 - g(\omega)}\right|^2 \frac{\int \cos^2\vartheta\,\mathrm{d}\Omega}{\int \sin^2\vartheta\,\mathrm{d}\Omega} = \frac{1}{2}\left|\frac{1 + 2g(\omega)}{1 - g(\omega)}\right|^2. \tag{50}$$

In the early 1980s, Moskovits pointed out the existence of three classes of vibrational modes with distinct spectral behaviour (unique excitation profile) [35,45]: (1) those excited only by the normal component of the field and resulting in an induced dipole with a strong component only in the direction perpendicular to the surface; (2) those excited only by the tangential component of the field and resulting in an induced dipole with a strong component tangential to the surface; and (3) mixed cases. EF for respective molecular vibrational modes will thus depend on the orientation of the molecule on the surface. Let us assume that a molecule possessing certain symmetry is adsorbed on the surface so that its principal axis ($z$ axis) is perpendicular to the sphere. Then, the modes of the first type are modes spanning the same irreducible representation as $\alpha_{zz}$. SERS intensity of these modes is expected to obey the relationship:

$$I_{nn} \sim |1 + 2g(\omega_i)|^2 |1 + 2g(\omega_s)|^2. \quad (51)$$

By contrast, modes spanning the same irreducible representation as $\alpha_{xx}$, $\alpha_{yy}$ or $\alpha_{xy}$ benefit only from the existence of the electric field tangential to the surface. Thus,

$$I_{tt} \sim 4|1 - g(\omega_i)|^2 |1 - g(\omega_s)|^2. \quad (52)$$

Finally, modes excited by the normal component of the field and resulting in an induced dipole with a strong component only in a direction parallel to the surface, or vice versa, will be characterized by the excitation profile:

$$I_{nt,tn} \sim \frac{1}{2}(|1 + 2g(\omega_i)|^2 |1 - g(\omega_s)|^2 + |1 + 2g(\omega_s)|^2 |1 - g(\omega_i)|^2). \quad (53)$$

As usual, $\omega_i$ denotes frequency of the excitation radiation and $\omega_s$ frequency of the scattered radiation. It is clear that the SERS excitation profiles associated with the three types of modes obey the wavelength dependence of the right-hand sides of Equations (51)–(53) (Figure 7). By contrast, when the molecule adsorbs with the $z$ axis tangential to the surface, the role of $z$ and $x$ (or $y$) in the character table is to be swapped. This fact provides a unique tool for determination of molecular orientation on nanostructured metallic surfaces [45–48].

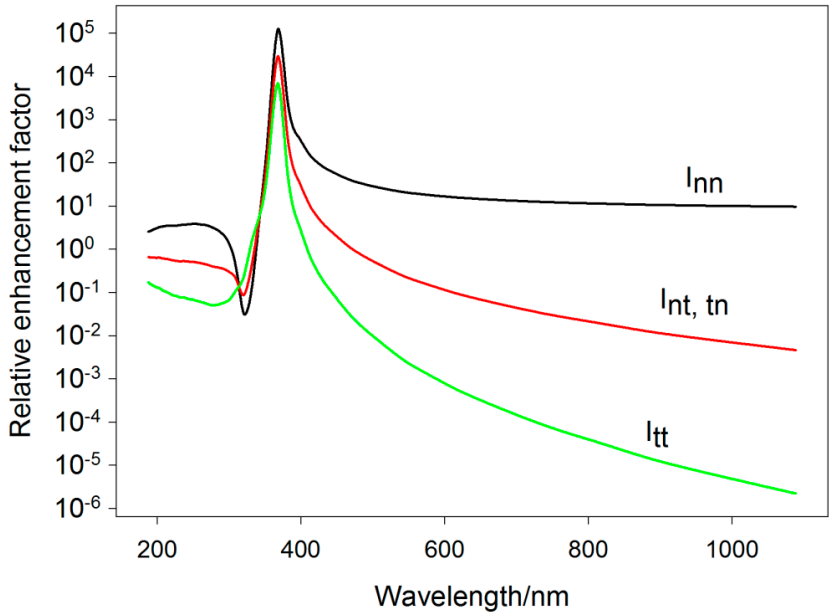


**Figure 7.** Calculated wavelength-dependent relative enhancement factor for molecules adsorbed in the vicinity of a small silver sphere for the three classes of Raman modes. $\varepsilon_r$ was assumed to be 1.33.

Due to disrupted spherical symmetry in the case of non-spherical particles, the polarization insensitive SERS EF is expected to split into two (or more) geometry-dependent components. For example, in the case of prolate spheroids, only the incident field polarized parallel to the long axis results in the greatest surface fields [49]. Such electrodynamic calculations were performed already in the 1980s and their understanding is a key for elucidation of the polarization-resolved optical response of more complex systems such as elongated particles or nanorods (NRs), which will be discussed in more detail in the second part of this section.

### *5.2. Local Field Distribution in Presence of Hot-Spots and Its Relation to Molecular Orientation*

Unfortunately, the optical response of very few plasmonic systems can be computed as straightforwardly as shown in Section 5.1. Both the experimental results as well as the theoretical calculations show that electromagnetic field can be confined in nanometer-sized metallic clefts. Analytical treatment of a two sphere system, performed already in the 1980s [50,51], suggests that

molecules residing in a nanogap between the NPs are subjected to ~ $10^5$× stronger electromagnetic field in comparison to the field enhanced by one single NP. Due to mutual interaction, electromagnetic field in such cavities is much larger than the sum of the fields caused by two non-interacting spheres, which has been explained by strong electromagnetic coupling between the NPs, giving rise to coupled plasmon resonances [13,35,52–54]. Coupled plasmon resonances are characterized by much dramatic difference in responses to different polarizations. Such an extreme enhancement occurs only if the incident polarization is along the interparticle axis. For light polarized across the interparticle axis, the enhancement is almost negligibly different from its value at a single, isolated particle [40,42]. Closer analysis shows that with NP radii of 45 nm (average size of the silver NPs used) and the separation distance of $d$ = 5.5 nm (diameter of a hemoglobin molecule, [52]), the enhancement effect adds another ~ 2–3 orders of magnitude in comparison to isolated NPs and further ~ 2–3 orders of magnitude after decreasing the NP gap down to ~ 1 nm, making the total EF of ~ $10^{11}$. Nowadays, SERS EFs of ~ $10^{11}$–$10^{12}$ are considered to be theoretical limits (for silver) on account of the electromagnetic contribution, sufficient even for observation of single-molecular SERS [55–57]. Not surprisingly, there often exists an inverse relationship between the EF and reproducibility of the substrate used ("SERS uncertainty principle").

The extremely spatially-localized sites providing extreme enhancement were dubbed hot-spots in the literature [13]. However, geometry of hot-spots is not restricted only to two mutually interacting spheres. Generally, for systems of aggregated particles with nanoscale crevices or junctions where interparticle separation can be made very small, extremely localized regions of ultrahigh enhancement were predicted [53] as well as experimentally demonstrated [56,58–60]. It means that the enhancement in the gap region where majority of the electromagnetic energy is packed completely overwhelms the surface average and produces the dominant contribution to single-molecular sensitivity in SERS. Besides, theory also predicts very strong enhancement of the electromagnetic field at sharp metallic tips and large curvature regions due to so-called lightning-rod effect. In hot-spot dominated systems, information on the symmetry of the Raman tensor (or molecular depolarization ratio, Equation (24)) is almost completely overridden by anisotropic pattern of the nanostructures.

Let us take a closer look at the simplest case of a hot-spot—a dimer formed by two metallic NPs. Let us adopt such a Cartesian system of coordinates that the dimer axis is parallel with the $x$ axis as depicted in Figure 8. In this case, the optical response of a molecule situated in the gap between the two NPs is completely dominated by polarization in the $x$ direction (Figure 9).

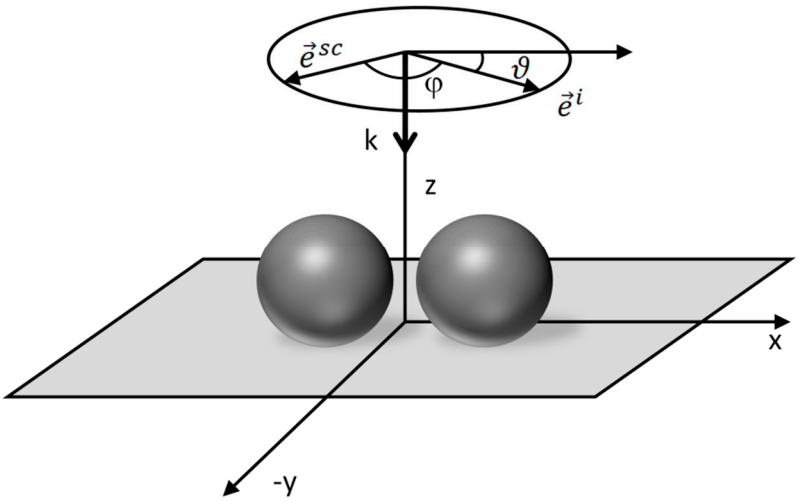


**Figure 8.** Geometry of a dimer. The Cartesian coordinate system is chosen so that the dimer axis lies in the $x$ direction, the excitation beam travells along the $z$ direction with the incident polarization making an angle $\vartheta$ with the $x$ axis. Scattered radiation is assumed to be collected in a backscattering geometry, allowing only the polarization making an angle $\varphi$ with respect to the incident polarization (i.e., making an angle $\vartheta + \varphi$ with respect to the $x$ axis) to be detected.

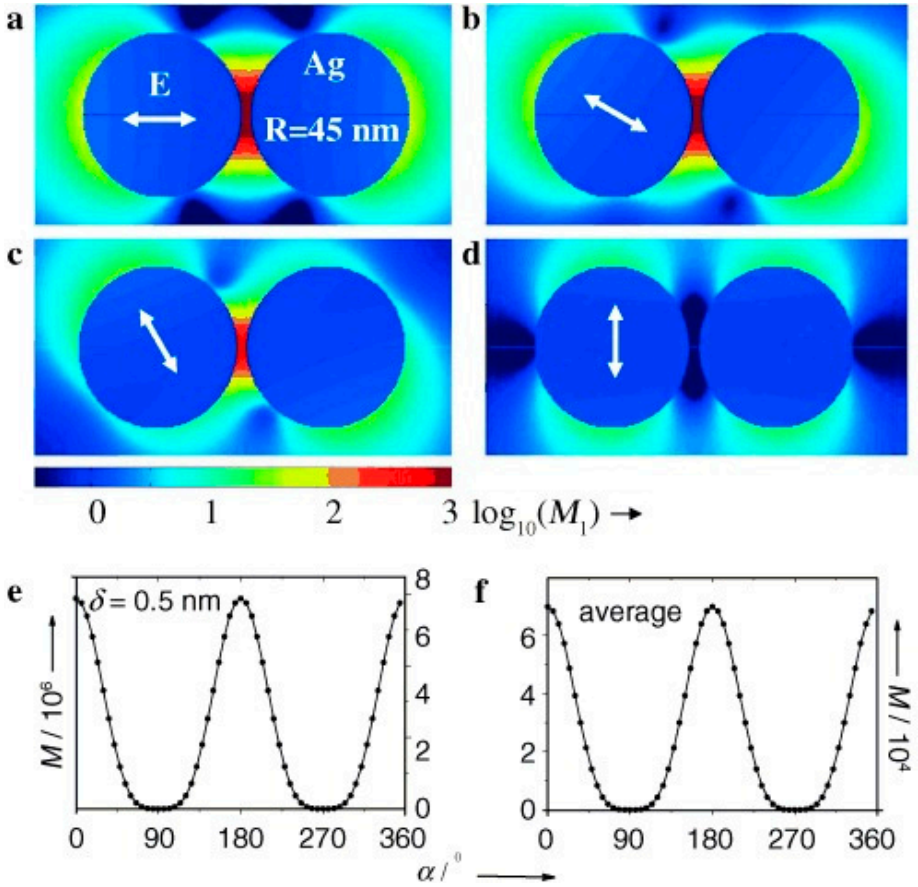


**Figure 9.** Local intensity enhancement $M_1 = (\frac{E_{loc}}{E_0})^2$ in a logarithmic scale in a plane through the centers of the Ag spheres and perpendicular to the incident wavevector $\vec{k}$ versus incident polarization: (**a**) 0°; (**b**) 30°; (**c**) 60° and (**d**) 90°. The incident wavelength was 514.5 nm in all cases. The arrows represent the different polarizations. In (**e**), the SERS enhancement factor $M = M_1^2$ is shown as a function of the incident polarization $\alpha$ for a point in the nanogap located at the dimer axis $\delta = 0.5$ nm away from one spherical surface, and the fit (solid line) to a $\cos^4\alpha$ dependence. In (**f**), $M$ averaged over all points $\delta = 0.5$ nm outside the Ag sphere surface versus $\alpha$ and fit to a $\cos^4\alpha$ dependency are shown. The radius $R = 45$ nm corresponds to the average size of the Ag nanoparticles used in the experiment while the separation distance $d = 5.5$ nm corresponds to the diameter of a hemoglobin molecule. Reprinted with permission from [54].

As already mentioned, the ratio of obtained intensities for polarization parallel/perpendicular to the dimer axis may amount to $10^5$. Therefore, the SERS response for polarization perpendicular to the dimer axis can be neglected (the enhancement effect of the dimer is comparable to that of one isolated particle in this case). Thus, assuming that the incident wavevector lies in the $z$ direction, local field strength for polarization making an angle $\vartheta$ with respect the $x$-axis will be:

$$E_{local} = \gamma E_0 \cos\vartheta. \tag{54}$$

In other words, amplification of the surface field is of tensorial nature and can be expressed as:

$$\overleftrightarrow{A} = \begin{pmatrix} \gamma & 0 & 0 \\ 0 & 1 & 0 \\ 0 & 0 & 1 \end{pmatrix}. \tag{55}$$

The factor $\gamma$ represents amplification of the laser field polarized along the $x$-axis. Similarly to the incident radiation, also the scattered radiation exhibits different coupling efficiency depending on the angle made between the dimer axis. Thus, the local field should scale as $\sim \cos\vartheta$ and the local intensity as $\sim \cos^2\vartheta$. Assuming the backscattering geometry and for simplicity the same EF for both the incident and the scattered radiation, respective intensities obey the following trends:

$$I\left(180°,\perp^{sc},\perp^{i}\right)=I\left(180°,\|^{sc},\|^{i}\right)\sim\cos^{4}\vartheta,\ \text{(parallel polarizations)},\tag{56}$$

$$I\left(180°,\|^{sc},\perp^{i}\right)=I\left(180°,\perp^{sc},\|^{i}\right)\sim\cos^{2}\vartheta\sin^{2}\vartheta,\ \text{(crossed polarizations)},\tag{57}$$

and the depolarization ratio is:

$$\rho=\mathrm{tg}^{2}\vartheta,\tag{58}$$

which diverges for $\vartheta=90°$. In this crudest approximation, the depolarization ratio is determined solely by the plasmonic nanostructures and is not by any way linked to the molecular depolarization ratio.

The theoretical predictions above may be easily verified experimentally in the case of colloids. Colloids may be regarded as a collection of randomly oriented hot-spots where the overall SERS signal usually originates from a few molecules residing in the hot-spot sites and the rest occupying the less enhancing sites [40]. Although an extremely small percentage (difficult to determine precisely) of molecules actually cover the hottest sites, their presence is decisive for the total enhancement [61,62]. Integration over random orientations of a collection of dimers in standard azimuthal coordinates (Equation (5)) yields:

$$\rho=\frac{\iint\cos^{2}\vartheta\,\sin^{2}\vartheta\,\cos^{2}\varphi\,\mathrm{d}\Omega}{\iint\cos^{4}\vartheta\,\mathrm{d}\Omega}=\frac{1}{3},\tag{59}$$

which is the expected value of the depolarization ratio observed experimentally [41,43]. Extremely low detection limits for molecules adsorbed on hot-spot dominated SERS active systems opposed to almost complete loss of more detailed information on the symmetry of the vibrations involved may be viewed as another consequence of the SERS uncertainty principle.

Let us demonstrate some of the previous theoretical aspects on the Raman spectra of methylene blue (MB) measured in our laboratory in both $\left(90°,\perp^{s},\perp^{i}\right)$ ($I_{vv}$) and $\left(90°,\|^{s},\perp^{i}\right)$ ($I_{vh}$) experimental configurations (Figure 10). MB was in the form of a water solution (concentration $10^{-4}$ M) and in hydroxylamine-reduced Ag NPs (final MB concentration of $10^{-6}$ M), prepared by the standard procedure [63]. In both cases the excitation wavelength was 532 nm, therefore both spectra should be considered as preresonance ones. This brings certain difficulty with fluorescence and the need for baseline subtraction in the case of non-SERS measurements, which makes determination of respective peak intensities more difficult, however, all basic principles highlighting the differences in Raman/SERS depolarization ratios are retained.

MB belongs to the $C_2$ point group possessing 108 normal vibrational modes distributed among A and B symmetry species as $\Gamma^{3N-6}=54\mathrm{A}\oplus54\mathrm{B}$ (A denoting the totally-symmetric vibrations and B the non-totally symmetric vibrations). Respective bands in Figure 10 are labelled as A or B on the basis of theoretical calculations adapted from [64].

From Figure 10, several conclusions can be drawn. First, it is obvious that the most intense bands in preresonance Raman (non-SERS) spectrum are almost entirely the A species, which is fully consistent with the theory of resonance Raman scattering. Second, evaluation of the Raman depolarization ratios reveals that for the A species $\rho$ lies between ~ 0.19 and 0.23 while for the B species $\rho$ is up to ~ 0.45, approximately twice as much as for A. This is again in full compliance with the theory according to which the depolarization ratio of symmetric vibrations (A) is always lower than for non-totally symmetric vibrations (B). However, this difference in the depolarization ratios between A and B species is wiped out completely when the measurement is performed on a silver colloid where the depolarization ratios are (within the experimental error) all around 1/3, irrespective of the symmetry of the vibration involved. Since at lower analyte concentrations, molecules are expected to adopt sub-monomolecular surface coverage and tend stack up in multiple layers at higher analyte concentrations, series of concentration-dependent polarization-resolved SERS measurements while monitoring the depolarization ratios could represent a unique way to distinguish these two regimes.

Figure 11 shows our results from concentration-dependent MB SERS measurements. Singular value decomposition algorithm [65] based on factor analysis was employed to treat the spectral set.

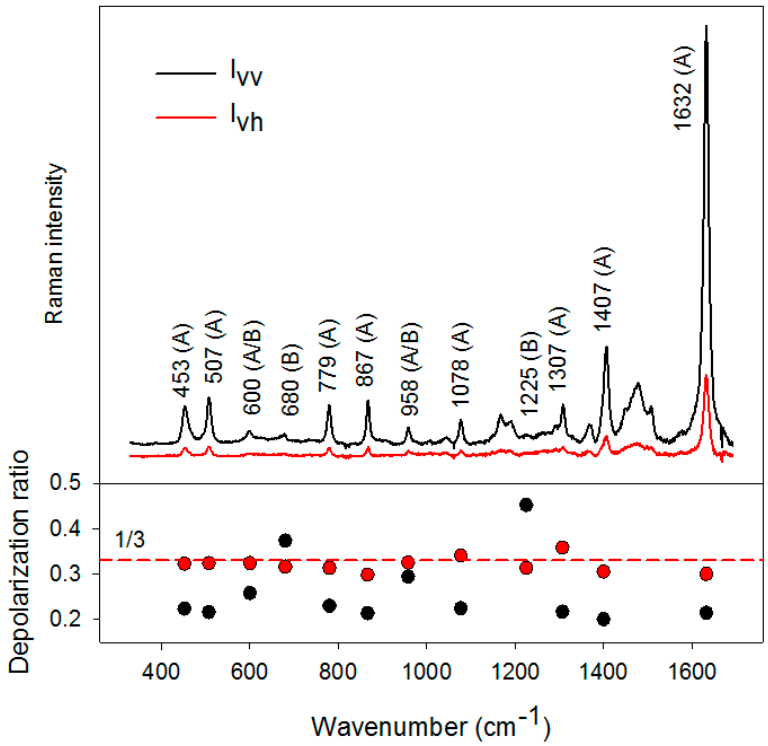


**Figure 10.** Polarized (preresonance) Raman spectra of methylene blue (MB) in a water solution (excitation wavelength 532 nm; after fluorescence baseline subtraction) and corresponding depolarization ratios (black dots). Symmetry species of respective vibrational modes are indicated in the upper part. Comparison with the depolarization ratios obtained from hydroxylamine-reduced Ag NPs is indicated by red dots (SERS spectra are not shown for better clarity). MB concentration was $10^{-4}$ M, laser power 100 mW, accumulation time 5 min.

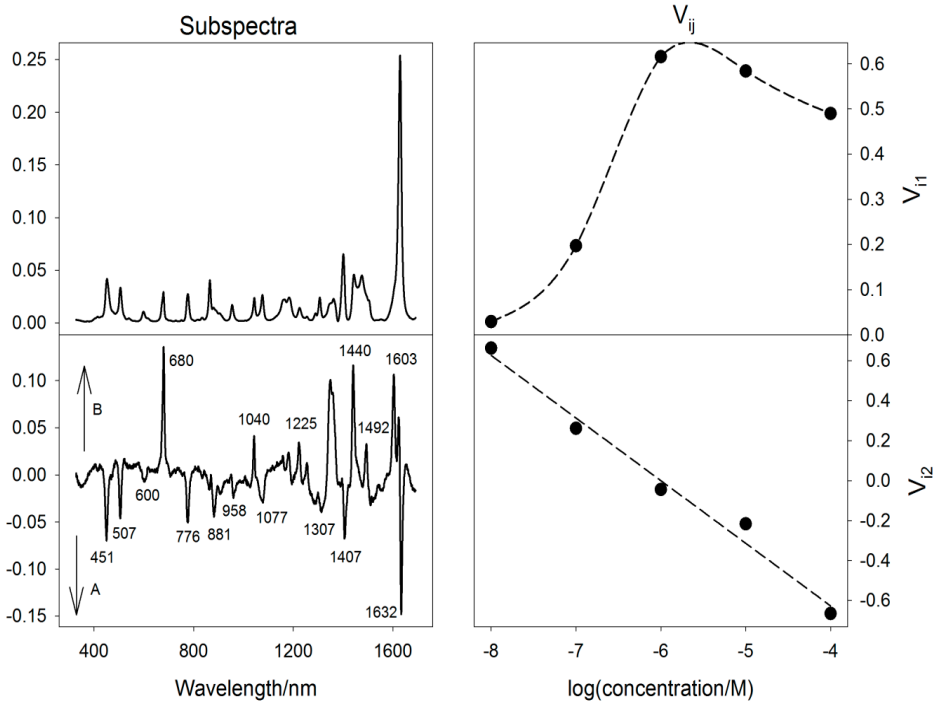


**Figure 11.** Results of factor analysis of concentration-dependent SERS measurements of methylene blue (MB). Profile of the $V_{i1}$ coefficients reflects the variation in MB SERS intensity with concentration. Profile of the $V_{i2}$ coefficients and the shape of the second subspectrum reveal a systematic decrease in the ratio of EFs for B/A modes with increasing concentration (cf. Figure 10).

Profile of the $V_{i1}$ coefficients reflects the variation in total MB intensity with concentration. As expected, Raman intensity rises when MB concentration is increased from $10^{-8}$ M to ~ $10^{-6}$ M concentration but starts to decrease when further increasing MB concentration, probably due to MB aggregation and less efficiency in occupying the highest-enhancing sites. After normalizing the original spectral set using the $V_{i1}$ coefficients, the $V_{i2}$ coefficients were found almost perfectly linear (in a semi-logarithmic scale) with concentration with the second subspectrum highlighting the differences between A and B symmetry modes. In other words, when increasing MB concentration, the ratio of EFs for B/A modes is systematically decreasing. This finding clearly reveals a change in MB adsorption geometry with concentration, adopting a face-on adsorptive stance at lower concentrations and a preferable edge-on adsorptive stance at higher concentrations [64,66].

Efforts to make use of the enhancement capability of dimers are still very lively in literature, which can be documented by numerous studies from the last years [67–74], benefiting from extremely high enhancement between two adjacent metallic NPs or between a metallic NP and a substrate. A very promising analytical tool for biosensing applications include DNA origami, [75–77] where NPs with defined distance can be constructed. However, all these illustrations raise a question about whether or not there exists a general rule to reveal some information regarding the Raman tensor elements of the analyte (intrinsic properties of the SERS probes) by measurements on nanostructured metallic surfaces. Correlation between the morphological anisotropy and symmetry of the vibrational species was found in [78]. Using a well-established pyridine molecule, the authors demonstrated that the in-plane (ring stretching) vibrational modes are sensitive to the morphological anisotropy while the out-of-plane (ring deformation) modes are not. A more in-depth approach was developed by P. Gucciardi et al. [31,39,43], who in his analysis went beyond the commonly used $E^4$ approximation. For a hot-spot represented by a dimer with the axis lying in the $x$ direction, the authors used the field enhancement tensor in the form:

$$\overleftrightarrow{A}(\omega_i) = \begin{pmatrix} \gamma & 0 & 0 \\ 0 & 1 & 0 \\ 0 & 0 & 1 \end{pmatrix}, \tag{60}$$

and the re-radiation enhancement tensor as:

$$\overleftrightarrow{A}(\omega_{sc}) = \begin{pmatrix} \gamma(1+\varepsilon) & 0 & 0 \\ 0 & 1 & 0 \\ 0 & 0 & 1 \end{pmatrix}, \tag{61}$$

where ε is a small perturbation accounting for the difference between the enhancement for the incident and the scattered radiation. The local field felt by the analyte and the amplified scattered field are thus:

$$\vec{E}_{local} = \overleftrightarrow{A}(\omega_i)\vec{E}_i, \qquad \vec{E}_{SERS} = \overleftrightarrow{A}(\omega_{sc})\vec{E}_{sc}. \tag{62}$$

These two fields are actually those that enter Equation (8). The theoretical SERS intensity for many randomly oriented molecules as a function of the angle $\vartheta$ and $\varphi$ (see Figure 8) was found to be:

$$\begin{aligned} I \sim \gamma^4(1+\varepsilon)^2\langle\alpha_{ii}^2\rangle\cos^2\vartheta\cos^2(\vartheta+\varphi) + \gamma^2(1+\varepsilon)\langle\alpha_{ii}^2\rangle[1/2\sin 2\vartheta \sin 2(\vartheta+\varphi)] + \\ + \gamma^2\langle\alpha_{ij}^2\rangle[\varepsilon\sin\vartheta\cos(\vartheta+\varphi) + \sin\varphi]^2 + \langle\alpha_{ii}^2\rangle\sin^2\vartheta\sin^2(\vartheta+\varphi). \end{aligned} \tag{63}$$

Equation (63) indicates that the total intensity contains a term proportional to $\gamma^4$ ( $E^4$ approximation) but also other terms beyond the $E^4$ approximation. More importantly, this equation also suggests how the molecular depolarization ratio (the quantity corresponding to $\langle\alpha_{ij}^2\rangle/\langle\alpha_{ii}^2\rangle$ that would be measured for a "free" molecule without the presence of metallic nanostructure) is influenced by the EF and the experimental geometry. The diagonal terms of the Raman tensor of the analyte are enhanced as $\sim\gamma^4$ but the non-diagonal terms only as $\sim\gamma^2$, which suggests that with higher $\gamma$, the effect of the geometrical shape of the nanostructure will be dominant. Since the role of the EF $\gamma$ in Equation (63) is crucial, virtually causing linearization of the polarization of both the incoming and the outgoing light, it remains very difficult to verify this formula experimentally [31,79]. More detailed discussion can be found in [31].

*5.3. Polarization Properties of Trimers and Aggregated NP Domains*

Polarization properties of trimers have been studied in [80]. The third particle breaks the dipolar symmetry of the two-particle junction, generating a wavelength-dependent polarization pattern, which was not observed in the case of a dimer. In general, polarization-dependent profile of more complex NP clusters is expected to exhibit multiple maxima and minima, often reflecting symmetry of the nanocluster array [40] (Figure 12). If the enhancement at one specific point were monitored (such as a gap between 2 adjacent NPs), full anisotropy would be observed. Although the SERS characteristics of any single probe-adsorption were found to depend on polarization for trimers in [81] as well as supported by finite-difference time-domain (FDTD) simulations, the periodic array of regular Ag NP trimers was found to form a polarization-independent SERS signal. This fact was attributed to a global structural $D_{3h}$ symmetry of the nanopit area. The polarization independence was even better as compared to large-area Ag nanowires and randomly disordered Ag NPs of uneven size, producing clearly discrepant SERS signals under different incident polarizations. Thus, supposing the surface is uniformly covered with an analyte, such clusters will show a considerable degree of isotropy as a whole [58,82,83].

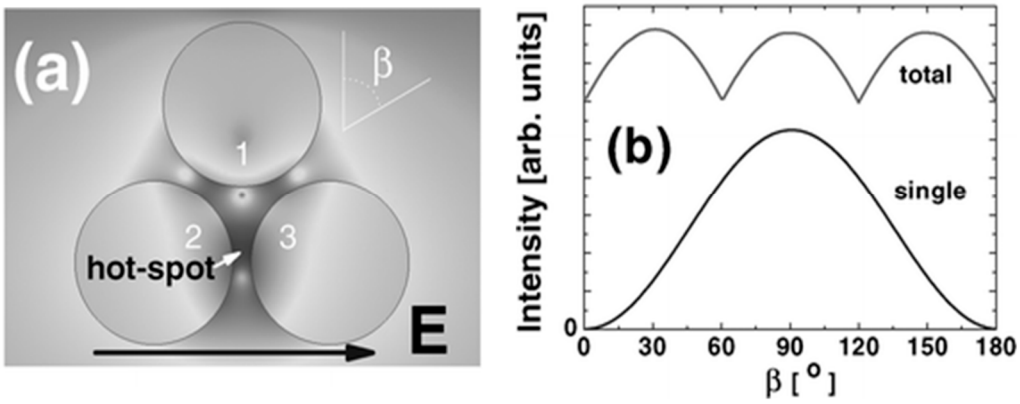


**Figure 12.** A simple example of a cluster with quasi-isotropy. In this case an example of a 2D cluster formed by three cylinders (radii = 25 nm) with a small separation gap ($d$ = 6.7 nm) is shown. The problem is solved in the electrostatic approximation, wavelength = 357 nm. The polarization is changed in the plane for different angles $\beta$ as shown in (**a**) where the electromagnetic intensity (on a logarithmic grey-scale) is explicitly shown for the case $\beta = 90°$. A hot-spot in between cylinders 2 and 3 can be easily seen. If we look at the maximum enhancement at any point on the surface of the cluster, there will always be a place that profits the most from the particular orientation of the field and we obtain the curve labelled as ''total'' in (**b**). The three maxima in the latter are the three possible two-cylinder hot-spots in this cluster that achieve their highest value when the field is aligned along the axis joining any two of them. If the surfaces were uniformly covered with analyte, an almost isotropic response is obtained. The degree of isotropy increases with the complexity of the cluster. However, if the enhancement at one specific point is monitored (in this case the enhancement in the gap in between 2 and 3) we obtain the curve labelled as ''single'' in (**b**) which shows the full anisotropy of any single hot-spot. Adapted from [40] with permission from The Royal Society of Chemistry.

Similar conclusion was supported in [84] using arrays of NRs prepared by inkjet printing technique, or by Shegai in [85]. Shegai attributed different depolarization ratios of different rhodamine 6G bands adsorbed on silver nanocrystal aggregates to charge transfer resonances since the electromagnetic field around the nanocrystals was found near-isotropic. A more theoretical approach was adopted in [86]. Making use of the group theory, the authors showed that a nanostructure that belongs to $C_n$ symmetry point group ($n \geq 3$) has an optical response that is insensitive to the light polarization when the wavevector is parallel to the $C_n$ axis. Attempts have been made to verify this claim experimentally using arrays of nanotriangles, nanostars and other nanoobjects [87]. However, due to non-negligible relative standard deviation of the SERS

measurements and the fact that the theoretical criteria mentioned above are not perfectly met, the decision whether or not there exists a polarization-dependent pattern is often difficult.

### *5.4. Polarization Properties of Regular Solid Plasmonic Platforms*

Considerations above can be analogously extended to many other plasmonic platforms possessing anisotropic morphology fabricated using various procedures [88]. For example, polarization properties of metallic nanocubes [89–91], arrays of silver NP rows [92], gold nanoassemblies [93], metallic gratings structures [94], half-shells [95] etc. were studied in literature. A frequently-studied SERS-active system from the point of view of polarization and angular characteristics are arrays of elongated NPs appearing under different names in literature such as NRs [96–99], nanowires [43,60,100–103], nanoantennas [104,105], nanorattles [106,107], nanobones [108] or NP-nanowire systems [109–111] where the $\sim \cos\vartheta$ trends were often observed (Figures 13–15). Published results indicate that the optical response for light polarized parallel/perpendicular to the long axis of the nanoobjects (related to excitation of longitudinal plasmon modes (LM) or transverse plasmon modes (TM), respectively) is indeed different. However, the SERS intensity profile with varying angle/polarization is a function of a wide range of parameters, such as the dimensions of the metallic objects, their aspect ratios and spatial arrangement, material (Ag or Au), the excitation wavelength or orientation of the probe molecules on the surface [85,112,113], which resulted in seemingly contradictory accounts appearing in literature. Last but not least, what hampers more precise analyses of the angular and polarization effects is sample bleaching and photodecomposition induced by the incident laser, which causes poorer reproducibility and brings further uncertainty to the set of experimentally measured points. This aspect was usually resolved in the literature by applying a correction assuming exponential decay of the SERS signal with time [81,97,109]. Polarization-dependent properties of SERS microarrays also found use in elimination of the polarization insensitive spurious bands originating from the bulk material [94].

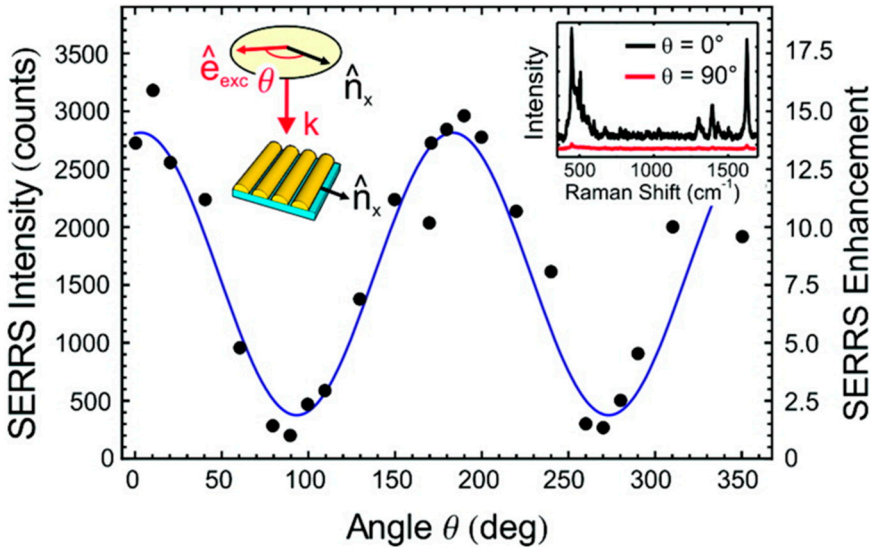


**Figure 13.** Unpolarized SERS intensity of methylene blue adsorbed on gold nanowires (NWs) versus excitation polarization $\theta$ as measured in a backscattering geometry. SERS intensity was found maximum for $\theta = 0°$ (inset, black line), i.e., for incident polarization vector (denoted as $\vec{e}_{exc}$) parallel to the nanocavity axis $\vec{n}_x$, and minimum for $\theta = 90°$ (inset, red line), i.e., $\vec{e}_{exc}$ parallel to the NWs long axis $\vec{n}_y$. The SERS intensity profile was well fitted with the $\sim \cos^2\vartheta$ law (blue line), plus low order terms (Equation (63)). Excitation wavelength was 633 nm, thus the SERS spectrum is considered as a resonance one (SERRS). Adapted with permission from [43]. Copyright 2011 American Chemical Society.

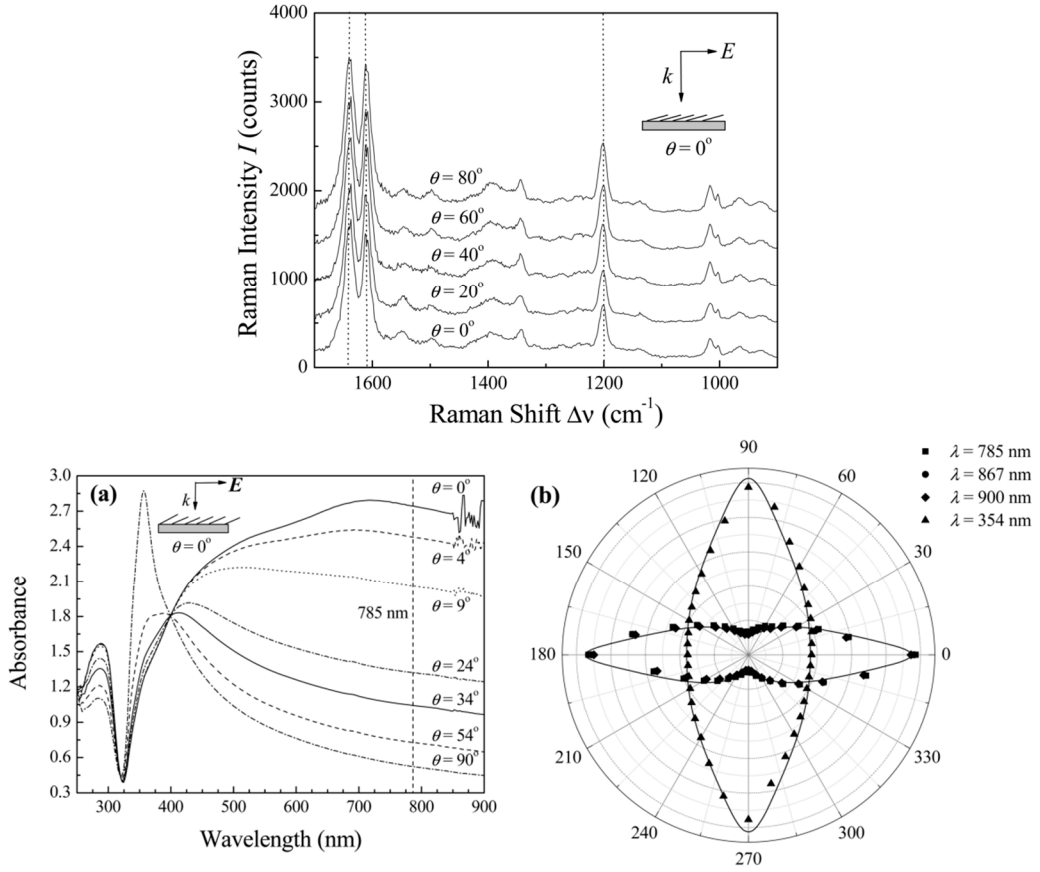


**Figure 14.** (**a**): Polarized SERS spectra of trans-1,2-bis(4-pyridyl)-ethene (BPE) on Ag nanorod substrates as a function of the incoming polarization angle measured in a backscattering geometry. (**b**): Polarized UV/Vis/NIR absorption spectra. Cross-section of the NR array is schematically depicted in the inset (inclination angle of the nanorods was ~ 71° with respect to the surface normal). Both diagrams show the p-polarization direction with the incident polarization almost parallel to the major long axis of the nanorods. The maximum SERS intensity was observed in the polarization direction perpendicular to the long axis of the Ag nanorods, while the UV/Vis absorbance was strongly polarized along the direction of the long axis of the NR array. Adapted with permission from [97]. Copyright 2006 American Chemical Society.

Although theory predicts the difference in the EFs for different light polarizations up to ~ $10^5$ (for an ideal structure [53,54]), in reality, this factor is much more modest. For example, the ratio of SERS responses in the directions parallel/perpendicular to the NRs was found to be around 0.8 for silver NRs as reported in [97]. This finding was attributed to the lateral arrangement of the NR lattice and strong electromagnetic coupling between adjacent metallic NRs instead of preferential molecular orientation of the probe molecule on the surface. A similar trend was observed for coupled metallic nanowires [60], oriented silver nanowire films [101], silver nanowire rafts [100] or self-organized gold nanowires [43]. In all these cases the SERS intensity ratios for light polarized perpendicular/parallel with respect to the NR axes was found around 5 (see Figure 13) and explained by excitation of a new plasmon mode trapped in the interstices between adjacent, parallel wires, similarly to the case of a dimer. However, this only happens if the interwire distance is sufficiently small (< ~ 10 nm) [60]. By contrast, antenna arrays similar to bent needles [104], nanorattles [106], single gold NRs [99] or aligned Ag NRs prepared by a dynamic oblique deposition technique [98] were all found to exhibit the enhancement higher for excitation light polarized parallel to the needle/NR direction than for the perpendicular case. Such results were, on the other hand, usually rationalized by intense local electromagnetic fields emanating from points of high curvature, such as NR tips ("lightning-rod effect") and the dominant role of the longitudinal plasmon modes. To sum up, the experimentally measured polarization dependences often may be understood as a result of "competition" between

the enhancement provided by longitudinal plasmon modes and by transverse plasmon modes. For example, for NRs growing on a substrate in one specific direction as indicated in Figure 14, the obtained SERS intensities are expected to be:

$$I \sim \left[a_{||}\left(\vec{e}^{\,i}\cdot\vec{l}\right)^2 + a_{\perp}\left(1-\left(\vec{e}^{\,i}\cdot\vec{l}\right)^2\right)\right]\cdot\left[a_{||}'\left(\vec{e}^{\,sc}\cdot\vec{l}\right)^2 + a_{\perp}'\left(1-\left(\vec{e}^{\,sc}\cdot\vec{l}\right)^2\right)\right], \quad (64)$$

where $\vec{e}^{\,i}$ is the unit incident field vector, $\vec{e}^{\,sc}$ is the unit scattered field vector, $\vec{l}$ is the unit vector determined by the long axis of the NRs and $a_{||}$ and $a_{\perp}$ are factors determining the plasmonic response to polarization parallel/perpendicular to the long axis of the NRs for the excitation light (unprimed values) and the scattered light (primed values). The first bracket in Equation (64) accounts for the enhancement of the incident radiation and the latter accounts for the enhancement of the scattered radiation. What matters is which of the two factors $a_{\perp}$ and $a_{||}$ is larger. In general, the answer to this question is not uniform since it is extremely sensitive to the specific preparation procedure of given plasmonic nanostructures. As a rule of thumb, for arrays of regular NRs stacked in close proximity to each other (gap < ~ 10 nm), the role of factor $a_{\perp}$ usually prevails. Similar conclusion holds true for NP-nanowire systems. On the other hand, for rather isolated or well-separated NRs, the most contributing term to the biggest SERS sensitivity will usually be the factor $a_{||}$ [114,115].

Sensitivity of the plasmonic anisotropy to the excitation wavelength was investigated in more detail in [116] where two different excitation wavelengths were used to study the polarization-dependent SERS on anisotropic Ag NP array. The study demonstrates that SERS nanostructures can possess completely different polarization characteristics when using two different wavelengths. The $\cos^2\vartheta$ and $\sin^2\vartheta$ trends were found using the 514 nm and 647 nm excitation wavelength, respectively (Figure 15). Completely different polarization characteristics were in good correspondence with the dielectric function parallel and perpendicular to the long axis of the nanostructures as determined by spectral ellipsometry. This approach is expected to open novel possibilities in biosensing applications due to increase in the specificity of target detection by using multiple excitation wavelengths.

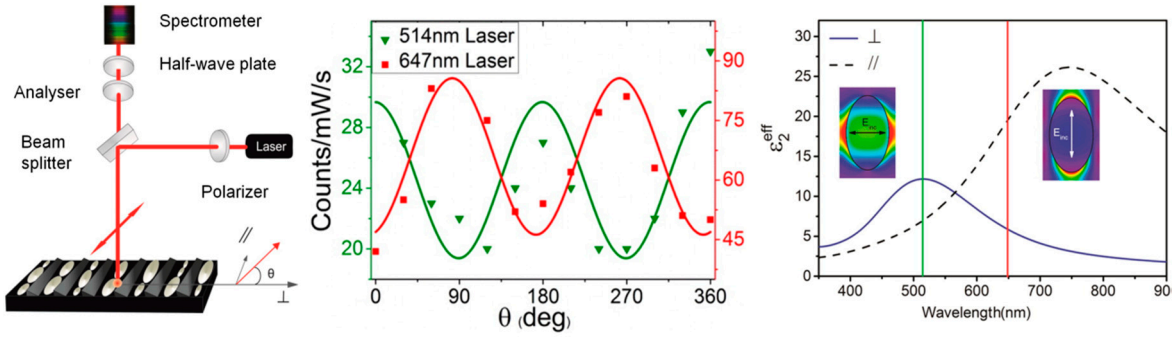


**Figure 15. Left:** Setup for Raman measurements used. Middle: Normalized intensity of the 1079 $cm^{-1}$ band of 4-mercaptobenzonitrile (MBN) adsorbed on anisotropic Ag nanoparticle arrays created by metal evaporation on rippled silicon substrates as a function of $\theta$ obtained with the 514 nm (green triangles) and the 647 nm (red squares) excitation. The respective solid lines correspond to fits of a $\cos^2\theta$ (green) and $\sin^2\theta$ (red) function to the data. **Right:** Imaginary part of the effective dielectric function of the Ag film parallel and perpendicular to the long axis of the ripples. Adapted with permission from [116]. Copyright 2016 American Chemical Society.

### *5.5. Angular Dependences in SERS*

As far as angular dependences are concerned, the situation in SERS is again more complicated in comparison to classical Raman measurements (Figure 4) due to the presence of a third element—the nanostructure, which imposes its own anisotropic pattern in the directional properties of the SERS signal. Moreover, the term angular dependences itself is rather ambiguous since "angle" may be understood either as the angle between laser wavevector/polarization vector and a specific nanostructure, or as the angle determining the specific illumination-observation geometry in a way analogous to that described in Section 3. From the point of view of the latter meaning, the vast

majority of experiments have been performed only in backscattering geometry, which means that a detailed inspection on the angular dependence of the SERS signal is somewhat exceptional in the literature. However, possible optimization of plasmon-based sensors for maximum signal enhancement relies, among other things, on the right choice of the excitation angle and/or the scattering angle. Geometric reasons, such as change in the size of the illuminated area and possibly different efficiency in collection of the scattered radiation must be also taken into account when aiming to retrieve angular dependences [112,113,117]. This was often neglected. The issue of optimum excitation and collection efficiency is of great importance also in the construction of optical waveguides with the aim to minimize losses where coupling of the SERS field to the waveguide modes must be carefully optimized. This approach is forecasted to open the way towards lab-on-a-chip sensing systems, allowing multiplexed detection of extremely weak Raman signals on a highly dense integrated platform [118,119].

A basic idea of the simplest models trying to elucidate the SERS angular characteristics again lies in the fact that the primary electric field felt by the molecule is the sum of the incident and the reflected field, which induces an oscillating dipole in the adsorbed molecule. A modified Greenler model [5] based on classical electrodynamic dipole radiation was used to explain the anisotropic nature of tilted Ag NRs, producing maximum SERS intensities at approximately 45° relative to the surface normal [96], but measured still in the backscattering configuration (Figure 16). Although the length of the NRs used (~ 868 nm) was comparable to the excitation wavelength (785 nm) in this case, the model was treating the surface of the NR as planar, neglecting the diffraction effect and calculating near-field intensities using the Fresnel equations. Later, the authors upgraded their model, assuming that the primary field at the NR surface is the sum of the incident and reflected fields from the Ag NR and from the supporting Ag film. The authors showed that the presence of an underlying Ag film plays a crucial role for the SERS enhancement due to its high reflectivity [120]. Although these simple considerations were proven to capture the essential angular characteristics in SERS, NRs of subwavelength dimensions can be misleading to treat as planar as demonstrated in [121]. There, a strong difference between the optical constants of the NR films and those of the constituent materials were found using generalized ellipsometry (Jones formalism).

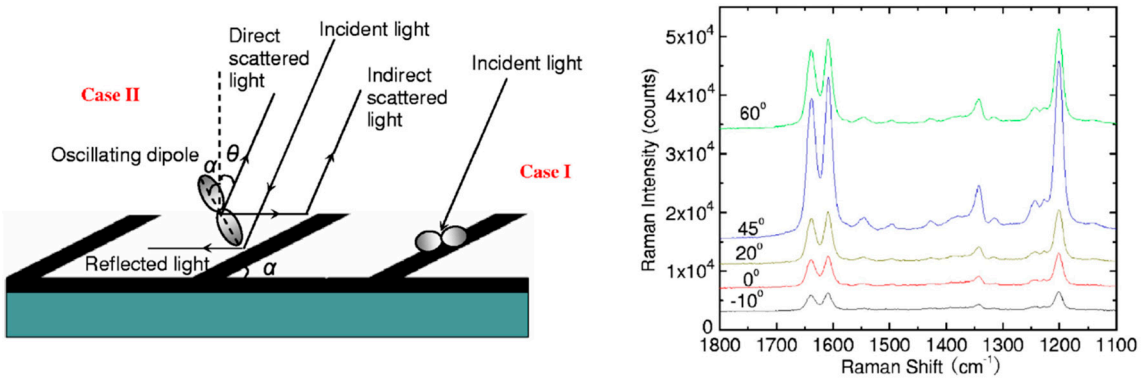


**Figure 16. Left:** Schematic illustration of the modified Greenler's model of an induced dipole on a Ag nanorod: Case I, where the dipole is perpendicular to the incident plane; Case II, where the dipole is on the incident plane. All the induced dipoles are perpendicular to the NR. **Right**: Representative SERS spectra of trans-1,2-bis(4-pyridyl)-ethene adsorbed on the Ag NR substrate at different incident angles θ. The peak intensity was strongest at the angle θ around 45°, which was in agreement with the model. Adapted with permission from [96].

Unlike optical constants of homogeneous materials, optical constants of nanostructured layers depend (due to the presence of subwavelength structures) also on the incident angle. For example, island-like Ag films in [122] exhibited uniaxial optical properties and NRs in [121] exhibited biaxial properties with the complex refractive index different for different orientations of the incident angle with respect to the NRs, similarly to the case of crystals [123]. A very similar conclusion was drawn

from our work [112] where we showed that the optical constants of silver NR arrays are sensitive to both the incident angle as well as rotation of the substrate by 90°. On the other hand, they were fairly insensitive to flipping the substrate by 180°. Moreover, surface roughness or the presence of plasmonic resonance may invoke a partial depolarization, i.e., a loss of coherence of the phase and amplitude of the electric field [124]. These phenomena lie beyond the validity of the Jones model and their full description requires using more complicated Stokes formalism [125].

An important contribution to angular- and polarization-resolved SERS was made in [113], probing adsorbate-covered gold NPs immobilized on a metallic substrate (Figure 17). Mathematical background combining local field enhancement tensor, intrinsic molecular Raman tensors and rotation tensors has been developed in order to elucidate the surface coverage depending on the analyte concentration. The authors also pointed out the role of the surface tension of the solution used, preventing access of the analyte molecules in between the nanospheres in the high concentration regime.

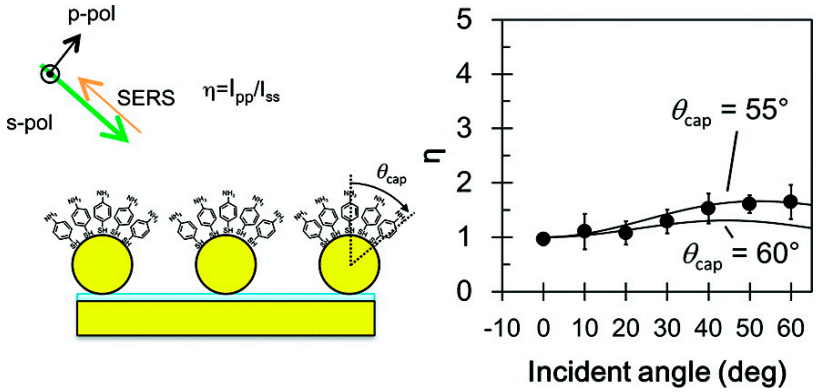


**Figure 17. Left:** Scheme of the angular-resolved polarized SERS of aminobenzenothiol immobilized on gold nanospheres. **Right:** Observed depolarization ratio ($\eta$) profile. The solid lines represent different $\eta$ profiles simulated for different $\theta_{cap}$ angles. Adapted with permission from [113]. Copyright 2012 American Chemical Society.

Another approach used for elucidation of polarization and angular dependences in SERS was employed in our recent work using MB adsorbed on silver NR arrays [112] (Figure 18). Although the nanostructures were morphologically anisotropic, the plasmonic properties around the excitation wavelength used (532 nm) were found rather isotropic. Therefore, it could not be the main reason for the anisotropic behaviour observed in the SERS experiments (anisotropy in the depolarization ratios measured under selected configurations). Instead, difference in the depolarization ratios after rotating the sample by 90° was attributed to different refractive indices along different directions (obtained using spectral ellipsometry) and explained within the framework of the surface selection rules. This fact was explained by slightly different periodicity along different directions instead of a specific angle made between the NR axes and incident/collected radiation. These results enabled quantitative analysis of MB Raman tensor elements, indicating that the molecules adsorb predominantly with the symmetry axis perpendicular to the surface. Interestingly, the depolarization ratio computed using Equation (24) produced the value of 0.29, which was in-between the depolarization ratio of MB molecules measured in a water solution (0.22) and the value of 1/3, predicted for a set of randomly-oriented hot-spots. It suggests that although the NRs were found plasmonically isotropic, the role of hot-spots is still manifested in the value of the depolarization ratio. The importance of the Fresnel mechanism-based enhancement at the metal-dielectric interface has also been highlighted in [126] where the origin of the additional SERS enhancement was explained on account of optical interference effects, giving rise to an enhancement ~ 3 times higher than in the case of direct illumination. The role of the surface-selection rules in SERS has also been experimentally demonstrated in [117] using a Nile blue molecule. By comparing the EF of various modes and relating these to their bare Raman tensors, the molecular orientation on a flat gold surface was inferred. Rich information about the Raman tensor components was obtained by SERS

measurements as a function of the incident angle and both incident and scattered polarizations. The authors reported the EF up to ~ 3, but still retained the term SERS for simplicity. In this case, the EF was caused solely by the geometric factors and interpreted in terms of the Fresnel coefficients. This concept was extended in [127], investigating the wavelength and refractive index dependence of the geometrically enhanced SERS signal. In this approach, the effective optical constants of the nanostructured metallic film were determined by spectral ellipsometry measurements, applying a homogeneous uniaxial model. This approach highlights the need for application of the surface-selection rules not only in the case of smooth surfaces, but also in the case of plasmonic nanostructures.

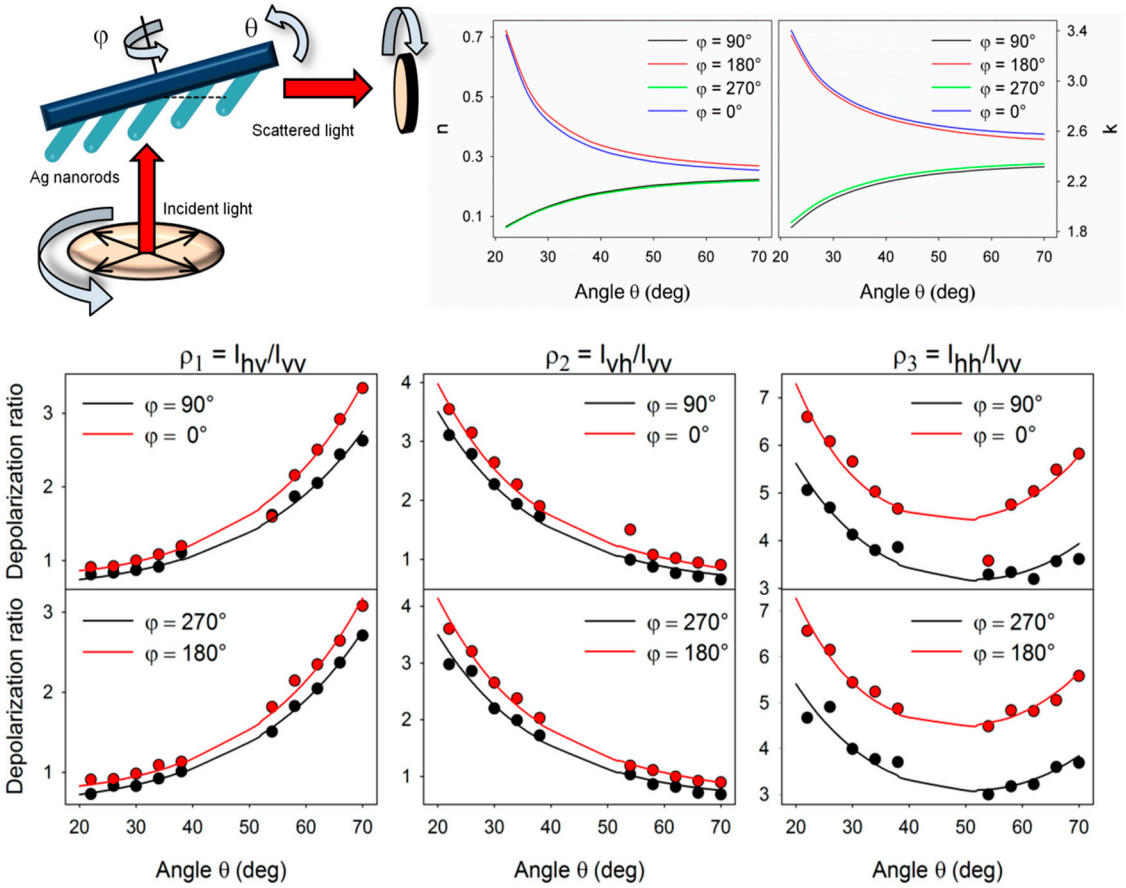


**Figure 18. Upper left:** Scheme of the experimental geometry used for polarization- and angular-resolved SERS on silver nanorod arrays using methylene blue (MB) as the probe molecule. **Lower part:** Depolarization ratio profiles for the 1628-cm$^{-1}$ MB band for different angular arrangements (colour points) and their fit by the surface-selection rules with pseudo-refractive indices obtained from ellipsometry measurements (lines). Excitation wavelength was 532 nm. **Upper right:** Real and imaginary part of pseudo-refractive index $\tilde{n} = n + ik$ of silver NR arrays and their variation with both angles as measured by standard ellipsometry [112].

### *5.6. Plasmonic Anisotropy in Polarized Absorption and Emission and Their Influence on SERS*

Anisotropic optical response of morphologically anisotropic plasmonic nanostructures is not only restricted to SERS. Polarization dependence of plasmon-enhanced fluorescence on individual Au NRs was reported in [99,128], producing maximum intensities with the excitation polarization oriented along the NR axis. Intensity profile obtained when the angle between the excitation polarization direction and the NR axis was varied was well fitted by a cosine squared function together with an exponential decay. Very similar trends were observed in [129] using Au NRs of different aspect ratios, or from a single Ag nanowire in [130]. Contradictory results appeared in [101].

Other instances where plasmonic anisotropy of metallic substrates is manifested include absorbance or reflectance measurements. Although the SERS properties of plasmonic nanostructures are very often derived from absorption or reflection measurements, this relationship works well only in the average SERS regime where the role of hot-spots is rather negligible, such as regular arrays of isotropic silver nanoislands [131]. In the case of more complicated (typically anisotropic and/or hot-spot dominated) plasmonic nanostructures, little correlation between these two phenomena ("near field" and "far field" properties of SERS substrates) was found [132,133]. Anisotropic SERS response surely is, in a more or less straightforward way, manifested in polarization-resolved absorbance or reflectance spectra with the difference in absorbance for different light polarization often even more pronounced than in the case of SERS. However, the exact relationship between the polarization providing the highest SERS enhancement and the polarization exhibiting the highest absorbance (or transmittance/reflectance) remains highly non-trivial.

In the case of NR arrays, absorbance typically features a sharp transverse peak (for Ag generally below 400 nm) and a red-shifted broad longitudinal peak which spill one into another when rotating the polarization direction [97,112,134]. For aligned silver NRs in [98], the magnitude of the SERS enhancement and of absorbance of the same polarization were almost a perfect match (Figure 19) with the biggest response provided by polarization along the NRs. Counterintuitively, in the case of metallic grating structures [94], light polarization exhibiting the biggest transmission was also found to dominate in the SERS spectrum over perpendicular polarization for which the transmitted intensity was lower. Such trends were also found for silver NR arrays in [97], although a bigger SERS response was found for polarization perpendicular to the adjacent NRs. In a more elaborate study [135], the authors investigated changes in absorbance and its polarization characteristics as a function of the NR height, concluding that smaller NRs are rather isotropic. With the increase of the NR size (>1000 nm), absorbance splits into at least two plasmon resonant modes.

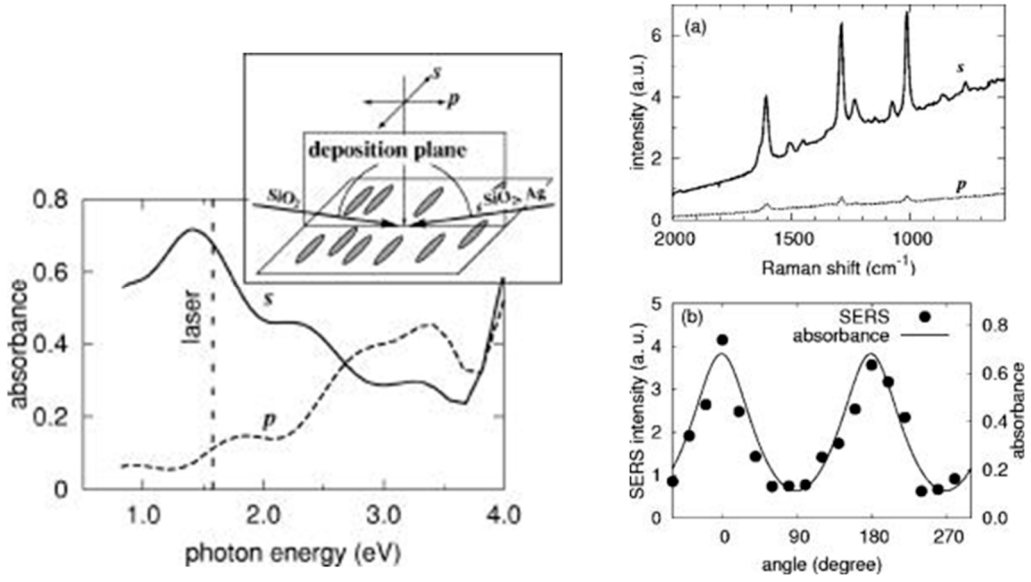


**Figure 19. Left:** The absorbance spectra of the Ag NR arrays tuned to the Raman spectroscopy at excitation wavelength of 785 nm (1.58 eV). The incident light was either p or s polarized, where an electric field vibrates parallel or perpendicular to the deposition plane, respectively, as shown schematically in the upper right box. **Right:** Polarization dependence of the Raman spectra (**a**) and the peak intensity at 1014 $cm^{-1}$ (**b**). The polarization dependence of the absorbance at the wavelength of 785 nm is also shown (**b**). Adapted with permission from [98].

The works mentioned above suggest that in the case of metallic NRs, the basic features or polarization-resolved absorbance is influenced by the specific preparation procedure of a given nanostructure less than polarization-resolved SERS. However, it has to be emphasized that

polarization-resolved absorbance has been studied less intensively in literature than polarization-resolved SERS and many aspects regarding their mutual correspondence are yet to be fully resolved.

In a study devoted to angle resolved SERS on metallic nanostructured plasmonic crystals [136], a correlation between plasmon-related absorption in the reflectivity and the Raman enhancement with the varied angle of incidence was found. The need for absorbance or reflectance spectra may also be supplemented by ellipsometry measurements [112,116,127]. Although the plasmonic properties of silver NRs in [112] were found rather isotropic using the 532 nm wavelength, a clear distinction between the extinction profiles (computed using the ellipsometry characteristics) after rotating the sample by 90° was observed. This distinction was attributed to different periodicity in different directions as the NRs used were almost perfectly aligned in one direction, but still exhibiting slight deviations from the perfectly-ordered state in the perpendicular direction. This slight inhomogeneity was reflected in the inhomogeneously broadened longitudinal plasmon peak and was found responsible for orientation-dependent depolarization ratios of the adsorbed molecule, although the extinction profiles suggested rather plasmonic homogeneity. In [116], the SERS response for two different wavelengths was in agreement with the imaginary part of the effective dielectric function of the Ag film.

## 6. Conclusions

In this review, we have focused mainly on polarization and directional/angular characteristics occurring in Raman spectroscopy and surface-enhanced Raman spectroscopy (SERS) on anisotropic metallic nanostructures. We have summarized basic formulas for Raman intensities as a function of light polarization and angular arrangement used for both liquid samples as well as crystals. We have demonstrated that polarization- and angular-resolved measurements allow one to retrieve information on the (orientation-averaged) Raman tensor components, which are useful for symmetry determination and/or obtaining information regarding the molecular orientation. The complexity of this problem rises when molecules are adsorbed in the vicinity of nanostructured metallic surfaces, where not only coupling between light and molecules, but also (and often mainly) between light and the anisotropic NP arrays determine the total intensity profile. The observed spectral pattern results from interplay between the material used, size and shape of the nanoobjects, their spatial arrangement as well as the excitation wavelength used. Periodicity of the NP array is also deciding since it is manifested in the NP optical properties, which in turn influences the SERS signal. Since details of the NP fabrication are often very subtle, this process is very difficult to reproduce and therefore the exact results often vary in literature. It is one of the reasons why all aspects of polarization- and angular resolved measurements are not yet fully understood and remain a challenge for future research. It is expected that study of the polarization and angular properties of molecules on plasmonic nanostructures will contribute to a deeper theoretical understanding of the enhancement mechanism. It will also provide a theoretical background for the design of plasmon-based molecular sensors for maximum signal enhancement.

**Author Contributions:** M.S. surveyed the literature, prepared the figures and wrote the manuscript. M.P. participated in editing the article and helping with final version of the manuscript.

**Funding:** This research was funded by Charles University research project GA UK No. 572216, Charles University Research Centre program UNCE/SCI/010, and the Czech Science Foundation No. 18-10897S.

**Acknowledgments:** The authors thank Ondřej Kylián from Department of Macromolecular Physics, Charles University, for fabrication of SERS-active substrates.

**Conflicts of Interest:** The authors declare no conflict of interest.

## References

1. Allemand, C.D. Depolarization Ratio Measurements in Raman Spectroscopy. *Appl. Spectrosc.* **1970**, *24*, 348–353.

2. Dawson, P. Polarization Measurements in Raman Spectroscopy. *Spectrochim. Acta Part A-Mol. Spectrosc.* **1972**, *28*, 715–723, doi:10.1016/0584-8539(72)80040-0.
3. Porto, S.P.S. Angular Dependence and Depolarization Ratio of the Raman Effect. *J. Opt. Soc. Am.* **1966**, *56*, 1585–1589.
4. Greenler, R.G. Infrared Study of Adsorbed Molecules on Metal Surfaces by Reflection Techniques. *J. Chem. Phys.* **1966**, *44*, 310–315, doi:10.1063/1.1726462.
5. Greenler, R.G.; Slager, T.L. Method for Obtaining Raman-Spectrum of a Thin-Film on a Metal Surface. *Spectrochim. Acta Part A-Mol. Spectrosc.* **1973**, *A 29*, 193–201, doi:10.1016/0584-8539(73)80022-4.
6. Pearce, H.A.; Sheppard, N. Possible Importance of a Metal-Surface Selection Rule in Interpretation of Infrared-Spectra of Molecules Adsorbed on Particulate Metals—Infrared-Spectra from Ethylene Chemisorbed on Silica-Supported Metal-Catalysts. *Surf. Sci.* **1976**, *59*, 205–209, doi:10.1016/0039-6028(76)90301-0.
7. Murphy, C.J.; Sau, T.K.; Gole, A.M.; Orendorff, C.J.; Gao, J.; Gou, L.; Hunyadi, S.E.; Li, T. Anisotropic Metal Nanoparticles: Synthesis, Assembly, and Optical Applications. *J. Phys. Chem. B* **2005**, *109*, 13857–13870, doi:10.1021/jp0516846.
8. Li, N.; Zhao, P.X.; Astruc, D. Anisotropic Gold Nanoparticles: Synthesis, Properties, Applications, and Toxicity. *Angew. Chem. Int. Ed.* **2014**, *53*, 1756–1789, doi:10.1002/anie.201300441.
9. Thorkelsson, K.; Bai, P.; Xu, T. Self-assembly and applications of anisotropic nanomaterials: A review. *Nano Today* **2015**, *10*, 48–66, doi:10.1016/j.nantod.2014.12.005.
10. Paramasivam, G.; Kayambu, N.; Rabel, A.M.; Sundramoorthy, A.K.; Sundaramurthy, A. Anisotropic noble metal nanoparticles: Synthesis, surface functionalization and applications in biosensing, bioimaging, drug delivery and theranostics. *Acta Biomater.* **2017**, *49*, 45–65, doi:10.1016/j.actbio.2016.11.066.
11. Barron, L.D. The development of biomolecular Raman optical activity spectroscopy. *Biomed. Spectrosc. Imaging* **2015**, *4*, 223–253, doi:10.3233/Bsi-150113.
12. Born, M.; Wolf, E. *Principles of Optics*, 7th ed.; Cambridge University Press: Cambridge, UK, 1999; ISBN 0-521-642221.
13. Le Ru, E.C.; Etchegoin, P.G. *Principles of Surface-Enhanced Raman Spectroscopy and Related Plasmonic Effects*; Elsevier: Amsterdam, The Netherlands, 2009; ISBN 978-0-444-52779-0.
14. Procházka, M. *Surface-Enhanced Raman Spectroscopy: Bioanalytical, Biomolecular and Medical Applications;* Springer: Cham, Switzerland, 2016; ISBN 978-3-319-23990-3.
15. Moore, T.J.; Moody, A.S.; Payne, T.D.; Sarabia, G.M.; Daniel, A.R.; Sharma, B. In Vitro and In Vivo SERS Biosensing for Disease Diagnosis. *Biosensors* **2018**, *8*, 46, doi:10.3390/bios8020046.
16. Štolcová, L.; Peksa, V.; Proška, J.; Procházka, M. Gold film over very small (107 nm) spheres as efficient substrate for sensitive and reproducible surface-enhanced Raman scattering (SERS) detection of biologically important molecules. *J. Raman Spectrosc.* **2017**, *49*, 499–505, doi:10.1002/jrs.5317.
17. Zhu, Q.; Yu, X.; Wu, Z.; Lu, F.; Yuan, Y. Antipsychotic drug poisoning monitoring of clozapine in urine by using coffee ring effect based surface-enhanced Raman spectroscopy. *Anal. Chim. Acta* **2018**, *1014*, 64–70, doi:10.1016/j.aca.2018.02.027.
18. Mukanova, Z.; Gudun, K.; Elemessova, Z.; Khamkhash, L.; Ralchenko, E.; Bukasov, R. Detection of Paracetamol in Water and Urea in Artifical Urine with Gold Nanoparticle@Al Foil Cost-efficient SERS Substrate. *Anal. Sci.* **2018**, *34*, 183–187.
19. Peksa, V.; Jahn, M.; Štolcová, L.; Schulz, V.; Proška, J.; Procházka, M.; Weber, K.; Cialla-May, D.; Popp, J. Quantitative SERS Analysis of Azorubine (E 122) in Sweet Drinks. *Anal. Chem.* **2015**, *87*, 2840–2844, doi:10.1021/ac504254k.
20. Ai, Y.-J.; Liang, P.; Wu, Y.-X.; Dong, Q.-M.; Li, J.-B.; Bai, Y.; Xu, B.-J.; Yu, Z.; Ni, D. Rapid qualitative and quantitative determination of food colorants by both Raman spectra and Surface-enhanced Raman Scattering (SERS). *Food Chem.* **2018**, *241*, 427–433, doi:10.1016/j.foodchem.2017.09.019.
21. Hakonen, A.; Wang, F.C.; Andersson, P.O.; Wingfors, H.; Rindzevicius, T.; Schmidt, M.S.; Soma, V.R.; Xu, S.; Li, Y.Q.; Boisen, A.; et al. Hand-Held Femtogram Detection of Hazardous Picric Acid with Hydrophobic Ag Nanopillar SERS Substrates and Mechanism of Elasto-Capillarity. *ACS Sens.* **2017**, *2*, 198–202, doi:10.1021/acssensors.6b00749.
22. Liyanage, T.; Rael, A.; Schaffer, S.; Zaidi, S.; Goodpaster, J.V.; Sardar, R. Fabrication of a self-assembled and flexible SERS nanosesor for explosive detection at parts-per-quadrillion levels from fingerprints. *Analyst* **2018**, *143*, 2012–2022, doi:10.1039/c8an00008e.

23. Cheng, H.-W.; Huan, S.-Y.; Yu, R.-Q. Nanoparticle-based substrates for surface-enhanced Raman scattering detection of bacterial spores. *Analyst* **2012**, *137*, 3601–3608, doi:10.1039/c2an35448a.
24. Morelli, L.; Zor, K.; Jendersen, C.B.; Rindzevicius, T.; Schmidt, M.S.; Nielsen, A.T.; Boisent, A. Surface Enhanced Raman Scattering for Quantification of p-Coumaric Acid Produced by Escherichia coli. *Anal. Chem.* **2017**, *89*, 3981–3987, doi:10.1021/acs.analchem.6b0442s8.
25. Sanchez-Purra, M.; Carre-Camps, M.; de Puig, H.; Bosch, I.; Gehrke, L.; Hamad-Schifferli, K. Surface-Enhanced Raman Spectroscopy-Based Sandwich Immunoassays for Multiplexed Detection of Zika and Dengue Viral Biomarkers. *ACS Infect. Dis.* **2017**, *3*, 767–776, doi:10.1021/acsinfecdis.7b00110.
26. Placzek, G. Rayleigh-Streuung und Raman-Effekt. In *Handbuch der Radiologie*; Marx, E., Ed.; Academische Verlag: Leipzig, Germany, 1934; Volume 6, pp. 205–374.
27. Long, D.A. *The Raman Effect: A Unified Treatment of the Theory of Raman Scattering by Molecules*; John Wiley & Sons Ltd.: Chichester, UK, 2002; ISBN 0-471-49028-8.
28. Smith, E.; Dent, G. *Modern Raman Spectroscopy—A Practical Approach*; John Wiley & Sons Ltd.: Chichester, UK, 2005; ISBN 0-471-49668-5.
29. Cotton, F.A. *Chemical Applications of Group Theory*, 3rd ed.; John Wiley & Sons Ltd.: Chichester, UK, 1990; ISBN 0-471-51094-7.
30. Ferraro, J.R.; Nakamoto, K.; Brown, C.W. *Introductory Raman Spectroscopy*, 2nd ed.; Elsevier: New York, NY, USA, 2003; ISBN 978-0-12-254105-6.
31. Gucciardi, P.G.; de la Chapelle, M.L.; Lidgi-Guigui, N. *Handbook of Enhanced Spectroscopy*; Pan Stanford Publishing Pte. Ltd.: Singapore, 2016; ISBN 978-981-4613-32-3.
32. Strommen, D.P. Specific Values of the Depolarization Ratio in Raman-Spectroscopy—Their Origins and Significance. *J. Chem. Educ.* **1992**, *69*, 803–807.
33. Damen, T.C.; Porto, S.P.S.; Tell, B. Raman Effect in Zinc Oxide. *Phys. Rev.* **1966**, *142*, 570–574, doi:10.1103/PhysRev.142.570.
34. Moskovits, M. Surface Selection-Rules. *J. Chem. Phys.* **1982**, *77*, 4408–4416, doi:10.1063/1.444442.
35. Moskovits, M. Surface-Enhanced Spectroscopy. *Rev. Mod. Phys.* **1985**, *57*, 783–826, doi:10.1103/RevModPhys.57.783.
36. Creighton, J.A. Surface Raman Electromagnetic Enhancement Factors for Molecules at the Surface of Small Isolated Metal Spheres—The Determination of Adsorbate Orientation from Sers Relative Intensities. *Surf. Sci.* **1983**, *124*, 209–219, doi:10.1016/0039-6028(83)90345-X.
37. Aroca, R. *Surface-Enhanced Vibrational Spectroscopy*; John Wiley & Sons Ltd.: Chichester, UK, 2006, ISBN 0-471-60731-2.
38. Johnson, P.B.; Christy, R.W. Optical Constants of Noble Metals. *Phys. Rev. B* **1972**, *6*, 4370–4379, doi:10.1103/PhysRevB.6.4370.
39. Foti, A.; D'Andrea, C.; Messina, E.; Irrera, A.; Marago, O.M.; Fazio, B.; Gucciardi, P.G. On the SERS depolarization ratio. *Nanospectroscopy* **2015**, *1*, 26–62.
40. Etchegoin, P.G.; Galloway, C.; Le Ru, E.C. Polarization-dependent effects in surface-enhanced Raman scattering (SERS). *Phys. Chem. Chem. Phys.* **2006**, *8*, 2624–2628, doi:10.1039/b603725a.
41. Le Ru, E.C.; Meyer, M.; Blackie, E.; Etchegoin, P.G. Advanced aspects of electromagnetic SERS enhancement factors at a hot spot. *J. Raman Spectrosc.* **2008**, *39*, 1127–1134, doi:10.1002/jrs.1945.
42. Moskovits, M. Surface-enhanced Raman spectroscopy: A brief retrospective. *J. Raman Spectrosc.* **2005**, *36*, 485–496, doi:10.1002/Jrs.1362.
43. Fazio, B.; D'Andrea, C.; Bonaccorso, F.; Irrera, A.; Calogero, G.; Vasi, C.; Gucciardi, P.G.; Allegrini, M.; Toma, A.; Chiappe, D.; et al. Re-radiation Enhancement in Polarized Surface-Enhanced Resonant Raman Scattering of Randomly Oriented Molecules on Self-Organized Gold Nanowires. *ACS Nano* **2011**, *5*, 5945–5956, doi:10.1021/nn201730k.
44. Wang, D.S.; Chew, H.; Kerker, M. Enhanced Raman-Scattering at the Surface (SERS) of a Spherical-Particle. *Appl. Opt.* **1980**, *19*, 2256–2257, doi:10.1364/Ao.19.002256.
45. Moskovits, M.; Suh, J.S. Surface Selection-Rules for Surface-Enhanced Raman Spectroscopy-Calculation and Application to the Surface-Enhanced Raman Spectrum of Phthalazine on Silver. *J. Phys. Chem.* **1984**, *88*, 5526–5530. doi:10.1021/j150667a013.
46. Macdonald, I.D.G.; Smith, W.E. Orientation of Cytochrome c Adsorbed on a Citrate-Reduced Silver Colloid Surface. *Langmuir* **1996**, *12*, 706–713, doi:10.1021/La950256w.

47. Gao, X.; Davies, J.P.; Weaver, M.J.A. Test of Surface Selection-Rules for Surface-Enhanced Raman-Scattering: The Orientation of Adsorbed Benzene and Monosubstituted Benzenes on Gold. *J. Phys. Chem.* **1990**, *94*, 6858–6864, doi:10.1021/j100380a059.
48. Carron, K.T.; Hurley, L.G. Axial and Azimuthal Angle Determination with Surface-Enhanced Raman-Spectroscopy: Thiophenol on Copper, Silver, and Gold Metal-Surfaces. *J. Phys. Chem.* **1991**, *95*, 9979–9984, doi:10.1021/J100177a068.
49. Barber, P.W.; Chang, R.K.; Massoudi, H. Surface-Enhanced Electric Intensities on Large Silver Spheroids. *Phys. Rev. Lett.* **1983**, *50*, 997–1000, doi:10.1103/PhysRevLett.50.997.
50. Aravind, P.K.; Nitzan, A.; Metiu, H. The Interaction between Electromagnetic Resonances and Its Role in Spectroscopic Studies of Molecules Adsorbed on Colloidal Particles or Metal Spheres. *Surf. Sci.* **1981**, *110*, 189–204, doi:10.1016/0039-6028(81)90595-1.
51. Aravind, P.K.; Metiu, H. The Effects of the Interaction between Resonances in the Electromagnetic Response of a Sphere-Plane Structure; Applications to Surface Enhanced Spectroscopy. *Surf. Sci.* **1983**, *124*, 506–528, doi:10.1016/0039-6028(83)90806-3.
52. Xu, H.; Bjerneld, E.J.; Käll, M.; Borjesson, L. Spectroscopy of single hemoglobin molecules by surface enhanced Raman scattering. *Phys. Rev. Lett.* **1999**, *83*, 4357–4360, doi:10.1103/PhysRevLett.83.4357.
53. Xu, H.; Aizpurua, J.; Käll, M.; Apell, P. Electromagnetic contributions to single-molecule sensitivity in surface-enhanced Raman scattering. *Phys. Rev. E* **2000**, *62*, 4318–4324, doi:10.1103/PhysRevE.62.4318.
54. Xu, H.; Käll, M. Polarization-Dependent Surface-Enhanced Raman Spectroscopy of Isolated Silver Nanoaggregates. *ChemPhysChem* **2003**, *4*, 1001–1005, doi:10.1002/cphc.200200544.
55. Le Ru, E.C.; Blackie, E.; Meyer, M.; Etchegoin, P.G. Surface Enhanced Raman Scattering Enhancement Factors: A Comprehensive Study. *J. Phys. Chem. C* **2007**, *111*, 13794–13803, doi:10.1021/jp0687908.
56. Camden, J.P.; Dieringer, J.A.; Wang, Y.; Masiello, D.J.; Marks, L.D.; Schatz, G.C.; Van Duyne, R.P. Probing the Structure of Single-Molecule Surface-Enhanced Raman Scattering Hot Spots. *J. Am. Chem. Soc.* **2008**, *130*, 12616–12617, doi:10.1021/ja8051427.
57. Hakonen, A.; Svedendahl, M.; Ogier, R.; Yang, Z.-J.; Lodewijks, K.; Verre, R.; Shegai, T.; Andersson, P.O.; Käll, M. Dimer-on-mirror SERS substrates with attogram sensitivity fabricated by colloidal lithography. *Nanoscale* **2015**, *7*, 9405–9410, doi:10.1039/c5nr01654a.
58. Wustholz, K.L.; Henry, A.I.; McMahon, J.M.; Freeman, R.G.; Valley, N.; Piotti, M.E.; Natan, M.J.; Schatz, G.C.; Van Duyne, R.P. Structure-Activity Relationships in Gold Nanoparticle Dimers and Trimers for Surface-Enhanced Raman Spectroscopy. *J. Am. Chem. Soc.* **2010**, *132*, 10903–10910, doi:10.1021/ja104174m.
59. Zang, Y.; Shi, H.; Huang, Y.; Zeng, X.; Pan, L.; Wang, S.; Wen, W. SERS polarization dependence of Ag nanorice dimer on metal and dielectric film. *Chem. Phys. Lett.* **2017**, *684*, 373–377, doi:10.1016/j.cplett.2017.07.027.
60. Tao, A.R.; Yang, P.D. Polarized surface-enhanced Raman spectroscopy on coupled metallic nanowires. *J. Phys. Chem. B* **2005**, *109*, 15687–15690, doi:10.1021/jp053353z.
61. Le Ru, E.C.; Etchegoin, P.G.; Meyer, M. Enhancement factor distribution around a single surface-enhanced Raman scattering hot spot and its relation to single molecule detection. *J. Chem. Phys.* **2006**, *125*, 204701, doi:10.1063/1.2390694.
62. Moskovits, M. Persistent misconceptions regarding SERS. *Phys. Chem. Chem. Phys.* **2013**, *15*, 5301–5311, doi:10.1039/C2cp44030j.
63. Leopold, N.; Lendl, B. A New Method for Fast Preparation of Highly Surface-Enhanced Raman Scattering (SERS) Active Silver Colloids at Room Temperature by Reduction of Silver Nitrate with Hydroxylamine Hydrochloride. *J. Phys. Chem. B* **2003**, *107*, 5723–5727, doi:10.1021/Jp027460u.
64. Roy, S.D.; Ghosh, M.; Chowdhury, J. Adsorptive parameters and influence of hot geometries on the SER(R)S spectra of methylene blue molecules adsorbed on gold nanocolloidal particles. *J. Raman Spectrosc.* **2015**, *46*, 451–461, doi:10.1002/jrs.4675.
65. Malinowski, E.R. *FactorAnalysis in Chemistry*, 3rd ed.; John Wiley & Sons: New York, NY, USA, 2002; ISBN 0-471-13479-1.
66. Zhong, L.; Hu, Y.J.; Xing, D.; Gu, H.M. Adsorption of Methylene Blue on Colloidal Silver-A Surface-Enhanced Raman Spectroscopy Study Combined with Density Functional Theory Calculations. *Spectrosc. Spectr. Anal.* **2010**, *30*, 90–94, doi:10.3964/j.issn.1000-0593(2010)01-0090-05.
67. Timmermans, F.J.; Lenferink, A.T.M.; van Wolferen, H.A.G.M.; Otto, C. Correlative SEM SERS for quantitative analysis of dimer nanoparticles. *Analyst* **2016**, *141*, 6455–6462, doi:10.1039/c6an01648k.

68. Sergiienko, S.; Moor, K.; Gudun, K.; Yelemessova, Z.; Bukasov, R. Nanoparticle-nanoparticle vs. nanoparticle-substrate hot spot contributes to the SERS signal: Studying Raman labelled monomers, dimers and trimers. *Phys. Chem. Chem. Phys.* **2017**, *19*, 4478–4487, doi:10.1039/c6cp08254h.
69. Xiang, Q.; Li, Z.; Zheng, M.; Liu, Q.; Chen, Y.; Yang, L.; Jiang, T.; Duan, H. Sensitive SERS detection at the single-particle level based on nanometer-separated mushroom-shaped plasmonic dimers. *Nanotechnology* **2018**, *29*, 105301, doi:10.1088/1361-6528/aaa691.
70. Zhang, Q.; Li, G.-C.; Lo, T.W.; Lei, D.Y. Polarization-resolved optical response of plasmonic particle-on-film nanocavities. *J. Opt.* **2018**, *20*, 024010, doi:10.1088/2040-8986/aaa1bc.
71. Cao, Z.; He, Y.; Cheng, Y.; Zhao, J.; Li, G.; Gong, Q.; Lu, G. Nano-gap between a gold tip and nanorod for polarization dependent surface enhanced Raman scattering. *Appl. Phys. Lett.* **2016**, *109*, 233103, doi:10.1063/1.4971832.
72. Haidar, I.; Levi, G.; Mouton, L.; Aubard, J.; Grand, J.; Lau-Truong, S.; Neuville, D.R.; Felidj, N.; Boubekeur-Lecaque, L. Highly stable silica-coated gold nanorods dimers for solution-based SERS. *Phys. Chem. Chem. Phys.* **2016**, *18*, 32272–32280, doi:10.1039/c6cp06218k.
73. Tang, L.; Li, S.; Han, F.; Liu, L.; Xu, L.; Ma, W.; Kuang, H.; Li, A.; Wang, L.; Xu, C. SERS-active Au@Ag nanorod dimers for ultrasensitive dopamine detection. *Biosens. Bioelectron.* **2015**, *71*, 7–12, doi:10.1016/j.bios.2015.04.013.
74. Aswathy, V.G.; Patra, P.P.; Kumar, G.V.P. Geometry-dependent anti-Stokes SERS radiation patterns from gold nanorod dimers. *J. Opt.* **2015**, *17*, 114011, doi:10.1088/2040-8978/17/11/114011.
75. Maune, H.T.; Han, S.-P.; Barish, R.D.; Bockrath, M.; Goddard, W.A., III; Rothemund, P.W.K.; Winfree, E. Self-assembly of carbon nanotubes into two-dimensional geometries using DNA origami templates. *Nat. Nanotechnol.* **2010**, *5*, 61–66, doi:10.1038/NNANO.2009.311.
76. Thacker, V.V.; Herrmann, L.O.; Sigle, D.O.; Zhang, T.; Liedl, T.; Baumberg, J.J.; Keyser, U.F. DNA origami based assembly of gold nanoparticle dimers for surface-enhanced Raman scattering. *Nat. Commun.* **2014**, *5*, 3448, doi:10.1038/ncomms4448.
77. Prinz, J.; Heck, C.; Ellerik, L.; Merk, V.; Bald, I. DNA origami based Au-Ag-core-shell nanoparticle dimers with single-molecule SERS sensitivity. *Nanoscale* **2016**, *8*, 5612–5620, doi:10.1039/c5nr08674d.
78. Pal, A.; Gohil, S.; Ghosh, S.; Ayyub, P. Polarization Selection Rules for Surface-Enhanced Raman Scattering from Anisotropic Microstructured Surfaces. *J. Phys. Chem. C* **2012**, *116*, 18504–18507, doi:10.1021/jp305136r.
79. Le Ru, E.C.; Grand, J.; Félidj, N.; Aubard, J.; Lévi, G.; Hohenau, A.; Krenn, J.R.; Blackie, E.; Etchegoin, P.G. Experimental Verification of the SERS Electromagnetic Model beyond the $|E|^4$ Approximation: Polarization Effects. *J. Phys. Chem. C* **2012**, *116*, 18504–18507, doi:10.1021/jp802219c.
80. Shegai, T.; Li, Z.; Dadosh, T.; Zhang, Z.; Xu, H.; Haran, G. Managing light polarization via plasmon-molecule interactions within an asymmetric metal nanoparticle trimer. *Proc. Natl. Acad. Sci. USA* **2008**, *105*, 16448–16453, doi:10.1073/pnas.0808365105.
81. Feng, C.; Zhao, Y.; Jiang, Y.J. Periodic array of regular Ag nanoparticle trimers: A reliable polarization-independent surface-enhanced Raman spectroscopy substrate. *RSC Adv.* **2016**, *6*, 83273–83279, doi:10.1039/c6ra14985e.
82. Shegai, T.; Brian, B.; Miljkovic, V.D.; Käll, M. Angular Distribution of Surface-Enhanced Raman Scattering from Individual Au Nanoparticle Aggregates. *ACS Nano* **2011**, *5*, 2036–2041, doi:10.1021/nn1031406.
83. Quinten, M. Local fields close to the surface of nanoparticles and aggregates of nanoparticles. *Appl. Phys. B-Lasers Opt.* **2001**, *73*, 245–255, doi:10.1007/s003400100650.
84. Dai, Z.; Xiao, X.; Wu, W.; Liao, L.; Mei, F.; Yu, X.; Guo, S.; Ying, J.; Ren, F.; Jiang, C. Side-to-side alignment of gold nanorods with polarization-free characteristic for highly reproducible surface enhanced Raman scattering. *Appl. Phys. Lett.* **2014**, *105*, 211902, doi:10.1063/1.4902812.
85. Shegai, T.O.; Haran, G. Probing the Raman Scattering Tensors of Individual Molecules. *J. Phys. Chem. B* **2006**, *110*, 2459–2461, doi:10.1021/jp055750f.
86. Shen, H.; Rouxel, J.; Guillot, N.; de la Chapelle, M.L.; Toury, T. Light polarization properties of three fold symmetry gold nanoparticles: Model and experiments. *C. R. Phys.* **2012**, *13*, 830–836, doi:10.1016/j.crhy.2012.09.004.
87. De la Chapelle, M.L.; Guillot, N.; Frémaux, B.; Shen, H.; Toury, T. Novel Apolar Plasmonic Nanostructures with Extended Optical Tunability for Sensing Applications. *Plasmonics* **2013**, *8*, 475–480, doi:10.1007/s11468-012-9413-x.

88. Reguera, J.; Langer, J.; de Aberasturi, D.J.; Liz-Marzán, L.M. Anisotropic metal nanoparticles for surface enhanced Raman scattering. *Chem. Soc. Rev.* **2017**, *46*, 3866–3885, doi:10.1039/c7cs00158d.
89. McLellan, J.M.; Li, Z.Y.; Siekkinen, A.R.; Xia, Y. The SERS Activity of a Supported Ag Nanocube Strongly Depends on Its Orientation Relative to Laser Polarization. *Nano Lett.* **2007**, *7*, 1013–1017, doi:10.1021/nl070157q.
90. Zhou, Y.; Zhou, X.; Park, D.J.; Torabi, K.; Brown, K.A.; Jones, M.R.; Zhang, C.; Schatz, G.C.; Mirkin, C.A. Shape-Selective Deposition and Assembly of Anisotropic Nanoparticles. *Nano Lett.* **2014**, *14*, 2157–2161, doi:10.1021/nl500471g.
91. Prezgot, D.; Ianoul, A. Probing the Anisotropy of SERS Enhancement with Spatially Separated Plasmonic Modes in Strongly Coupled Silver Nanocubes on a Dielectric Substrate. *J. Phys. Chem. C* **2015**, *119*, 3293–3301, doi:10.1021/jp512142a.
92. Luo, W.; van der Veer, W.; Chu, P.; Mills, D.L.; Penner, R.M.; Hemminger, J.C. Polarization-Dependent Surface Enhanced Raman Scattering from Silver 1D Nanoparticle Arrays. *J. Phys. Chem. C* **2008**, *112*, 11609–11613, doi:10.1021/jp803455s.
93. Hossain, M.K.; Huang, G.G.; Tanaka, Y.; Kaneko, T.; Ozaki, Y. Anisotropic gold nanoassembly: A study on polarization-dependent and polarization-selective surface-enhanced Raman scattering. *Phys. Chem. Chem. Phys.* **2015**, *17*, 4268–4276, doi:10.1039/c4cp05375c.
94. Hong, K.Y.; Brolo, A.G. Polarization-dependent surface-enhanced Raman scattering (SERS) from microarrays. *Anal. Chim. Acta* **2017**, *972*, 73–80, doi:10.1016/j.aca.2017.04.003.
95. Farcau, C.; Vallée, R.A.L.; Boca, S.; Astilean, S. Polarized SERS on linear arrays of silver half-shells: SERS re-radiation modulated by local density of optical states. *J. Opt.* **2015**, *17*, 114017, doi:10.1088/2040-8978/17/11/114007.
96. Liu, Y.; Fan, J.; Zhao, Y.P.; Shanmukh, S.; Dluhy, R.A. Angle dependent surface enhanced Raman scattering obtained from a Ag nanorod array substrate. *Appl. Phys. Lett.* **2006**, *89*, 173134, doi:10.1063/1.2369644.
97. Zhao, Y.P.; Chaney, S.B.; Shanmukh, S.; Dluhy, R.A. Polarized Surface Enhanced Raman and Absorbance Spectra of Aligned Silver Nanorod Arrays. *J. Phys. Chem. B* **2006**, *110*, 3153–3157, doi:10.1021/jp057406o.
98. Suzuki, M.; Maekita, W.; Wada, Y.; Nakajima, K.; Kimura, K.; Fukuota, T.; Mori, Y. In-line aligned and bottom-up Ag nanorods for surface-enhanced Raman spectroscopy. *Appl. Phys. Lett.* **2006**, *88*, 203121, doi:10.1063/1.2205149.
99. Ming, T.; Zhao, L.; Yang, Z.; Chen, H.; Sun, L.; Wang, J.; Yan, C. Polarization Dependence of Plasmon-Enhanced Fluorescence on Single Gold Nanorods. *Nano Lett.* **2009**, *9*, 3896–3903, doi:10.1021/nl902095q.
100. Jeong, D.H.; Zhang, Y.X.; Moskovits, M. Polarized Surface Enhanced Raman Scattering from Aligned Silver Nanowire Rafts. *J. Phys. Chem. B* **2004**, *108*, 12724–12728, doi:10.1021/jp037973g.
101. Zhou, W.; Hu, A.; Bai, S.; Ma, Y.; Bridges, D. Anisotropic optical properties of large-scale aligned silver nanowire films via controlled coffee ring effects. *RSC Adv.* **2015**, *5*, 39103–39109, doi:10.1039/c5ra04214c.
102. Chen, W.; Shi, H.; Wan, F.; Wang, P.; Gu, Z.; Li, W.; Ke, L.; Huang, Y. Substrate influence on the polarization dependence of SERS in crossed metal nanowires. *J. Mater. Chem. C* **2017**, *5*, 7028–7034, doi:10.1039/c7tc01385j.
103. Yoon, I.; Kang, T.; Choi, W.; Kim, J.; Yoo, Y.; Joo, S.-W.; Park, Q.-H.; Ihee, H.; Kim, B. Single Nanowire on a Film as an Efficient SERS-Active Platform. *J. Am. Chem. Soc.* **2009**, *131*, 758–762, doi:10.1021/ja807455s.
104. Chen, L.; Zhai, T.; Zhang, X.; Unger, C.; Koch, J.; Chichkov, B.N.; Klar, P.J. Polarization-dependent SERS effects of laser-generated sub-100 nm antenna structures. *Nanotechnology* **2014**, *25*, 265302, doi:10.1088/0957-4484/25/26/265302.
105. Kessentini, S.; Barchiesi, D.; D'Andrea, C.; Toma, A.; Guillot, N.; Di Fabrizio, E.; Fazio, B.; Marago, O.M.; Gucciardi, P.G.; de la Chapelle, M.L. Gold Dimer Nanoantenna with Slanted Gap for Tunable LSPR and Improved SERS. *J. Phys. Chem. C* **2014**, *118*, 3209–3219, doi:10.1021/jp409844y.
106. Liu, K.K.; Tadepalli, S.; Kumari, G.; Banerjee, P.; Tian, L.; Jain, P.K.; Singamaneni, S. Polarization-Dependent Surface-Enhanced Raman Scattering Activity of Anisotropic Plasmonic Nanorattles. *J. Phys. Chem. C* **2016**, *120*, 16899–16906, doi:10.1021/acs.jpcc.6b00955.
107. Zhang, X.; Wang, T.; Li, Y.; Fu, Y.; Guo, L. Optimally designed gold nanorattles with strong built-in hotspots and weak polarization dependence. *Nanotechnology* **2017**, *28*, 495201, doi:10.1088/1361-6528/aa96ea.

108. Zhu, J.; Zhang, Q.; Zhang, C.-H.; Weng, G.-J.; Zhao, J.; Li, J.-J.; Zhao, J.-W. Synthesis of colloidal gold nanobones with tunable negative curvatures at end surface and their application in SERS. *J. Nanopart. Res.* **2017**, *19*, 364, doi:10.1007/s11051-017-4058-5.
109. Lee, S.J.; Baik, J.M.; Moskovits, M. Polarization-Dependent Surface-Enhanced Raman Scattering from a Silver-Nanoparticle-Decorated Single Silver Nanowire. *Nano Lett.* **2008**, *8*, 3244–3247, doi:10.1021/nl801603j.
110. Dai, Z.G.; Xiao, X.H.; Liao, L.; Ying, J.J.; Mei, F.; Wu, W.; Ren, F.; Li, W.Q.; Jiang, C.Z. Enhanced and polarization dependence of surface-enhanced Raman scattering in silver nanoparticle array-nanowire systems. *Appl. Phys. Lett.* **2015**, *107*, 129901, doi:10.1063/1.4931366.
111. Li, J.; Zhang, W.; Lei, H.; Li, B. Ag nanowire/nanoparticle-decorated $MoS_2$ monolayers for surface-enhanced Raman scattering applications. *Nano Res.* **2018**, *11*, 2181–2189, doi:10.1007/s12274-017-1836-4.
112. Šubr, M.; Petr, M.; Kylián, O.; Štěpánek, J.; Veis, M.; Procházka, M. Anisotropic Optical Response of Silver Nanorod Arrays: Surface Enhanced Raman Scattering Polarization and Angular Dependences Confronted with Ellipsometric Parameters. *Sci. Rep.* **2017**, *7*, 4293, doi:10.1038/S41598-017-04565-0.
113. Nagai, Y.; Yamaguchi, T.; Kajikawa, K. Angular-Resolved Polarized Surface Enhanced Raman Spectroscopy. *J. Phys. Chem. C* **2012**, *116*, 9716–9723, doi:10.1021/jp211234p.
114. Ranjan, M.; Facsko, S. Anisotropic surface enhanced Raman scattering in nanoparticle and nanowire arrays. *Nanotechnology* **2012**, *23*, doi:10.1088/0957-4484/23/48/485307.
115. Khlebtsov, B.N.; Khlebtsov, N.G. Multipole Plasmons in Metal Nanorods: Scaling Properties and Dependence on Particle Size, Shape, Orientation, and Dielectric Environment. *J. Phys. Chem. C* **2007**, *111*, 11516–11527, doi:10.1021/jp072707e.
116. Gkogkou, D.; Schreiber, B.; Shaykhutdinov, T.; Ly, H.K.; Kuhlmann, U.; Gernert, U.; Facsko, S.; Hildebrandt, P.; Esser, N.; Hinrichs, K.; et al. Polarization- and Wavelength-Dependent Surface-Enhanced Raman Spectroscopy Using Optically Anisotropic Rippled Substrates for Sensing. *ACS Sens.* **2016**, *1*, 318–323, doi:10.1021/acssensors.5b00176.
117. Le Ru, E.C.; Meyer, S.A.; Artur, C.; Etchegoin, P.G.; Grand, J.; Lang, P.; Maurel, F. Experimental demonstration of surface selection rules for SERS on flat metallic surfaces. *Chem. Commun.* **2011**, *47*, 3903–3905, doi:10.1039/c1cc10484e.
118. Peyskens, F.; Dhakal, A.; Van Dorpe, P.; Le Thomas, N.; Baets, N. Surface Enhanced Raman Spectroscopy Using a Single Mode Nanophotonic-Plasmonic Platform. *ACS Photonics* **2016**, *3*, 102–108, doi:10.1021/acsphotonics.5b00487.
119. Dhakal, A.; Peyskens, F.; Clemmen, S.; Raza, A.; Wuytens, P.; Zhao, H.; Le Thomas, N.; Baets, R. Single mode waveguide platform for spontaneous and surface-enhanced on-chip Raman spectroscopy**.** *Interface Focus* **2016**, *6*, 20160015, doi:10.1098/rsfs.2016.0015.
120. Liu, Y.J.; Zhao, Y.P. Simple model for surface-enhanced Raman scattering from tilted silver nanorod array substrates. *Phys. Rev. B* **2008**, *78*, 075436, doi:10.1103/PhysRevB.78.075436.
121. Benson, M.; Shah, P.; Marciniak, M.; Sarangan, A.; Urbas, A. Optical Characterization of Silver Nanorod Thin Films Grown Using Oblique Angle Deposition. *J. Nanomater.* **2014**, 694982, doi:10.1155/2014/694982.
122. Perera, M.N.M.N.; Schmidt, D.; Gibbs, W.E.K.; Juodkazis, S.; Stoddart, P.R. Effective optical constants of anisotropic silver nanoparticle films with plasmonic properties. *Opt. Lett.* **2016**, *41*, 5495–5498, doi:10.1364/Ol.41.005495.
123. Grundmann, M.; Sturm, C.; Kranert, C.; Richter, S.; Schmidt-Grund, R.; Deparis, C.; Zuniga-Perez, J. Optically anisotropic media: New approaches to the dielectric function, singular axes, microcavity modes and Raman scattering intensities. *Phys. Status Solidi-Rapid Res. Lett.* **2017**, *11*, 1600295, doi:10.1002/pssr.201600295.
124. Oates, T.W.H.; Ranjan, M.; Facsko, S.; Arwin, H. Highly anisotropic effective dielectric functions of silver nanoparticle arrays. *Opt. Express* **2011**, *19*, 2014–2028, doi:10.1364/Oe.19.002014.
125. Jellison, G.E. Spectroscopic ellipsometry data analysis: Measured versus calculated quantities. *Thin Solid Films* **1998**, *313*, 33–39.
126. Jayawardhana, S.; Rosa, L.; Juodkazis, S.; Stoddart, P.R. Additional Enhancement of Electric Field in Surface-Enhanced Raman Scattering due to Fresnel Mechanism. *Sci. Rep.* **2013**, *3*, 2335, doi:10.1038/Srep02335.
127. Perera, M.N.M.N.; Gibbs, W.E.K.; Juodkazis, S.; Stoddart, P.R. Wavelength and refractive index dependence of the geometrical enhancement in surface-enhanced Raman scattering. *J. Raman Spectrosc.* **2017**, *48*, 1182–1189, doi:10.1002/jrs.5190.

128. Ming, T.; Chen, H.; Jiang, R.; Li, Q.; Wang, J. Plasmon-Controlled Fluorescence: Beyond the Intensity Enhancement. *J. Phys. Chem. Lett.* **2012**, *3*, 191–202, doi:10.1021/jz201392k.
129. Liaw, J.-W.; Tsai, H.-Y.; Huang, C.-H. Size-Dependent Surface Enhanced Fluorescence of Gold Nanorod: Enhancement or Quenching. *Plasmonics* **2012**, *7*, 543–553, doi:10.1007/s11468-012-9341-9.
130. Song, M.; Chen, G.X.; Liu, Y.; Wu, E.; Wu, B.T.; Zeng, H.P. Polarization properties of surface plasmon enhanced photoluminescence from a single Ag nanowire. *Opt. Express* **2012**, *20*, 22290–22297, doi:10.1364/Oe.20.022290.
131. Šubr, M.; Petr, M.; Kylián, O.; Kratochvíl, J.; Procházka, M. Large-scale Ag nanoislands stabilized by a magnetron-sputtered polytetrafluoroethylene film as substrates for highly sensitive and reproducible surface-enhanced Raman scattering (SERS). *J. Mater. Chem. C* **2015**, *3*, 11478–11485, doi:10.1039/c5tc02919h.
132. Le Ru, E.C.; Galloway, C.; Etchegoin, P.G. On the connection between optical absorption/extinction and SERS enhancements. *Phys. Chem. Chem. Phys.* **2006**, *8*, 3083–3087, doi:10.1039/b605292d.
133. Kleinman, S.L.; Sharma, B.; Blaber, M.G.; Henry, A.I.; Valley, N.; Freeman, R.G.; Natan, M.J.; Schatz, G.C.; Van Duyne, R.P. Structure Enhancement Factor Relationships in Single Gold Nanoantennas by Surface-Enhanced Raman Excitation Spectroscopy. *J. Am. Chem. Soc.* **2013**, *135*, 301–308, doi:10.1021/ja309300d.
134. Aizpurua, J.; Bryant, G.W.; Richter, L.J.; de Abajo, F.J.G.; Kelley, B.K.; Mallouk, T. Optical properties of coupled metallic nanorods for field-enhanced spectroscopy. *Phys. Rev. B* **2005**, *71*, 235420, doi:10.1103/Physrevb.71.235420.
135. Zhao, Y.P.; Chaney, S.B.; Zhang, Z.Y. Absorbance spectra of aligned Ag nanorod arrays prepared by oblique angle deposition. *J. Appl. Phys.* **2006**, *100*, 063527, doi:10.1063/1.2349549.
136. Baumberg, J.J.; Kelf, T.A.; Sugawara, Y.; Cintra, S.; Abdelsalam, M.E.; Bartlett, P.N.; Russell, A.E. Angle-Resolved Surface-Enhanced Raman Scattering on Metallic Nanostructured Plasmonic Crystals. *Nano Lett.* **2005**, *5*, 2262–2267, doi:10.1021/nl051618f.


# Attachment A6

A. Kuzminova, **M. Šubr**, O. Kylián, P. Kúš, J. Hanuš, M. Procházka: Nanostructured metal coatings for surface-enhanced Raman spectroscopy (SERS) prepared by means of low-pressure plasma. Under consideration for publication in Vacuum.

# Nanostructured metal coatings for surface-enhanced Raman spectroscopy (SERS) prepared by means of low-pressure plasma

Anna Kuzminova[1,*], Martin Šubr[2], Ondřej Kylián[1], Peter Kúš[3], Jan Hanuš[1], Marek Procházka[2]

[1] *Charles University, Faculty of Mathematics and Physics, Department of Macromolecular Physics, V Holešovičkách 2, 180 00 Prague, Czech Republic*

[2] *Charles University, Faculty of Mathematics and Physics, Institute of Physics, Ke Karlovu 5, 121 16 Prague, Czech Republic*

[3] *Charles University, Faculty of Mathematics and Physics, Department of Surface and Plasma Science, V Holešovičkách 2, 180 00 Prague, Czech Republic*

## Abstract

Development of surface-enhanced Raman scattering (SERS)-based sensing platforms has recently received increasing attention, which relates mainly to the improvement of the Raman detection sensitivity. The commonly studied SERS platforms are based on Ag or Au nanostructures that both exhibit localized surface plasmon resonance (LSPR) responsible for SERS enhancement in the visible spectral region. In this study we demonstrate that sequential deposition of Ag and Au significantly enhances SERS signal as compared to single metal nanostructured coatings, which is connected with the possibility to increase LSPR intensity without alteration of its position in the case of Au/Ag coatings.

**Keywords**: magnetron sputtering; surface-enhanced Raman scattering; SERS; nanostructured metallic coatings

[*] Corresponding author: annakuzminova84@gmail.com

## 1 Introduction

Since its discovery in the 70s of the last century [1-3], surface-enhanced Raman spectroscopy (SERS) has become one of the most attractive techniques for molecular detection [4,5]. This is not only due to the high molecular specificity but also due to very low detection limits of SERS that make this technique applicable even for the single-molecule detection [6-9]. It is generally recognized that although the short-distance chemical enhancement may promote the SERS effect [10], the dominant contribution to the SERS enhancement is due to the electromagnetic effect [11]. This phenomenon arises from enhanced optical fields due to the excitation of electromagnetic resonances in the nano-sized metal structures – localized surface plasmon resonances (LSPRs) [12]. However, in spite of enormous progress in the field of SERS in the last decades, the development of platforms for SERS still remains an active area of research that which to the possibility to produce robust, cheap, easy-to-use materials with sufficiently high enhancement of the Raman signal with good uniformity and spectral reproducibility.

Due to the fact that the LSPR and consequently the SERS enhancement can be tuned by the size and the shape of the metallic structures [13], main attention has been devoted to the production and testing of metallic nanomaterials with architectures that offer good SERS performance. Large number of different “top-down”, “bottom-up” or template-assisted routes were already applied for the production of single metal SERS-active nanostructures (usually silver, gold and copper that exhibit LSPR in the visible spectral region) [14]. They involve for instance nanorods, nanoparticles, nanoislands or nanoplates with different shapes [15-23]. However, properties of LSPR depend not only on the size and the shape of the produced nanostructures but also their chemical structure has to be considered. The advantage of silver is the biggest SERS scattering cross section out of all metals [11]. On the other hand, gold may be sometimes preferred due to its chemical inactivity, lower susceptibility to oxidation, high affinity to specific molecular groups and biocompatibility. From this point of view, bi-metallic materials prepared typically in the form of alloy or core@shell nanoparticles, nanorods or nanostructured films represent highly interesting option for the production of SERS-active materials with enhanced performance [24-36].

In this work we present simple, two-step strategy suitable for the production of bi-metallic Ag/Au nanostructured coatings which is based on the magnetron sputtering. As shown on the example of methylene blue, selected as a testing molecule in this study, sequential deposition

of Ag and Au significantly improves the SERS signal as compared to single metal nanostructured coatings.

## 2 Experimental

### 2. 1 Sample preparation

Silver and gold nanoislands were prepared in the deposition chamber equipped with a DC water-cooled magnetron with 2-inch Au or Ag targets (both sourced from Safina a.s.). For both metals, magnetron sputtering was performed in an Ar atmosphere at a pressure of 4.3 Pa. The distance between the DC magnetron and the sample holder was 7 cm. For the preparation of Au nanoislands the DC magnetron current was maintained at 50 mA (voltage on magnetron 315 V), while for the deposition of Ag nanoislands the DC magnetron current was 30 mA (voltage on magnetron 256 V). At these working conditions, the deposition rate of gold and silver nanoislands was 8 nm/min and 5 nm/min, respectively. The deposition time was limited to 30 seconds as longer deposition times led to the formation of a homogeneous continuous metal film. For the fabrication of bi-metallic samples, step-by-step deposition of Au or Ag nanoislands was performed. We used either glass slides (soda lime glass, 1 mm thick, Marienfeld) or one-side polished Si wafers (OnSemi, <100>, thickness 525 μm) as substrates. In order to ensure the same properties of deposited nanoisland films, both substrate materials were pre-coated with 40 nm thick C:F smooth films produced by RF magnetron sputtering from polytetrafluoroethylene (PTFE) target in an Ar atmosphere (details may be found in [23]).

### 2.2 Sample characterization

Optical properties of prepared samples were determined by UV-Vis spectrophotometer Hitachi U-3300 in the spectral range from 325 nm to 900 nm. Glass slides were used as substrates in this case. The surface morphology of prepared structures was investigated by scanning electron microscopy (SEM, TESCAN Mira 3, 15 kV accelerating voltage). The elemental composition of the produced nanostructures was determined from the X-ray photoelectron spectra (XPS) acquired by an XPS spectrometer that consists of Al Kα X-ray source (Specs, XR-50) and a hemispherical electron analyzer (Specs, Phoibos 100). The spectra were measured from 1100 eV to 0 eV with a pass energy 40 eV and energy step 0.5 eV.

### 2.3 SERS measurements

SERS testing was carried out using methylene blue (MB, Sigma-Aldrich) selected as a testing molecule. Si wafers were used as substrates in this case. Before SERS measurements, the substrates were dipped in MB aqueous solution diluted to the concentration of $1\times10^{-6}$ M for 30 minutes, then removed from the solution and dried by an air stream. SERS spectra were acquired at room temperature by means of an integrated confocal Raman microscopic system LabRam HR800 (Horiba Jobin-Yvon). The Raman microscope was equipped with a diffraction grating with 300 grooves/mm and a liquid nitrogen cooled CCD detector. He-Ne laser (wavelength 632.8 nm) was used as an excitation source. The beam was focused onto the sample to a spot of approximately 1 μm diameter, using a 100× objective with the numerical aperture 0.9. Scattered radiation was collected in a back-scattering geometry and filtered by an edge filter for Rayleigh rejection before focusing it onto the 100 μm entrance slit of the spectrometer. All SERS spectra presented in this study were collected with the laser power at the sample of 0.02 mW. For each sample, array of 10x10 spots (increment 5 μm) on the substrate was measured and statistically processed.

## 3 Results and Discussion

The first step of this study was the characterization of single metal nanostructured coatings from the point of view of their morphology and optical properties. In agreement with previous studies (e.g. [37-40]) island growth mode of Ag and Au nanoislands was observed. This growth mode supposes several consecutive phases [41,42]. In the initial one, the metallic atoms arriving from the gas phase diffuse on the substrate until they meet a second diffusing adatom and create a stable dimer. Such created dimers serve as condensation nuclei that capture new incoming atoms that in turn give rise to the many small nanoislands randomly distributed all over the substrate. As soon as the surface density of formed nanoislands reaches a sufficiently large value, i.e. when the probability that a diffusing adatom encounters already formed nanoisland is bigger than the probability that the diffusing adatom meets one of other diffusing adatoms, any further deposition will lead to the island growth. In other words, in this second phase, created nanoislands grow in their size with increasing fluence of metallic atoms (deposition time). Examples of nanostructures produced in this phase are presented in **fig. 1A** and **fig. 2A** for silver and gold, respectively. Moreover, due to the non-wetting behaviour of gold and silver on fluorocarbon substrates the growing nanoislands tend to minimize their interface to the surface which leads to the formation of structures with hemi-

spheroidal geometry [43]. When the fraction of surface covered by nanoislands reaches about one half, the third phase starts in which the nanoislands start to coalesce. This leads both to the reduction of the number of nanoislands and to the increase in their size. Examples of nanostructures typical for this phase are shown in **fig. 1B** and **fig. 2B**. At this point it is important to note that for approximately the same amount of deposited gold and silver[†], formed Ag and Au structures are very similar – according to the statistical analysis of acquired SEM images the surface coverage for Au films deposited for 12 seconds and Ag films deposited for 25 seconds is in the range from 55% to 61% and the mean size of individual grains is between 500-700 $nm^2$. Further prolongation of the deposition time subsequently leads to the formation of interconnected metallic network and finally to the creation of a continuous film.

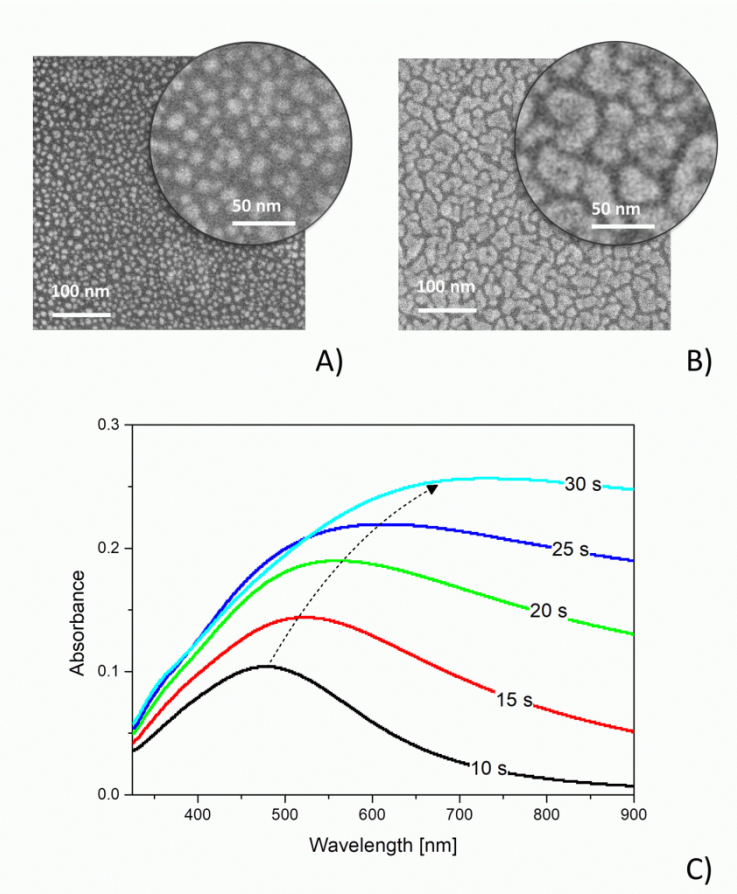


**Figure 1**. SEM images of Ag nanostructures produced by magnetron sputtering with deposition time A) 10 seconds and B) 25 seconds. C) UV-Vis spectra of produced Ag coatings for different deposition times.

[†] The difference in deposition times for Ag and Au coatings is due to the almost two times higher deposition rate of gold as compared to silver at the selected operational conditions.

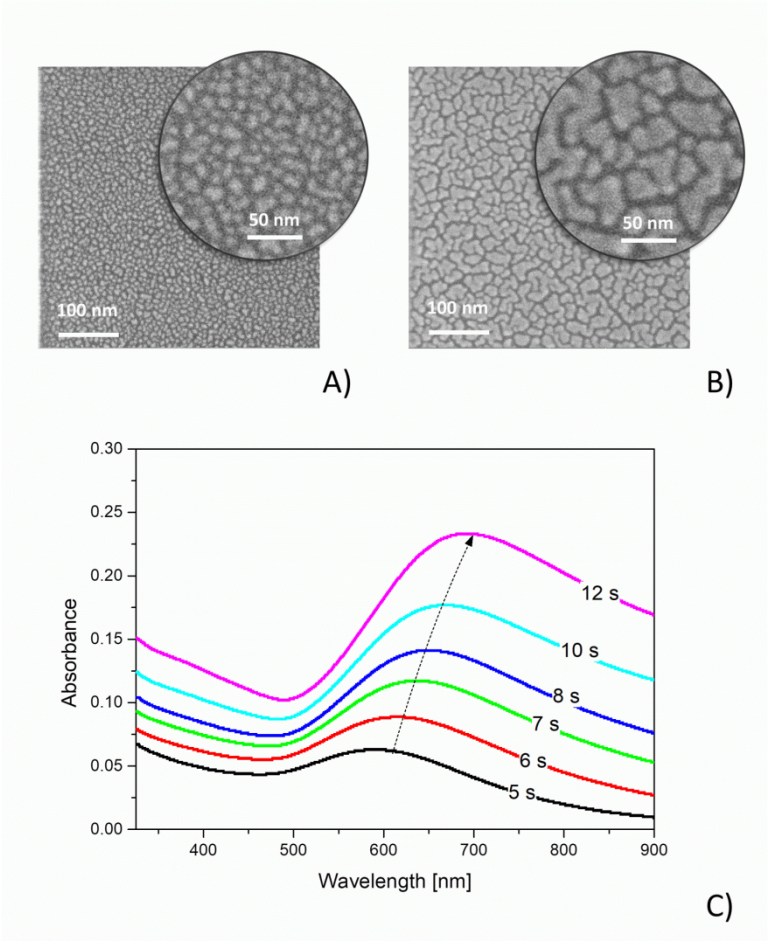


**Figure 2.** SEM images of Au nanostructures produced by magnetron sputtering with deposition time A) 6 seconds and B) 12 seconds. C) UV-Vis spectra of produced Au coatings for different deposition times.

The above described evolution of the morphology of Ag and Au films with the deposition time has a strong impact on their optical properties. As depicted in **fig. 1C** and **fig. 2C**, increasing deposition time causes for both metals shift in the position of the LSPR towards the higher wavelengths. Observed red-shift in the LSPR is consistent with previous studies that reported variation in the LSPR peak in dependence on the size [44] and mutual distance between individual metallic nanostructures [45]. This phenomenon is rather advantageous with respect to the possibility to tailor, at least in a certain spectral range, the position of the LSPR peak and thus to optimize the SERS performance of the coatings depending on the excitation wavelength and a tested biomolecule used. Indeed, significant variation in intensity of the SERS signal with the change of the position of the LSPR peak was observed (see **Fig. 3**). For both metals the signal initially increases with the deposition time which is accompanied by the shift of the LSPR peak and increase in its intensity. The optimal LSPR

position was found to be between 600-680 nm and 670-697 nm for silver and gold, respectively. In the latter case (gold), the maximal SERS signal seems to be red-shifted from the excitation wavelength (632.8 nm), which was observed previously in SERS study of porphyrin adsorbed on immobilized Au nanoparticles [46]. In the case of silver, evaluation of the optimum LSPR condition is less precise as small increase in the deposition time leads to significant change in the spectral position of the LSPR maximum. This is also due to rather broad LSPR curves. Under the optimum conditions, the maximal SERS signal on silver is ~ 5× bigger in comparison to gold, which is in agreement with previous studies [5].

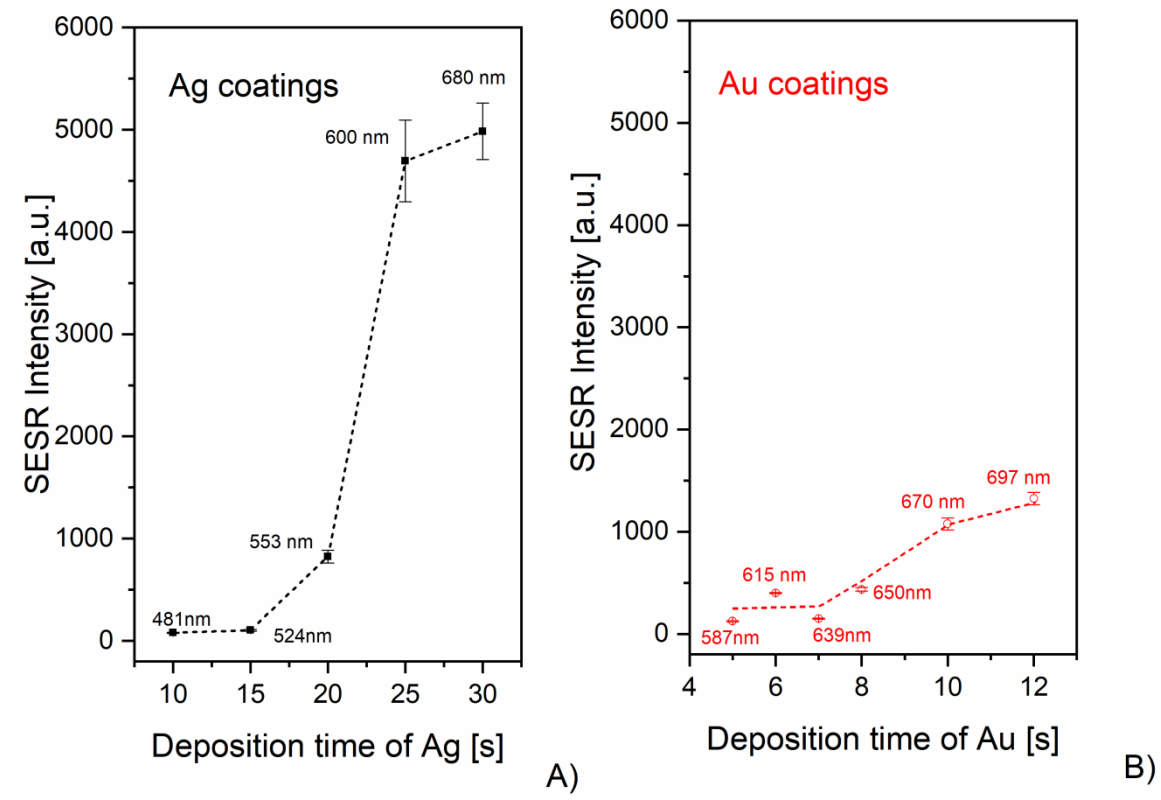


**Figure 3.** SERS intensity of MB peak at 1632 $cm^{-1}$ that corresponds to vibrations of C-C ring on A) silver and B) gold nanostructured coatings. The numbers display the wavelength of the maximum of the LSPR peak.

The results presented in **fig. 1C** and **fig. 2C** clearly show the main limitation of magnetron sputtering of single metals – it is impossible by this technique to control independently the position and the intensity of LSPR peak as these two parameters are coupled. In order to test the possibility to vary these two parameters independently by use of bi-metallic coatings, further experiments were focused on the two-step deposition procedure. The substrates were

first seeded with gold nanostructures that were in the second step overcoated with silver. In these preparations the deposition time of the base gold layer was fixed at 12 seconds, i.e. the deposition time that offered the highest SERS signal of pure Au coating, and only the deposition time of Ag was varied (from 3 up to 30 seconds). The examples of SEM images of such produced nanostructured coatings are given in **fig. 4A** and **fig. 4B**. As can be seen, the resulting structures had almost the same character as the bare Au coating deposited for 12 seconds (compare with **fig. 2B**) independently of the deposition time of silver. Furthermore, it was found that the surface area covered by the Au/Ag nanostructures stayed for almost all deposition times very close to the one observed for Au. Only in the case of the longest deposition times a slight increase in the surface coverage by Au/Ag was observed (e.g. for Au/Ag with 12 seconds of deposition of Au followed by 25 seconds deposition of Ag the surface coverage was 64%). Analogously also the mean size of the grains remained comparable for Au and Au/Ag coatings. In other words, the nanostructures do not grow laterally, but they grow mainly in the direction perpendicular to the substrate. This was confirmed by AFM measurements that revealed a slight increase in the mean height of the coatings with increasing deposition time of Ag on Au nanoislands (data not shown). This finding may be explained by the assumption that silver preferentially grows on gold nanoislands and does not fill the voids in between them. It is consistent also with the XPS data. As depicted in **fig. 5,** the increasing deposition time of Ag on top of Au coatings causes an increase in Ag/Au ratio, but at the same time the signal coming from F that is present in the base layer stays constant, i.e. the C:F layer is still visible by highly surface sensitive XPS.

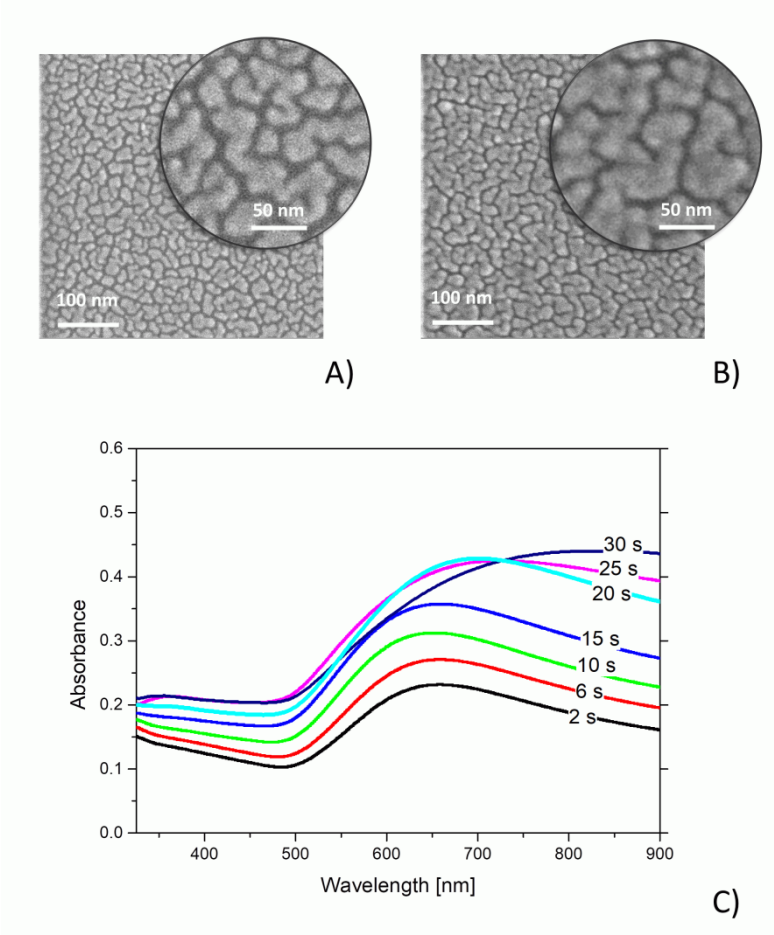


**Figure 4.** SEM images of Au nanostructures overcoated with Ag. Deposition time of gold was 12 seconds and deposition time of silver was A) 10 seconds and B) 25 seconds. C) UV-Vis spectra of produced Au/Ag coatings with fixed deposition time of pre-coated gold (12 seconds) and different deposition times of silver overcoat.

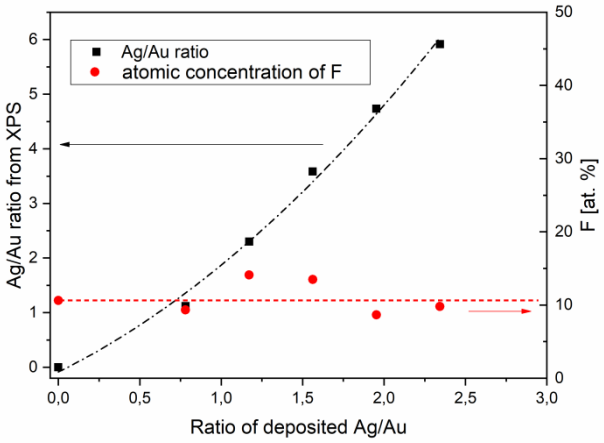


**Figure 5.** Ag/Au ratio and atomic concentration of fluorine as measured by means of XPS on the coatings prepared using fixed Au deposition time (12 seconds) and different deposition times of silver overcoat.

The fact that the Ag deposition over Au nanostructures does not increase dramatically the lateral size of resulting nanostructures implies that also the mean distance between the individual nanoislands remains almost unchanged. Furthermore, as the effective thickness of deposited silver corresponds only to 2 nm for the longest Ag deposition time (30 seconds), we can conclude that also the height of produced nanoislands is not substantially changed. This has a strong impact on the optical properties of produced coatings. In agreement with the previous study [47], owing to the good miscibility of silver and gold, Au/Ag coatings exhibit a single-peak LSPR (see **Fig. 4C**). In addition, due to the very similar morphology of Au/Ag nanostructures with different Ag fraction, the position of LSPR peak does not change except for the longest Ag deposition times for which slight deviation in the size of Au/Ag nanoislands was observed. The only change is thus for Ag deposition times up to approximately 20 seconds when the LSPR intensity increases with increasing amount of deposited silver.

The possibility to obtain the higher LSPR intensity without the necessity to change its position enables to improve also the SERS performance of the produced nanomaterial. This is demonstrated in **fig. 6A** where intensities of MB peak at 1632 $cm^{-1}$ are plotted in dependence on the deposition time of silver over Au nanostructures. As can be seen, the SERS signal rapidly rises when the silver fraction in the nanostructures increases. After reaching the maximal value for the deposition time about 15 seconds, the detected signal starts to decrease with further addition of Ag. This may be explained by slight shift of the LSPR from its optimal position. In order to highlight the advantageous properties of bi-metallic coatings SERS spectra recorded on optimized Ag, Au and Au/Ag nanostructures are presented in **fig. 6B**. According to these spectra, Au/Ag nanostructured films offer almost 4 – 20× higher SERS signals as compared to single silver and gold coatings, respectively.

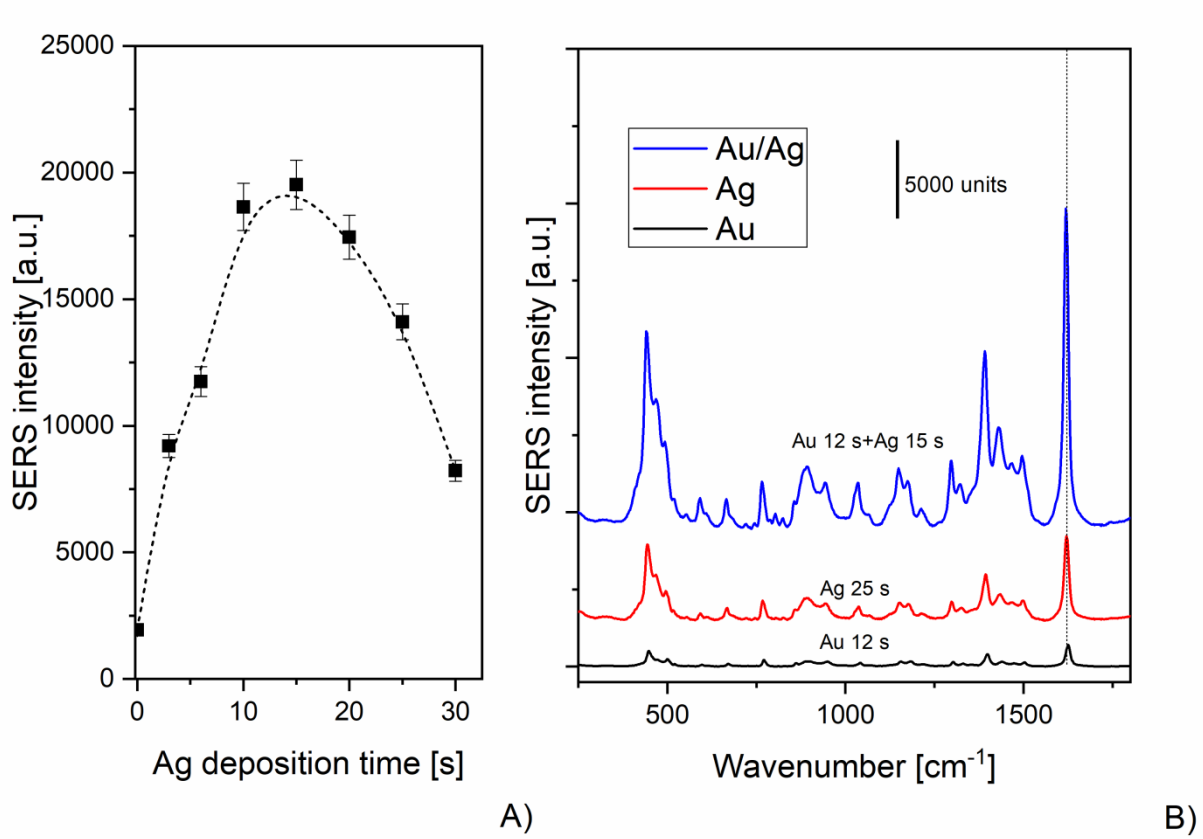


**Figure 6.** A) Dependence of MB SERS intensity (peak at 1632 $cm^{-1}$) on the deposition time of silver for Au/Ag bi-metallic nanostructured coatings. B) Comparison of SERS spectra of MB for optimized Au, Ag and Au/Ag nanostructured coatings.

## 4 Conclusion

To conclude, we have demonstrated that it is possible in the case of Au/Ag bi-metallic nanostructured coatings to tune in a certain range independently the position and the intensity of LSPR peak. It is not attainable for single metal Ag and Au coatings prepared by the same technique. This difference is connected with different growth modes of Ag and Au coatings on one hand and Au/Ag coatings on the other hand. In the case of single metals, increasing deposition time leads to substantial increase in the size of formed nanoislands and to lowering of the mean distance between them. Both of these effects in turn contribute to the bathochromic shift of LSPR. In contrast, when Ag is deposited on a substrate pre-coated with Au nanoislands, no significant variation in the sizes and distances between individual nanoislands was observed for short Ag deposition times. It is due to the preferential vertical growth of Ag on top of Au nanostructures. The same morphology of different Au/Ag coatings then results only in the change of LSPR intensity and has negligible influence on its spectral position. Finally, the possibility to increase the LSPR intensity with fixed LSPR position by

Au/Ag coatings was demonstrated. It also improved the SERS performance as the Au/Ag bi-metallic coatings offered much higher SERS signal as compared to Ag and Au ones.

**Acknowledgements**

This research was funded by Czech Science Foundation P205/12/G118, Charles University research project GA UK No. 572216 and Charles University Research Centre program UNCE/SCI/010.

[1] M. Fleischmann, P.J. Hendra, A.J. McQuillan, Raman spectra of pyridine adsorbed at a silver electrode, Chem. Phys. Lett. 26 (1974) 163–166. doi:10.1016/0009-2614(74)85388-1.

[2] M.G. Albrecht, J.A. Creighton, Anomalously intense Raman spectra of pyridine at a silver electrode, J. Am. Chem. Soc. 99 (1977) 5215–5217. doi:10.1021/ja00457a071.

[3] D.L. Jeanmaire, R.P. Van Duyne, Surface raman spectroelectrochemistry, J. Electroanal. Chem. Interfacial Electrochem. 84 (1977) 1–20. doi:10.1016/S0022-0728(77)80224-6.

[4] B. Sharma, R.R. Frontiera, A.-I. Henry, E. Ringe, R.P. Van Duyne, SERS: Materials, applications, and the future, Mater. Today. 15 (2012) 16–25. doi:10.1016/S1369-7021(12)70017-2.

[5] M. Procházka, Surface-Enhanced Raman Spectroscopy: Bioanalytical, Biomolecular and Medical Applications. Springer, Switzerland, 2016, ISBN: 978-3-319-23990-3.

[6] K. Kneipp, Y. Wang, H. Kneipp, L.T. Perelman, I. Itzkan, R.R. Dasari, M.S. Feld, Single Molecule Detection Using Surface-Enhanced Raman Scattering (SERS), Phys. Rev. Lett. 78 (1997) 1667–1670. doi:10.1103/PhysRevLett.78.1667.

[7] A.M. Michaels, M. Nirmal, L.E. Brus, Surface Enhanced Raman Spectroscopy of Individual Rhodamine 6G Molecules on Large Ag Nanocrystals, J. Am. Chem. Soc. 121 (1999) 9932–9939. doi:10.1021/ja992128q.

[8] H. Xu, E.J. Bjerneld, M. Käll, L. Börjesson, Spectroscopy of Single Hemoglobin Molecules by Surface Enhanced Raman Scattering, Phys. Rev. Lett. 83 (1999) 4357–4360. doi:10.1103/PhysRevLett.83.4357.

[9] S. Nie and S.R. Emory, Probing single molecules and single nanoparticles by surface-

enhanced Raman scattering, Science 275 (1997) 1102-1106. doi: 10.1126/science.275.5303.1102

[10] A. Otto, The 'chemical' (electronic) contribution to surface-enhanced Raman scattering, J. Raman. Spectrosc. 36 (2005) 497-509. doi: 10.1002/jrs.1355.

[11] E.C. Le Ru and P.G. Etchegoin, Principles of surface enhanced Raman spectroscopy and related plasmonic effects, Elsevier, Amsterdam, 2009, ISBN: 978-0-444-52779-0.

[12] M. Moskovits, Surface-enhanced spectroscopy, Rev. Mod. Phys. 57 (1985) 783–826. doi:10.1103/RevModPhys.57.783.

[13] T.R. Jensen, M.D. Malinsky, C.L. Haynes, R.P. Van Duyne, Nanosphere lithography: tunable localized surface plasmon resonance spectra of silver nanoparticles, J. Phys. Chem. B 104, (2000) 10549-10556. doi: 10.1021/jp002435e.

[14] P. Mosier-Boss, Review of SERS Substrates for Chemical Sensing, Nanomaterials. 7 (2017) 142. doi:10.3390/nano7060142.

[15] B. Nikoobakht, M.A. El-Sayed, Surface-enhanced Raman scattering studies on aggregated gold nanorods, J. Phys. Chem. A. 107 (2003) 3372–3378. doi:10.1021/jp026770.

[16] S.B. Chaney, S. Shanmukh, R.A. Dluhy, Y.-P. Zhao, Aligned silver nanorod arrays produce high sensitivity surface-enhanced Raman spectroscopy substrates, Appl. Phys. Lett. 87 (2005) 31908. doi:10.1063/1.1988980.

[17] M. Šubr, M. Petr, V. Peksa, O. Kylián, J. Hanuš, M. Procházka, Ag Nanorod Arrays for SERS: Aspects of Spectral Reproducibility, Surface Contamination, and Spectral Sensitivity, J. Nanomater. 2015 (2015) 1–7. doi:10.1155/2015/729231.

[18] C.G. Khoury, T. Vo-Dinh, Gold Nanostars For Surface-Enhanced Raman Scattering: Synthesis, Characterization and Optimization, J. Phys. Chem. C. 112 (2008) 18849–18859. doi:10.1021/jp8054747.

[19] Y. Yang, S. Matsubara, L. Xiong, T. Hayakawa, M. Nogami, Solvothermal Synthesis of Multiple Shapes of Silver Nanoparticles and Their SERS Properties, J. Phys. Chem. C. 111 (2007) 9095–9104. doi:10.1021/jp068859b.

[20] P. Žvátora, P. Řezanka, V. Prokopec, J. Siegel, V. Švorčík, V. Král, Polytetrafluorethylene-Au as a substrate for surface-enhanced Raman spectroscopy,

Nanoscale Res. Lett. 6 (2011) 366. doi:10.1186/1556-276X-6-366.

[21] F. Tian, F. Bonnier, A. Casey, A.E. Shanahan, H.J. Byrne, Surface enhanced Raman scattering with gold nanoparticles: effect of particle shape, Anal. Methods. 6 (2014) 9116–9123. doi:10.1039/C4AY02112F.

[22] I. Pastoriza-Santos, L.M. Liz-Marzán, Colloidal silver nanoplates. State of the art and future challenges, J. Mater. Chem. 18 (2008) 1724. doi:10.1039/b716538b.

[23] M. Šubr, A. Kuzminova, O. Kylián, M. Procházka, Surface-enhanced Raman scattering (SERS) of riboflavin on nanostructured Ag surfaces: The role of excitation wavelength, plasmon resonance and molecular resonance, Spectrochim. Acta Part A Mol. Biomol. Spectrosc. 197 (2018) 202–207. doi:10.1016/j.saa.2018.01.055.

[24] O. Olea-Mejía, M. Fernández-Mondragón, G. Rodríguez-de la Concha, M. Camacho-López, SERS-active Ag, Au and Ag–Au alloy nanoparticles obtained by laser ablation in liquids for sensing methylene blue, Appl. Surf. Sci. 348 (2015) 66–70. doi:10.1016/j.apsusc.2015.01.075.

[25] Q. Han, C. Zhang, W. Gao, Z. Han, T. Liu, C. Li, Z. Wang, E. He, H. Zheng, Ag-Au alloy nanoparticles: Synthesis and in situ monitoring SERS of plasmonic catalysis, Sensors Actuators B Chem. 231 (2016) 609–614. doi:10.1016/j.snb.2016.03.068.

[26] M. Vinod, K.G. Gopchandran, Au, Ag and Au:Ag colloidal nanoparticles synthesized by pulsed laser ablation as SERS substrates, Prog. Nat. Sci. Mater. Int. 24 (2014) 569–578. doi:10.1016/j.pnsc.2014.10.003.

[27] E. Chaffin, R.T. O'Connor, J. Barr, X. Huang, Y. Wang, Dependence of SERS enhancement on the chemical composition and structure of Ag/Au hybrid nanoparticles, J. Chem. Phys. 145 (2016) 54706. doi:10.1063/1.4960052.

[28] M. Fan, F.-J. Lai, H.-L. Chou, W.-T. Lu, B.-J. Hwang, A.G. Brolo, Surface-enhanced Raman scattering (SERS) from Au:Ag bimetallic nanoparticles: the effect of the molecular probe, Chem. Sci. 4 (2013) 509–515. doi:10.1039/C2SC21191B.

[29] B. Khlebtsov, V. Khanadeev, N. Khlebtsov, Surface-enhanced Raman scattering inside Au@Ag core/shell nanorods, Nano Res. 9 (2016) 2303–2318. doi:10.1007/s12274-016-1117-7.

[30] Y. Zhang, C. Yang, B. Xue, Z. Peng, Z. Cao, Q. Mu, L. Xuan, Highly effective and chemically stable surface enhanced Raman scattering substrates with flower-like 3D

Ag-Au hetero-nanostructures, Sci. Rep. 8 (2018) 898. doi:10.1038/s41598-018-19165-9.

[31] Y. Fleger, M. Rosenbluh, Surface Plasmons and Surface Enhanced Raman Spectra of Aggregated and Alloyed Gold-Silver Nanoparticles, Res. Lett. Opt. 2009 (2009) 1–5. doi:10.1155/2009/475941.

[32] J. Tang, Q. Zhang, C. Zeng, S.-Q. Man, Preparation of large-area surface-enhanced Raman scattering active Ag and Ag/Au nanocomposite films, Appl. Phys. A. 111 (2013) 1099–1105. doi:10.1007/s00339-013-7568-8.

[33] L. Zhang, C. Wang, Y. Zhang, A facile strategy to synthesize bimetallic Au/Ag nanocomposite film by layer-by-layer assembly technique, Appl. Surf. Sci. 258 (2012) 5312–5318. doi:10.1016/j.apsusc.2012.01.101.

[34] R.A. Alvarez-Puebla, J.P. Bravo-Vasquez, P. Cheben, D.-X. Xu, P. Waldron, H. Fenniri, SERS-active Ag/Au bimetallic nanoalloys on Si/SiOx, J. Colloid Interface Sci. 333 (2009) 237–241. doi:10.1016/j.jcis.2009.01.070.

[35] L. Zhang, J. Fang, C. Wang, T. Xu, Y. Jin, Fabrication of Superior Au–Ag Composites Surface-Enhanced Raman Scattering Active Substrates Based on One-Step Method of Chemical Etching, Nano. 11 (2016) 1650080. doi:10.1142/S1793292016500806.

[36] H.-Z. Zhao, Y. Xu, C.-Y. Wang, R. Wang, S.-T. Xiang, L. Chen, Design and fabrication of a microfluidic SERS chip with integrated Ag film@nanoAu, RSC Adv. 6 (2016) 14105–14111. doi:10.1039/C5RA25018H.

[37] C. Charton, M. Fahland, Growth of Ag films on PET deposited by magnetron sputtering, Vacuum. 68 (2002) 65–73. doi:10.1016/S0042-207X(02)00289-0.

[38] V. Švorčík, J. Siegel, P. Slepička, V. Kotál, J. Švorčíková, M. Špirková, Au nanolayers deposited on polyethyleneterephtalate and polytetrafluorethylene degraded by plasma discharge, Surf. Interface Anal. 39 (2007) 79–85. doi:10.1002/sia.2512.

[39] P. Asanithi, S. Chaiyakun, P. Limsuwan, Growth of Silver Nanoparticles by DC Magnetron Sputtering, J. Nanomater. 2012 (2012) 1–8. doi:10.1155/2012/963609.

[40] J. Kratochvíl, A. Kuzminova, O. Kylián, H. Biederman, Comparison of magnetron sputtering and gas aggregation nanoparticle source used for fabrication of silver nanoparticle films, Surf. Coatings Technol. 275 (2015) 296–302. doi:10.1016/j.surfcoat.2015.05.003.

[41] J.A. Venables, G.D.T. Spiller, M. Hanbucken, Nucleation and growth of thin films, Reports Prog. Phys. 47 (1984) 399–459. doi:10.1088/0034-4885/47/4/002.

[42] H. Brune, Microscopic view of epitaxial metal growth: nucleation and aggregation, Surf. Sci. Rep. 31 (1998) 125–229. doi:10.1016/S0167-5729(99)80001-6.

[43] M. Schwartzkopf, A. Buffet, V. Körstgens, E. Metwalli, K. Schlage, G. Benecke, J. Perlich, M. Rawolle, A. Rothkirch, B. Heidmann, G. Herzog, P. Müller-Buschbaum, R. Röhlsberger, R. Gehrke, N. Stribeck, S. V. Roth, From atoms to layers: in situ gold cluster growth kinetics during sputter deposition, Nanoscale. 5 (2013) 5053. doi:10.1039/c3nr34216f.

[44] K.L. Kelly, E. Coronado, L.L. Zhao, G.C. Schatz, The optical properties of metal nanoparticles: the influence of size, shape, and dielectric environment, J. Phys. Chem. B 107 (2003) 668-677, doi: 10.1021/jp026731y.

[45] P.K. Jain, W. Huang, M.A. El-Sayed, On the universal scaling behavior of the distance decay of plasmon coupling in metal nanoparticle Pairs: a plasmon ruler equation, Nano Lett. 7 (2007) 2080-2088, doi: 10.1021/nl071008a.

[46] N.Hajduková-Šmídová, M. Procházka, M. Osada, SE(R)RS excitation profile of free-base 5,10,15,20-tetrakis(1-methyl-4-pyridyl) porphyrin on immobilized gold nanoparticles, Vib. Spectrosc. 62 (2012) 115-120. doi: 10.1016/j.vibspec.2012.04.007.

[47] M. Petr, O. Kylián, A. Kuzminova, J. Kratochvíl, I. Khalakhan, J. Hanuš, H. Biederman, Noble metal nanostructures for double plasmon resonance with tunable properties, Opt. Mater. (Amst). 64 (2017) 276–281. doi:10.1016/j.optmat.2016.12.021.